
Exploring the electrical and physical properties of 2D atomically layered materials with advanced scanning probe microscopy

Adrian J. Peasey

2022

A thesis submitted to the University of Manchester for the degree of
Doctor of Philosophy in the Faculty of Science and Engineering

School of Engineering
Department of Computer Science

Contents

List of Figures	8
List of Tables	14
Abstract	15
Declaration of Originality	16
Copyright Statement	17
1 Introduction	18
1.1 Atomic force microscopy	18
1.2 FeRh	19
1.3 Multiferroics	19
1.4 Objectives and thesis outline	20
2 Fundamental background phenomena	22
2.1 Introduction to crystals and lattices	22
2.1.1 Unit cells and lattice vectors	22
2.1.2 Miller indices	24
2.1.3 Point groups, space groups, and crystals	24
2.1.4 Hermann-Mauguin notation	25
2.2 Crystal systems	27
2.2.1 The triclinic system	27
2.2.2 The monoclinic system	28
2.2.3 The orthorhombic system	30
2.2.4 The tetragonal system	31
2.2.5 The hexagonal family	32
2.2.6 The cubic system	34
2.3 Named crystal prototypes	35
2.3.1 Perovskites	35

2.3.2	Caesium-Chloride	39
2.3.3	Heusler alloys	40
2.4	Introduction to magnetism and spintronics	41
2.4.1	Magnetic dipoles	42
2.4.2	Magnetic fields	43
2.5	Atomic origins of magnetic ordering	44
2.5.1	Classical dipole interaction energy	44
2.5.2	Exchange interaction energy	46
2.5.3	RKKY interaction	51
2.5.4	Atomic orbitals and magnetic dipole ordering	52
2.6	Induced magnetisation	53
2.7	Ordered magnetisation	54
2.7.1	Ferromagnetism	54
2.7.2	Antiferromagnetism	56
2.7.3	Ferrimagnetism	57
2.7.4	Spin-flop transitions	57
2.7.5	Spin canting	58
2.8	Magnetic domains	59
2.8.1	Magnetostatic energy and anisotropy	59
2.8.2	Formation of domains	60
2.8.3	Domain walls	62
2.8.4	Domain nucleation	63
2.9	Dependence of crystal properties on magnetisation	63
2.9.1	Elastic response	63
2.9.2	Magnetoresistance	65
2.10	Introduction to electric fields and polarisation	68
2.10.1	Electric dipoles	68
2.10.2	Electric fields	69
2.11	Electrostriction	69
2.12	Piezoelectricity	71
2.12.1	The piezoelectric coefficient	72
2.12.2	Pyroelectricity	74
2.12.3	Relation to crystallographic point groups	75
2.13	Ordered polarisation	75
2.13.1	Ferroelectricity	76
2.13.2	Landau theory	82

2.13.3	Relaxor ferroelectrics	84
2.14	Multiferroic materials	85
2.14.1	Ferroic properties	85
2.14.2	Magnetoelectric coupling	86
2.14.3	Artificial multiferroics	87
2.14.4	Use of multiferroic devices	87
2.15	Summary	88
3	Materials for artificial multiferroics	89
3.1	Phase diagram of FeRh	89
3.2	Metamagnetic transition of equiatomic FeRh	91
3.2.1	Magnetisation curves	92
3.2.2	Tuning the metamagnetic transition	93
3.3	FeRh metamagnetic phase change properties	94
3.3.1	Potential applications	97
3.4	FeRh growth and patterning	98
3.4.1	Thin film growth optimisation	98
3.4.2	Noble ion irradiation of FeRh	99
3.5	FeRh oxide layer	100
3.6	Phase diagram of PMN-PT	101
3.6.1	The rhombohedral boundary	103
3.7	Piezoelectric behaviour of PMN-PT	103
3.7.1	Effect of PT ratio	104
3.7.2	Ferroelectric coercive field dependence	106
3.8	PMN-PT observations	107
3.8.1	Effect of polishing PMN-PT	107
3.8.2	Weakness under strain	108
3.9	Summary	108
4	Fundamental principles of atomic force microscopy	109
4.1	Introduction to atomic force microscopy	109
4.1.1	Tip geometry	112
4.1.2	Probe calibration	115
4.1.3	Lock-in amplifiers	116
4.2	Contact and tapping AFM modes	117
4.3	Magnetic force microscopy	118
4.4	Quantitative nanomechanics	120

4.4.1	The Sneddon and Hertzian models	122
4.4.2	Tip-sample contact area	124
4.4.3	Characterising elastic modulus using AFM	125
4.4.4	The DMT and JKR models	126
4.5	PeakForce and DataCube	126
4.6	Measurements of electrical resistivity	127
4.6.1	Resistive heating	130
4.7	Kelvin probe force microscopy	133
4.7.1	Probe capacitance and capacitive forces	135
4.8	Piezoresponse force microscopy	137
4.8.1	PFM phase	137
4.8.2	PFM amplitude	139
4.8.3	Piezoelectric resonance	141
4.8.4	High-voltage PFM	141
4.9	The nanoscope Python package	143
4.10	Sample preparation for AFM measurements	144
4.11	Thermal measurement stage	145
4.12	Summary	147
5	Metallic resistivity characterisation on the AFM	148
5.1	Motivation and aims	148
5.2	Sources of resistance	149
5.2.1	Discussion of values and comparison of probes	153
5.2.2	Limitations of existing electrical resistivity characterisation techniques	154
5.3	Resistive heating of the AFM probe	155
5.3.1	Simple modelling of Joule heating	155
5.3.2	Preece equation applied to an AFM probe	157
5.3.3	Discussion of resistive heating and choice of probe	157
5.4	Setpoint and spatial resolution	158
5.4.1	Spatial resolution of the measurement	159
5.5	Surface contamination and oxide layers	159
5.6	Measuring the electrical resistance of metallic surfaces	163
5.7	Postulated alternative approach	167
5.8	Summary	168
6	Electrical and mechanical characterisation of FeRh	169
6.1	Introduction	169

6.2	Experimental procedure	170
6.3	Analysis of erosion procedure	171
6.3.1	Erosion of site A	171
6.3.2	Erosion of site B	172
6.3.3	Erosion of site C	173
6.3.4	Erosion summary	174
6.4	Characterisation of surface resistivity	175
6.4.1	Resistivity of site A	175
6.4.2	Resistivity of site B	176
6.4.3	Resistivity of site C	178
6.4.4	Resistivity summary	179
6.5	Mechanical measurements of magnetically patterned FeRh	180
6.5.1	Unification of techniques	182
6.5.2	Custom probe requirements	182
6.6	Summary	183
7	Magnetic characterisation of noble ion irradiated FeRh	184
7.1	Preparation of magnetically patterned FeRh thin films	184
7.1.1	Deposition of FeRh thin films	184
7.1.2	Magnetic patterning	185
7.1.3	Expected domain structure	187
7.2	Initial XMCD-PEEM characterisation of the sample	188
7.2.1	Introduction to XMCD-PEEM	188
7.2.2	XMCD-PEEM characterisation results	188
7.3	Ambient MFM characterisation	189
7.3.1	Edge of the patterned region	192
7.3.2	Stripe widths	193
7.3.3	Stripe periodicity	195
7.3.4	Persistence of the magnetic structure	197
7.3.5	Effect of external fields	198
7.4	Heated MFM characterisation	201
7.5	Summary	206
8	Nanoscale characterisation of PMN-PT ferroelectric substrates	207
8.1	Motivations and aims	207
8.2	Distribution of piezoelectric properties	209
8.2.1	Effective piezoelectric response	212

8.2.2	Theoretical distribution of ferroelectric parameters	213
8.3	Theoretical electrostatic probe dynamics for homogeneous relaxors	216
8.3.1	Polarisation and relative electrical permittivity	216
8.3.2	Field between probe and ground	220
8.3.3	Capacitive probe deflection	221
8.4	Residual surface charges induced by potentials	226
8.5	Strain behaviour of relaxor ferroelectrics during ON-field HV-PFM	228
8.6	Point-and-Shoot Spectroscopy (PSS)	231
8.6.1	Resonance characterisation	232
8.6.2	Coercive field characterisation	233
8.6.3	Analysis of the PSS measurement at site A	236
8.6.4	Analysis of the PSS measurement at site B	238
8.6.5	PSS conclusions	239
8.7	MultiScan Spectroscopy (MSS)	240
8.7.1	Resonance characterisation	240
8.7.2	In situ sample polarisation	243
8.7.3	Phase characterisation	244
8.7.4	MSS conclusions	248
8.8	Summary	248
9	Conclusions and future work	250
9.1	Metallic resistivity characterisation on the AFM	250
9.1.1	Future work	252
9.2	Magnetic characterisation of noble ion irradiated FeRh	252
9.2.1	Future work	254
9.3	Ferroelectric characterisation of thick samples of PMN-PT	254
9.3.1	Future work	256
	References	257
A	Derivations	274
A.1	Crystal plane separation - equation (2.7)	274
A.2	Deformation in the Hertzian model - equation (4.26)	276
A.3	Resistance of a truncated cone - equation (5.2)	276
A.3.1	Resistance of a hollow truncated cone - equation (5.3)	277
A.4	Resistance of a truncated spherical cap - equation (5.4)	277

Word Count: 70795

List of Figures

2.1	The unit cell of the triclinic crystal system	23
2.2	An example of a point group with C_6 symmetry	25
2.3	The unit cell of the primitive monoclinic crystal system	29
2.4	The unit cells of the base-centred monoclinic crystal system	29
2.5	The conventional unit cells for the orthorhombic system	30
2.6	The conventional unit cells for the tetragonal system	31
2.7	The conventional unit cells for the hexagonal family	33
2.8	The primitive unit cell of the rhombohedral lattice system	33
2.9	The conventional unit cells for the cubic system	35
2.10	The ABX_3 perovskite in the cubic structure $Pm\bar{3}m$	36
2.11	The ABX_3 perovskite in the tetragonal structure $P4mm$	37
2.12	The ABX_3 perovskite in the monoclinic structure Pm	37
2.13	The ABX_3 perovskite in the monoclinic structure Cm	38
2.14	The ABX_3 perovskite in the trigonal structure $R\bar{3}m$	39
2.15	The CsCl structure	40
2.16	The full-Heusler structure X_2YZ	41
2.17	The magnetic field lines for a magnetic dipole	42
2.18	The symmetric and antisymmetric spatial wavefunctions for two $1s$ electrons	48
2.19	The symmetric and antisymmetric spatial probability distributions for two $1s$ electrons	49
2.20	The Bethe-Slater curve	52
2.21	The density of states for an electrically conductive material in zero field and applied field	54
2.22	A representation of ferromagnetism in one dimension	55
2.23	The magnetisation hysteresis loop for a ferromagnetic material	55
2.24	A representation of antiferromagnetism in one dimension	56
2.25	Three common types of antiferromagnetism	57
2.26	A representation of ferrimagnetism in one dimension	57
2.27	The effect of canting on the three common types of antiferromagnetism	58
2.28	The demagnetising field which forms for an elongated magnetised crystal	59
2.29	The magnetisation and stray fields for different domain structures	61

2.30	A domain structure with multiple cyclical domains to eliminate stray field whilst also minimising magnetostrictive strain	62
2.31	The rotation of magnetic dipole moments across the two types of domain wall	63
2.32	Stress-strain curves for magnetoelastic systems	64
2.33	The density of states for the incomplete energy band of electron dipoles in metals	66
2.34	The piezoelectric effect in a six ion system	72
2.35	The polarisation hysteresis loop for a ferroelectric material	76
2.36	The polarisation and edge charges for different domain structures	78
2.37	The idealised strain arising from a parallel or antiparallel poling field	81
2.38	Macroscale and nanoscale examples of magnetic toroidal moments	86
3.1	The FeRh phase diagram for temperature and Rh content	90
3.2	The magnetisation against temperature for multiple samples of equiatomic FeRh	93
3.3	The temperature dependent magnetisation of equiatomic FeRh	93
3.4	The phase diagram for equiatomic FeRh at a range of temperatures and external fields	94
3.5	The FeRh unit cell in antiferromagnetic and ferromagnetic configurations	95
3.6	The temperature dependent resistivity of equiatomic FeRh	95
3.7	The FM-FeRh unit cell in a thin film	96
3.8	The temperature dependent mechanical properties of equiatomic FeRh	96
3.9	The reading process for a memristor using the magnetoresistance effect of an antiferromagnetic film	98
3.10	The metamagnetic curves for ion irradiated FeRh	99
3.11	The PMN-PT phase diagram	102
3.12	The thermal hysteresis width of the Curie temperature of PMN-PT for a range of PT concentrations	103
3.13	The piezoelectric coefficient of PMN-PT for a range of PT concentrations	104
3.14	The coercive field of PMN-PT for a range of PT concentrations	107
3.15	The terraces formed by polishing PMN-PT crystal surfaces	108
4.1	The Bruker Dimension Icon AFM used in this work	110
4.2	The basic operation of an AFM measuring the topography of a sample surface	110
4.3	Schematic of a silicon probe with a thin functional coating	111
4.4	The geometry of the actuators within the Dimension Icon scanner head	112
4.5	Trace and retrace paths of the probe during typical AFM scans using the Dimension Icon scanner head	112
4.6	The geometry of the tip of an AFM probe	113
4.7	The artefact resulting from finite tip dimensions on small features	114

4.8	Schematic of a lift mode measurement being taken	119
4.9	The phase shift experienced by an MFM probe as it crosses a domain wall between different orientations of domains	120
4.10	The Lennard-Jones function used to approximate AFM tip-sample interactions	121
4.11	The linear piecewise function used to approximate AFM tip-sample interactions for hard samples	122
4.12	The Sneddon and Hertzian indentation models	124
4.13	A PF-TUNA application module mounted onto a Dimension Icon scanning head	128
4.14	Repeated I-V curves performed over a metal-coated probe on a 100 nm platinum film	133
4.15	Two PFM phase curves for the same set of data points which have differing constant offsets	138
4.16	An example calibration plot for phase offset due to the measuring equipment	139
4.17	PFM amplitude against thickness for an exemplar piezoelectric sample	140
4.18	The structures produced by applying high potentials to AFM probes in contact with insulating crystals	142
4.19	The signal access module for the NanoScope Controller V system	143
4.20	The heater stage on the Dimension Icon system	146
4.21	A comparison of applied and measured temperatures for the heater stage	147
4.22	The normalised magnetisation of thermally cycled equiatomic FeRh as measured using MFM and VSM	147
5.1	The main sources of resistance in an electrical AFM measurement	149
5.2	The contact radius of two probes over a range of setpoints	151
5.3	The simulated Joule heating of the RMN-25PT300B AFM probe over 2304 DataCube cycles	156
5.4	The dummy application module used to directly connect BNC components to the AFM probe	164
5.5	The constituent resistances of the system as part of a voltage divider circuit	165
5.6	The voltage divider circuit overlaid onto a simplified schematic of the components	166
5.7	The multilayer stack required for an alternative electrical measurement methodology	168
6.1	Topography of site A following oxide erosion	172
6.2	Topography of site B following oxide erosion	173
6.3	Topography of site C following oxide erosion	174
6.4	Resistivity characterisation of site A	175
6.5	Resistivity characterisation of site B	177
6.6	Resistivity characterisation of site C	179

6.7	The DMT modulus data for a ForceVolume measurement on FeRh	181
7.1	The simulated magnetisation expected at the edge of an ion patterned strip of FeRh	186
7.2	Possible domain orientations in ferromagnetic strips which would not exhibit any stray field	187
7.3	XMCD-PEEM images of magnetically patterned FeRh above and below the transition temperature	189
7.4	The normalised magnetic phase data for magnetically patterned FeRh over two different scan sizes	190
7.5	Magnetic images obtained using XMCD-PEEM and MFM	191
7.6	The relative contrast between magnetic phase data measurements using two different scan sizes	192
7.7	MFM phase image of the border of the magnetically patterned region of FeRh	192
7.8	A cross-section taken from Figure 7.4a	194
7.9	Normalised magnetic phase data over a scan size of 500 nm	194
7.10	Mean row-by-row FFT curves for multiple MFM phase measurements over different scan sizes	196
7.11	Mean row-by-row FFT curves for multiple topographic measurements over different scan sizes	196
7.12	A series of MFM scans of the same site taken over an extended period of time and on different stages	197
7.13	MFM phase data before and after an in-plane field of 2 T is applied	199
7.14	MFM phase data before and after two perpendicular in-plane fields of 2 T are applied	200
7.15	MFM phase measurements before and after an AC demagnetisation was performed	201
7.16	MFM phase data for magnetically patterned FeRh as the temperature is cycled	202
7.17	The 80 °C scans from Figure 7.16	203
7.18	A 500 nm wide region compared for each of the MFM phase measurements in Figure 7.16	203
7.19	Mean FFT curves for the second 140 °C scan in Figure 7.16	204
7.20	MFM phase data for magnetically patterned FeRh as the temperature is raised past the AF-FM transition temperature	205
7.21	MFM phase data for magnetically patterned FeRh as the temperature is cooled past the FM-AF transition temperature	205
8.1	The Voigt curves and their ratios	209
8.2	XRD data for the PMN-PT sample at a range of potentials	211

8.3	The Lorentzian behaviour of the piezoelectric coefficient and the Gaussian distribution in x	213
8.4	The expected distribution of coercive field $E_{c,3}$ within the PMN-PT sample	214
8.5	The expected distribution of OFF-field piezoelectric coefficient d_{33} within the PMN-PT sample	215
8.6	The theoretical normalised polarisation for the PMN-PT sample under investigation . .	217
8.7	The ferroelectric dependence of the relative electrical permittivity of the PMN-PT sample on applied electric field	217
8.8	The distribution of the electrostriction originated longitudinal piezoelectric effect d_{33}^Q .	218
8.9	The ferroelectric dependence of the piezoelectric response of PMN-PT on applied electric field	220
8.10	The schematised electric field lines between a positively charged tip and negatively charged stage	221
8.11	The dependence of tip-stage capacitance on applied field for four AFM probes	222
8.12	The dependence of tip-stage capacitance gradient on applied field for four AFM probes	223
8.13	The dependence of the DC electrostatic force on applied field for four AFM probes . .	223
8.14	The dependence of the deformation arising from DC electrostatic force on applied field for four AFM probes	224
8.15	The dependence of AC electrostatic deflection on applied field for four AFM probes . .	225
8.16	The potentials used for OFF-field PFM measurements	226
8.17	Piezoelectric amplitude of uncharged PMN-PT	227
8.18	Topography and piezoelectric amplitude data following charging scans	228
8.19	Models of the height-change and differential height-change for HV-PFM measurements of PMN-PT	231
8.20	Piezoelectric resonance curves for PMN-PT	233
8.21	PSS characterisation of resonance frequency over PMN-PT	233
8.22	An example field sweep from a PSS field-spectroscopy measurement	235
8.23	Two example field sweeps from a PSS field-spectroscopy measurement	235
8.24	PSS characterisation of coercive field at site A	237
8.25	PSS characterisation of empirical coefficient at site A	237
8.26	The PMN-PT sample surface before and after carrying out PSS measurements	238
8.27	PSS characterisation of coercive field at site B	239
8.28	Example amplitude curve from MSS frequency-spectroscopy	241
8.29	MSS characterisation of resonance frequency over PMN-PT	241
8.30	Histogram of the resonance frequency from MSS frequency-spectroscopy	242
8.31	Drift of the PMN-PT sample during the resonance frequency characterisation	243

8.32	Topography of PMN-PT following a trial of MSS field-spectroscopy	245
8.33	Topography of the PMN-PT sample during and after the MSS field-spectroscopy measurement	246
8.34	Example phase curves from MSS field-spectroscopy data demonstrating the phase correction algorithm	246
8.35	MSS characterisation of the coercive field over PMN-PT	247

List of Tables

2.1	The seven conventional unit cells and their Hermann-Mauguin symbols	26
2.2	The basis vectors for the ABX_3 perovskite in the cubic structure $Pm\bar{3}m$	36
2.3	The basis vectors for the ABX_3 perovskite in the monoclinic structure Cm	38
2.4	The basis vectors for the ABX_3 perovskite in the trigonal structure $R\bar{3}m$	39
2.5	The basis vectors for the CsCl structure	40
2.6	The basis vectors for the conventional unit cell of the full-Heusler structure X_2YZ . . .	41
2.7	Conversion between SI and CGS units for four key magnetic parameters	42
2.8	The dipole interaction energy for four relative orientations of dipole moments	45
2.9	The non-zero demagnetisation tensor components for spheroids	60
2.10	The 32 crystallographic point groups in abbreviated Hermann-Mauguin notation	75
2.11	The four ferroic properties as characterised by their response to space inversion and time reversal	85
3.1	Summary of the allotropes present in the FeRh phase diagram	91
5.1	The main sources of resistance in an electrical AFM measurement	150
5.2	The quantifiable resistance for each of the probes and FeRh magnetic ordering of interest	153
5.3	The Hertzian contact radius and sample deformation for different combinations of probe and sample	162
8.1	The spring constant and geometry of each of the four probes under consideration . . .	222
8.2	The elastic modulus and Poisson's ratio of PMN-PT and four probes under consideration	224

Abstract

The atomic force microscope (AFM) was first created in 1986^[1] and was initially used to measure topography and magnetisation^[2], but has continually evolved over the 30 years since its introduction. A common application is in precise measurements of electrical properties including the local resistivity of semiconducting materials^[3], however metallic samples cannot presently be characterised due to the complexities of applying nanoscale resistivity measurements to such surfaces. This missing technique needs to be addressed, and in this work a solution is developed and evaluated which uses a voltage divider to measure the contact resistance between a solid-metal probe and a metallic conducting surface. The oxide layer of the FeRh sample under investigation has to be removed prior to characterisation, but following this the expected pattern is resolved and it is concluded that any non-oxidising metallic sample with resistivities varying by at least one order of magnitude should be resolvable with this methodology.

Antiferromagnetic (AF) spintronic devices are an active area of study at present and FeRh is one of the most promising materials for these devices. Equiatomic FeRh is antiferromagnetic at room temperature and becomes ferromagnetic at around 100°C, with the transition temperature being $\sim 10^\circ\text{C}$ higher during heating than cooling^[4;5]. The room temperature magnetic ordering may be manipulated by irradiating the surface with noble gas ions^[6;7], and the possibility of using lithography to produce magnetic patterns is being explored. This work provides nanoscale magnetic characterisation of an FeRh thin film which has been patterned into 100 nm stripes. The patterning is shown to be successful and is not disrupted by exposure to magnetic fields of up to 2 T nor by temperatures above the FeRh transition temperature. It is seen that the specific FM domain structure of the irradiated regions remains stable throughout the heating and cooling cycle.

An artificial magnetoelectric multiferroic may be formed by depositing FeRh onto the ferroelectric substrate PMN-PT, where the coupling between ferroic layers is mediated through strain^[7]. The local piezoelectric coefficient and coercive field are related to the local stoichiometry^[8;7;9] so the distributions of these characteristics are therefore needed to be modelled and characterised on the nanoscale. It is shown that rapid charging and discharging causes damage to the surface and that electrostatic effects are dominant over relatively thick materials with high electric permittivity, so a series of OFF-field scans are determined to be the optimal solution with the localised spectroscopy achieved through concatenation of the measured piezoelectric response values. This characterisation agrees with the models which suggest the inhomogeneity in piezoelectric coefficient to be negligible, and so PMN-PT is an ideal candidate for the ferroelectric substrate used in artificial magnetoelectric multiferroics.

Declaration of Originality

I hereby confirm that no portion of the work referred to in the thesis has been submitted in support of an application for another degree or qualification of this or any other university or other institute of learning.

Copyright Statement

The author of this thesis (including any appendices and/or schedules to this thesis) owns certain copyright or related rights in it (the “Copyright”) and s/he has given The University of Manchester certain rights to use such Copyright, including for administrative purposes.

Copies of this thesis, either in full or in extracts and whether in hard or electronic copy, may be made *only* in accordance with the Copyright, Designs and Patents Act 1988 (as amended) and regulations issued under it or, where appropriate, in accordance with licensing agreements which the University has from time to time. This page must form part of any such copies made.

The ownership of certain Copyright, patents, designs, trademarks and other intellectual property (the “Intellectual Property”) and any reproductions of copyright works in the thesis, for example graphs and tables (“Reproductions”), which may be described in this thesis, may not be owned by the author and may be owned by third parties. Such Intellectual Property and Reproductions cannot and must not be made available for use without the prior written permission of the owner(s) of the relevant Intellectual Property and/or Reproductions.

Further information on the conditions under which disclosure, publication and commercialisation of this thesis, the Copyright and any Intellectual Property and/or Reproductions described in it may take place is available in the University IP Policy (see <http://documents.manchester.ac.uk/DocuInfo.aspx?DocID=24420>), in any relevant Thesis restriction declarations deposited in the University Library, The University Library’s regulations (see <http://www.library.manchester.ac.uk/about/regulations/>) and in The University’s policy on Presentation of Theses.

Chapter 1

Introduction

This chapter aims to provide an overview of the work contained in this thesis. The concept of atomic force microscopy is introduced, along with the materials of interest and some of the motivations for characterising them using bespoke advanced measurement techniques. One of these is FeRh, a metal exhibiting unusual magnetic properties and of great interest in spintronics, and the other is PMN-PT, a ferroelectric ceramic featuring strongly piezoelectric behaviour and of great interest for use in artificial multiferroics. The aims of the work are outlined and the structure of the thesis is summarised.

1.1 Atomic force microscopy

Scanning probe microscopy (SPM) has been responsible for significant advances in nanoscale research since the invention of the scanning tunnelling microscope (STM) by Binnig and Rohrer in 1981^[10], who were awarded the Nobel Prize in 1986^[11]. Binnig subsequently created the atomic force microscope (AFM) in 1986^[1], which consists of a sharp tip on a cantilever that is deflected by particular forces produced by a sample, nominally the van der Waals forces. This deflection was initially measured using an electron microscope but this was later replaced by a diode laser and quadrant photodetector.

AFM was initially used to measure the topology and magnetisation^[2] of samples, but has continually evolved over the 30 years since its introduction. In this time, resolution has been increased and further modes added^[12;13], and AFM has been adapted to operate in a range of thermal and magnetic environments. The tip can additionally be used to measure the mechanical properties of the sample via nanoindentation^[12], and using novel techniques precise measurements of electrical properties can be made including resistivity, capacitance, and tunnelling^[3]. These modes, along with further novel modes, can together produce a more comprehensive analysis of a sample. However, the localised characterisation of electrical resistivity has been restricted to semiconductor materials until now due to the complexities of applying nanoscale resistivity measurements to metallic surfaces. The consequence is a missing characterisation methodology that needs to be developed in order to enable electrical resistivity characterisation of samples such as metal thin films using AFM techniques.

The umbrella term SPM describes any measurement technique utilising some probe being rastered over a sample, and so includes all STM and AFM derived modes. Some authors define AFM to purely describe characterisations using the basic van der Waals repulsion and categorise the derived modes such as magnetic measurements to be SPM techniques, while other authors use AFM to describe characterisation via any force acting on a tip that is mounted on a cantilever and brought close to a sample surface. This thesis shall use the latter definition, using atomic force microscopy to describe all cantilever-based techniques and clearly distinguish them from other SPM modes such as STM. The device upon which these measurements are performed shall be referred to as the atomic force microscope.

1.2 FeRh

In 1939, Fallot and Hocart^[4] published their seminal paper demonstrating a sudden rise in the magnetisation of bulk equiatomic FeRh when heated past a certain temperature, which exhibited a hysteresis of $\sim 10^\circ\text{C}$ upon cooling. It was later determined by Muldower and de Bergevin^[14] to be a consequence of the magnetic ordering transitioning from antiferromagnetic at room temperature, to ferromagnetic above some threshold temperature, and to be accompanied by a positive strain in the lattice. This transition is also accompanied by sudden changes in other properties, including a decrease in the electrical resistivity^[5] and a rise in the elastic modulus^[15].

This means that by heating to the readily achievable temperature of $\sim 100^\circ\text{C}$, the properties of this material may be toggled between two values which may be exploited in spintronic devices. One possible application is in data storage^[16], where the bit may be written at elevated temperatures but read at ambient temperatures when it is insensitive to external magnetic fields. It is even possible to deposit the FeRh film on a flexible MgO(001) substrate^[17] which may eventually permit flexible data storage devices.

It has recently been shown that irradiation of equiatomic FeRh thin films with energetic noble ions such as neon can induce ferromagnetic ordering at room temperature^[6,18]. This has been demonstrated for uniform irradiation of thin films, but utilising this phenomenon requires that it be localisable and so work must be done to investigate the feasibility of patterning an FeRh thin film with localised ferromagnetic regions. The characterisation work involved may be performed using magnetic measurement techniques on an AFM.

1.3 Multiferroics

A multiferroic is a material or structure which features two or more ferroic properties with large coupling constants between them^[19], and the four primary ferroic properties are ferromagnetism, ferroelectricity,

ferroelasticity, and ferrotoroidicity. Ferroic properties are bistable with a hysteretic transition between states, meaning that once switched they remain fixed in the induced state until they are coerced into the opposite state. This allows them to be used as toggle switches and through the coupling enables one ferroic property to be used to reverse a second. Magnetoelectric multiferroic materials are of great interest in spintronics because they demonstrate both ferromagnetic and ferroelectric behaviour with some magnetoelectric coupling between them^[20].

There are very few natural multiferroic materials but these are supplemented by artificial, or ‘composite’, multiferroics^[19]. These are formed by layering thin films of ferroic materials onto a substrate which may itself be ferroic, and interlayer coupling arises between these which typically yields a superior magnetoelectric coupling than observed in natural multiferroics^[21]. The interlayer coupling in composite magnetoelectrics is mediated through strain, generated by the ferroelectric layer, which induces a change in magnetic ordering of the ferromagnetic layer^[7]. An FeRh film deposited onto a substrate formed from the solid solution of lead magnesium niobate and lead titanate, commonly abbreviated to PMN-PT, is a good candidate for a composite magnetoelectric multiferroic, and electric fields applied to the PMN-PT substrate are demonstrably able to manipulate the ferromagnetic properties of the FeRh film via mechanical strain^[7]. This manipulation is of great interest and applications include reversing a magnetic logic bit via magnetoelectric coupling, which can use orders of magnitude less energy than direct reversal, allowing for reduced power consumption and improved miniaturisation^[19].

PMN-PT is of particular interest for use as a substrate for multiferroic devices because it exhibits a large piezoelectric response^[22] and thus forms an unusually strong magnetoelectric coupling. However, this application requires a homogeneous piezoelectric coefficient across the surface in order to achieve precise control of the magnetic ordering of the ferromagnetic layer. The piezoelectric coefficient is related to local stoichiometry, which is known to be inhomogeneous^[7], and there is seemingly contradictory data in the literature regarding the significance of this variation^[8;7]. This contradiction must be resolved and nanoscale characterisation performed so that PMN-PT substrates may be used in multiferroic applications, however no suitable AFM measurement mode exists for such thick samples. A surface characterisation methodology such as AFM is required for this application though, rather than an existing bulk characterisation technique. This is because the magnetoelectric coupling between the two ferroic materials comprising the multiferroic is governed by piezoelectric strain, and so is critically dependent on the local distribution of the piezoelectric coefficient at the interface.

1.4 Objectives and thesis outline

The work described in this thesis has a predominantly metrological focus. This means that the development and evaluation of novel AFM methodologies are primary aims of the work, in addition to the

results obtained from the characterisations performed. One aim of the project was to satisfy the need for localised resistivity measurements of metallic films, by developing a new methodology to achieve this and demonstrating the proof-of-concept. This characterisation has not been available until now, and so developing this will significantly expand the electrical measurement capabilities of the atomic force microscope. A second aim was to investigate the magnetic patterning of an FeRh thin film on the nanoscale, initially by verifying the success of the patterning and then by characterising the domain structure during heating and cooling the patterned film past the FeRh transition temperature. The third and final aim was to investigate thick ferroelectric samples for use as substrates for composite multiferroics, including modelling the expected distribution of ferroelectric behaviour. This involved developing a new measurement methodology to enable piezoelectric characterisation to be performed by the AFM over samples which are prohibitively thick for the use of existing modes.

The structure of this thesis is outlined below.

Chapter 2 provides a detailed introduction to the fundamental background phenomena for this work. This comprises crystals and lattices, magnetic fields and magnetism, and electric fields and polarisation.

Chapter 3 introduces the properties and applications of the two materials under investigation in this work, which are equiatomic FeRh thin films and PMN-PT ferroelectric substrates.

Chapter 4 details the principles of atomic force microscopy and introduces the series of established modes which are utilised and modified in this work.

Chapter 5 discusses the development of a localised resistivity measurement methodology using the atomic force microscope, and **Chapter 6** evaluates this technique by applying it to a magnetically patterned FeRh thin film.

Chapter 7 reports the magnetic investigation of the patterned FeRh thin film, with regards to the success and stability of the patterning.

Chapter 8 presents and evaluates the multiple models and methodologies developed in order to characterise the surface of a thick ferroelectric sample, exemplified by a PMN-PT substrate.

Chapter 9 summarises the results from the experimental work in this thesis and proposes future work that may be carried out.

Chapter 2

Fundamental background phenomena

This chapter aims to provide an introduction to basic crystallography and the different crystal and lattice systems, and introduce the named crystal prototypes which correlate to the samples under investigation. Additionally, it aims to provide an introduction to magnetism, starting with dipoles and continuing through to ferromagnetic ordering and domains. The related phenomena of magnetoresistance, magnetostriction, and the elastic modulus defect will also be discussed. Finally, the electrical analogue of this magnetic ordering will be introduced in a more quantitative manner. The ferroelectric switching process and ensuing effects will be explained and the subcategory of relaxor ferroelectrics will be introduced.

2.1 Introduction to crystals and lattices

2.1.1 Unit cells and lattice vectors

A crystal is a term for a group of atoms arranged in a repeating structure, which may be described by the 'lattice' and the 'basis'^[23]. The lattice is the principal arrangement of atoms in the structure that best describes the symmetries contained therein and may not include all of the atoms present. The atoms in the vicinity of each lattice point form the basis.

There are two classifications of unit cells: primitive and conventional^[23]. A primitive unit cell is the smallest cell possible, containing one lattice point in its basis and having discrete translational symmetry across the crystal. More commonly used is the conventional unit cell, this is the smallest unit cell whose symmetries describe the highest order symmetries in the lattice^[24]. For example, as will be seen in Section 2.2.2.2, the Cm crystal structure may be described by either triclinic or monoclinic unit cells; the monoclinic system has higher order symmetry thus this is the system used to describe the structure. The result is that the crystal axes of the conventional unit cell align with the symmetry axes of the overall crystal^[24], so any reference to crystal axes equally refer to the lattice vectors of this cell. The conventional cell may be the same as the primitive cell in some lattices, such as simple cubic, whilst being different in others, such as body-centred cubic^[24].

The term ‘basis’ is usually used for conventional unit cells, while the ‘primitive basis’ is the basis in the primitive unit cell description^[23]. The basis vectors for each atom are typically defined in at least one of the following two coordinate systems, both of which define the host lattice point to be the origin^[24]. The first is fractional coordinates, which state the relative distance along each of the lattice vectors; for example, fractional coordinates $(0.1, 0.2, 0.3)$ refer to the point $0.1\vec{a} + 0.2\vec{b} + 0.3\vec{c}$. The second is to just use Cartesian coordinates, so $(0.1, 0.2, 0.3)$ instead refers to the point $0.1\vec{x} + 0.2\vec{y} + 0.3\vec{z}$.

The conventional unit cell is the one typically used to describe the lattice and is defined by the lattice vectors \vec{a} , \vec{b} , \vec{c} and lattice angles α , β , γ which are colour-coded on the unit cell of the triclinic crystal system in Figure 2.1. The lattice constants a , b , c are simply the magnitudes of the respective lattice vectors and the order of labelling these vectors is somewhat arbitrary, but the typical choice is such that $a \leq b \leq c$ ^[24]. The angle between two lattice vectors is labelled by the Greek counterpart of the third vector^[24], which means

$$\begin{aligned}\cos(\alpha) &= \frac{\vec{b} \cdot \vec{c}}{bc} \\ \cos(\beta) &= \frac{\vec{a} \cdot \vec{c}}{ac} \\ \cos(\gamma) &= \frac{\vec{a} \cdot \vec{b}}{ab} .\end{aligned}\tag{2.1}$$

Finally, the faces of the conventional unit cells are defined by the plane described by two of the lattice vectors and these are labelled using the capital of the third. For example, face C contains \vec{a} and \vec{b} and so both the top and bottom faces of Figure 2.1, shaded blue, are C faces.

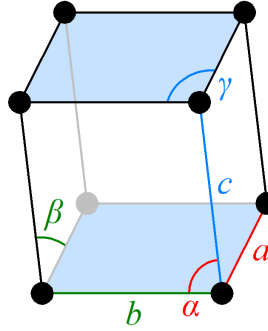


Figure 2.1: The unit cell of the triclinic crystal system with lattice angles and lattice vectors colour-coded. Red, green, and blue denote \vec{a} and α , \vec{b} and β , and \vec{c} and γ respectively. The faces shaded blue are the C faces.

In most, but not all, cases, the underlying Cartesian basis is oriented such that the lattice vector \vec{a} is parallel to the Cartesian unit vector \hat{x} . The volume of a unit cell is given by^[24]

$$\mathcal{V} = \vec{a} \cdot (\vec{b} \times \vec{c}) .\tag{2.2}$$

In lattices where primitive cells and conventional cells differ the parameters of the primitive unit cell will be indicated with a prime, so the primitive unit cell vectors would be \vec{a}' , \vec{b}' , \vec{c}' .

2.1.2 Miller indices

It is commonly necessary to describe plane orientation in a crystal and this is typically done using Miller indices^[25]. One reason for doing so is to describe how a sample is oriented relative to the surface or a substrate. These are a set of three integers h , k , l , which uniquely define a family of parallel planes.

The index values are determined by considering the plane closest to, but not passing through, a particular lattice point, and recording the fractional distance from this point to where the plane intersects each crystal axis^[25]. The plane may be defined for every lattice point hence this is a family of planes with constant separation d and not just a single plane. The reciprocals of these intercepts are then taken and the values multiplied by the lowest common multiple of any denominators to obtain three integer values. Any common factors of these integers are not cancelled^[25], so for example if the plane had intercepts $0.5\vec{a}$, $0.25\vec{b}$, $0.125\vec{c}$ then the Miller indices would be (248), which is parallel to but has half the spacing of the family of planes (124). Negative values are represented by a bar above the number.

A Miller index of 0 means the plane is parallel to that crystal axis, thus the value of the intercept tends to infinity which becomes 0 when the reciprocal is taken. This means that crystal plane A has Miller indices (100), B has indices (010), and C has indices (001). In some lattices, such as simple cubic, the symmetry of the structure means the order of the indices is irrelevant in which case braces $\{hkl\}$ are used^[25]. Vectors orthogonal to these planes are given using square brackets, so the vector orthogonal to (hkl) is $h\vec{a} + k\vec{b} + l\vec{c}$ which is written $[hkl]$ ^[25]. If the index order of the vectors is irrelevant then angled brackets $\langle hkl \rangle$ are used^[25].

2.1.3 Point groups, space groups, and crystals

A point group is a mathematical group of geometric symmetry operations that results in the transformed structure mapping onto itself whilst keeping at least one point unchanged^[26], thereby excluding any translational symmetries. The allowed operations are thus rotational, reflective, inversion, or improper rotation (rotation plus inversion, also known as rotoinversions). The 'symmetry elements' are any rotation axes, reflection planes, and centres of symmetry present in a point group. These need not describe lattice-style arrays of single points; Figure 2.2 shows a point group with C_6 symmetry.

A space group is a point group with the relaxation of the rule requiring a fixed point, allowing translational, screw (translation plus rotation), and glide (translation plus reflection) symmetries^[26]. The result of allowing translations is a repeating space in all directions, in the context of lattices this forms a Bravais lattice where the repeating space is the unit cell.

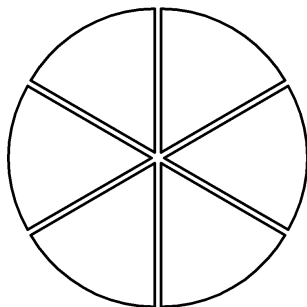


Figure 2.2: An example of a point group with C_6 symmetry. The C stands for cyclic and describes rotations, whilst the 6 describes the number of non-zero rotations less than or equal to 360° which will map the group onto itself.

A point or space group has inversion symmetry if each unique point has a corresponding point to which it maps exactly upon inversion through the origin^[25], which in the case of space groups may be arbitrarily defined. A point group with inversion symmetry is said to be centrosymmetric. The piezoelectric effect discussed in Section 2.12 can only occur in crystals with no inversion symmetry^[27].

It is important here to define the terms crystal system, lattice system, and crystal families. These are very similar and are at times mistakenly used interchangeably, but there are important distinctions between them. A crystal system is related to the underlying point groups and describes the mathematical properties of the structure, while the lattice system describes the underlying Bravais lattice^[24]. In three-dimensions there are seven crystal systems, discussed in detail below, and fourteen Bravais lattices which may be grouped into the seven named lattice systems^[25].

Five of the crystal and lattice systems are identical in name and categorisation, however the trigonal and hexagonal crystal systems do not correlate directly to the remaining rhombohedral and hexagonal lattice systems; trigonal crystal systems may have rhombohedral or hexagonal lattice systems and hexagonal lattice systems may have trigonal or hexagonal crystal systems^[24]. Note that there is no such term as a trigonal lattice system or rhombohedral crystal system. One mitigation for this confusion is to speak instead of there being six crystal families and grouping the hexagonal and trigonal crystal systems into the hexagonal crystal ‘family’.

2.1.4 Hermann-Mauguin notation

A widely used notation style to concisely describe point and space groups is Hermann-Mauguin notation, also known as international notation following its inclusion in the *International Tables for Crystallography* from 1935^[26]. It was introduced by Carl Hermann in 1928 and later modified by Charles-Victor Mauguin in 1931 into the form used today^[26]. It describes the system more thoroughly than some other styles, such as Schoenflies notation, because it includes more detail on symmetries and orientation^[26]. Figure

2.2 used Schoenflies notation.

The notation consists of a capital letter to denote the conventional cell type followed by up to three more terms which uniquely identify the point group^[25]. It is common for the full description to be condensed slightly to a simpler shorthand in regular use. The leading capitals are summarised in Table 2.1.

Symbol	Name	Multiplicity	Notes
P	Primitive	1	In this case the conventional unit cell is just the primitive unit cell.
I	Body-centred	2	The symbol comes from the German 'Innenzentriert'.
F	Face-centred	4	The symbol comes from the German 'Flächenzentriert'.
A	Base-centred on A faces only	2	
B	Base-centred on B faces only	2	
C	Base-centred on C faces only	2	
R	Rhombohedrally- centred	3	The base is a rhombus but \vec{c} runs perpendicular to C to form a right rhombic prism with the next rhombus directly above.

Table 2.1: The seven conventional unit cells and their Hermann-Mauguin symbols^[26]. The multiplicity is the ratio of conventional cell volume to primitive cell volume.

In space groups the three trailing terms describe the lattice symmetries in the directions of the crystal axes^[25], with any directions lacking non-translational symmetries being denoted by 1 or absent. An integer represents the smallest fraction of 360° through which a rotation may map the lattice onto itself, so the value for Figure 2.2 in the direction of an axis perpendicular to the page would be 6. A bar above the index means each rotation is accompanied by an inversion through some point on the axis meaning these are improper rotations. A letter m denotes a reflection in the plane normal to the axis and is equivalent to $\bar{2}$; as such the symbol $\bar{2}$ is never used. If both a rotation and reflection are present then the two are written as a fraction, with the integer on the top and the m on the bottom^[25]. Any even numbered improper rotations inherently include the symmetry $\bar{2}$ so are never written in this way because m is accounted for by the improper rotation itself. A rotation of 1 means that only translational symmetries are present for this axis, whilst a rotoinversion of $\bar{1}$ means the group is additionally centrosymmetric^[25].

If a rotation and rotoinversion are both present for the same axis then the operation with higher symmetry

is chosen^[25]. In this context the symmetry refers to the number of times the transformation must be applied before the points are restored to their initial position, so for rotation 3 the symmetry is 3 whilst for rotoinversion $\bar{3}$ the symmetry is 6. If both transformations have the same symmetry then the rotation takes precedence.

There are further symbols and subscripts used in Hermann-Mauguin notation of space groups that cover additional symmetry operations, however these are not relevant for the space groups of the crystals in this thesis so will not be discussed here.

2.2 Crystal systems

The seven crystal systems are triclinic, monoclinic, orthorhombic, tetragonal, trigonal, hexagonal, and cubic^[24]. Each of these are detailed in the following pages.

2.2.1 The triclinic system

In the triclinic system the three lattice constants are all different and the three lattice angles are not equal to each other or to 90° ^[24]. The conventional and primitive unit cells are equal and the structure is shown in Figure 2.1. There are only two space groups in this system^[24] and this is the only lattice type to have no mirror planes.

The lattice vectors for this system are^[24]

$$\begin{aligned}\vec{a} &= a\hat{x} \\ \vec{b} &= b \cos(\gamma) \hat{x} + b \sin(\gamma) \hat{y} \\ \vec{c} &= c_x \hat{x} + c_y \hat{y} + c_z \hat{z}\end{aligned}\tag{2.3}$$

where

$$\begin{aligned}c_x &= c \cos(\beta) \\ c_y &= c [\cos(\alpha) - \cos(\beta) \cos(\gamma)] \csc(\gamma)\end{aligned}\tag{2.4}$$

and

$$\begin{aligned}c_z &= \sqrt{c^2 - c_x^2 - c_y^2} \\ &= c [1 - \cos^2(\alpha) - \cos^2(\beta) - \cos^2(\gamma) + 2 \cos(\alpha) \cos(\beta) \cos(\gamma)]^{1/2} \csc(\gamma) .\end{aligned}\tag{2.5}$$

The unit cell volume is thus

$$\begin{aligned}\mathcal{V} &= abc_z \sin(\gamma) \\ &= abc [1 - \cos^2(\alpha) - \cos^2(\beta) - \cos^2(\gamma) + 2 \cos(\alpha) \cos(\beta) \cos(\gamma)]^{1/2} .\end{aligned}\tag{2.6}$$

The plane separation d for planes with Miller indices (hkl) in the triclinic lattice system satisfies

$$\frac{1}{d^2} = \frac{\frac{2hk}{ab} [\cos(\alpha) \cos(\beta) - \cos(\gamma)] + \frac{2hl}{ac} [\cos(\alpha) \cos(\gamma) - \cos(\beta)] + \frac{2kl}{bc} [\cos(\beta) \cos(\gamma) - \cos(\alpha)] + \frac{h^2}{a^2} \sin^2(\alpha) + \frac{k^2}{b^2} \sin^2(\beta) + \frac{l^2}{c^2} \sin^2(\gamma)}{1 - \cos^2(\alpha) - \cos^2(\beta) - \cos^2(\gamma) + 2 \cos(\alpha) \cos(\beta) \cos(\gamma)} \quad (2.7)$$

with the full derivation provided in Appendix A.1.

This crystal system may be obtained by straining a primitive cubic system in the direction $\langle hkl \rangle$ where $l > k > h > 0$.

2.2.2 The monoclinic system

In the monoclinic system the lattice constants are again all unequal but two of the angles now equal 90° ^[24]. This means the system forms a conventional unit cell akin to a slanted cuboid, with four of the faces being rectangular and two being parallelograms. There are 13 space groups in this system, split into two lattice types: 8 being primitive and 5 being base-centred^[24]. The primitive monoclinic lattice has equivalent primitive and conventional unit cells; however, the base-centred system has an extra lattice point in the centre of two of the rectangular faces, with the coordinate system defined such that these are the C -oriented faces. PMN-PT forms two monoclinic space groups: Pm and Cm ^[28].

2.2.2.1 The Pm space group

The Pm space group, numbered 6 in the International Tables for Crystallography, is the short form of the Hermann-Mauguin notation $P1m1$ or $P11m$ ^[26]. $P11m$ describes a simple monoclinic lattice with the C -oriented planes being parallelograms and the others rectangular, while $P1m1$ describes the version where the B -oriented planes are the parallelograms^[26]. The difference between these is just choice of crystal axes and by modern convention $P1m1$ is typically chosen in symmetry to the base-centred lattice. The point group $m11$ is never used because it can always be changed to $1m1$ by a trivially different choice of axes. The unit cell for $P1m1$ is shown in Figure 2.3.

The lattice vectors for the primitive monoclinic crystal system with $\alpha = \gamma = 90^\circ$ are^[24]

$$\begin{aligned} \vec{a} &= a\hat{x} \\ \vec{b} &= b\hat{y} \\ \vec{c} &= c \cos(\beta) \hat{x} + c \sin(\beta) \hat{z} \end{aligned} \quad (2.8)$$

giving the unit cell volume to be

$$\mathcal{V} = abc \sin(\beta) . \quad (2.9)$$

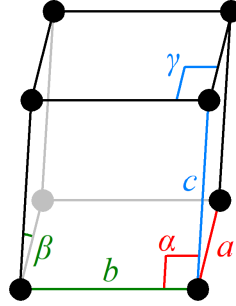


Figure 2.3: The unit cell of the primitive monoclinic crystal system when $\alpha = \gamma = 90^\circ$, with lattice angles and lattice vectors colour-coded as in Figure 2.1.

The plane separation for planes with Miller indices (hkl) in the monoclinic lattice system is described by substituting $\alpha = \gamma = 90^\circ$ into equation (2.7) yielding

$$\frac{1}{d^2} = \left(\frac{h^2}{a^2} + \frac{k^2 \sin^2(\beta)}{b^2} + \frac{l^2}{c^2} - \frac{2hl \cos(\beta)}{ac} \right) \csc^2(\beta). \quad (2.10)$$

This crystal system may be obtained by straining a primitive cubic system in the direction $[h0l]$ where $l > h > 0$.

2.2.2.2 The Cm space group

The Cm space group, numbered 8 in the International Tables, is the short form of the equivalent Hermann-Mauguin notations $C1m1$ or $B11m$. The former is typically used by modern convention so that β is the only non-perpendicular lattice angle. This results in a more intuitive geometry. Figure 2.4 shows the unit cells for the base-centred monoclinic system with $\alpha = \gamma = 90^\circ$.

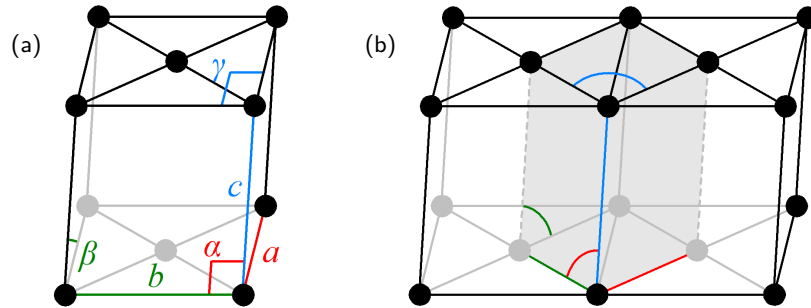


Figure 2.4: The unit cells of the base-centred monoclinic crystal system when $\alpha = \gamma = 90^\circ$, with their respective lattice angles and lattice vectors colour-coded as in Figure 2.1. (a) The conventional unit cell. (b) The primitive unit cell of this system shown as a shaded region spanning two conventional unit cells.

The conventional lattice vectors are the same as in the primitive monoclinic crystal system, while the

primitive lattice vectors are^[24]

$$\begin{aligned}\vec{a}' &= \frac{1}{2}\vec{a} - \frac{1}{2}\vec{b} = \frac{a}{2}\hat{x} - \frac{b}{2}\hat{y} \\ \vec{b}' &= \frac{1}{2}\vec{a} + \frac{1}{2}\vec{b} = \frac{a}{2}\hat{x} + \frac{b}{2}\hat{y} \\ \vec{c}' &= \vec{c} = c \cos(\beta)\hat{x} + c \sin(\beta)\hat{y}\end{aligned}\tag{2.11}$$

giving the primitive unit cell volume to be

$$\mathcal{V} = \frac{1}{2}abc \sin(\beta) .\tag{2.12}$$

The resulting primitive cell has half of the volume of the conventional cell and is shaped somewhat like a rhombohedral lattice. However, only two of the lattice constants (a' and b') and two of the lattice angles (α' and β') are equal so it is actually classed as triclinic.

This crystal structure may be obtained by straining a primitive cubic system in the direction $[hhl]$ where $l > h > 0$.

2.2.3 The orthorhombic system

The orthorhombic system is similar to the monoclinic except the angle β now also equals 90° ^[24] yielding a cuboid lattice structure. This system is the second most populous, with 59 space groups divided across four lattice groups: primitive, body-centred, face-centred, and base-centred^[24]. The structures of these are all shown in Figure 2.5.

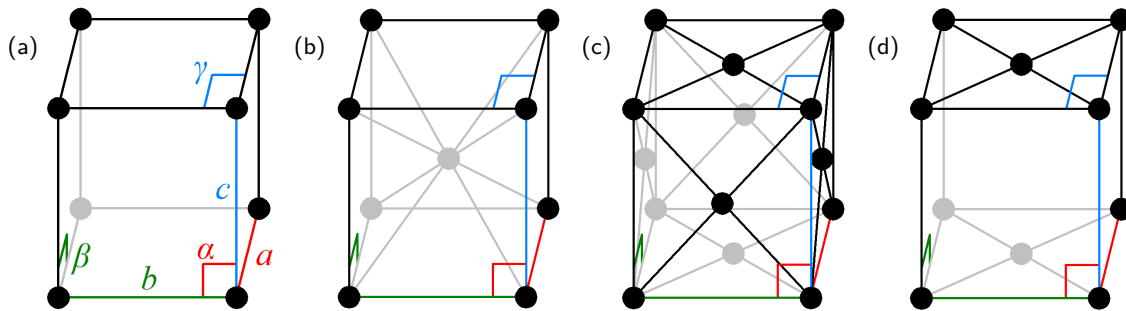


Figure 2.5: The conventional unit cells for the orthorhombic system with lattice angles and lattice vectors colour-coded as in Figure 2.1. C -centring is shown for the base-centred case, although A -centred orthorhombic lattices also exist as defined space groups. (a) The primitive lattice. (b) The body-centred lattice. (c) The face-centred lattice. (d) The base-centred lattice.

The conventional lattice vectors for this system are trivially defined as^[24]

$$\begin{aligned}\vec{a} &= a\hat{x} \\ \vec{b} &= b\hat{y} \\ \vec{c} &= c\hat{z}\end{aligned}\tag{2.13}$$

giving the unit cell volume to be

$$\mathcal{V} = abc .\tag{2.14}$$

The plane separation for planes with Miller indices (hkl) in the orthorhombic lattice system is described by substituting $\alpha = \beta = \gamma = 90^\circ$ into equation (2.7) yielding

$$\frac{1}{d^2} = \frac{h^2}{a^2} + \frac{k^2}{b^2} + \frac{l^2}{c^2} .\tag{2.15}$$

The primitive unit cells for the body-centred, face-centred, and base-centred lattices will not be discussed here because they are not relevant for this work.

The primitive, body-centred, or face-centred orthorhombic structures may be obtained by straining the respective primitive, body-centred, or face-centred cubic system in the direction $\langle 110 \rangle$.

2.2.4 The tetragonal system

The tetragonal system is similar to the orthorhombic except the two lattice constants a and b are now equal^[24] making the conventional unit cell a square-ended cuboid. This system is the most populous with 68 space groups divided between two lattice groups: primitive and body-centred^[24]. The structures of these are both shown in Figure 2.6.

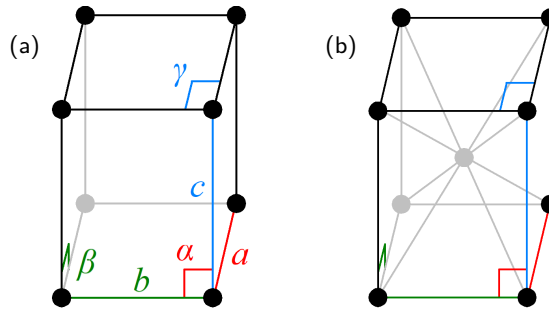


Figure 2.6: The conventional unit cells for the tetragonal system with lattice angles and lattice vectors colour-coded as in Figure 2.1. (a) The primitive lattice. (b) The body-centred lattice.

The conventional lattice vectors for this system are trivially defined as^[24]

$$\begin{aligned}\vec{a} &= a\hat{x} \\ \vec{b} &= a\hat{y} \\ \vec{c} &= c\hat{z}\end{aligned}\tag{2.16}$$

giving the unit cell volume to be

$$\mathcal{V} = a^2 c .\tag{2.17}$$

The plane separation for planes with Miller indices (hkl) in the tetragonal lattice system is described by substituting $\alpha = \beta = \gamma = 90^\circ$ and $a = b$ into equation (2.7) yielding

$$\frac{1}{d^2} = \frac{h^2 + k^2}{a^2} + \frac{l^2}{c^2} .\tag{2.18}$$

PMN-PT and FeRh both form lattices in the same primitive tetragonal space group: $P4mm$, number 99 in the International Tables^[28;29]. The primitive unit cell for the body-centred lattice will not be discussed here because it is not relevant for this work.

The primitive or body-centred tetragonal structures may simply be obtained by straining the respective primitive or body-centred cubic system in the direction \vec{c} .

2.2.5 The hexagonal family

The hexagonal family will be described together because of the significant overlap. The core structure of this family is that the atoms in the C plane form a triangular lattice, which could be thought of as tessellating rhombi, equilateral triangles, or regular hexagons. The lattice constants are related as $a = b \neq c$, with the lattice angles being $\alpha = \beta = 90^\circ$ and $\gamma = 120^\circ$ ^[24]. There are 25 space groups in the trigonal crystal system, split between the rhombohedral and hexagonal lattice systems, and 27 in the hexagonal crystal system, all of which are the hexagonal lattice system^[24]. The conventional unit cells for each lattice are shown in Figure 2.7. The conventional unit cell in the hexagonal lattice is equivalent to its primitive unit cell, whilst in the rhombohedral lattice the primitive unit cell is a rhombohedron.

A hexagonal lattice may have six-fold or three-fold symmetry about an axis, depending on subtleties in the structure, while a rhombohedral lattice may only have three-fold symmetry because the extra two lattice points in the cell prohibit any higher symmetries. Recall that space groups are representations of the symmetries of a system, with the crystal system names trigonal ('tri') and hexagonal ('hex') referring to the orders of symmetries of their respective space groups. Typically the symmetries of the lattice and crystal align but in the hexagonal family this is not the case. The result is the hexagonal lattice system straddling both crystal systems and the trigonal crystal system straddling both lattice systems.

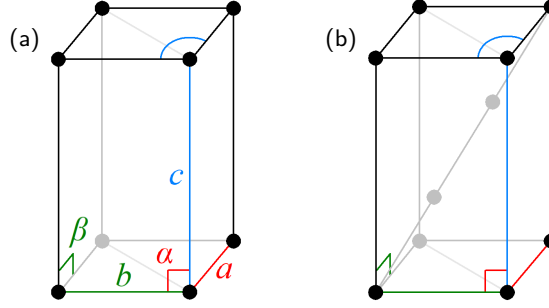


Figure 2.7: The conventional unit cells for the hexagonal family with lattice angles and lattice vectors colour-coded as in Figure 2.1. (a) The hexagonal lattice. (b) The rhombohedral lattice, with two atoms on the long diagonal between the bottom-left and top-right.

The conventional lattice vectors for this family are defined as^[24]

$$\begin{aligned}\vec{a} &= \frac{a}{2}\hat{x} - \frac{\sqrt{3}a}{2}\hat{y} \\ \vec{b} &= \frac{a}{2}\hat{x} + \frac{\sqrt{3}a}{2}\hat{y} \\ \vec{c} &= c\hat{z}\end{aligned}\tag{2.19}$$

giving the unit cell volume to be

$$\mathcal{V} = \frac{\sqrt{3}}{2}a^2c.\tag{2.20}$$

The primitive unit cell of the rhombohedral lattice system runs up the middle of three neighbouring unit cells as shown in Figure 2.8.

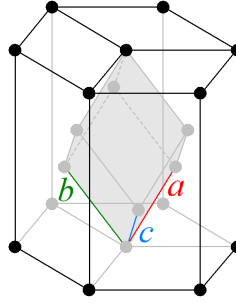


Figure 2.8: The primitive unit cell of the rhombohedral lattice system shown as a shaded region in the centre of a hexagonal supercell, with lattice vectors colour-coded as in Figure 2.1. Primitive lattice angles are all equal but not shown here.

The corresponding primitive lattice vectors are^[24]

$$\begin{aligned}\vec{a}' &= \frac{2}{3}\vec{a} + \frac{1}{3}\vec{b} + \frac{1}{3}\vec{c} = \frac{a}{2}\hat{x} - \frac{a}{2\sqrt{3}}\hat{y} + \frac{c}{3}\hat{z} \\ \vec{b}' &= -\frac{1}{3}\vec{a} + \frac{1}{3}\vec{b} + \frac{1}{3}\vec{c} = \frac{a}{\sqrt{3}}\hat{y} + \frac{c}{3}\hat{z}\end{aligned}$$

$$\vec{c} = -\frac{1}{3}\vec{a} - \frac{2}{3}\vec{b} + \frac{1}{3}\vec{c} = -\frac{a}{2}\hat{x} - \frac{a}{2\sqrt{3}}\hat{y} + \frac{c}{3}\hat{z} \quad (2.21)$$

giving the primitive unit cell volume to be

$$\mathcal{V} = \frac{1}{2\sqrt{3}}a^2c. \quad (2.22)$$

The resulting primitive cell has one third of the volume of the conventional cell and forms a rhombohedral lattice because all three primitive lattice constants and all three primitive lattice angles are equal.

The plane separation for planes with Miller indices (hkl) in the hexagonal lattice is described by substituting $\alpha = \beta = 90^\circ$, $\gamma = 120^\circ$, and $a = b$ into equation (2.7) yielding

$$\frac{1}{d^2} = \frac{4}{3} \left(\frac{h^2 + hk + k^2}{a^2} \right) + \frac{l^2}{c^2}. \quad (2.23)$$

The plane separation for planes with Miller indices (hkl) in the primitive rhombohedral lattice is described by substituting $\alpha' = \beta' = \gamma'$ and $a' = b' = c'$ into equation (2.7) yielding

$$\frac{1}{d^2} = \frac{(h^2 + k^2 + l^2) \sin^2(\alpha') + 2(hk + kl + hl)(\cos^2(\alpha') - \cos(\alpha'))}{a^2(1 - 3\cos^2(\alpha') + 2\cos^3(\alpha'))}. \quad (2.24)$$

In addition to the previously mentioned space groups, PMN-PT also forms $R3m$ ^[28] which is a rhombohedral lattice in the trigonal crystal system and is number 160 in the International Tables.

The rhombohedral crystal structure, albeit with an additional lattice atom in the centre of the primitive unit cell, may be obtained by straining a cubic system in the direction $\langle hkl \rangle$ where $h = k = l > 0$. For comparison, the hexagonal crystal structure may be obtained by instead straining in the direction $[hk0]$ where $h = k > 0$.

2.2.6 The cubic system

The cubic system is a special case of the orthorhombic or tetragonal systems where all three lattice constants are equal^[24], producing the simplest of the crystal systems. There are 36 space groups in this system divided amongst three lattice groups: primitive, body-centred, and face-centred^[24]. The structures of these are all shown in Figure 2.9.

The conventional lattice vectors for this system are trivially defined as^[24]

$$\begin{aligned} \vec{a} &= a\hat{x} \\ \vec{b} &= a\hat{y} \\ \vec{c} &= a\hat{z} \end{aligned} \quad (2.25)$$

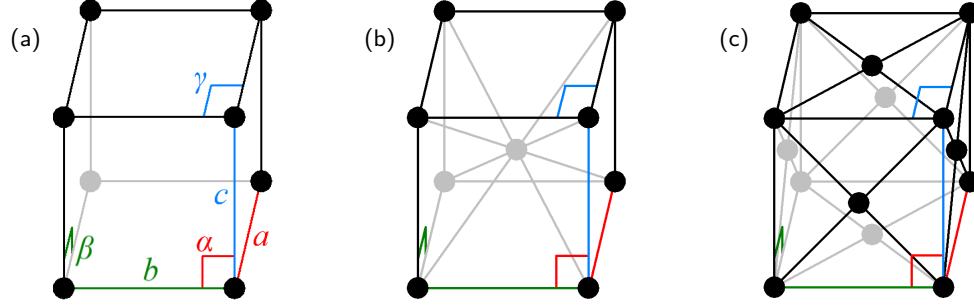


Figure 2.9: The conventional unit cells for the cubic system with lattice angles and lattice vectors colour-coded as in Figure 2.1. (a) The primitive lattice. (b) The body-centred lattice. (c) The face-centred lattice.

giving the unit cell volume to be

$$\mathcal{V} = a^3. \quad (2.26)$$

The plane separation for planes with Miller indices (hkl) in the cubic lattice system is described by substituting $\alpha = \beta = \gamma = 90^\circ$ and $a = b = c$ into equation (2.7) yielding

$$\frac{1}{d^2} = \frac{h^2 + k^2 + l^2}{a^2}. \quad (2.27)$$

The primitive unit cells for the body-centred and face-centred lattices will not be discussed here because they are not relevant for this work.

PMN-PT and FeRh both also form space group $Pm\bar{3}m$ ^[28;30], numbered 221 in the International Tables, and FeRh additionally forms $Fm\bar{3}m$ (number 225) and $Im\bar{3}m$ (number 229)^[30]. These three space groups are all based on the $\frac{4}{m}\bar{3}\frac{2}{m}$ point group which shortens to $m\bar{3}m$ in common usage^[25].

2.3 Named crystal prototypes

Some lattices and their associated basis appear frequently in nature and so are given natural-language names to aid description and signify their importance. These include perovskite and caesium-chloride structures.

2.3.1 Perovskites

The eponymous mineral of this structure is calcium titanate (CaTiO_3) which was first discovered in 1839 in the Ural Mountains, and is named after the Russian mineralogist Lev Perovski^[31]. The perovskite PMN-PT is of interest in this work due to exhibiting strong ferroelectric properties^[32].

The perovskite structure has the general form ABX_3 . A and B denote cations, typically metals, while X denotes an anion^[32]. This anion is usually oxygen, although one of the halogens may instead occupy the X site in some perovskite structured minerals. The space group is determined using the A cations with the B and X sites defined in the basis, and within this lattice the X sites form vertex-sharing octahedra with the B site at their centroids^[32].

The idealised structure is $Pm\bar{3}m$, shown in Figure 2.10, with basis vectors stated in Table 2.2. In this case the A ions form a simple cubic structure, with the B site at the body-centre and the X sites at the face-centres, forming a regular octahedron around the B site. It should be noted that some authors reverse the labelling of A and B and some papers consider the lattice to be in the B cation rather than the A. This is just a case of notation and both cases are physically identical due to the centring.

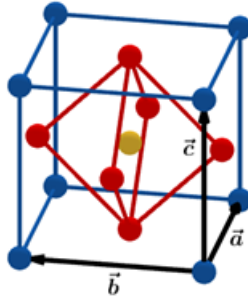


Figure 2.10: The ABX_3 perovskite in the idealised cubic structure $Pm\bar{3}m$. The A cations are coloured blue, the body-centred B cation yellow, and the face-centred X anions red. The lines joining the ions are purely geometric and should not be taken as representative of the chemical bonds.

Ion	Basis vector
A	$(0, 0, 0)$
B	$(\frac{1}{2}, \frac{1}{2}, \frac{1}{2})$
X	$(\frac{1}{2}, \frac{1}{2}, 0)$
X	$(\frac{1}{2}, 0, \frac{1}{2})$
X	$(0, \frac{1}{2}, \frac{1}{2})$

Table 2.2: The basis vectors in fractional coordinates for the ABX_3 perovskite in the cubic structure $Pm\bar{3}m$ ^[32].

This structure is readily distorted and as such the $Pm\bar{3}m$ space group is rarely observed; orthorhombic and tetragonal structures are far more common^[32]. Calcium titanate itself typically forms the orthorhombic space group $Pnma$ (number 62) rather than the idealised $Pm\bar{3}m$. In the tetragonal case, such as the $P4mm$ space group observed for room temperature lead titanate^[28], the perovskite structure is strained from the cubic group in the \vec{c} direction by a factor of c/a , as stated in Section 2.2.4. The

resulting structure is shown in Figure 2.11 and has the same basis vectors in fractional coordinates as in Table 2.2.

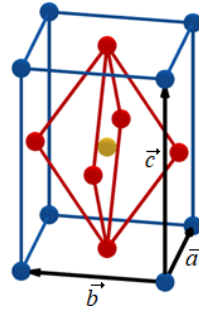


Figure 2.11: The ABX_3 perovskite in the tetragonal structure $P4mm$, colour-coded as in Figure 2.10.

PMN-PT also forms the monoclinic structures Pm and Cm ^[28], via the strains stated in Section 2.2.2, and this is where the structure starts to become more complex. In the case of the simpler Pm the perovskite octahedron still just fills the primitive unit cell. This is shown in Figure 2.12 and still has the same basis vectors in fractional coordinates as in Table 2.2.

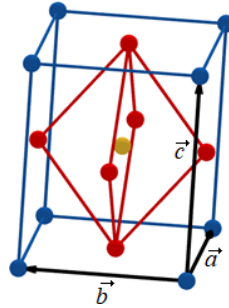


Figure 2.12: The ABX_3 perovskite in the monoclinic structure Pm , colour-coded as in Figure 2.10.

The case for the base-centred structure Cm is more interesting. The perovskite octahedron clearly does not occupy the conventional unit cell due to the extra A cations that would be present in lieu of two of the X sites. Instead, when the lattice forms a Cm space group the perovskite octahedra fill the primitive unit cells. The resulting primitive and conventional unit cells are shown in Figure 2.13 with basis vectors given in Table 2.3.

The final perovskite structure that is relevant for this work is the $R3m$ trigonal space group; this is by far the most complex of the space groups discussed in this section. One would naively assume at first glance that the perovskite may occupy the primitive unit cell, shown in Figure 2.8, in the same manner that it does for the Cm space group. Instead, the deformation from the $Pm\bar{3}m$ group results in a rhombohedral lattice with an additional A site at the centroid of each of the principal unit cell rhombohedra, with the unexpected result that the primitive basis contains two A sites^[33]. This means that the ABX_3 perovskite has structure A_2BX_3 in the primitive basis.

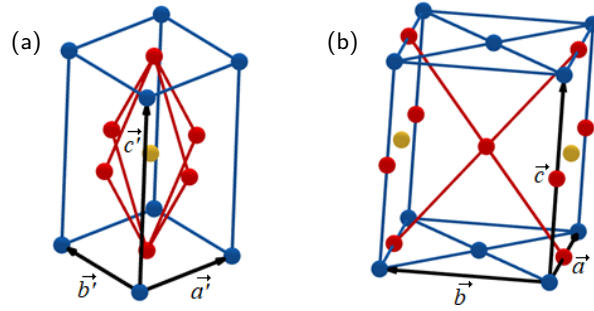


Figure 2.13: The ABX_3 perovskite in the monoclinic structure Cm , colour-coded as in Figure 2.10. (a) The primitive unit cell, clearly showing the perovskite octahedron. (b) The conventional unit cell showing the monoclinic crystal structure, but the perovskite structure is much harder to see.

Ion	Basis vector	
	Primitive	Conventional
A	(0, 0, 0)	(0, 0, 0)
A	N/A	($\frac{1}{2}$, $\frac{1}{2}$, 0)
B	($\frac{1}{2}$, $\frac{1}{2}$, $\frac{1}{2}$)	($\frac{1}{2}$, 0, $\frac{1}{2}$)
X	($\frac{1}{2}$, $\frac{1}{2}$, 0)	($\frac{1}{2}$, 0, 0)
X	($\frac{1}{2}$, 0, $\frac{1}{2}$)	(0, 0, $\frac{1}{2}$)
X	(0, $\frac{1}{2}$, $\frac{1}{2}$)	($\frac{1}{2}$, $\frac{1}{2}$, $\frac{1}{2}$)

Table 2.3: The basis vectors in fractional coordinates for the ABX_3 perovskite in the monoclinic structure Cm . The primitive basis vectors are given in terms of the primitive lattice vectors. Note that there is one less A ion in the primitive basis than in the conventional.

The consequence is that the A sites form a ‘pseudocubic’ structure within the rhombohedral lattice, and the perovskite octahedra instead populate this lattice^[33]. Pseudocubic lattices are qualitatively defined structures used to describe perovskites where the cells are close to being cubic, but are not actually so. These cells are geometrically rhombohedral, but they do not display the requisite symmetry operations to form the $R3m$ space group by themselves. This lack of symmetry is the reason the lattice is defined such that there are two perovskite octahedra per unit cell^[33] rather than following the pseudocubic perovskite structure.

The primitive and conventional unit cells for the $R3m$ perovskite are shown in Figure 2.14 with basis vectors given in Table 2.4.

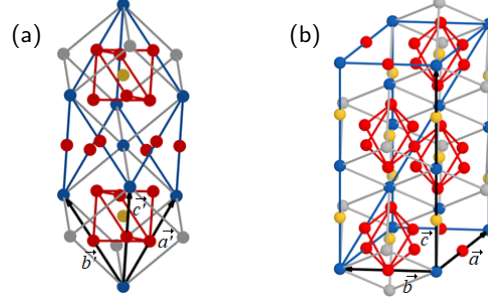


Figure 2.14: The ABX_3 perovskite in the trigonal structure $R\bar{3}m$, colour-coded as in Figure 2.10, with the addition of grey ions representing the centroid ions of the neighbouring primitive cells which form half of the vertices of the pseudocubes. (a) The rhombohedral primitive unit cell showing the two perovskite octahedra. (b) The conventional unit cell showing the trigonal crystal structure containing four perovskite octahedra.

Ion	Basis vector				
	Primitive		Conventional		
A	$(0, 0, 0)$	$(\frac{1}{2}, \frac{1}{2}, \frac{1}{2})$	$(0, 0, 0)$	$(0, 0, \frac{1}{2})$	$(\frac{1}{2}, \frac{2}{3}, \frac{1}{6})$
A	N/A	N/A	$(\frac{2}{3}, \frac{1}{3}, \frac{1}{3})$	$(\frac{1}{3}, \frac{2}{3}, \frac{2}{3})$	$(\frac{2}{3}, \frac{1}{3}, \frac{5}{6})$
B	$(\frac{1}{4}, \frac{1}{4}, \frac{1}{4})$	$(\frac{3}{4}, \frac{3}{4}, \frac{3}{4})$	$(0, 0, \frac{1}{4})$	$(0, 0, \frac{3}{4})$	$(\frac{2}{3}, \frac{1}{3}, \frac{1}{12})$
B	N/A	N/A	$(\frac{1}{3}, \frac{2}{3}, \frac{5}{12})$	$(\frac{2}{3}, \frac{1}{3}, \frac{7}{12})$	$(\frac{1}{3}, \frac{2}{3}, \frac{11}{12})$
X	$(\frac{1}{2}, 0, 0)$	$(0, \frac{1}{2}, 0)$	$(\frac{1}{2}, 0, 0)$	$(0, \frac{1}{2}, 0)$	$(\frac{1}{2}, \frac{1}{2}, 0)$
X	$(0, 0, \frac{1}{2})$	N/A	$(\frac{1}{3}, \frac{1}{6}, \frac{1}{6})$	$(\frac{5}{6}, \frac{1}{6}, \frac{1}{6})$	$(\frac{5}{6}, \frac{2}{3}, \frac{1}{6})$
X	$(\frac{1}{2}, \frac{1}{2}, 0)$	$(\frac{1}{2}, 0, \frac{1}{2})$	$(\frac{1}{6}, \frac{1}{3}, \frac{1}{3})$	$(\frac{1}{6}, \frac{5}{6}, \frac{1}{3})$	$(\frac{2}{3}, \frac{5}{6}, \frac{1}{3})$
X	$(0, \frac{1}{2}, \frac{1}{2})$	N/A	$(\frac{1}{2}, 0, \frac{1}{2})$	$(0, \frac{1}{2}, \frac{1}{2})$	$(\frac{1}{2}, \frac{1}{2}, \frac{1}{2})$
X	$(\frac{1}{2}, 1, 0)$	$(1, 0, \frac{1}{2})$	$(\frac{1}{3}, \frac{1}{6}, \frac{2}{3})$	$(\frac{5}{6}, \frac{1}{6}, \frac{2}{3})$	$(\frac{5}{6}, \frac{2}{3}, \frac{2}{3})$
X	$(0, \frac{1}{2}, 1)$	N/A	$(\frac{1}{6}, \frac{1}{3}, \frac{5}{6})$	$(\frac{1}{6}, \frac{5}{6}, \frac{5}{6})$	$(\frac{2}{3}, \frac{5}{6}, \frac{5}{6})$

Table 2.4: The basis vectors in fractional coordinates for the ABX_3 perovskite in the trigonal structure $R\bar{3}m$. The primitive basis vectors are given in terms of the primitive lattice vectors. Note that there are far fewer ions in the primitive basis than the conventional.

2.3.2 Caesium-Chloride

Another named structure of significance in this work is the two-element caesium chloride (CsCl) structure, named after the common salt which forms this lattice at room temperature and pressure as do certain phases of FeRh ^[30]. This may be described as an interpenetrative primitive cubic structure^[25] because both of the elemental atoms form identical $Pm\bar{3}m$ lattices offset from one another by the fractional vector $(\frac{1}{2}, \frac{1}{2}, \frac{1}{2})$. Alternatively, one may consider it to be an $Im\bar{3}m$ lattice with alternating atoms.

In this work the former definition shall be used. It can be intuited that this structure tends to present itself in compounds that are at or around the equiatomic regime. The CsCl structure is shown in Figure 2.15 with basis vectors given in Table 2.5.

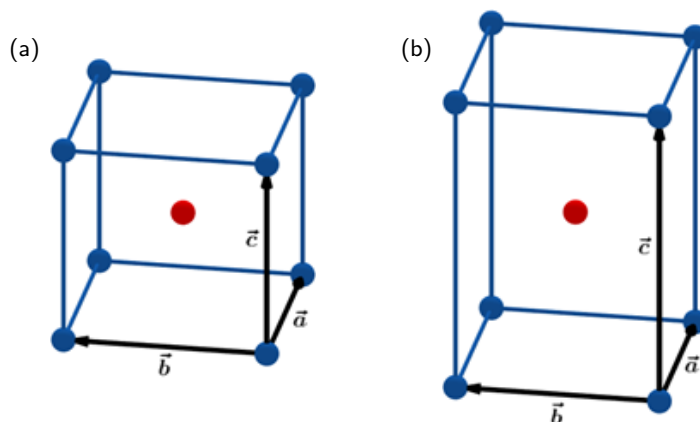


Figure 2.15: The CsCl structure with the two atoms colour-coded for clarity. The lines joining the ions are purely geometric and should not be taken as representative of the chemical bonds. (a) The typical $Pm\bar{3}m$ structure. (b) The less common tetragonal $P4mm$ structure which forms under inhomogeneous strain conditions.

Atom	Basis vector
Blue	$(0, 0, 0)$
Red	$(\frac{1}{2}, \frac{1}{2}, \frac{1}{2})$

Table 2.5: The basis vectors in fractional coordinates for the CsCl structure.

2.3.3 Heusler alloys

This structure is named after the German mining engineer and chemist Friedrich Heusler who published his studies of AlCu_2Mn in 1903^[34]. Heusler compounds are of great interest in spintronics^[35], due to some examples demonstrating large magnetoresistance via half-metallicity, Hall effects, and long-range magnetic ordering via the double-exchange effect.

Heusler compounds have two forms: full-Heuslers X_2YZ and half-Heuslers XYZ ^[35]. In true Heusler compounds X and Y are transition metals and Z is one of the p-block elements, which are those located to the right of the transition metals in the periodic table (excluding helium). However, the Heusler structure can also be used to describe a geometrically-similar lattice which does not satisfy the latter criterion. The structure of a full-Heusler may be thought of as a CsCl lattice in alternating Y and Z with X forming the centroid atom^[30], as shown in Figure 2.16b. In the case of a half-Heusler, alternate X atoms are missing from this lattice, meaning X forms an $Fm\bar{3}m$ lattice with lattice constants doubled from the full-Heusler case.

An alternative way of viewing the full-Heusler structure is as Y and Z forming a pair of interpenetrating $Fm\bar{3}m$ lattices^[35] offset from one another by half a lattice vector. In this case the X lattice would present itself as a cube concentric to and with half the side length of the lattice cubes. This choice of conventional unit cell is the one shown in Figure 2.16a with basis vectors given in Table 2.6.

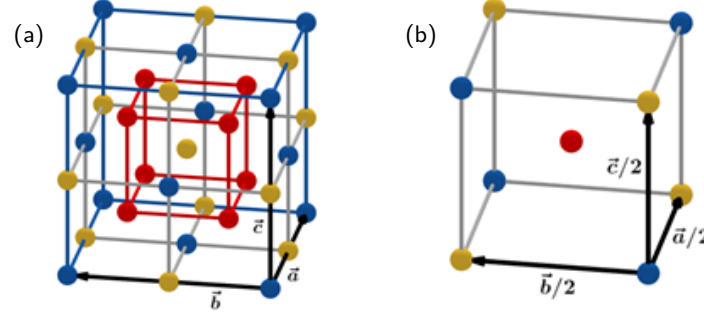


Figure 2.16: The full-Heusler structure X_2YZ . X is shown in red, Y in blue, and Z in yellow. The lines joining the ions are purely geometric and should not be taken as representative of the chemical bonds. (a) The conventional unit cell for the $Fm\bar{3}m$ lattice. (b) The underlying CsCl type structure in the full-Heusler lattice.

Atom	Basis vector			
Y	$(0, 0, 0)$	$(\frac{1}{2}, \frac{1}{2}, 0)$	$(\frac{1}{2}, 0, \frac{1}{2})$	$(0, \frac{1}{2}, \frac{1}{2})$
Z	$(\frac{1}{2}, \frac{1}{2}, \frac{1}{2})$	$(0, 0, \frac{1}{2})$	$(0, \frac{1}{2}, 0)$	$(\frac{1}{2}, 0, 0)$
X	$(\frac{1}{4}, \frac{1}{4}, \frac{1}{4})$	$(\frac{1}{4}, \frac{1}{4}, \frac{3}{4})$	$(\frac{1}{4}, \frac{3}{4}, \frac{1}{4})$	$(\frac{3}{4}, \frac{1}{4}, \frac{1}{4})$
X	$(\frac{3}{4}, \frac{3}{4}, \frac{3}{4})$	$(\frac{3}{4}, \frac{3}{4}, \frac{1}{4})$	$(\frac{3}{4}, \frac{1}{4}, \frac{3}{4})$	$(\frac{1}{4}, \frac{3}{4}, \frac{3}{4})$

Table 2.6: The basis vectors in fractional coordinates for the conventional unit cell of the full-Heusler structure X_2YZ , which is considered to be an $Fm\bar{3}m$ lattice in Y.

2.4 Introduction to magnetism and spintronics

Electromagnetism is one of the four fundamental forces and underpins a significant quantity of atomic interactions. Magnetism is the result of atomic and electronic spins hence the area of research seeking to create devices from magnetic properties is known as spintronics. There are two main unit systems in use in the study of magnetism: the SI system is of course one of these, while the second is the centimetre-gram-second (CGS) unit system, often favoured in earlier work. This thesis will be using the SI system for the most part and any use of the CGS system will be made explicit.

The conversion between the two systems is mostly through powers of 10, however 4π is also a common factor and the vacuum permeability^[36]

$$\mu_0 = 1.256637 \dots \times 10^{-6} \text{ N A}^{-2} \approx 4\pi \times 10^{-7} \text{ N A}^{-2} \quad (2.28)$$

appears in SI equations whilst in CGS units the vacuum permeability is unity. The four most useful conversion factors are provided in Table 2.7.

Quantity	Symbol	SI Unit	CGS Unit
Magnetic flux density	\vec{B}	1 T	$= 10^4$ G
Magnetic field strength	\vec{H}	1 A m ⁻¹	$\approx 4\pi \times 10^{-3}$ Oe
Magnetisation	\vec{M}	1 A m ⁻¹	$\approx 10^{-3}$ emu cm ⁻³
Magnetic moment	$\vec{\mu}$	1 Am ²	$\approx 10^3$ emu

Table 2.7: Conversion between SI and CGS units for four key magnetic parameters. The CGS units are the gauss, the oersted, and the electromagnetic unit. The definition of μ_0 is no longer exact following the 2019 SI redefinition^[37]. Table adapted from the appendix of *Magnetism in Condensed Matter*^[38].

The following sections aim to provide an overview of relevant magnetic phenomena. A rigorous treatment is not necessary because this work was focussed on advanced metrology and a qualitative understanding will be more than adequate to understand this thesis.

2.4.1 Magnetic dipoles

A dipole is essentially a nanoscale bar magnet, with two opposite poles and magnetic field lines looping around the outside and connecting the poles externally^[39], as shown in Figure 2.17. The Biot-Savart law states that for a closed loop of moving charge a magnetic field is produced normal to the centre of the loop, with magnitude proportional to current and inversely proportional to radius^[19]. On the atomic scale both of these are small and not well-defined, however the ratio is much larger and thus better defined, and this allows a macroscopic magnetic field to be observed. The orbital angular motion of an electron around an atom forms such a loop and thus individual atoms are able to form magnetic dipoles^[19].

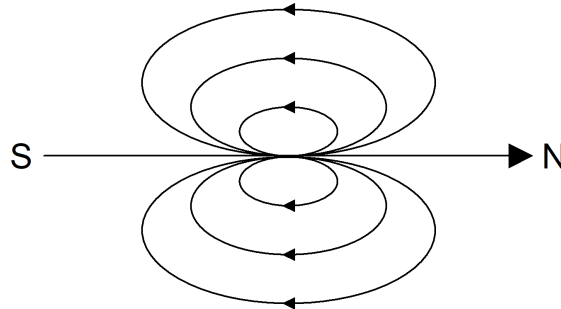


Figure 2.17: The magnetic field lines for a magnetic dipole.

These orbital magnetic dipoles only occur in atoms with non-zero orbital angular momentum, because when the net orbital angular momentum is zero then the opposing orbits will mean the ‘current’ cancels

out. Hund's rules state that orbital angular momentum states are populated with spin-up electrons first, followed by spin-down electrons^[19], meaning that a net magnetic moment is observed for the electrons surrounding an atom when a particular spin state of the outermost shell is partially filled. This typically occurs when there are unequal numbers of spin-up and spin-down electrons, with the exception of the special case when spin-up electrons occupy all orbital states and no spin-down electrons are present.

The dipole moment $\vec{\mu}$, also denoted \vec{m} in the literature, is a measure of the field direction and strength and has SI units of A m^2 ^[19]. The terminology 'moment' is because this is also a measure of the moment required to alter the dipole orientation. The potential energy U of a dipole in an external field \vec{H} is given by^[39]

$$U = -\mu_0 \vec{\mu} \cdot \vec{H} \quad (2.29)$$

and the resulting torque $\vec{\tau}$ is given by^[39]

$$\vec{\tau} = \mu_0 \vec{\mu} \times \vec{H} . \quad (2.30)$$

The potential energy, known as the Zeeman energy when the dipoles are formed by electrons^[19], is minimised when dipole moment and external field are parallel and maximised when dipole moment and external field are anti-parallel. The torque $\vec{\tau}$ acts to minimise this energy.

The magnetisation \vec{M} of a medium is a measure of the alignment of magnetic dipole moments, and as such is also known as the intensity of magnetisation. It is defined with respect to volume \mathcal{V} as^[39]

$$\vec{M} \equiv \frac{\partial \vec{\mu}}{\partial \mathcal{V}} . \quad (2.31)$$

2.4.2 Magnetic fields

The field observed outside a magnetic medium is the \vec{H} field and in this case is related to magnetic flux density \vec{B} by simply multiplying by the vacuum permeability, i.e.^[19]

$$\vec{B} = \mu_0 \vec{H} . \quad (2.32)$$

Permeability is the measure of induced magnetisation in a medium^[39]. In CGS units the \vec{B} , \vec{H} , and \vec{M} fields share the same units, so the vacuum permeability is unity, while in the SI system it has value solely for purposes of unit conversion.

The flux density is a measure of the number of field lines per unit area, meaning inside a magnetic medium the magnetisation also contributes to the flux density, with this relationship being^[39]

$$\vec{B} = \mu_0 \left(\vec{H} + \vec{M} \right) . \quad (2.33)$$

Some authors also define a magnetic polarisation $\vec{I} \equiv \mu_0 \vec{M}$ [39], analogous to the electric polarisation, giving

$$\vec{B} = \mu_0 \vec{H} + \vec{I}. \quad (2.34)$$

However, this will not be used here.

2.5 Atomic origins of magnetic ordering

2.5.1 Classical dipole interaction energy

The classical model is to consider a series of dipoles interacting with one another as if they were just a series of localised bar magnets [19]. In this model the magnetic potential energy of two dipoles is calculated using equation (2.29), where the field is now produced by one of the dipoles. It may be shown from the magnetic potential field \vec{A} that the field produced by a dipole at some point \vec{r} relative to the dipole location is [40]

$$\vec{B}(\vec{\mu}, \vec{r}) = \nabla \times \vec{A}(\vec{\mu}, \vec{r}) = \frac{\mu_0}{4\pi} \nabla \times \left(\vec{\mu} \times \frac{\vec{r}}{|\vec{r}|^3} \right) = \frac{\mu_0}{4\pi} \left[\frac{3\hat{r}(\vec{\mu} \cdot \hat{r}) - \vec{\mu}}{|\vec{r}|^3} \right]. \quad (2.35)$$

Thus for two dipoles of moments $\vec{\mu}_1$ and $\vec{\mu}_2$ with a separation \vec{r}_{12} the magnetic energy is

$$U(\vec{\mu}_1, \vec{\mu}_2, \vec{r}_{12}) = -\vec{\mu}_2 \cdot \vec{B}(\vec{\mu}_1, \vec{r}_{12}) = \frac{\mu_0}{4\pi} \left[\frac{\vec{\mu}_1 \cdot \vec{\mu}_2 - 3(\vec{\mu}_1 \cdot \hat{r}_{12})(\vec{\mu}_2 \cdot \hat{r}_{12})}{|\vec{r}_{12}|^3} \right]. \quad (2.36)$$

The \vec{B} field is used here in lieu of $\mu_0 \vec{H}$ to reflect the fact this is occurring within a magnetic medium.

The total energy for each of four common alignments are given in Table 2.8 where the shorthand

$$U_0 \equiv |\vec{\mu}_1| |\vec{\mu}_2| \frac{\mu_0}{4\pi |\vec{r}_{12}|^3} \geq 0 \quad (2.37)$$

has been used. The result of these calculations is that from a classical dipole perspective

$$U(\rightarrow\leftarrow) \geq U(\uparrow\uparrow) \geq U(\uparrow\downarrow) \geq U(\rightarrow\rightarrow). \quad (2.38)$$

This helps to explain why in thin films the dominant arrangements are ferromagnetic dipoles parallel to the surface and antiferromagnetic dipoles normal to the surface: energy may be minimised by arranging the highest energy alignment to be in the smallest crystal dimension.

It can be shown that the magnetic moment for some angular contribution i for some particle with mass m and charge q is given by [19]

$$\vec{\mu}_i = \frac{g_i q}{2m} \vec{i}, \quad (2.39)$$

where g_i is the a corresponding constant known as the g-factor. The most significant contribution is for electron spin S , where S_z may take the value of $\pm\hbar/2$; nuclear contributions are suppressed by the

Alignment	$\vec{\mu}_1 \cdot \vec{\mu}_2$	$(\vec{\mu}_1 \cdot \hat{r}_{12})(\vec{\mu}_2 \cdot \hat{r}_{12})$	$U(\vec{\mu}_1, \vec{\mu}_2, \vec{r}_{12})$
$\rightarrow \leftarrow$	$- \vec{\mu}_1 \vec{\mu}_2 $	$- \vec{\mu}_1 \vec{\mu}_2 $	$2U_0$
$\uparrow \downarrow$	$- \vec{\mu}_1 \vec{\mu}_2 $	0	$-U_0$
$\rightarrow \rightarrow$	$ \vec{\mu}_1 \vec{\mu}_2 $	$ \vec{\mu}_1 \vec{\mu}_2 $	$-2U_0$
$\uparrow \uparrow$	$ \vec{\mu}_1 \vec{\mu}_2 $	0	U_0

Table 2.8: The dipole interaction energy for four relative orientations of dipole moments of an idealised two-dipole system.

mass term in equation (2.39). Thus equation (2.39) becomes

$$\mu_z = \frac{-g_S e}{2m_e} \left(\pm \frac{\hbar}{2} \right) = \mp \frac{g_S}{2} \frac{e\hbar}{2m_e} \equiv \mp \frac{g_S}{2} \mu_B, \quad (2.40)$$

where \hbar is the reduced Planck constant, e is the elementary charge, m_e is the electron mass, and μ_B is the Bohr magneton^[19], a useful constant in dipole dynamics.

The electron g-factor g_e has a value^[36] of

$$g_e \approx -2.0023, \quad (2.41)$$

and would be exactly -2 if not for the effects of quantum electrodynamics^[41]. The electron spin g-factor g_S is defined as

$$g_S \equiv |g_e| \approx 2, \quad (2.42)$$

thus

$$\mu_z = \mp \mu_B. \quad (2.43)$$

The magnitude of the dipole interaction energy U_0 can now be calculated for FeRh where $|\vec{r}_{12}| \approx 3 \text{ \AA}$ and $|\vec{\mu}_1| = |\vec{\mu}_2| = \mu_B$, using equation (2.37) to give

$$U_0 \approx 3.19 \times 10^{-25} \text{ J} \approx 1.99 \text{ \mu eV}. \quad (2.44)$$

In comparison, the electrostatic potential energy between these electrons may be calculated using the Coulomb energy^[19],

$$U_{\text{ele}} = \frac{q_1 q_2}{4\pi\epsilon_0 |\vec{r}_{12}|}, \quad (2.45)$$

where ϵ_0 is vacuum permittivity, to be

$$U_{\text{ele}} \approx 7.69 \times 10^{-19} \text{ J} \approx 4.80 \text{ eV} \gg U_0. \quad (2.46)$$

Thus showing that the energy from classical dipole interactions is inadequate to cause significant magnetic effects on its own without being overridden by electrostatic interactions. This suggests that there must also be some other large contribution to the energy of the system occurring.

2.5.2 Exchange interaction energy

This section discusses the exchange interaction energy in more analytical detail than the other magnetic concepts introduced in this chapter thus far. This is because it is the least intuitive magnetic interaction due to its quantum mechanical nature, and following the analytical origins of the behaviour can aid in comprehending the phenomenon.

Consider two neighbouring protons a and b located at \vec{R}_a and \vec{R}_b respectively, and two electrons 1 and 2 located at \vec{r}_1 and \vec{r}_2 respectively. The spatial wavefunctions of the electrons surrounding protons a and b will be denoted ϕ_a and ϕ_b respectively, thus the difference between $\phi_a(\vec{r}_1), \phi_b(\vec{r}_2)$ and $\phi_a(\vec{r}_2), \phi_b(\vec{r}_1)$ is merely which nucleus the electrons are considered to be affiliated with.

2.5.2.1 The overlap integral

The overlap integral S_{ab} , confusingly defined using the same symbol as spin, describes the overlap of the orbitals of two atoms and is given by^[42]

$$S_{ab} \equiv \int_{\mathcal{V}} \phi_a^*(\vec{r}) \phi_b(\vec{r}) d\vec{r}, \quad (2.47)$$

where the integral runs over all space \mathcal{V} .

In Dirac notation this is

$$S_{ab} \equiv \langle \phi_a | \phi_b \rangle. \quad (2.48)$$

Note that for any normalised wavefunction $S_{aa} = S_{bb} = 1$ by definition, and if the wavefunctions $\phi_a(\vec{r})$ and $\phi_b(\vec{r})$ are orthogonal then $S_{ab} = 0$. Note also that $S_{ab} = S_{ba}^*$, but the wavefunctions dealt with in this section are all real so $S_{ab} = S_{ba}$. Some authors^[39;19] assume the overlap to be maximal and just set S_{ab} to 1, but it will be retained here for a more complete picture.

For the two electron positions \vec{r}_1 and \vec{r}_2 it can be seen that^[42]

$$\begin{aligned} \int_{\mathcal{V}} \int_{\mathcal{V}} \phi_a^*(\vec{r}_1) \phi_b^*(\vec{r}_2) \phi_b(\vec{r}_1) \phi_a(\vec{r}_2) d\vec{r}_1 d\vec{r}_2 &= \int_{\mathcal{V}} \phi_a^*(\vec{r}_1) \phi_b(\vec{r}_1) d\vec{r}_1 \int_{\mathcal{V}} \phi_b^*(\vec{r}_2) \phi_a(\vec{r}_2) d\vec{r}_2 \\ &= S_{ab} S_{ba} = S_{ab}^2. \end{aligned} \quad (2.49)$$

Defining $|\phi_a \phi_b\rangle \equiv \phi_a(\vec{r}_1) \phi_b(\vec{r}_2)$ and $|\phi_b \phi_a\rangle \equiv \phi_b(\vec{r}_1) \phi_a(\vec{r}_2)$, this means

$$S_{ab}^2 = \langle \phi_a \phi_b | \phi_b \phi_a \rangle = \langle \phi_b \phi_a | \phi_a \phi_b \rangle. \quad (2.50)$$

2.5.2.2 Spin singlets and triplets

The total spin S of two electrons can either be 0 or 1.

In the $S = 0$ case the spin wavefunction is antisymmetric and is described by^[42]

$$\chi_S(\sigma_a, \sigma_b) = \frac{1}{\sqrt{2}} [\chi_\uparrow(\sigma_a) \chi_\downarrow(\sigma_b) - \chi_\downarrow(\sigma_a) \chi_\uparrow(\sigma_b)] \equiv \frac{1}{\sqrt{2}} (|\uparrow\downarrow\rangle - |\downarrow\uparrow\rangle) \quad (2.51)$$

where σ_a and σ_b are the respective spin states of protons a and b , while χ_\uparrow and χ_\downarrow describe the direction of the encapsulated spin state.

In the $S = 1$ case there are three possible wavefunctions, which are symmetric and described by^[42]

$$\chi_{T,1}(\sigma_a, \sigma_b) = |\uparrow\uparrow\rangle \quad S_z = +1, \quad (2.52)$$

$$\chi_{T,2}(\sigma_a, \sigma_b) = \frac{1}{\sqrt{2}} (|\uparrow\downarrow\rangle + |\downarrow\uparrow\rangle) \quad S_z = 0, \quad (2.53)$$

$$\chi_{T,3}(\sigma_a, \sigma_b) = |\downarrow\downarrow\rangle \quad S_z = -1. \quad (2.54)$$

2.5.2.3 Spatial wavefunctions

There are two possible spatial wavefunctions for the system^[19],

$$|\phi_\pm\rangle = A_\pm (|\phi_a\phi_b\rangle \pm |\phi_b\phi_a\rangle), \quad (2.55)$$

where ϕ_+ is the symmetric wavefunction, ϕ_- is the antisymmetric wavefunction, and

$$A_\pm = (2 \pm 2S_{ab}^2)^{-1/2} \quad (2.56)$$

is the corresponding normalisation constant.

The total wavefunction is the product of spatial and spin components. The Pauli exclusion principle requires that the total wavefunction of a fermion must be antisymmetric, thus the symmetry of the spatial wavefunction must oppose that of the spin wavefunction^[19].

This means that the singlet and triplet spatial wavefunctions are given by

$$|\phi_S\rangle = |\phi_+\rangle = (2 + 2S_{ab}^2)^{-1/2} (|\phi_a\phi_b\rangle + |\phi_b\phi_a\rangle) \quad (2.57)$$

and

$$|\phi_T\rangle = |\phi_-\rangle = (2 - 2S_{ab}^2)^{-1/2} (|\phi_a\phi_b\rangle - |\phi_b\phi_a\rangle). \quad (2.58)$$

Each electron is assumed to be independent^[42] so the spatial wavefunctions are separable into

$$|\phi_\pm\rangle \propto [(1+i)|\phi_a\rangle + (\pm 1-i)|\phi_b\rangle] \otimes [(\pm 1+i)|\phi_a\rangle + (1-i)|\phi_b\rangle] \quad (2.59)$$

which holds because the coefficients in equation (2.55) are merely the real components of the true wavefunction. The real components shall once again be taken to aid comprehension by reducing the number of dimensions and enabling the drawing of 2D curves, yielding

$$|\phi_\pm\rangle \propto (|\phi_a\rangle \pm |\phi_b\rangle) \otimes (|\phi_a\rangle \pm |\phi_b\rangle) \quad (2.60)$$

where a factor of ± 1 has been applied and thus each electron independently satisfies $|\phi\rangle \propto |\phi_a\rangle \pm |\phi_b\rangle$.

These spatial wavefunctions are typically considered for the case of the hydrogen atom with only the innermost $1s$ orbitals occupied. The expression for the wavefunction of a $1s$ electron at some spatial radius r is^[43]

$$|\phi\rangle \propto \exp\left(-\frac{r}{a_B}\right) \quad (2.61)$$

where $a_B \approx 53 \text{ pm}$ ^[36] is the Bohr radius, and this modifies for the two electron system to give

$$|\phi_a\rangle \propto \exp\left(-\frac{|r - a/2|}{a_B}\right) \quad (2.62)$$

and

$$|\phi_b\rangle \propto \exp\left(-\frac{|r + a/2|}{a_B}\right) \quad (2.63)$$

where the host nuclei have separation a with the origin at the midpoint. The symmetric and antisymmetric wavefunctions are shown in Figure 2.18 and the corresponding spatial probability distributions are shown in Figure 2.19. The overlap area of the absolute value of the wavefunctions is the overlap integral.

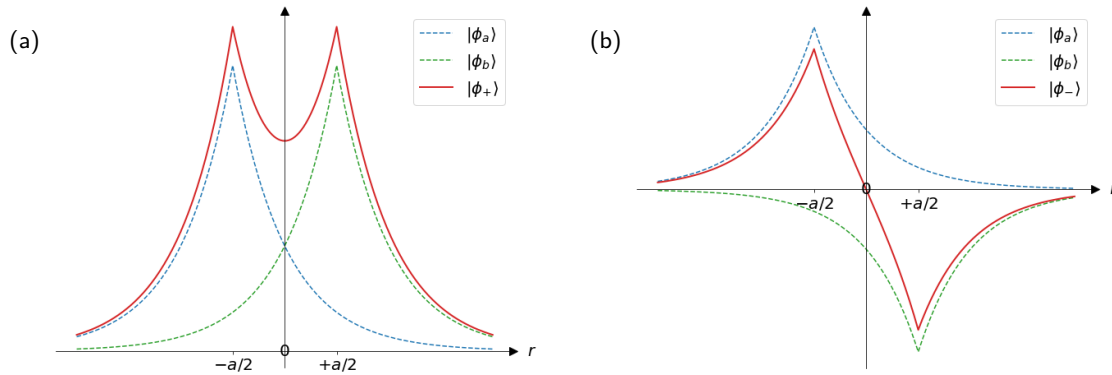


Figure 2.18: The symmetric and antisymmetric spatial wavefunctions for two $1s$ electrons such as those in a H_2 hydrogen molecule. (a) The symmetric wavefunction $|\phi_+\rangle$ (b) The antisymmetric wavefunction $|\phi_-\rangle$.

The symmetric spatial wavefunction, correlating to the antisymmetric spin wavefunction, permits the electrons to occupy any location between and around the two nuclei whilst the antisymmetric spatial wavefunction, correlating to the symmetric spin wavefunction, directly prohibits the electron from being located midway between the two. This is a consequence of the Pauli exclusion principle which prohibits symmetric spin states from occupying the same spatial state and thus each electron must be localised to a specific nucleus. In a real crystal this is much more complex, however, with $1s$ orbitals being occupied and higher orbitals instead mediating the interatomic bonding and magnetic properties. For example,

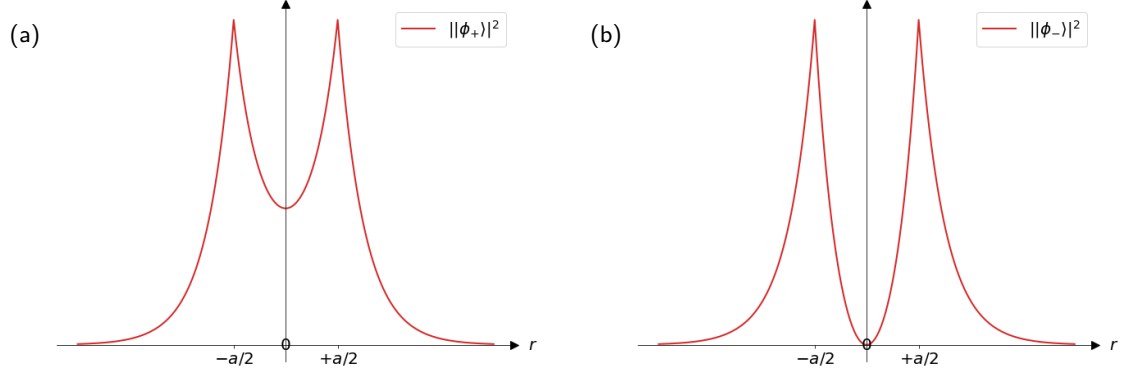


Figure 2.19: The symmetric and antisymmetric spatial probability distributions for two $1s$ electrons such as those in a H_2 hydrogen molecule. (a) The symmetric probability distribution $||\phi_+\rangle|^2$. (b) The antisymmetric probability distribution $||\phi_-\rangle|^2$.

the incomplete orbital for the transition metal Fe is $3d$ for which^[43]

$$|\phi\rangle \propto \exp\left(-\frac{r}{3a_B}\right) r^2 \quad (2.64)$$

and thus the spatial wavefunctions are far more localised than those in the H_2 molecule.

2.5.2.4 Coulomb integral

Consider the case where $|\vec{R}_a - \vec{R}_b| \rightarrow \infty$, so the energy of each atom is the ground energy E_0 . The stationary Schrödinger equation may then be used^[42] which states that

$$\hat{H} |\phi\rangle = E_0 |\phi\rangle, \quad (2.65)$$

where for the two electron system

$$\hat{H}_{2e} = \hat{H}_a + \hat{H}_b. \quad (2.66)$$

As the atoms approach one another additional Coulomb terms appear^[44] due to interactions between the two nuclei, the two electrons, and each electron with the nucleus of the other atom. The result is that equation (2.66) becomes

$$\hat{H}_{2e} \equiv \hat{H}_a + \hat{H}_b + H_{ab} \quad (2.67)$$

where H_{ab} has been used to represent the non-operator terms.

The total energy is thus obtained using this operator, yielding diagonal matrix elements of

$$\langle \hat{H}_{2e} \rangle = \langle \phi_a \phi_b | \hat{H}_{2e} | \phi_a \phi_b \rangle = E_0 + E_0 + \langle \phi_a \phi_b | H_{ab} | \phi_a \phi_b \rangle \quad (2.68)$$

$$\equiv 2E_0 + C, \quad (2.69)$$

where $C \equiv \langle \phi_a \phi_b | H_{ab} | \phi_a \phi_b \rangle \geq 0$ is the two-site two-electron Coulomb integral.

2.5.2.5 Exchange integral

In contrast to the Coulombic effects of the diagonal matrix elements, the cross-terms are purely quantum mechanical in origin^[19]. Evaluating them gives

$$\langle \phi_a \phi_b | \hat{H}_{2e} | \phi_b \phi_a \rangle = E_0 |S_{ab}|^2 + E_0 |S_{ab}|^2 + \langle \phi_a \phi_b | H_{ab} | \phi_b \phi_a \rangle \quad (2.70)$$

$$\equiv 2E_0 |S_{ab}|^2 + J_{ex}, \quad (2.71)$$

where $J_{ex} \equiv \langle \phi_a \phi_b | H_{ab} | \phi_b \phi_a \rangle \geq 0$ is the exchange integral.

2.5.2.6 Energy of the singlet and triplet states

The energies of the two states are given by

$$E_{\pm} = \langle \phi_{\pm} | \hat{H}_{ab} | \phi_{\pm} \rangle = 2E_0 + \frac{C \pm J_{ex}}{1 \pm |S_{ab}|^2}. \quad (2.72)$$

This means the singlet state, with antisymmetric spin wavefunction, has an energy of

$$E_S = E_+ = 2E_0 + \frac{C + J_{ex}}{1 + |S_{ab}|^2} \quad (2.73)$$

and the triplet state, with symmetric spin wavefunctions, has an energy of

$$E_T = E_- = 2E_0 + \frac{C - J_{ex}}{1 - |S_{ab}|^2}. \quad (2.74)$$

The difference in energy between the two states is therefore

$$E_S - E_T = \frac{2C |S_{ab}|^2 - 2J_{ex}}{1 - |S_{ab}|^4}. \quad (2.75)$$

2.5.2.7 Exchange constant

The exchange constant J_{ab} is defined as half of the energy difference between the singlet and triplet states^[44], thus

$$J_{ab} \equiv \frac{1}{2} (E_S - E_T) = \frac{C |S_{ab}|^2 - J_{ex}}{1 - |S_{ab}|^4}. \quad (2.76)$$

The magnitude of J_{ab} is a measure of the strength of the exchange interaction, because this is the energy that must be overcome by the thermal excitations in order to disrupt the magnetic ordering.

The sign of J_{ab} , and thus the preferred arrangement of the system, is determined by the relative sizes of J_{ex} and $C |S_{ab}|^2$. If $J_{ab} < 0$ then the singlet state is preferred with its antisymmetric spin states and antiferromagnetic behaviour is favoured, while if $J_{ab} > 0$ then the triplet state is preferred with its symmetric spin state and ferromagnetic behaviour is favoured.

The exchange integral is a measure of how ‘exchangeable’ the electrons are. This is due to the indistinguishable nature of electrons^[42] which allows their properties to be exchanged without creating a degenerate microstate. A small value of J_{ex} means the electrons are minimally coupled and thus their parameters are not correlated and they have low exchangeability, whilst a larger value reflects stronger coupling and higher exchangeability. The Coulomb integral is a measure of electrostatic interaction strength between the two halves of the system.

A large value of J_{ex} and small CS_{ab}^2 ($J_{ab} < 0$) suggests electrons are minimally interacting but are spread between both nuclei. This would require antisymmetric spins to minimise occupied energy levels due to the Pauli exclusion principle and indeed equation (2.76) returns the antisymmetric configuration as the minimal energy state in this case. On the other hand a small value of J_{ex} and large CS_{ab}^2 ($J_{ab} > 0$) suggests the electrons are keeping to their respective nuclei but strongly interacting. In this case the Pauli exclusion principle does not prohibit parallel spins and in fact the Coulombic interactions will encourage the electrons to synchronise their spins, yielding symmetric ferromagnetic ordering. Once again equation (2.76) agrees. If the orbitals are orthogonal then $S_{ab} = 0$ and $J_{ab} = -J_{ex}$. This occurs for electrons orbiting the same atom^[44], where symmetric spins clearly cannot occupy the same orbital.

This is a useful model of the quantum mechanical magnetic interactions between dipoles, however this model makes the assumption that electrons are localised to the vicinity of a host nucleus. The delocalised electrons present in a conducting system cause issues with this nearest-neighbour focus^[45].

2.5.3 RKKY interaction

A correction to address the limitations of the exchange model discussed in Section 2.5.2 is the Ruderman-Kittel-Kasuya-Yosida (RKKY) interaction^[46;45;47]. This provides a coupling mechanism between nuclear spins^[46] or between non-neighbouring, localised, inner-shell electrons in systems where both delocalised and localised single-orbital electrons are present^[45]. The nuclear spin is not significant for the magnetic material discussed in this thesis, and it is the latter application which is of interest.

In rare-earth metal systems there are both localised and delocalised electrons^[45]. The dipole moments of the localised electrons would naively be expected to interact following the nearest-neighbour exchange interaction, but this model yields interaction energies with far lower magnitude than are observed, so evidently another interaction is dominating. The RKKY interaction is a long range magnetic ordering phenomenon using the conducting electrons as intermediaries. A localised electron couples to a nearby conducting electron through the exchange interaction, which then travels through the medium and couples to another localised electron through another exchange interaction^[45]. The result is the two localised electrons being able to establish long-range interaction between one another and this has a magnification effect on the strength of the magnetic ordering.

2.5.4 Atomic orbitals and magnetic dipole ordering

The emergence of ordered magnetism requires the presence of unpaired electrons so that a net spin and thus dipole moment may be observed^[19]. The s and p orbitals are not suitable because these readily form covalent bonds with neighbouring atoms and create shared electron pairs^[48]. Additionally, the limited population of electron levels in these orbitals do not provide a high enough density of states at the Fermi energy for ferromagnetic ordering^[49]; the need for high density of states is explained in Section 2.9.2 using Figure 2.33.

This suggests that unpaired d or f orbitals are the condition for magnetic ordering, but it is the $3d$ orbital in particular which is primarily responsible^[50]. This is because the orbitals in $4d$ and higher are further away from the nucleus and so are less tightly bonded and thus able to overlap with neighbouring orbitals to form covalent bonds, while the orbital $3d$ is close enough that the nuclear attraction dominates and any overlap with neighbouring atoms is very weak^[50]. The $4f$ orbitals are similarly tightly bonded to the nuclear charge and thus the lanthanide elements, which feature incomplete $4f$ orbitals, are also magnetically ordered^[50]; however these are not common elements. The importance of the $3d$ orbital led to the development of the Bethe-Slater curve^[39] shown in Figure 2.20.

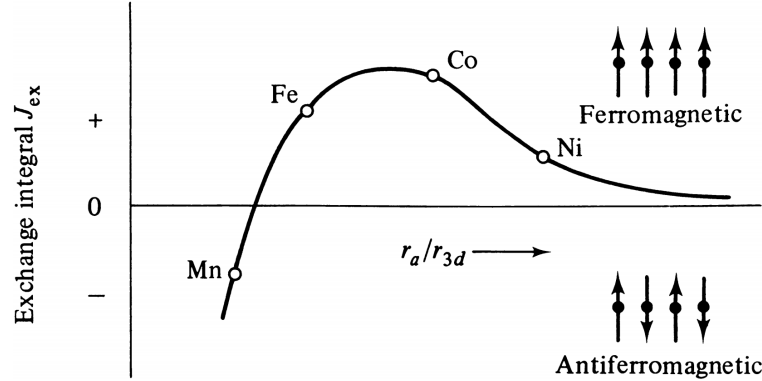


Figure 2.20: The Bethe-Slater curve showing the dependence of the exchange integral J_{ex} on the ratio of atomic radius r_a to the radius of the $3d$ orbital r_{3d} . Figure reproduced from *Introduction to Magnetic Materials*^[39].

The concept behind the Bethe-Slater curve was published in 1930^[51;48] by Slater and is used to predict the magnetic properties of a lattice using the $3d$ shell radius r_{3d} and overall atomic radius r_a ; the atomic diameter $2r_a$ is equal to the lattice spacing due to the close-packed nature of solids^[39]. The curve shows negative exchange coupling for smaller atoms and thus AF ordering and positive exchange coupling for larger atoms and thus FM ordering. The exchange coupling falls off for very large atoms.

2.6 Induced magnetisation

The magnetic properties of a material are well characterised by the magnetisation, more specifically the relationship between \vec{M} and \vec{H} . Magnetisation curves are drawn to show how an applied field is able to manipulate the magnetisation of the medium, and the differential of this curve is the magnetic susceptibility $\chi^m(\vec{H})$ ^[39]. Magnetic susceptibility is always a dimensionless property due to \vec{M} and \vec{H} sharing the same units in both unit systems. This susceptibility depends on the dipole moment per unit volume so is also known as the volume susceptibility^[39]. Other susceptibilities may be defined by considering dipole moment per some other quantity such as mass or moles.

There are two common types of magnetism which have linear but shallow magnetisation curves, and thus exhibit a constant but small susceptibility. These are diamagnetism and paramagnetism, and the linear relationship allows the definition of a constant relative permeability μ_r , where^[39]

$$\vec{B} = \mu_0 (\vec{H} + \vec{M}) = \mu_0 (\vec{H} + \chi^m \vec{H}) = \mu_0 (1 + \chi^m) \vec{H} \equiv \mu_0 \mu_r \vec{H}. \quad (2.77)$$

Diamagnetism occurs in all materials and is a nanoscale manifestation of Lenz's law. The applied field acts on the charged electrons driving the 'current' in such a way that the magnetisation forms opposing the field^[39]. This causes a negative susceptibility and repels the medium from the field. However, due to the electrostatic force between electron and nucleus, and the restrictions imposed by the Pauli exclusion principle, this susceptibility is very slight^[39]. It is typically of order $\chi^m \sim -10^{-6}$ ^[19] and as such overshadowed by any other magnetism manifestations.

Paramagnetism on the other hand occurs only in materials with unpaired electrons. These are free to align with the applied field without hindrance from such phenomena as Pauli's exclusion principle, and result in a magnetisation which is aligned with the applied field and possesses a positive susceptibility, meaning the material is attracted to the field^[39]. The alignment is limited by thermal excitations, however, so the induced magnetisation is not as strong as in ordered magnetic systems^[39]. Hund's rules require orbitals to be populated singly where possible^[19] so there may be multiple unpaired electrons in each atom resulting in a stronger paramagnetic effect. The paramagnetic susceptibility is typically of order 10^{-5} to 10^{-3} ^[19].

In an electrically conductive material the electrons are delocalised and the phenomenon differs somewhat. The applied field shifts the energy levels of the up and down spin states to be offset by the dipole potential energy, as shown in Figure 2.21, resulting in a net magnetisation aligned with the field^[19]. This induces Pauli paramagnetism which is a weaker form of paramagnetism than the localised form, and is of similar order of magnitude to the diamagnetic effect but of opposite sign.

Materials which exhibit paramagnetic and diamagnetic responses have no inherent magnetisation of

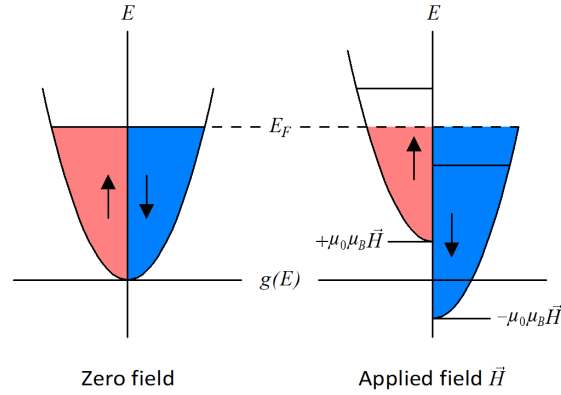


Figure 2.21: The density of states for an electrically conductive material in zero field (left) and applied field (right). The arrows show the electron spins and are opposite to the dipole moment directions due to the negative electron charge. The blue region represents magnetic dipole moments aligned with the field and the red represents those opposed. The relative change in density of states results in a net magnetisation parallel to the applied field. The Bohr magneton μ_B is the magnitude of the electron spin dipole moment and is discussed further in Section 2.5.1.

their own and only align in the presence of an external field. This is because there is insufficient energy exchange occurring between neighbouring dipoles to overcome the thermal excitations of each dipole^[39].

2.7 Ordered magnetisation

Unlike in paramagnetic and diamagnetic materials, some materials are able to sustain magnetic ordering after the external field has been removed. The exchange energy in these materials is able to surpass the thermal excitations and maintain stable alignment. There are three types of magnetism in this category: ferromagnetism, antiferromagnetism, and ferrimagnetism^[39]. However, all of these may be heated past some critical temperature at which point thermal excitations become dominant and paramagnetic behaviour ensues.

2.7.1 Ferromagnetism

In ferromagnetism the exchange energy is minimised when neighbouring dipole moments are aligned in parallel^[19], as shown in Figure 2.22. This produces a strong magnetisation which persists when the field is removed. The magnetisation curve is non-linear and forms a hysteresis loop^[39] as shown in Figure 2.23.

The magnetisation rises monotonically with magnetic field and plateaus once the saturation magnetisation M_s is reached. This is the point where all magnetic dipole moments are aligned with the field. Upon field removal the interactions between dipoles ensure they remain parallel, maintaining the remanence

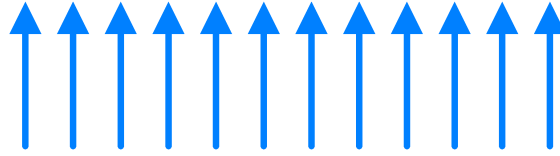


Figure 2.22: A representation of ferromagnetism in one dimension. The arrows represent relative dipole moment orientations and magnitudes.

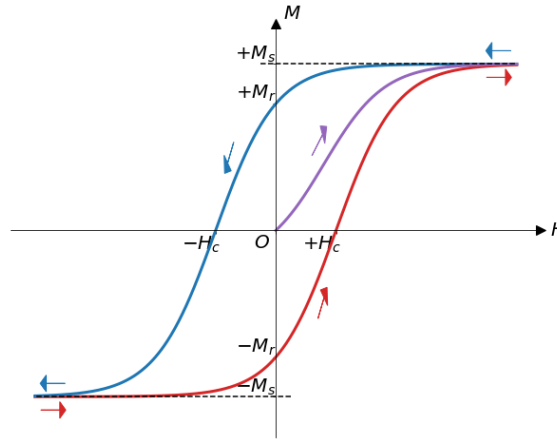


Figure 2.23: The magnetisation hysteresis loop for a ferromagnetic material. The curve from the origin O is the virgin curve and describes the initial magnetisation process. The curve crosses the zero-magnetisation axis at the coercive magnetic field H_c and crosses the zero-field axis at the remanence magnetisation $\pm M_r$. The magnetisation asymptotes to the saturation magnetisation $\pm M_s$ for fields much larger than the coercive field.

magnetisation M_r . This is less than the saturation magnetisation and in a homogeneous crystal this difference may be analytically described by the Stoner-Wohlfarth model^[39].

The magnetically ordered structure remains unchanged until an opposing field of critical magnitude is reached, known as the coercive field H_c . This field strength is able to overcome the energy barrier between the existing alignment and the alignment parallel to the new field direction resulting in a magnetisation reversal^[39]. This shift also results in a change in the density of states, which is asymmetric due to the field in a magnified version of the offset seen for Pauli paramagnetism^[19] in Figure 2.21. The energy difference is now provided by the exchange interaction which is discussed in Section 2.5.2.

This process is repeatable indefinitely with a stable and consistent hysteresis loop. The area within the loop is the energy cost of each cycle and this is typically dissipated as heat^[39]. Ideally the loop would be a pair of step functions, however due to multiple factors such as inhomogenieties the coercive window is widened and a sigmoid is more appropriate.

The loop may be collapsed and magnetisation reset by heating the ferromagnet past a critical temperature above which it becomes paramagnetic^[39]; this temperature is the Curie temperature T_C . If the material is cooled back down in the absence of an external field the magnetisation will remain zero until an external field is reapplied. A second method to reduce the remanence to zero is to apply a series of magnetic fields with decreasing magnitude in alternating directions. This forms a series of diminishing hysteresis loops which spiral towards the origin of the magnetisation axes^[39]. The process is called AC demagnetisation.

2.7.2 Antiferromagnetism

Antiferromagnetism is an alternate dipole ordering with no net magnetisation in contrast to the high magnetisation of ferromagnetism. The exchange interaction now minimises energy for antiparallel neighbours^[19] resulting in an alternating dipole moment pattern, as shown in Figure 2.24. The structure may also be thought of as a pair of opposed ferromagnetic lattices each with double the lattice spacing of the crystal. Typically only one alignment exists, but it is possible to instead have two interlocking antiferromagnetic lattices oriented perpendicular to one another^[52].

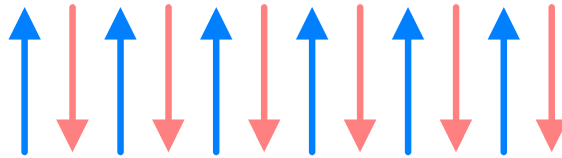


Figure 2.24: A representation of antiferromagnetism in one dimension. The arrows represent relative dipole moment orientations and magnitudes.

The alternating spins result in no net magnetisation, thus making this structure unresponsive to external magnetic fields unlike ferromagnetic materials. A material which supports magnetic ordering while being unresponsive to disruptive external magnetic fields is an interesting concept, and this will be discussed in Section 3.3.1. In antiferromagnets the threshold temperature above which paramagnetic behaviour is observed is the Néel temperature T_N . This is often much lower than room temperature^[39], so crystals with antiferromagnetic properties may appear to simply be paramagnetic when first studied.

Figure 2.25 shows the three types of antiferromagnetic ordering which commonly occur in three dimensional crystals. A-type ordering occurs when the crystal planes perpendicular to the magnetisation direction alternate dipole orientation, C-type occurs when a particular family of planes parallel to magnetisation direction are alternating, and G-type occurs when all nearest neighbour dipole pairs are opposing each other. Equiatomic FeRh is an example of a G-type antiferromagnet^[30].

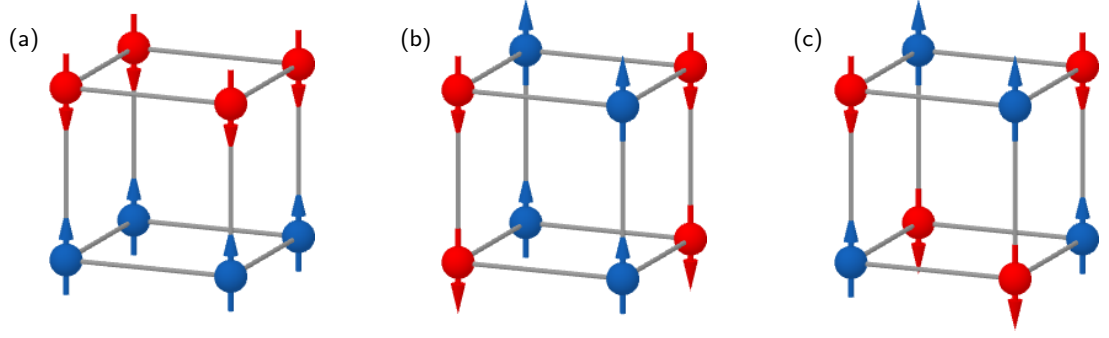


Figure 2.25: Three common types of antiferromagnetic ordering, the arrows represent relative dipole moment orientations. (a) A-type antiferromagnetism. (b) C-type antiferromagnetism. (c) G-type antiferromagnetism.

2.7.3 Ferrimagnetism

There exists a hybrid example of the two magnetic orderings mentioned thus far. Ferrimagnetism occurs when the moments of the constituent dipoles are arranged antiferromagnetically but the two directions have differing magnitudes, for example due to differing elements^[39]. This is represented in Figure 2.26. The result is reduced strength ferromagnetic behaviour, where the magnetisation still forms hysteresis loops and a Curie temperature still applies. This ordering is not relevant for this work and is included solely for completeness.

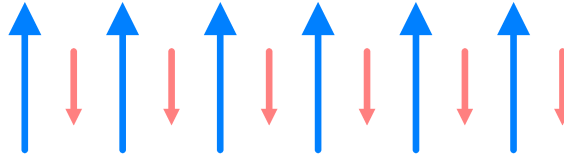


Figure 2.26: A representation of ferrimagnetism in one dimension. The arrows represent relative dipole moment orientations and magnitudes.

2.7.4 Spin-flop transitions

A crystal naturally magnetises along the easy axis with the result that the susceptibility perpendicular to the magnetisation direction χ_{\perp}^m is greater than the susceptibility in the parallel direction χ_{\parallel}^m ^[39]. The energy density in an external field \vec{H} is obtained from differentiating equation (2.29) to obtain

$$\frac{\partial U}{\partial \mathcal{V}} = -\mu_0 \vec{M} \cdot \vec{H} = -\mu_0 \chi_*^m H^2, \quad (2.78)$$

where $*$ has been used to represent \perp or \parallel . This equation being negative shows that dipoles oriented perpendicularly to \vec{H} with susceptibility χ_{\perp}^m feature lower potential energies than those oriented parallel and antiparallel with susceptibility χ_{\parallel}^m ^[39].

Low field strengths cannot overcome anisotropy so magnetisation initially grows with applied field as $\chi_{\parallel}^m \vec{H}$ [39]. This magnetisation of an antiferromagnetic lattice is possible because it can be considered to be formed from two interpenetrating FM lattices, one of which increases in magnetisation and the other decreases in response to the external field [19]. As the field strength continues to rise the anisotropic energy barrier is overcome by dipole energies, and the dipoles rotate to form a new antiferromagnetic ordering perpendicular to the applied field. Magnetisation now grows more rapidly due to following $\chi_{\perp}^m \vec{H}$ and this process is described as a spin-flop [39]. Continuing to raise the applied field strength overcomes the exchange energy and causes the dipole moments to cant in the direction of the field by increasing angles and ultimately lie parallel to it in a ferromagnetic state [39].

Strongly anisotropic crystals have anisotropic energies not less than the exchange energy. The result is a crystal that forgoes the spin-flop stage and rotates directly from AF to FM alignments [39]. This is the metamagnetic effect and induces an artificial ferromagnetism that is not a consequence of a phase transition [39].

2.7.5 Spin canting

Spin canting occurs in some antiferromagnetic crystals and is a rotational offset of magnetic dipole moments from the magnetisation axis [53]. This induces a net magnetic moment perpendicular to the antiferromagnetic ordering direction and thus weak ferromagnetic properties are observed [53]. The effect of canting in the three types of antiferromagnetic ordering introduced in Figure 2.25 are shown in Figure 2.27.

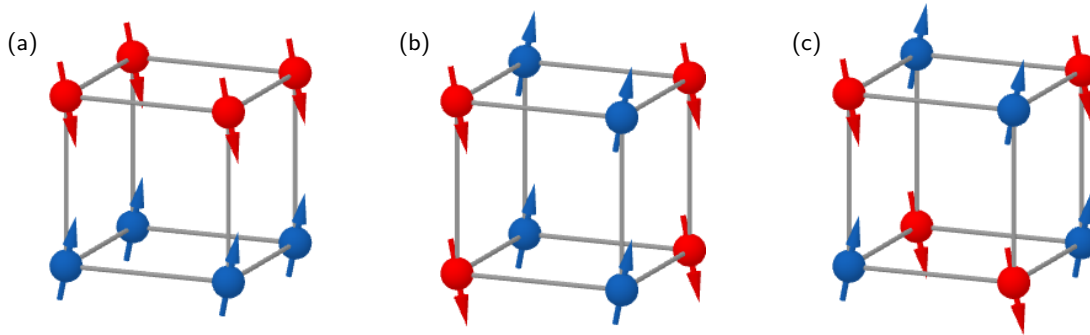


Figure 2.27: The effect of canting on the three common types of antiferromagnetic ordering introduced in Figure 2.25 with net magnetic moment perpendicular to magnetisation direction. The arrows represent relative dipole moment orientations. (a) Canted A-type antiferromagnetism. (b) Canted C-type antiferromagnetism. (c) Canted G-type antiferromagnetism.

Spin canting is a result of the Dzyaloshinskii-Moriya interaction (DMI) which is the antisymmetric exchange interaction [53] and is of particular importance in skyrmionic research [54]. The canting angle and thus the strength of the net magnetic moment is determined by the relative magnitudes of the

isotropic and antisymmetric exchange interactions which respectively seek to align neighbouring dipoles to be antiparallel (dot-product of spins in the Hamiltonian) or perpendicular (cross-product of spins in the Hamiltonian) and this ratio is typically sufficient that the canting angle is only minor^[53].

2.8 Magnetic domains

2.8.1 Magnetostatic energy and anisotropy

A magnetically ordered material has minimised exchange energy^[39], however there is a stray field emanating from the two ends of the magnetically ordered material and looping around the outside of the surface. This stray field \vec{H}_d is also known as the demagnetising field^[39] because it opposes the applied field \vec{H} being used to induce the magnetisation \vec{M} . This is shown in Figure 2.28.

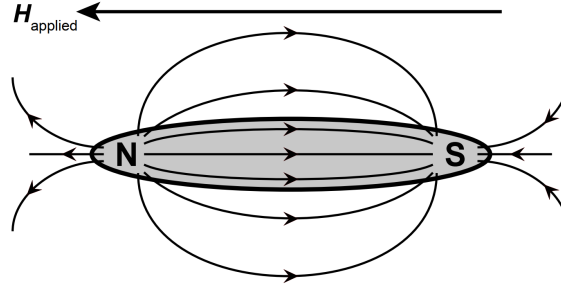


Figure 2.28: The demagnetising field which forms for an elongated magnetised crystal. Figure reproduced from *Magnetic materials: fundamentals and applications*^[19].

The stray field may be calculated using^[39]

$$H_{d,i} = -N_{d,ij}M_j \quad (2.79)$$

where M_j is the j^{th} component of the magnetisation vector \vec{M} and $N_{d,ij}$ is the demagnetising tensor which depends on the material geometry.

The flux within a rectangular magnetised crystal is variable due to divergence of the field lines towards the ends of the crystal, but it has been shown that an ellipsoid of revolution is analytically calculable because the shape perfectly counters this divergence and thus sustains a constant flux within^[39]. The divergence means that the demagnetisation tensor $N_{d,ij}$ of a rectangular crystal is not analytical, so for convenience crystals are approximated as ellipsoids where possible and thin films are approximated as very flat oblate spheroids^[39]. However, ellipsoids have well-known analytic demagnetising tensor components where only the leading diagonal is non-zero and the values sum to 1^[39]. The three radii of an ellipsoid are labelled a , b , and c and so the Voigt notation used for these diagonal components is $N_a \equiv N_{d,11}$, $N_b \equiv N_{d,22}$, and $N_c \equiv N_{d,33}$. The tensor components for the three types of spheroids are provided in Table 2.9 where the ratio $m \equiv c/a$ is used for clarity.

Spheroid	Radii relation	N_a	N_b	N_c
Sphere	$a = b = c$	$\frac{1}{3}$	$\frac{1}{3}$	$\frac{1}{3}$
Prolate	$a = b < c$	$\frac{1 - N_c}{2}$	$\frac{1 - N_c}{2}$	$\frac{1}{m^2 - 1} \left[\frac{m}{\sqrt{m^2 - 1}} \ln \left(m + \sqrt{m^2 - 1} \right) - 1 \right]$
Oblate	$a = b > c$	$\frac{1 - N_c}{2}$	$\frac{1 - N_c}{2}$	$\frac{1}{m^2 - 1} \left[\frac{m}{\sqrt{1 - m^2}} \arcsin \left(\sqrt{1 - m^2} \right) - 1 \right]$

 Table 2.9: The non-zero demagnetisation tensor components for spheroids^[39].

The oblate spheroid used to approximate thin films has $a = b \gg c$ so $m \ll 1$ and the demagnetisation components may be approximated from the expressions in Table 2.9 to yield

$$N_a = N_b \approx \frac{\pi c}{4a} \sim 0 \quad (2.80)$$

and

$$N_c \approx 1 - \frac{\pi c}{2a} \sim 1. \quad (2.81)$$

Flux outside the magnetic material comes with an energy penalty and the total magnetostatic energy U_{mag} may be determined using the Zeeman energy equation (2.29), where the applied field is now the stray field arising as the result of the other dipoles. The energy may be found by summing over all dipoles $\vec{\mu}_i$ and introducing a factor of $1/2$ to avoid double counting each dipole pairing, and in the case of an ellipsoid this yields^[39]

$$U_{\text{mag}} = \frac{1}{2} \sum_i \left(-\mu_0 \vec{\mu}_i \cdot \vec{H}_d \right) = -\frac{1}{2} \mu_0 (N_a M_1^2 + N_b M_2^2 + N_c M_3^2) \quad (2.82)$$

where M_1 , M_2 , and M_3 are the three components of the magnetisation vector \vec{M} .

The stray field strength is higher, with larger N_{ij} , for shorter pole separations^[39]. This encourages the magnetisation to point along the longest axis of a crystal and is the classical mechanism responsible for encouraging ferromagnetic domains in thin films to lie in-plane where possible as discussed in Section 2.5.1. This favoured direction is known as the easy axis and is the result of crystalline structural properties such as defects^[39], while the other axes are known as hard axes. A single easy axis such as in prolate spheroids results in uniaxial anisotropy where the magnetisation seeks to align parallel or antiparallel to this axis where possible. In oblate spheroids such as approximated thin films there is instead an easy plane because all in-plane directions have equal dimension^[39].

2.8.2 Formation of domains

Once the magnetising field has been removed, and Zeeman energy no longer contributes, a magnetic material must find a compromise between exchange energy, related to ordering, and magnetostatic

energy, related to lossy stray fields.

This may be done by creating ferromagnetic regions of different alignment to one another, known as domains^[19]. The basic case with a single homogeneous domain is shown in Figure 2.29a. In a uniaxial crystal a pair of these may lie antiparallel, so the stray field is eliminated from the sides and exists only between adjacent poles, as seen in Figure 2.29b. The exchange energy *within* each domain is still minimised, however. The stray field may only be wholly eliminated and magnetostatic energy reduced to zero in cubically anisotropic crystals^[19], and this is achieved by creating perpendicular domains at each end of the antiparallel domains, forming a closed loop as shown in Figure 2.29c. The stray field extends from one pole and seeks the nearest opposite pole, but in this domain structure all poles are in direct contact with their opposing counterpart without requiring flux outside the crystal boundary.

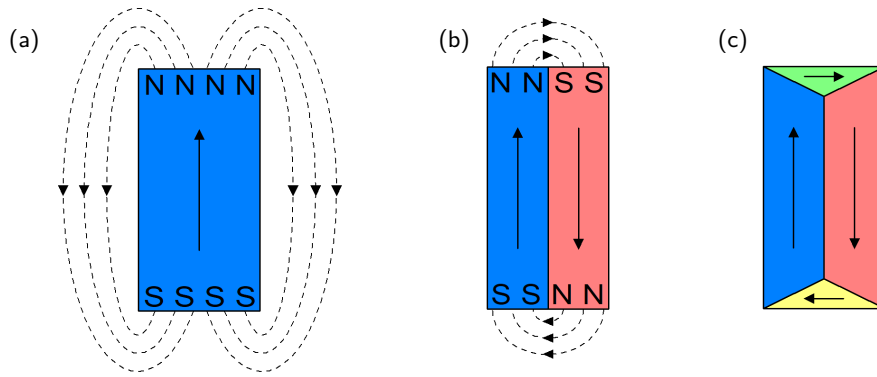


Figure 2.29: The magnetisation and stray fields for different domain structures. (a) Homogeneous magnetisation with significant stray field. (b) Antiparallel magnetisation with reduced stray field. (c) Cyclical magnetisation with no stray field.

An additional energy penalty arises in the form of magnetostriction^[39], which is a phenomenon whereby a crystal expands in the direction of magnetic flux, including the flux from magnetisation, due to the structure seeking to minimise the free energy. In strongly magnetostrictive materials this limits the creation of adjacent domains along differing easy axes due to the competing strains causing significant lattice mismatch at the domain boundary^[39]. The solution is the creation of additional domains to minimise total energy^[19], and Figure 2.30 shows a domain structure that seeks to minimise exchange, magnetostatic, and magnetostrictive energies.

A large number of domains results in a crystal with no significant net magnetisation in the absence of an applied field. This can occur through multiple mechanisms, including heating past the Curie temperature, AC demagnetising, or sharp impacts.

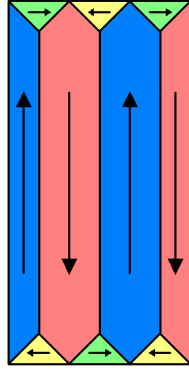


Figure 2.30: A domain structure with multiple cyclical domains to eliminate stray field whilst also minimising magnetostrictive strain.

2.8.3 Domain walls

It is immediately apparent that there is an energy penalty to creating domains. The dipoles either side of the boundary will have very high exchange energies due to being antiparallel in close proximity. The solution is to spread the wall across multiple dipoles, each at a small angle from one another, and these rotating dipoles form a domain wall^[39]. The exchange interaction would be minimised if the domain wall were infinite, but a second phenomenon is present and conversely seeks to minimise wall width. The dipoles in the wall are either not aligned along an easy axis of the crystal, and thus have anisotropic energy penalties, or induce poles across a narrow region of the crystal, and thus have magnetostatic energy penalties^[55].

The exchange length of a magnetic material is the distance over which the exchange interaction dominates the anisotropic or magnetostatic effects^[56], and this is related to the thickness of the domain walls which form within this material to minimise the energy from these competing interactions^[56]. There are two types of domain walls commonly found in magnetic materials: Bloch walls and Néel walls, both shown in Figure 2.31. In Bloch walls (Figure 2.31a) the dipoles rotate in the plane of the wall, so the moments of the wall dipoles point within the plane of the wall rather than through the wall itself and the resulting magnetic poles form on the crystal surface. In Néel walls (Figure 2.31b) the dipoles instead rotate out of the plane of the wall, meaning the moments point through the wall and the poles form on either end of it. This difference controls which type appears in a particular crystal, because magnetostatic energy is maximised over shorter distances so the dipoles forming the wall will attempt to orient along the longest axis available. This means that if the thickness of the domain wall is smaller than the crystal thickness then Bloch walls will form, while if the film is thinner than the domain wall thickness then Néel walls will form. Domain walls typically span up to a few hundred atoms^[39], which is large enough that individual atom defects or vacancies do not significantly disrupt domain wall structures^[39].

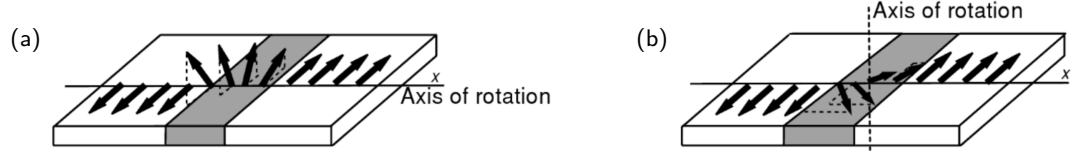


Figure 2.31: The rotation of magnetic dipole moments across the two types of domain wall. Figures reproduced from *Magnetism and Magnetic Materials*^[56]. (a) A Bloch wall. (b) A Néel wall.

2.8.4 Domain nucleation

Domain walls cost energy so a ferromagnetic crystal will seek to minimise how many it creates. Thus a crystal becoming magnetically ordered will expand existing domains where possible rather than pay the penalty of creating additional domains. When an external influence is used to magnetise a crystal, the first dipoles to align with the applied field will form a small domain surrounded by a domain wall^[56] and multiple seed domains will form across the crystal; as the field rises the Zeeman energy rises with it causing additional dipoles to align until the crystal is fully magnetised. In certain crystals such as FeRh films^[57] the sites of these seed domains are consistent between magnetisation/demagnetisation cycles and arise due to some local crystal properties. The exact cause of this is still not fully understood.

2.9 Dependence of crystal properties on magnetisation

2.9.1 Elastic response

The magnetostrictive strain discussed in Section 2.8.2 has a significant effect on the elastic properties of a crystal. Previously this phenomenon was discussed in terms of strain arising from magnetic flux, however this is a two-way process and strain can also induce a magnetic flux by reorienting dipoles to align with the strain direction which induces a local magnetisation. This inverse process is the magnetoelastic effect, and the ensuing magnetisation then adds an additional strain to the applied elastic strain^[39].

The result is that the elastic modulus of a demagnetised crystal E_d under a stress T is^[39]

$$E_d = \frac{T}{S_e + S_m} \quad (2.83)$$

while the modulus of a magnetically saturated crystal E_s will be the usual

$$E_s = \frac{T}{S_e}, \quad (2.84)$$

where the elastic strain is S_e and the magnetoelastic strain is S_m . This means that when a crystal is magnetised the modulus will change by

$$\frac{\Delta E}{E} = \frac{E_s - E_d}{E_d} = \frac{S_m}{S_e}. \quad (2.85)$$

The stress-strain curves for these, in which the gradient is elastic modulus, are shown in Figure 2.32^[39]. The saturated curve is a simple straight line through the origin as is expected for purely elastic behaviour. The curves for demagnetised crystals of differing anisotropies are also shown and curve initially due to magnetoelastic dominance at small stresses, before tending to another linear slope once local saturation is achieved, albeit offset from the saturated curve by the magnetoelastic strain S_m .

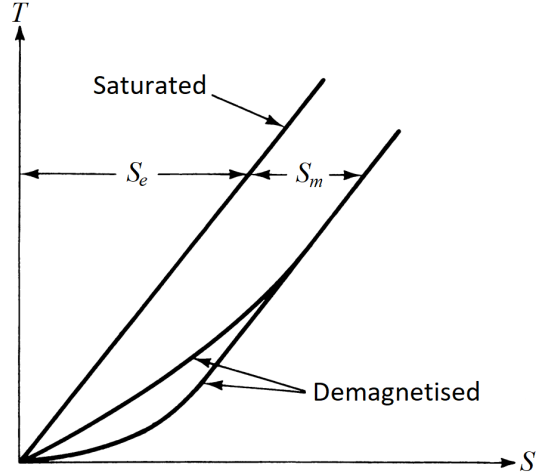


Figure 2.32: The stress-strain curves for magnetoelastic systems, adapted from *Introduction to Magnetic Materials*^[39]. A magnetically-saturated crystal will produce a straight line through the origin while a demagnetised crystal will produce a curve. The upper demagnetised curve describes a crystal with lower anisotropy than the lower curve.

Intuitively it can be expected that the Poisson's ratio ν will fall by the same fraction. This is because the Poisson ratio is the negative ratio of transverse strain S_t to longitudinal elastic strain S_e ^[58]. The transverse strain has two components, the elastic $S_{t,e}$ and magnetoelastic $S_{t,m}$ strains, both manifesting via the Poisson effect. This gives

$$\nu_d = -\frac{S_{t,m} + S_{t,e}}{S_e} \quad (2.86)$$

and

$$\nu_s = -\frac{S_{t,e}}{S_e}, \quad (2.87)$$

thus the ratio is

$$\frac{\Delta\nu}{\nu} = \frac{\nu_s - \nu_d}{\nu_d} = -\frac{S_{t,m}}{S_{t,e}}. \quad (2.88)$$

Assuming that the unmodified Poisson's ratio ν_s applies equally to both of these transverse strains, this becomes

$$\frac{\Delta\nu}{\nu} = -\frac{S_m}{S_e} = -\frac{\Delta E}{E}. \quad (2.89)$$

The value of S_m is highly variable and depends on the crystal anisotropy as well as extrinsic properties such as applied stress. This means that even the method used to measure the modulus can affect

the result, with $\Delta E/E$ being $\sim 1\%$ for direct measurements using stress-strain curves and $> 100\%$ for indirect measurements using resonance of small amplitude vibrations^[39].

This is an example of the ‘modulus defect’ which makes the elastic modulus a fickle parameter to measure precisely using small scale measurements. The magnetoelastic effect is not the only property to affect it, strain arising from any other mechanism can replace S_m and alter the measured value^[39].

2.9.2 Magnetoresistance

The electrical resistance of a magnetic material is also affected by the magnetisation through the mechanism of magnetoresistance.

One origin of this effect is the magnetisation direction relative to current flow and so magnetoresistance manifests in any ferromagnetic metal^[39]. The orientation driven resistance is maximal when the magnetisation is parallel to current flow and minimal when it is perpendicular. This is due to the electron cloud around each nucleus deforming as a result of the angle between dipole moment and current, via spin-orbit coupling, and this deformation results in a difference in the local resistivity^[39]. The effect is the same for parallel or antiparallel dipoles and so the magnetoresistance effect also manifests in antiferromagnets^[16].

There is also a second resistance phenomenon which occurs due to magnetisation and is significant in transition metals such as Fe and Rh. The electrical resistance of a magnetic material with localised and delocalised electrons, as seen in transition metals or certain multilayer stacks, alters significantly with the presence of magnetisation^[59;45].

The exchange interaction between these electrons has a scattering effect on the delocalised electron^[45], and this has two consequences. One of these is the second-order process by which the spin-spin coupling occurs and is the RKKY interaction discussed in Section 2.5.3. The first-order scattering process causes electrical resistivity.

A qualitative understanding of the effect of magnetic ordering comes from considering the non-magnetic and ferromagnetic density of states, shown in Figure 2.33. This large density of states is also a requirement for metallic conduction and thus it is common for ferromagnetic materials to be metals^[49]. If the Fermi energy in Figure 2.33 were slightly higher then all spin-down states would be filled and only spin-up states would be available. This would make the material a conductor to spin-up electrons but an insulator to spin-down electrons, and such a material is called a half-metal.

The shifted energy levels of the up and down spins relative to the Fermi level result in most of the down spin states being filled and most of the up spin states being empty^[19]. Consequently a spin-down electron

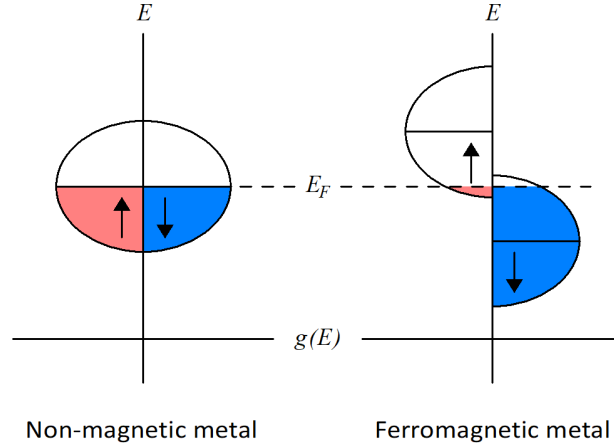


Figure 2.33: The density of states for the incomplete energy band of electron dipoles in metals, with Fermi energy E_F labelled. The shape is purely schematic and does not reflect the true band distribution. The arrows show the electron spins while the blue region represents magnetic dipole moments aligned with the field and the red represents those opposed. The relative change in density of states results in a net magnetisation parallel to the lower energy dipoles.

scattering process has fewer destination states to choose from and so the likelihood of a scattering event for a spin-down delocalised electron is reduced^[59]. This results in a decrease of scattering events and increase in relaxation time^[60].

Resistivity is a measure of expected number of scattering events and so a fall in scattering probability is a fall in resistivity. Due to the overlapping nature of bands in a transition metal and the relative probabilities of inter-subshell and intra-subshell scattering, the scattering electrons for resistive events have an even chance of initially being spin-up or spin-down^[59]. This means the asymmetric density of states need only be considered for the destination state and not the prior state.

A quantitative discussion will now follow, considering a two-channel model of resistivity. As previously stated, the probability P of a scattering event is proportional to the energy density of states $g(E)$ of the destination subshell. Close to the Fermi level E_F the 3D density of states is very well known to have the energy dependence^[61]

$$g(E) \propto E^{1/2}. \quad (2.90)$$

The Fermi energy itself is also very well known, and depends on the electron number density n as^[58]

$$E_F \propto n^{2/3} \quad (2.91)$$

thus giving

$$g(E \approx E_F) \propto n^{1/3}. \quad (2.92)$$

The number density of each spin direction depends on the magnetisation M and saturation magnetisation M_s of the metal as^[59]

$$n_{\mp} \propto 1 \mp \frac{M}{M_s} \quad (2.93)$$

where electrons with spin parallel to the magnetisation are $-$ and antiparallel are $+$. Recall that the negative charge of the electron means the magnetic dipole moment opposes spin direction, so antiparallel spins equate to parallel, and thus aligned, dipole moments.

The scattering event probability of the two spins is therefore

$$P_{\mp} \propto \left(1 \mp \frac{M}{M_s}\right)^{1/3}. \quad (2.94)$$

Consider an antiferromagnetic or non-magnetic material which has $M = 0$ so $P_- \propto 1$ and $P_+ \propto 1$. In other words the probability of the spins scattering is equally weighted, as would be expected for a symmetric density of states.

Now consider a ferromagnet which has $M = M_s$ so $P_- \propto 0$ and $P_+ \propto 2^{1/3}$. Only one spin direction is allowed to scatter but the weighting parameter $2^{1/3} > 1$, so the remaining spin is more likely to scatter than either spin in an antiferromagnet.

Each conduction electron changes spin multiple times whilst traversing the conducting path across the metal^[59]. Assuming that this spin reversal occurs over time and distance scales which are much smaller than the total duration and distance of the conducting path, the resistivity ρ depends on the average scattering probability of both spin states, thus

$$\rho_{AF} \propto \frac{1}{2} (1 + 1) = 1 \quad (2.95)$$

and

$$\rho_{FM} \propto \frac{1}{2} \left(2^{1/3} + 0\right) = 2^{-2/3}. \quad (2.96)$$

Hence the ratio of expected scattering resistances for the two magnetic orderings is

$$\frac{\rho_{FM}}{\rho_{AF}} = 2^{-2/3} \approx 0.63. \quad (2.97)$$

This theoretical change in resistance does not usually manifest cleanly due to a myriad of factors, and so this full change is rarely seen in practice. Certain materials such as FeRh do show this property^[5,60], however, and this can also be artificially engineered for ferromagnetic/non-magnetic/ferromagnetic stacks^[62]. The local resistivity of a such a material can therefore be modified by manipulating the local magnetic ordering of the constituent dipoles. For example, it is discussed in Section 3.4.2 that a room temperature thin film of FeRh may be precisely transitioned from antiferromagnetic to ferromagnetic ordering using a beam of noble ions, and the resulting pattern should be accompanied by a corresponding drop in local resistivity.

An additional contribution to the total resistivity is electron-phonon scattering, which arises from the thermal excitations of lattice atoms and is the phenomenon responsible for the temperature dependence of resistance. This is characterised as^[58]

$$R = R_0 (1 + \alpha \Delta \mathcal{T}) \quad (2.98)$$

where R_0 is the reference resistance at room temperature, α is the thermal coefficient of resistance, and $\Delta \mathcal{T}$ is the change in temperature from the reference temperature, which is typically 20 °C^[63].

2.10 Introduction to electric fields and polarisation

Magnetism has now been introduced, however the remaining half of electromagnetism is of equal interest for this work and must now be considered. Much of the earlier parts of this discussion will be familiar due to the parallels between magnetic and electric field phenomena but one key difference is that the polarisation behaviour is very strongly tied to the lattice structure, in contrast to the magnetic behaviour being governed by quantum mechanical spin interactions.

The CGS unit system is much less commonly used in modern literature for electric field investigations than in magnetic work. Once again 4π appears in conversions between the unit systems, with the vacuum permittivity^[36]

$$\varepsilon_0 = 8.854187 \dots \times 10^{-12} \text{ F m}^{-1} \quad (2.99)$$

appearing in SI equations whilst in CGS units the vacuum permittivity is $1/4\pi$.

The following sections aim to provide an introduction to relevant electrical polarisation phenomena and draw comparisons to the magnetism counterparts of these effects which were introduced in Section 2.4. The approach is somewhat more quantitative than the magnetic overview, which is necessary due to the additional complexities and subtleties involved in nanoscale piezoelectric characterisation.

2.10.1 Electric dipoles

Similarly to magnetic fields, electric field phenomena are also underpinned by dipoles. However, an electric dipole is typically formed from a pair of oppositely charged electric monopoles such as oppositely charged ions^[58], in contrast to the point dipoles considered for magnetic dipoles in Section 2.4.1 where magnetic monopoles do not exist. Alternatively, an electron cloud may be deformed relative to its host nucleus and the centres of charge of the cloud and nucleus form the ends of the dipole^[58]. Electric dipoles have a moment \vec{p} given by

$$\vec{p} = q\vec{d} \quad (2.100)$$

where q is the magnitude of charge of each pole and \vec{d} is the vector running from the negative pole to the positive pole.

The dipole moment is a measure of the field direction and strength and has SI units of C m. The potential energy U of a dipole in an external field \vec{E} is^[64]

$$U = -\vec{p} \cdot \vec{E} \quad (2.101)$$

and the resulting torque $\vec{\tau}$ is given by^[64]

$$\vec{\tau} = \vec{p} \times \vec{E}. \quad (2.102)$$

As in the magnetic case, the potential energy is minimised when dipole moment and external field are parallel and maximised when dipole and external field are anti-parallel, and the torque $\vec{\tau}$ acts to minimise this energy.

The polarisation \vec{P} of a medium is a measure of the alignment of electric dipole moments, and is defined with respect to volume \mathcal{V} as^[64]

$$\vec{P} \equiv \frac{\partial \vec{p}}{\partial \mathcal{V}}. \quad (2.103)$$

2.10.2 Electric fields

The field observed outside a medium is the \vec{E} field and in this case is related to electric flux density \vec{D} , also known as the displacement field, by simply multiplying by the vacuum permittivity, i.e.^[65]

$$\vec{D} = \epsilon_0 \vec{E}. \quad (2.104)$$

Permittivity is the measure of induced polarisation in a medium and describes the ability of said medium to support an electric field, hence in CGS units the vacuum permittivity multiplied by the unit system constant 4π is unity.

The flux density is a measure of the number of field lines per unit area so inside a medium the polarisation also contributes to the flux density. Polarisation is induced by displacing charge carriers to form dipoles, hence the term displacement field for \vec{D} ^[65]. The relationship between fields within a medium is

$$\vec{D} = \epsilon_0 \vec{E} + \vec{P}. \quad (2.105)$$

Polarisation curves are again drawn to show how an applied electric results in a polarisation of the medium, and the gradient of the curve is ϵ_0 multiplied by the dimensionless electric susceptibility χ^e ^[65], so

$$\chi_{ij}^e \equiv \frac{1}{\epsilon_0} \frac{\partial P_i}{\partial E_j}. \quad (2.106)$$

2.11 Electrostriction

Any electrical insulator is a dielectric^[65], which simply refers to the ability to polarise the crystal into electric dipoles using an external field. Conductors do not support any internal electric fields because the

free electrons will be attracted by the positive electrode of the poling field until the charge imbalance cancels out the applied field. The basic relationship is linear, allowing the definition of a constant relative permittivity ε_r where^[65]

$$\vec{D} = \varepsilon_0 \vec{E} + \vec{P} = \varepsilon_0 \vec{E} + \varepsilon_0 \chi^e \vec{E} = \varepsilon_0 (1 + \chi^e) \vec{E} \equiv \varepsilon_0 \varepsilon_r \vec{E} . \quad (2.107)$$

The electric susceptibility is often anisotropic due to crystal symmetries and so is usually written as a tensor χ_{ij}^e .^[65] In contrast to the magnetic case only one direction of linear induced polarisation is possible: parallel to the field. Diaelectricity is not possible in a monopole driven mechanism such as electric polarisation because an electric monopole will never freely displace against the poling field. Paraelectricity describes a variation from the basic linear case where the polarisation initially rises quickly with field strength^[66] before resuming with linear dielectric behaviour.

Magnetic fields were shown in Section 2.8.2 to induce an expansion in the direction of magnetisation and electric fields are no different. The result is electrostriction, which may occur in all crystals. There are actually two electrostriction coefficients, M and Q , with the choice made depending on whether applied field or polarisation is the parameter of interest^[67]; M relates strain to electric field while Q relates strain to polarisation. These are rank-4 tensors, relating the square of the poling field or polarisation to the rank-2 strain tensor, thus^[67]

$$S_{ij} = M_{ijkl} E_k E_l \quad (2.108)$$

or

$$S_{ij} = Q_{ijkl} P_k P_l . \quad (2.109)$$

Due to symmetries in some crystals Voigt notation can be used^[67], reducing the tensors to

$$S_i = M_{ij} E_j^2 \quad (2.110)$$

and

$$S_i = Q_{ij} P_j^2 . \quad (2.111)$$

The polarisation accounts for any non-linearities in the field response, such as from ferroelectrics which shall be discussed in Section 2.13.1, so Q is only weakly field dependent to the point that it may be considered to be constant^[68]. On the other hand it is clear that the coefficient M must instead account for the non-linearities when relating strain to field thus is highly field-dependent. Consequently, Q is the preferred value when considering in non-linear dielectrics with high permittivities^[67], including relaxor ferroelectrics such as PMN-PT.

The value of Q can vary by several orders of magnitude between crystals and can even be negative in some cases^[67]. It is usually much smaller than other electromechanical effects and thus negligible,

however there is a great interest in electrostrictive ceramics which exhibit significant electrostriction, such as for use as highly accurate actuators^[67], and PMN-PT is one such ceramic.

In this work the applied field is $\vec{E} = E_3 \hat{z}$ inducing a polarisation $\vec{P} = P_3 \hat{z}$ and the measured strain is the out-of-plane strain S_3 , thus the relations of interest are

$$S_3 = M_{33} E_3^2 \quad (2.112)$$

and

$$S_3 = Q_{33} P_3^2 . \quad (2.113)$$

An important note here is that due to the nature of the strain response in non-linear crystals these equations may not be simply rearranged to be

$$Q_{33} = \frac{S_3}{P_3^2} , \quad (2.114)$$

but instead the differential must be taken with respect to field^[68]. The first derivative of equation (2.113) yields an additional piezoelectric contribution, which shall be discussed in Section 2.12.1. Additionally, the second derivatives of equations (2.112) and (2.113) provide the quantified relation^[68]

$$M_{33} = \frac{1}{2} \frac{\partial^2 S_3}{\partial E_3^2} = Q_{33} [\varepsilon_0 (\varepsilon_{r,33} - 1)]^2 + Q_{33} P_3 \varepsilon_0 \frac{\partial \varepsilon_{r,33}}{\partial E_3} \quad (2.115)$$

between the constant and variable electrostriction coefficients.

2.12 Piezoelectricity

The piezoelectric effect is a coupling of mechanical and polar properties which occurs in inversionally asymmetric crystals^[27]. These are crystals which are not symmetric in at least one plane.

This mechanism has two forms: the direct piezoelectric effect, where deformation leads to polarisation, and the inverse piezoelectric effect, where poling leads to deformation^[65]. The underlying mechanism is best understood by considering the respective ‘centres of charge’ of the positively and negatively charged particles. Figure 2.34 shows this for a simple six ion system in a hexagonal arrangement.

Figure 2.34a shows the equilibrium state where both centres of charge overlap (purple) and there is no net dipole moment. If the system is deformed then the rearrangement in the lattice means that the centres of charge no longer overlap (shown by small circles in the centres of Figures 2.34b and 2.34c) and a net dipole moment appears. In a circuit this would cause a current pulse to flow as electrons in the leads equilibrate with the edge charges induced by the net moment. Alternatively, applying a field would cause the ions to move in the same way which would result in some strain being induced.

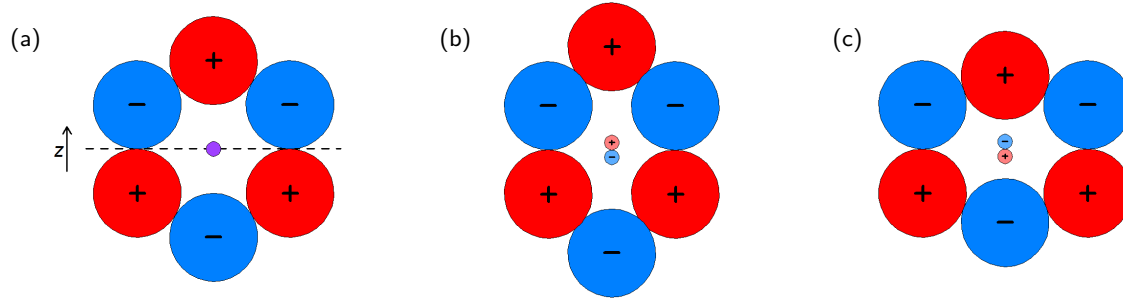


Figure 2.34: The piezoelectric effect in a six ion system. The field or polarisation is in the z -direction and the plane of inversion asymmetry is marked with the dashed line. The centres of charge are shown as small circles within the hexagonally arranged ions. (a) The equilibrium position with equal centres of charge. (b) The vertically extended (horizontally compressed) position with dipole moment parallel to \hat{z} . (c) The vertically compressed (horizontally extended) position with dipole moment antiparallel to \hat{z} .

An interesting property to note is that Figure 2.34b could equally be created by compressing the crystal horizontally as extending it vertically, and in both cases the moment appears in the direction of inversion asymmetry. This reflects the tensorial nature of the piezoelectric effect.

2.12.1 The piezoelectric coefficient

The direct and inverse piezoelectric effects are not actually true opposites and instead couple different pairs of parameters^[65]. The direct piezoelectric effect couples some applied stress T_{ij} to an induced polarisation

$$\vec{P} = P_1\hat{x} + P_2\hat{y} + P_3\hat{z}, \quad (2.116)$$

whilst the inverse effect couples some applied field

$$\vec{E} = E_1\hat{x} + E_2\hat{y} + E_3\hat{z} \quad (2.117)$$

to an induced strain S_{ij} ; the stress and strain are rank-2 tensors with six distinct components each. Voigt notation is usually used to set the strain subscripts 11 to 1, 22 to 2, 33 to 3, 23 to 4, 31 to 5, and 12 to 6^[27]. This allows each tensor to be written as a 6×1 matrix where the latter three elements are shear terms. Consequently, the piezoelectric coefficient may be written as an 18-component rank-2 tensor^[27].

The direct effect relates stress to polarisation in constant external field, and is given by^[65]

$$d_{ij} = \left(\frac{\partial D_i}{\partial T_j} \right) = \epsilon_0 \left(\frac{\partial E_i}{\partial T_j} \right) + \left(\frac{\partial P_i}{\partial T_j} \right) = \left(\frac{\partial P_i}{\partial T_j} \right). \quad (2.118)$$

On the other hand, the inverse effect relates applied field to strain, and is given by^[65]

$$d_{ij} = \left(\frac{\partial S_j}{\partial E_i} \right). \quad (2.119)$$

Similarly to electrostriction, these differentials are significant and cannot simply be treated as ratios as is done in most introductions to piezoelectricity which assume linear polarisation properties. The ratio gives the effective piezoelectric coefficient d_{ij}^{eff} , which is equal to the differential coefficient for linear responses but differs significantly in non-linear crystals, such as ferroelectrics where d_{ij} is in fact a function of E_i itself^[68]. This plays a critical role in the piezoelectric work in this thesis. The notation $d_{ij,0}$ will be used to indicate the constant form in the linear regime of such curves where $d_{ij} = d_{ij}^{eff}$.

The non-zero terms of the d_{ij} tensor are dictated by the crystal geometry and the form of the effective values can be looked up for the each space group in the literature^[27]. The inverse effect is of interest in this work, and so the strains for PMN-PT in some field $\vec{E} = E_3 \hat{z}$ are

$$S(m\bar{3}m) = \begin{pmatrix} S_1 \\ S_2 \\ S_3 \\ S_4 \\ S_5 \\ S_6 \end{pmatrix} = \begin{pmatrix} 0 & 0 & 0 \\ 0 & 0 & 0 \\ 0 & 0 & 0 \\ d_{14}^{eff} & 0 & 0 \\ 0 & d_{14}^{eff} & 0 \\ 0 & 0 & d_{14}^{eff} \end{pmatrix} \begin{pmatrix} 0 \\ 0 \\ E_3 \end{pmatrix} = \begin{pmatrix} 0 \\ 0 \\ 0 \\ 0 \\ 0 \\ d_{14}^{eff} E_3 \end{pmatrix} \quad (2.120)$$

$$S(3m) = \begin{pmatrix} S_1 \\ S_2 \\ S_3 \\ S_4 \\ S_5 \\ S_6 \end{pmatrix} = \begin{pmatrix} 0 & -d_{22}^{eff} & d_{31}^{eff} \\ 0 & d_{22}^{eff} & d_{31}^{eff} \\ 0 & 0 & d_{33}^{eff} \\ 0 & d_{15}^{eff} & 0 \\ d_{15}^{eff} & 0 & 0 \\ -d_{22}^{eff} & 0 & 0 \end{pmatrix} \begin{pmatrix} 0 \\ 0 \\ E_3 \end{pmatrix} = \begin{pmatrix} d_{31}^{eff} E_3 \\ d_{31}^{eff} E_3 \\ d_{33}^{eff} E_3 \\ 0 \\ 0 \\ 0 \end{pmatrix} \quad (2.121)$$

$$S(m) = \begin{pmatrix} S_1 \\ S_2 \\ S_3 \\ S_4 \\ S_5 \\ S_6 \end{pmatrix} = \begin{pmatrix} d_{11}^{eff} & 0 & d_{31}^{eff} \\ d_{12}^{eff} & 0 & d_{31}^{eff} \\ d_{13}^{eff} & 0 & d_{33}^{eff} \\ 0 & d_{24}^{eff} & 0 \\ d_{15}^{eff} & 0 & d_{35}^{eff} \\ 0 & d_{26}^{eff} & 0 \end{pmatrix} \begin{pmatrix} 0 \\ 0 \\ E_3 \end{pmatrix} = \begin{pmatrix} d_{31}^{eff} E_3 \\ d_{31}^{eff} E_3 \\ d_{33}^{eff} E_3 \\ 0 \\ d_{35}^{eff} E_3 \\ 0 \end{pmatrix} \quad (2.122)$$

$$S(4mm) = \begin{pmatrix} S_1 \\ S_2 \\ S_3 \\ S_4 \\ S_5 \\ S_6 \end{pmatrix} = \begin{pmatrix} 0 & 0 & d_{31}^{eff} \\ 0 & 0 & d_{31}^{eff} \\ 0 & 0 & d_{33}^{eff} \\ 0 & d_{15}^{eff} & 0 \\ d_{15}^{eff} & 0 & 0 \\ 0 & 0 & 0 \end{pmatrix} \begin{pmatrix} 0 \\ 0 \\ E_3 \end{pmatrix} = \begin{pmatrix} d_{31}^{eff} E_3 \\ d_{31}^{eff} E_3 \\ d_{33}^{eff} E_3 \\ 0 \\ 0 \\ 0 \end{pmatrix}. \quad (2.123)$$

The piezoelectric measurements performed on the AFM can measure the in-plane or out-of-plane components, but not the shear components. This means the cubic structure $m\bar{3}m$ exhibits no measurable piezoelectric response at all, which is as expected from simple symmetry considerations. The other space groups show two distinct measurable strains, the out-of-plane contribution

$$S_3 = d_{33}^{eff} E_3 \quad (2.124)$$

and the in-plane contribution

$$S_1 = S_2 = d_{31}^{eff} E_3. \quad (2.125)$$

This means contour maps of out-of-plane response show contrast in the longitudinal coefficient d_{33} and maps of in-plane responses show contrast in the transverse coefficient d_{31} . The out-of-plane response shows highest contrast and is easiest to probe, and so in this work the piezoelectric coefficient of interest is the longitudinal d_{33} .

An additional longitudinal piezoelectric contribution arises from the first derivative of the electrostriction equation (2.113) which yields^[68]

$$d_{33}^Q = \frac{\partial S_3}{\partial E_3} = 2Q_{33}P_3 \frac{\partial P_3}{\partial E_3} = 2Q_{33}P_3 \epsilon_0 (\epsilon_{r,33} - 1). \quad (2.126)$$

In crystals with induced polarisation this term provides expansion independent of the sign of the applied field, while in an electrically ordered crystal such as a ferroelectric this response has sign dependence and so piezoelectric behaviour is seen, even if the crystal is centrosymmetric. Relaxors feature large values of Q_{33} and $\epsilon_{r,33}$ and so exhibit strong longitudinal piezoelectric effects regardless of centrosymmetry.

2.12.2 Pyroelectricity

Pyroelectrics are a subset of piezoelectrics and are crystals exhibiting a coupling of electric fields and thermal energy^[65]. The positions of the lattice ions are a direct function of temperature \mathcal{T} and so as temperature changes so does the induced polarisation, known as the spontaneous polarisation P_s due to occurring in the absence of an external field. The pyroelectric coefficient in the i^{th} direction is simply^[65]

$$p_i = \frac{\partial P_{s,i}}{\partial \mathcal{T}}. \quad (2.127)$$

The changing polarisation results in a temporary change in edge charges and thus bias, inducing a current when the crystal temperature changes^[65].

This mechanism is not relevant for the work in this thesis and was just included for completeness.

2.12.3 Relation to crystallographic point groups

Hermann-Mauguin notation may be used without the leading capital to describe the 32 crystallographic point groups^[27] and these are provided in Table 2.10.

Crystal System	Point groups (short form)					
Cubic	23	$m\bar{3}$	432	$\bar{4}3m$	$m\bar{3}m$	
Hexagonal	6	$\bar{6}$	$\frac{6}{m}$	622	$6mm$	$\bar{6}m2$ $\frac{6}{m}mm$
Trigonal	3	$\bar{3}$	32	$3m$	$\bar{3}m$	
Tetragonal	4	$\bar{4}$	$\frac{4}{m}$	422	$4mm$	$\bar{4}2m$ $\frac{4}{m}mm$
Orthorhombic			222		$mm2$	mmm
Monoclinic	2	$\frac{2}{m}$		m		
Triclinic	1	$\bar{1}$				

Table 2.10: The 32 crystallographic point groups in abbreviated Hermann-Mauguin notation. The 11 point groups exhibiting centrosymmetry are highlighted in red and the 10 polar point groups are highlighted in blue^[27].

Piezoelectricity may only occur in non-centrosymmetric crystals so only the 21 point groups in black or blue in Table 2.10 are candidates^[27]. Uniquely, point group 432 has other symmetry properties that forbid piezoelectricity being sustained, and thus there are 20 piezoelectric point groups^[27].

Pyroelectricity occurs in polar point groups^[27]. These are groups where every symmetry operation in the group leaves a line, a plane, or the entire 3D space unchanged. Axes of rotation and planes of symmetry are examples of such unchanging points. The triclinic point group 1 is the trivial case which leaves all of space unchanged, because this is the simplest point group containing no symmetry operations at all; the vertices of a scalene triangle form this point group.

The subset of pyroelectric crystals that are also ferroelectric is not a purely crystallographic distinction^[27], but instead depends on the interactions between specific elements in the crystal. Thus any of the pyroelectric point groups in Table 2.10 may or may not exhibit ferroelectricity.

2.13 Ordered polarisation

Similarly to ferromagnetism, some crystals are able to sustain polarisation after the external poling field has been removed. The interaction energy in these materials is able to surpass the thermal excitations and maintain long-range stable alignment. All three ordered magnetisation alignments are also present for

polarisation: ferroelectricity, antiferroelectricity, and ferrielectricity; but only ferroelectricity is relevant for this work. Once again there is a Curie temperature above which thermal excitations reign and paraelectric behaviour ensues^[65].

2.13.1 Ferroelectricity

In a ferroelectric the interaction energy of the electric dipoles is minimised when neighbouring dipole moments are aligned in parallel, this produces a strong polarisation which persists when the field is removed. The polarisation curve is non-linear and forms a hysteresis loop^[65] as shown in Figure 2.35. Following the conclusions of Section 2.12.1 the third components S_3 and E_3 of the strain and electric field vectors are of interest in this work, along with the coupling piezoelectric coefficient d_{33} , and so the subscripts of any related tensor or vector components used in this thesis will also be 3 or 33.

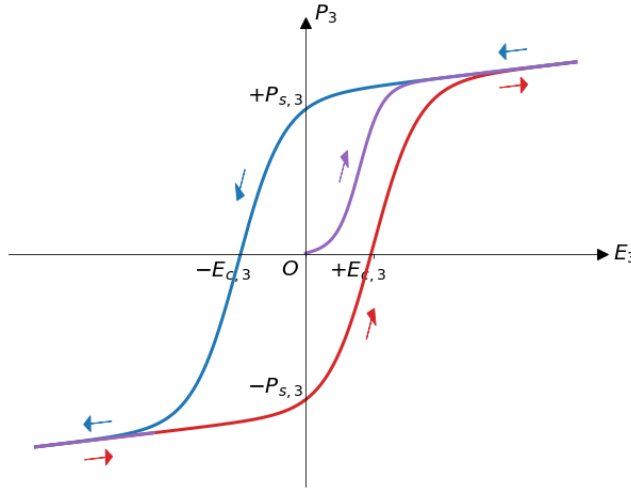


Figure 2.35: The polarisation hysteresis loop for a ferroelectric material. The curve from the origin O is the virgin curve describing the initial polarisation process. The curve crosses the zero-field axis at the spontaneous polarisation $P_{s,3}$ and crosses the zero-magnetisation axis at the coercive electric field $E_{c,3}$.

The polarisation rises monotonically with electric field and plateaus once the saturation polarisation $P_{sat,3}$ is reached. This is the point where all electric dipole moments are aligned with the field. When the field is removed the interactions between dipoles ensure they remain parallel, maintaining the spontaneous polarisation $P_{s,3}$ ^[69]. This is less than the saturation polarisation due to a similar mechanism as remanence magnetisation in ferromagnetism, and thus is also described as the remanence polarisation $P_{r,3}$.

The polarised structure remains unchanged until an opposing field of critical magnitude is reached, known as the coercive field $E_{c,3}$ ^[65]. This field strength is able to overcome the energy barrier between remaining in the existing alignment and aligning with the new field direction, resulting in a polarisation reversal.

Similarly to ferromagnetism this occurs via the nucleation and growth of ferroelectric domains^[65]. Unexpectedly the coercive field is dependent on the thickness of the crystal, following

$$E_{c,3} \propto z_0^{-2/3} \quad (2.128)$$

where z_0 is the thickness^[70]. This relation holds down to $z_0 \sim 100$ nm in most crystals, and even holds as low as 40 nm in some cases such as PZT^[70]. The consequence is that any reference to literature values for the coercive field of a particular material must also consider the thickness of the crystal.

Ideally the polarisation curves would be a Heaviside step function located at the reversal point E_c for ferroelectrics, or at zero for non-ferroelectrics. However, in a real system the dipoles do not all flip simultaneously as the field passes the coercive value thus a sigmoid is more appropriate. A hyperbolic tangent function can therefore be used to describe the polarisation^[71], such as

$$P_3^\pm(E_3) = P_{\text{sat},3} \tanh[a_3(E_3 \mp E_{c,3})] \quad (2.129)$$

where a_3 is a positive weighting constant equal to half of the inverse of the sigmoid width. The field direction is represented by \pm with $P_3^+(E_3)$ giving polarisation for increasing field and $P_3^-(E_3)$ giving polarisation for decreasing field. This function is not strictly derived from theoretical principles but is a very close mathematical description and is a convenient function to work with^[71]. The susceptibility χ_{33}^e and hence permittivity $\varepsilon_{r,33}$ are therefore no longer constant parameters but instead functions of applied field E_3 , determined using equation (2.106) to be

$$\varepsilon_{r,33} - 1 = \chi_{33}^{e,\pm} \equiv \frac{1}{\varepsilon_0} \frac{\partial}{\partial E_3} P_3^\pm = \frac{a_3 P_{\text{sat},3}}{\varepsilon_0} \text{sech}^2[a_3(E_3 \mp E_{c,3})] . \quad (2.130)$$

The remanence polarisation may be determined using $\mp P_r = P_3^\pm(0)$ to be

$$P_{r,3} = P_{\text{sat},3} \tanh(a_3 E_{c,3}) \quad (2.131)$$

and thus the weighting constant is given by

$$a_3 = \frac{1}{E_{c,3}} \text{arctanh}\left(\frac{P_{r,3}}{P_{\text{sat},3}}\right) = \frac{1}{2E_{c,3}} \ln\left(\frac{P_{\text{sat},3} + P_{r,3}}{P_{\text{sat},3} - P_{r,3}}\right) . \quad (2.132)$$

After full polarisation reversal a non-zero gradient is still permitted for the polarisation curve. This is because the increasing magnitude field can stretch the dipoles and increase their individual moments, although this is insignificant when compared to other phenomena involved so will be considered negligible in this work.

As was the case for ferromagnetism, this reversal process is repeatable indefinitely with a stable and consistent hysteresis loop. The area within the loop is again the energy cost of each cycle and is also typically dissipated as heat. Again, as in the ferromagnetic case the loop may be collapsed and

polarisation reset by heating the polarised material past the ferroelectric Curie temperature T_C . If the material is cooled back down in the absence of a poling field the polarisation will remain zero until a poling field is reapplied. A second method to reduce the spontaneous polarisation to zero is to apply a series of poling fields with decreasing magnitude in alternating directions. This forms a series of diminishing hysteresis loops which spiral towards the origin of the polarisation axes. The process is called AC depolarisation.

Ferroelectrics form domains via a similar mechanism to that described for ferromagnets in Section 2.8.2^[69]. The polarisations result in an effective charge at the ends of the crystal, with positive charges replacing the north pole and negative charges replacing the south pole, shown in Figure 2.36. The demagnetising field \vec{H}_d opposing magnetisation is replaced by a depoling field \vec{E}_d opposing polarisation^[65].

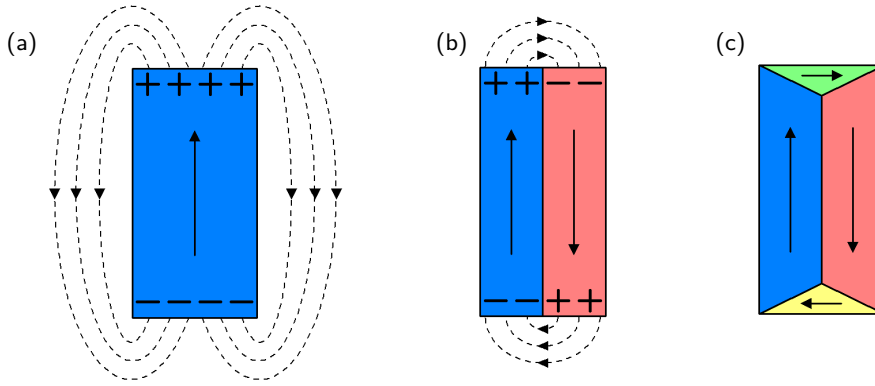


Figure 2.36: The polarisation and edge charges for different domain structures. (a) Homogeneous polarisation with significant edge charges. (b) Antiparallel polarisation with reduced edge charges. (c) Cyclical polarisation with no edge charges.

Cyclical polarisation does not necessarily imply the electric dipole moments to be wholly in-plane and can still occur in the presence of an applied external field. For example, an $R3m$ perovskite crystal polarises in the $\langle 111 \rangle$ direction, but this means the polarisations aligned by a $[001]$ poling field may be $[111]$, $[\bar{1}\bar{1}1]$, $[1\bar{1}\bar{1}]$, or $[\bar{1}\bar{1}\bar{1}]$. These are mutually orthogonal whilst still being polarised in the same direction, and provide four degenerate positions^[8] which may be used to form domains and reduce edge charges.

Electrostriction may require the creation of additional domains to minimise total energy^[69], as per ferromagnetism, to reduce conflicting strain between neighbouring domains of different polarisation axes.

2.13.1.1 Switching time and capacitive currents

Ferroelectric switching is not an instantaneous process and some switching time applies after the requisite field is applied^[72]. The naive picture would be simultaneous reversal of dipoles across the whole crystal, which is predicted by Landau theory alongside a coercive field three orders of magnitude higher than is observed in real structures^[72]. The lower reversal field is achieved through the formation of nucleations and domain wall movement, with only rare exceptions where simultaneous reversal is indeed observed^[72].

There are three intrinsic contributors to switching time: nucleation time t_n , forward-growth time t_{fg} , and side-growth time t_{sg} ^[72]. The first step of any polarisation reversal is the formation of surface nucleations of critical minimum size $\sim 1 - 10$ nm, which in oxide ferroelectrics takes $t_n \sim 1$ ns^[72].

The second step is the forward-growth, meaning the extension of the nucleation through the crystal thickness z_0 . This occurs at the speed of sound v_s which is approximated by^[58]

$$v_s = \sqrt{\frac{E}{\rho_m}} \quad (2.133)$$

where E is the elastic modulus and ρ_m is the mass density. This expression is truly applicable to rods rather than bulk solids, but serves for an approximate measure. The resulting forward-growth time is given by

$$t_{fg} = \frac{z_0}{v_s} = z_0 \sqrt{\frac{\rho_m}{E}}, \quad (2.134)$$

and is again expected to be ~ 1 ns for oxide ferroelectrics with thicknesses in the micrometre regime^[72].

The final contributor is the most significant. The side-growth time describes the time taken for the forward-growing columns to also expand their domain walls laterally to fill the entire crystal^[72], a process which may occur simultaneously with forward-growth. The time depends on field as $t_{sg} \propto E^{-3/2}$ and in thick-film or bulk ABX_3 perovskites is the dominant factor, typically taking up to microseconds to complete^[72]. Unlike ferromagnetic domain walls these are constrained by the speed of sound of the crystal, although the Coulombic field emanating from the wall is able to induce nucleations ahead of the moving wall leading to an observed group velocity higher than v_s ^[72].

In practice there is a further time constraint arising from the limitations of the poling system. Applying an electric field to a dielectric involves creating a circuit where the dielectric forms a capacitor. Charging a capacitor from the ground state by applying a potential V induces a charging current^[58]

$$I_c(t) = \frac{V}{R} \exp\left(-\frac{t}{RC}\right) \equiv \frac{V}{R} \exp\left(-\frac{t}{\tau}\right) \quad (2.135)$$

where t is time, R is circuit resistance, and C is the capacitance. The time constant $\tau \equiv RC$ is the time taken for the current to fall to $1/e = 37\%$ of the initial value^[58] and for the stored charge q to reach 63% of the equilibrium value; this is also known as the relaxation time^[58]. A good threshold for approximate

steady state behaviour is five time constants because after this time the charging current will have fallen below 1% of the initial value and the stored charge will have exceeded 99% of the equilibrium value. The actual time for the switching to occur after the field has been set is therefore dependent on the sample capacitance and the system resistance as well as intrinsic switching time.

The maximum ability of the power supply to physically provide the charging electrons and apply the target potential enforces an additional empirical constraint to total switching time. This is negligible for slowly changing fields, such as low field setpoints or sweeping values, but in this work high potentials were required and a response time of ~ 10 ms was observed when attempting to apply > 90 V from a grounded start. This was most likely due to power supply limitations via the high-voltage supply line.

Significantly, the capacitor charging process may be used to observe ferroelectric polarisation reversal^[73]. A time-varying potential $V(t)$ starting from $V(0) = 0$ V induces a charging current

$$I_c = \frac{\partial q}{\partial t} = \frac{\partial (CV)}{\partial t} = C \frac{\partial V}{\partial t}. \quad (2.136)$$

This means applying triangle waves of potential with constant $|dV/dt|$ will produce a constant baseline $|I_c|$. Upon reaching the coercive field the reversing dipoles produce a sudden change in potential over the capacitor and thus the capacitive current spikes providing an additional contribution from the ferroelectric switching current I_{fe} ^[73]. An approximately simultaneous reversal of polarisation direction produces a tall and thin current spike, whilst a more gradual reversal will result in a shorter and broader peak.

There is also a third current present, the resistive leakage current I_l ^[73]. This is a consequence of dielectric leakage and may be calibrated by applying a series of voltages and holding each for at least 5τ then measuring the current^[73]. This will be the same for all cycles so can be subtracted from other current measurements to leave I_c and I_{fe} .

2.13.1.2 Strain response

The idealised strain response S_3 arising from some field E_3 is shown in Figure 2.37. This figure assumes a simultaneous 180° polarisation reversal at a coercive field strength of $E_{c,3}$.

A ferroelectric is ultimately a piezoelectric whose polarisation curve has been offset from the origin by the value of the coercive field, so the strain nominally follows the linear response^[74] with a gradient of $\pm d_{33,0}$. If a field with magnitude beyond the coercive field is applied then the crystal dipoles will be poled parallel to this field and so positive piezoelectric strain is observed. Reducing this field to zero also reduces the strain to zero, then as the field passes zero and the direction reverses the piezoelectric strain becomes negative. Once the field strength reaches the coercive field in the antiparallel direction the dipoles undergo reversal, which reverts the system to a parallel polarisation to the field and the

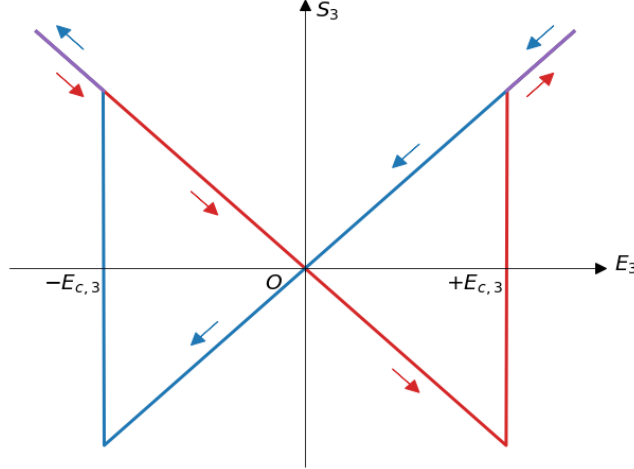


Figure 2.37: The idealised strain S_3 arising from a parallel or antiparallel poling field E_3 for a ferroelectric with coercive field strength $E_{c,3}$.

piezoelectric strain jumps back into positive values. In reality the reversal is not simultaneous or through 180° so is nowhere near as straight and sharp, and is instead widened and rounded. This is a much more complex model with significantly varying d_{33} and this is derived as part of the work in Chapter 8.

The full cycle of the ferroelectric strain curve forms a symmetric pattern which is reminiscent of a butterfly, especially in a real system with rounded curves, and so these are referred to in the literature as butterfly curves^[74]. Any electrostrictive strain is independent of polarisation direction so in systems with large M_{33} an asymmetric butterfly curve is seen^[7].

2.13.1.3 Long-range coordination

The interaction energy U of a pair of dipoles with separation r is described using similar expressions for both magnetic and electric cases, except with one important distinction. The energy for a magnetic dipole pair is^[69]

$$U_{mag} = \frac{\mu_0 \mu_B}{4\pi r^3} \approx \frac{\alpha^2}{4\pi} \left(\frac{a_B}{r} \right)^3 \quad (2.137)$$

where μ_0 is the permeability of free space, μ_B is the Bohr magneton, $\alpha \approx 1/137$ ^[36] is the fine-structure constant, and $a_B \approx 53 \text{ pm}$ ^[36] is the Bohr radius. Conversely, the energy for an electric dipole pair is^[69]

$$U_{ele} = \frac{p^2}{8\pi\epsilon_0 r^3} \approx \frac{\Delta^2}{4\pi} \left(\frac{a_B}{r} \right)^3 \quad (2.138)$$

where $p = e\Delta a_B$ is the electric dipole magnitude and $\Delta \approx 1$ is a parameter relating to atomic displacements and transverse electric charges. This shows that the ferroelectric energy is larger than its equivalent ferromagnetic counterpart by a ratio of

$$\frac{U_{ele}}{U_{mag}} \approx \frac{1}{\alpha^2} \approx 137^2 = 18769, \quad (2.139)$$

demonstrating how the long-range direct interaction effects of ferroelectricity are several orders of magnitude above those for ferromagnetism. This is the reason electric dipoles are able to be described classically whilst magnetic dipoles must rely on quantum mechanical exchange interactions.

2.13.2 Landau theory

Landau theory provides a symmetry based approach for determining equilibrium behaviour in the vicinity of a thermodynamic phase transition^[69]. It assumes that local fluctuations over the sample average out thus is best suited for systems with long-range interactions such as ferroelectrics and superconductors. Landau-Devonshire theory is the formulation applied to poled bulk ferroelectrics whilst the Landau-Ginsberg formulation relates to thin film and unpoled bulk ferroelectrics^[69].

A phase boundary between regions of different symmetries, such as different space groups, must be discontinuous by the need to rearrange the crystal from one space group to the other^[69]. However, the local thermodynamic state of the two bordering crystal structures must be continuous across the phase boundary, which requires that the symmetries of one space group must form a subset of the other, and so one crystal phase must have a higher symmetry than the other^[69]. Landau theory uses this to characterise the transition, by using some 'order parameter' which is zero in the higher-symmetry (disordered) phase and some finite value in the lower-symmetry phase. In ferroelectrics this order parameter is the polarisation P of the crystal^[69].

The higher-symmetry phase being the disordered phase seems somewhat contradictory at first glance, because one would expect an ordered system to have more symmetry than a disordered one. However, the parameter that is disordered, such as the electric dipole polarisation directions, is so randomised that they may be neglected when considering the symmetries of the system because they have no effect on the overall structure of the crystal^[69]. The ordering induces a preferred direction in the system which inherently reduces the overall symmetry.

The state of the system in equilibrium is calculated by expanding the free energy density \mathcal{F} as a power series of the order parameter P , and setting the coefficients of any terms incompatible with the symmetries of the system to 0^[69]. Any other coefficients may be determined empirically or derived from first principles. This function may then be minimised via differentiation to find the equilibrium polarisation, and non-zero values of this in the absence of any external stimuli give the spontaneous polarisation P_s ^[69]. However, this expansion is only valid in the vicinity of the transition. An additional caveat is that fluctuations of the order parameter must be very small relative to the order parameter itself^[69], which is usually safe to assume in poled ferroelectrics due to the long-range nature of electric dipole interactions.

2.13.2.1 Interpretation of free energy density

Landau-Devonshire is a formulation of the Landau theory targeting bulk and largely homogeneous crystals, such as PMN-PT substrates. This is a weighty topic which is beyond the scope of this thesis, however there are some results of note which bear discussing.

The free energy density of an electrically polarised crystal may be written as a power series in polarisation P , as stated previously, and how it depends on crystal strain S is a matter of symmetry. This power series expansion is^[69]

$$\mathcal{F}_S = aS^2 + bSP + cSP^2 + \dots - ST \quad (2.140)$$

where T is the applied stress and a, b, c are expansion coefficients.

The equilibrium occurs when^[69]

$$\frac{\partial \mathcal{F}_S}{\partial S} = 0, \quad (2.141)$$

yielding

$$S = \frac{T}{2a} - \frac{b}{2a}P - \frac{c}{2a}P^2 - \dots \quad (2.142)$$

This is another instance of modulus defect, discussed for the magnetoelastic effect in Section 2.9.1, where this is the electrical analogue. The coefficient $2a$ is the unmodified elastic modulus for the crystal^[69], and is recovered for zero net polarisation. The latter two terms of equation (2.142) are the direct piezoelectric and electrostriction effects, so $-b/2a$ is the piezoelectric coefficient d_{ij} and $-c/2a$ is the electrostriction coefficient Q_{ij} .

In ferroelectrics there is always some spontaneous polarisation, on the nanoscale even if not macroscopically observed, meaning P never truly goes to zero^[69]. This strain is therefore permanent, as is the case for magnetoelastic strain. The result is the distortion of any crystals from their rest states, such as perovskites rarely being seen to be $Pm\bar{3}m$ ^[32]. This always occurs in the direction $\langle 111 \rangle$, and in lead magnesium niobate (PMN) just one strain direction is induced so the unit cells deform in that direction forming a rhombohedral structure^[49]. However, in other crystals this polarisation strain occurs along multiple axes simultaneously resulting in an alternate unit cell symmetry, such as monoclinic or tetragonal^[49]. The polarisation angle of the solid solution of two ferroelectrics is therefore a monotonic function of the ratio of the constituents, so considering the perovskite primitive unit cells in Section 2.3.1 an alloy of PMN and PT would be expected to rotate from rhombohedral to Cm monoclinic to Pm monoclinic to tetragonal with rising PT content. This is indeed what the phase diagram of PMN-PT shows in ambient conditions^[28], as will be discussed in Section 3.6.

2.13.3 Relaxor ferroelectrics

Ferroelectrics fall into two groups. The normal or conventional ferroelectric has been discussed in the prior sections, but there is a second category known as relaxor ferroelectrics^[75]. Relaxors feature no inversion asymmetry yet are still able to demonstrate a piezoelectric effect in addition to exhibiting an unusually strong electrostrictive response^[32]. The exact reasons for both of these phenomena are still unknown^[76]. Relaxation covers a variety of phenomena, and in ferroelectrics it refers to the polarisation reversal in the presence of an applied field^[77]. The relaxation time in this case is simply the switching time, and the nucleation and forward- and side-growth processes are the dipole and domain wall relaxations.

A conventional ferroelectric demonstrates long-range ordering as discussed in Section 2.13.1.3. This results in coordinated polarisation and a single common relaxation^[75]. No such long-range ordering manifests in a relaxor, instead the constituent dipoles form polar nanoregions (PNRs) which are nanoscale polarisation domains formed via short-range interactions^[75]. Each of these have their own relaxation properties hence the term relaxor ferroelectric. These have multiple effects including the broadening of the temperature dependence of the relative permittivity^[77], allowing a thermal stability in relaxor ferroelectric response which is not observed for conventional ferroelectrics. This stability, along with being able to form large single crystals, makes relaxors very good candidates for substrates in multiferroic devices^[7].

The PNRs break down above the Curie temperature but in relaxors there are arguably more important thermal limits to discuss. The Burns temperature T_B is the limit above which thermal energy supersedes the PNR polarisation direction energy barriers and so the PNRs rotate randomly relative to one another whilst internally remaining a coordinated collective, although they may be aligned by an external field in paraelectric style behaviour^[75]. This differs from a truly paraelectric state because the presence of PNRs mean that local dipole moments remain non-zero.

As the temperature falls below the Burns temperature the PNRs become larger and more numerous which results in a larger energy barrier between orientations and lower thermal energy fluctuations^[75]. Once cooled to some freezing temperature T_F the PNRs become locked in place^[75] in an electric analogue of magnetic spin-glass^[76], and conventional ferroelectric behaviour is observed^[75]. At temperatures between T_F and T_B relaxor properties occur, and the peak of the thermally dependent permittivity is in this range^[75] resulting in a large value of M_{33} and thus large electrostrictive strain via equation (2.110). The relaxor ferroelectric crystal PMN has a freezing temperature of $T_F \approx 210$ K and Burns temperature of $T_B \approx 620$ K^[32].

The large permittivity and thus strongly non-linear strain curve result in a highly variable differential

piezoelectric coefficient d_{33} and so the effective piezoelectric coefficient d_{33}^{eff} is of limited use for these materials. There is very little discussion of this in the literature, especially so when considering nanoscale behaviour. The dependencies of these parameters on field will be derived and applied to data as part of this work, and this will be covered in Chapter 8.

2.14 Multiferroic materials

2.14.1 Ferroic properties

A multiferroic is a material or structure which features two or more ferroic properties with large coupling constants between them^[19]. Ferroic properties are bistable with a hysteretic transition between states, meaning that once switched they remain fixed in the induced state until they are coerced into the opposite state. This allows them to be used as toggle switches and through the coupling enables one ferroic property to be used to reverse a second. There are considered to be four ferroic properties, characterised by the variance of the bistable property upon space inversion and time reversal^[78], which are summarised in Table 2.11.

Time reversal \ Space inversion	Space inversion	Invariant	Transformed
	Time reversal	Invariant	Transformed
Invariant		Ferroelastic	Ferroelectric
Transformed		Ferromagnetic	Ferrotoroidic

Table 2.11: The four ferroic properties as characterised by their response to space inversion and time reversal^[78].

Ferromagnetics and ferroelectrics were explained in Sections 2.7.1 and 2.13.1 respectively, and the remaining ferroics will now be briefly described for completeness. Ferroelasticity is conceptually the simplest and requires a crystal system featuring degenerate skew directions such as rhombohedral and monoclinic structures^[19]. These may be oriented in different directions and still maintain their polarisation direction, as stated in Section 2.13.1, and this results in different strain directions within the crystal. Ferroelasticity occurs if the strain direction is configurable using an applied mechanical stress^[19], resulting in a stable yet reversible macroscopic deformation.

The remaining ferroic property is ferrotoroidicity, where a looped magnetic field induces a magnetic toroidal moment along the axis normal to the plane of the loop^[78]. A macroscopic example is a solenoid arranged into a torus as shown in Figure 2.38a, where the electric current induces a magnetic field within which in turn induces a toroidal moment^[78]. On the nanoscale a circle of spins, and thus magnetic dipole moments, may induce a much reduced toroidal moment as shown in Figure 2.38b and these moments align locally to form domains^[78]. These are both electric and magnetic and the toroidisation

is theoretically reversible using orthogonal electric and magnetic fields^[78].

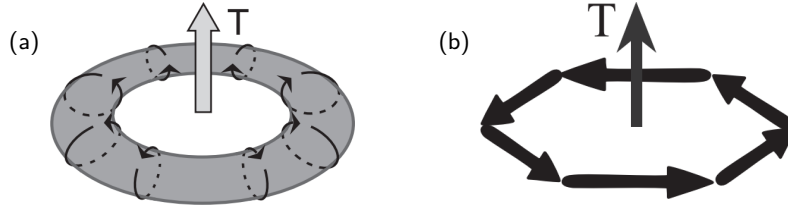


Figure 2.38: Macroscale and nanoscale examples of magnetic toroidal moments, denoted T , reproduced from Spaldin et al^[78]. (a) A solenoid with the magnetic field induced by an electric current. (b) A circle of spins forming a nanoscale toroidal moment.

2.14.2 Magnetoelectric coupling

Magnetoelectric multiferroic materials are of great interest in spintronics because they demonstrate both ferromagnetic and ferroelectric behaviour with some magnetoelectric coupling between them^[20]. Multiferroic coupling is a tensor property and for magnetoelectric coupling is defined as^[19]

$$\alpha_{ij} \equiv \frac{\partial B_i}{\partial E_j} = \mu_0 \frac{\partial M_i}{\partial E_j}. \quad (2.143)$$

Magnetoelectric coupling requires the absence of space inversion and time reversal symmetries so magnetoelectric media must be both ferroelectric and ferromagnetic in order to break these respective symmetries and permit coupling to occur^[19].

Additionally, as one may expect there is a magnitude constraint enforced by the susceptibilities of the two phenomena, thus^[19]

$$\alpha_{ij} \leq \sqrt{\chi_{ii}^m \chi_{jj}^e}. \quad (2.144)$$

The two susceptibilities are rarely co-optimised due to the incompatible prerequisites of the d orbital for these phenomena to occur: a ferroelectric requires the d orbital to be unoccupied^[49] but it was outlined in Section 2.5.4 that a d orbital must contain unpaired electrons to exhibit ferromagnetism. The presence of these unpaired electrons provide a polarisation field which counteracts ionic polarisation and weakens it relative to the repulsive field between cations, which can thereby suppress ferroelectric ordering due to removing the inversion asymmetry arising from the ionic displacements^[49]. This mechanism is the reason that crystal structure alone cannot predict ferroelectric behaviour, as stated in Section 2.12.3.

The result is that magnetoelectric coupling relies upon non-linear coupling using the ion displacement polarisation observed in perovskite crystals^[19], and this is the reason the perovskite crystal prototype is of such interest in ferroelectric research. The only known crystal featuring undisputed room temperature multiferroic magnetoelectric coupling is BiFeO_3 ^[19], which is a perovskite featuring canted G-type anti-ferromagnetic ordering. The non-linearity refers to the fact that the magnetisation direction is unaffected by reversing the polarisation, meaning only the magnetisation magnitude is tunable^[19].

2.14.3 Artificial multiferroics

The limited selection of natural multiferroic materials may be mitigated through the use of artificial, or 'composite', multiferroics^[19]. These are formed by layering thin films of ferroic materials onto a substrate which may itself be ferroic, and interlayer coupling arises between these which for magnetoelectrics are typically at least $10\times$ the size of the typical coupling tensor components for natural multiferroics^[21]. The interlayer coupling in composite magnetoelectrics is mediated through strain, whereby the piezoelectric response of the ferroelectric layer deforms the ferromagnetic unit cells which induces a change in magnetic ordering^[7]. An FeRh film deposited onto a PMN-PT substrate is a good candidate for a composite magnetoelectric multiferroic, and electric fields applied to the PMN-PT relaxor substrate are demonstrably able to manipulate the ferromagnetic properties of the FeRh film via mechanical strain^[7].

However, there are limitations on the feasibility of strain-mediated multiferroic reversal. An imperfectly formed interface between ferroic media will result in an internal strain in at least one of them and this will weaken the effect of the strain induced by the actuating layer^[7]. Additionally, the induced strain will dissipate as the thickness of the responding layer increases, requiring very thin films be used where possible. Poisson's ratio describes the lateral strain induced by the longitudinal strain from the actuator, and this lateral contribution provides an additional interfering strain which will again weaken the desired strain response^[7].

2.14.4 Use of multiferroic devices

The advantage of using multiferroics lies in the large and bistable response of one parameter to a second, allowing the use of a low-energy and focussed input to toggle a ferroic ordering that is ordinarily far less precise^[19]. For example, ferromagnetic reversal using an \vec{H} field is imprecise and typically involves solenoids and a large consumption of energy, whilst ferroelectric reversal simply requires the application of potentials to specific locations; magnetoelectric coupling allows this precise potential application to control the local magnetisation direction^[19].

The applications of multiferroics range from simply replacing inductor and capacitor pairs with single components, to doubling potential data storage through polarisation and magnetisation, and on to the previously mentioned ability to use electric fields to manipulate magnetic properties^[19]. This latter application is of great interest because reversing a magnetic logic bit via magnetoelectric coupling can use orders of magnitude less energy than direct reversal, allowing for reduced power consumption and improved miniaturisation^[19]. Another application of these structures is to utilise the induced ferromagnetic domain walls themselves. These may be able to be used as metallic transport conductive pathways through otherwise insulating ferroelectrics, and given the relative ease of manipulating domain walls this would allow nanoscale circuits to be created, moved, and annihilated on demand^[20].

2.15 Summary

The work presented in this thesis involves analysis and interpretation of crystalline materials with multiple structures. In order to understand this work, especially the piezoelectric studies, a background knowledge of crystals is required and these sections aimed to provide this information. A discussion of each lattice type was provided and the properties of the CsCl and perovskite prototypes were explained, which form the two exemplar samples under investigation in this thesis.

An introduction to ferromagnetism and ferroelectricity was essential due to these being the properties of interest in the samples under investigation. A qualitative discussion of induced and ordered magnetic dipole ordering and the mechanisms involved was presented alongside the effects of magnetisation on other crystal properties. The origins and thermal hysteresis of ferromagnetic ordering were also provided.

A corresponding yet more quantitative discussion of electric dipole ordering was also presented and correlated to crystal point groups. The different strain mechanisms were explained and the contrast between effective and differential piezoelectric coefficients was acknowledged. The ferroelectric polarisation reversal process was discussed in detail along with the resulting phenomena, and the lesser-understood subcategory of relaxors was also explained. The two ferroics may be combined to form multiferroic materials and so these were explained and the significance of such structures has been discussed.

Chapter 3

Materials for artificial multiferroics

The work in this thesis involves studies of FeRh and PMN-PT solid solutions so an introduction to the properties of these materials is required. This chapter will begin by presenting and discussing the thermal phase diagram for FeRh. The unusual metamagnetic transition of equiatomic FeRh is the phenomenon of interest for the material so this will be introduced and the properties explained in detail. Possible applications and required growth conditions will be discussed alongside the effects of and motivation for noble ion irradiation of the film and complications arising from the oxide layer which forms on ferrous films such as FeRh. The thermal phase diagram for the relaxor ferroelectric PMN-PT will be introduced and in particular the phase boundary between the rhombohedral and monoclinic structures will be discussed. The mechanism of the high piezoelectric response will be explained and the specific effect of PMN to PT ratio on crystal structure will be considered. The dependence of the ferroelectric coercive field on the PT content will also be introduced. Finally, the surface effects arising from polishing will be discussed along with the difficulties of working with such brittle substrates.

3.1 Phase diagram of FeRh

The structure and magnetic properties of the intermetallic $\text{Fe}_{1-x}\text{Rh}_x$ vary significantly with temperature, applied magnetic field, and rhodium content, and thus the phase diagrams of this alloy are of great interest. The most significant phase diagram for this work is on axes of temperature and rhodium atomic fraction x . The diagram in common use was first published by Swartzendruber in 1984^[30] and is shown in Figure 3.1. This builds on and corroborates the initial diagram published by Fallot and Hocart in 1939^[4].

Many of the phase boundaries are marked by dashed lines reflecting the significant extrapolation involved in devising the diagram, and Swartzendruber does state the caveat that the thermodynamic model used only calculated an approximate diagram. However, Balun et al. empirically investigated the phase diagram in 2007^[79] and confirmed the Swartzendruber phase diagram to be an accurate representation. An overview of the phases present in this diagram is given in Table 3.1.

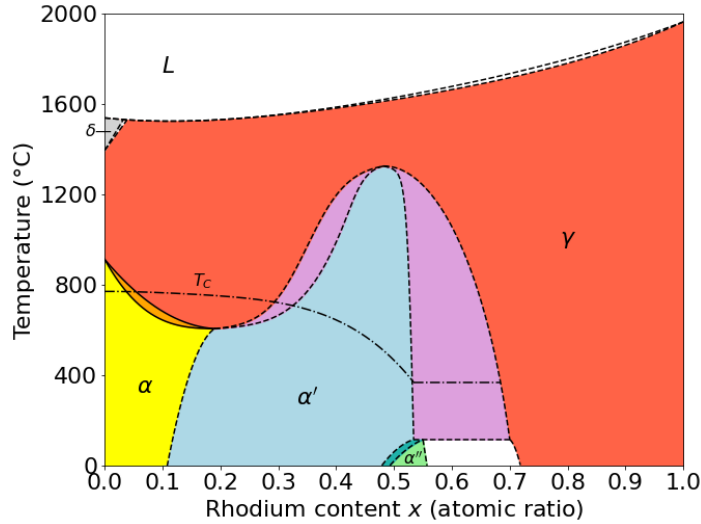


Figure 3.1: The FeRh phase diagram for temperature and Rh content adapted from the work of Swartzendruber^[30]. Each phase is labelled with the corresponding allotrope of iron and has been coloured for clarity. The coloured phases with no label are metastable phases where both neighbouring phases may coexist.

At the top of the phase diagram in Figure 3.1 is the liquid phase, which is expected in thermal phase diagrams. Below this in the top left is the small region of δ phase, coloured grey, which is a disordered $Im\bar{3}m$ structure where the few Rh atoms simply substitute for Fe atoms in the lattice. This is a purely paramagnetic phase due to being significantly above the Curie temperature. Following this is the γ phase in red which occurs for high temperatures or high Rh content x . This is a disordered $Fm\bar{3}m$ structure where the thermal excitations allow all atoms to redistribute across the lattice thus each lattice site has an equal chance of being occupied by an Fe or Rh atom. Note from the edges of the diagram that this is also the structure of pure Fe for $912^\circ\text{C} < T < 1394^\circ\text{C}$ and for pure Rh at all temperatures. This phase demonstrates paramagnetic behaviour throughout.

In the bottom left of Figure 3.1, in yellow, is the α phase. This is a disordered $Im\bar{3}m$ structure as for δ , except that it exists for lower temperatures and higher x . It is ferromagnetic for the most part, however it can exist just above the Curie temperature under certain conditions in which case it becomes paramagnetic. The central phase α' of Figure 3.1, shaded blue, is one of the phases of interest in this work. This is a CsCl structure which is ferromagnetic or paramagnetic depending on the temperature. The peak at $x = 0.5$ is expected due to the stability of equiatomic CsCl structures. CsCl structures with $x < 0.5$ feature vacancies which decrease the stability of the lattice ordering and allow thermal excitations to more easily disrupt the structure into the disordered FCC phase γ .

The α/γ and α'/γ phase transitions are very broad and are shaded with orange and purple respectively

Fe allotrope	Rh at. content x	Phase notation	Crystal structure	Space group	Magnetic state
δ	0 – 0.03	A2	Disordered BCC	$Im\bar{3}m$	PM
α	0 – 0.19	A2	Disordered BCC	$Im\bar{3}m$	FM (below T_C)
γ	0 – 1	A1	Disordered FCC	$Fm\bar{3}m$	PM
α'	0.11 – 0.55	B2	CsCl	$Pm\bar{3}m$	FM (below T_C)
α''	0.48 – 0.55	B2	CsCl/Heusler	$Pm\bar{3}m/Fm\bar{3}m$	AF

Table 3.1: Further details on the phases present in Figure 3.1^[30]. BCC and FCC denote body-centred and face-centred cubic lattices and PM, FM, and AF denote paramagnetic, ferromagnetic, and antiferromagnetic ordering respectively. T_C is the Curie temperature.

on Figure 3.1. These regions are populated by metastable states where both bordering phases can coexist simultaneously. Additionally, the boundaries where $x \lesssim 0.3$ exhibit significant hysteresis and the stated boundaries are estimated values based on this. As such, there may be α or α' phases present in the region demarcated as γ hence it is indeed meaningful to mark a Curie temperature in this ostensibly paramagnetic regime.

The most significant region for this work is α'' , which is one of the smallest regions of the phase diagram and is located at the bottom-middle of Figure 3.1 and shaded green. This region is G-type antiferromagnetic^[80] and as such may be described as a full-Heusler structure $Rh_2Fe_{\uparrow}Fe_{\downarrow}$ ^[30], although most authors simply label it as a CsCl structure^[14]. This region is an area of active research because it enables equiatomic FeRh to metamagnetically transition from antiferromagnetic ordering to ferromagnetic via heating to the readily achievable temperature of $\sim 100^\circ\text{C}$ where the structural phase transitions to α' . There is a significant hysteresis between the two phases, as seen from the wide phase boundary, and a crystal located within the phase diagram hysteresis is populated by metastable domains and thus characterising this transition is of great interest.

The remaining white region to the right of α'' is left undefined in the literature, with many authors opting to neglect the upper phase boundary of this region and to instead consider it part of the metastable overlap between α' and γ .

3.2 Metamagnetic transition of equiatomic FeRh

The phase transition of most interest for this work is the metamagnetic α'/α'' transition which is accompanied by a series of changes in crystal properties including electrical resistivity^[5] and elastic response^[15]. The α'/α'' transition is called metamagnetic because it is induced by raising an external

parameter until FM ordering is achieved, which then disappears once the external influence is removed. The difference here is that temperature is used in lieu of a magnetic field, so the terminology is a misnomer. In this thesis the different magnetic orderings of an FeRh crystal will be given the respective shorthand labels AF-FeRh and FM-FeRh for the antiferromagnetic and ferromagnetic cases, and a hybrid crystal with both magnetic phases coexisting in coherent domains, for example one where the temperature is close to the transition temperature T_0 , will be denoted HY-FeRh.

This transition is particularly remarkable because it occurs at readily achievable temperatures^[4], unlike the cryogenic temperatures required for other thermally metamagnetic crystals^[39]. In addition it is accompanied by changes in multiple other properties, as discussed further in Section 3.3, meaning such a material has applications in a range of devices where consistent and reversible property switching is required on demand^[16]. This is therefore a material under active investigation in recent research^[81;57;17;82;18;83;84;7;85].

3.2.1 Magnetisation curves

The magnetisation of samples of $\text{Fe}_{1-x}\text{Rh}_x$ against temperature was first recorded and plotted by Fallot and Hocart for multiple values of x ^[4] and their results are presented in Figure 3.2. These curves were used to generate the initial 1939 phase diagram and show remarkable agreement with the phase diagram in Figure 3.1, although the rhodium percentages appear to be offset slightly from the corresponding values in Figure 3.1 and the curves do not accurately follow the shape predicted by the Brillouin function used for magnetic modelling^[5]. This offset and the imperfect curve shape are likely to be consequences of the inevitably qualitative nature of this early work and the low applied magnetic fields used^[5]. The temperature dependence of the phase boundaries is very clearly visible, however, including hystereses.

In macroscopic sample measurements such as these the transition occurs via a conventional first-order process and Figure 3.3 shows the typical curve for equiatomic FeRh as recorded for a 50 nm thick film on a vibrating sample magnetometer^[57]. The curved sigmoidal transition in lieu of a clean Heaviside transition describes a distributed transition temperature across the volume of the sample, which is likely due in part to inhomogeneity in the $\text{Fe}_{1-x}\text{Rh}_x$ solid solution^[57]. Another suggested mechanism is strain inhomogeneity arising naturally from the epitaxial film growth^[86].

On the nanoscale the transition occurs via a series of FM domain nucleations, which form and expand during heating and shrink and divide during cooling and have been characterised using both magnetic force microscopy^[57] and XMCD-PEEM^[87]. The nucleation sites remain identical over repeated cycles and the fraction of the film surface showing FM ordering at a range of temperatures aligns with the normalised magnetisation curve in Figure 3.3^[57], supporting the prior statement that the curve shape is due to inhomogeneous transition temperature and local crystal structure.

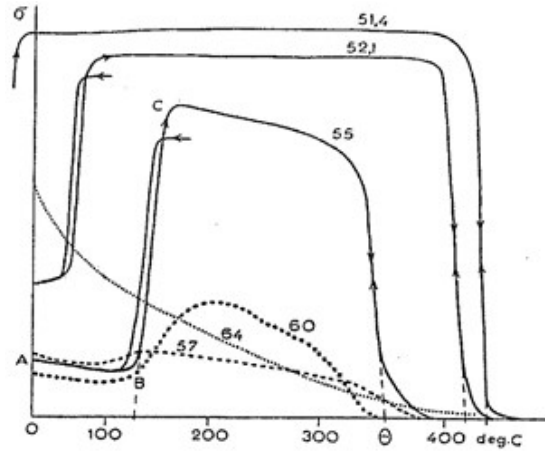


Figure 3.2: The magnetisation σ , in arbitrary units, against temperature, in Celsius, for multiple samples of $\text{Fe}_{1-x}\text{Rh}_x$ as recorded by Fallot and Hocart in their initial 1939 work^[4]. The atomic percentage of rhodium is given next to each plot and the Curie temperature of the $x = 55\%$ curve is labelled Θ .

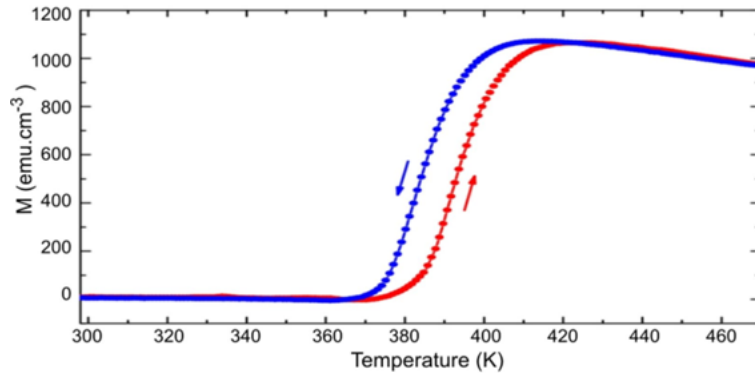


Figure 3.3: The temperature dependent magnetisation of equiatomic FeRh showing the phase transition hysteresis via the first-order metamagnetic phase transition. Figure reproduced from Warren et al^[57].

3.2.2 Tuning the metamagnetic transition

The metamagnetic transition may occur through either the application of temperature or high magnetic fields, and each may be used to set the transition value of the other. Figure 3.4 shows the phase diagram for equiatomic FeRh at a range of temperatures and magnetic fields^[30].

There is an inverse relationship between the two external stimuli: the application of a high field reduces the metamagnetic transition temperature and increases the hysteresis width, whilst low temperatures increase the metamagnetic transition field and decrease the hysteresis width. This does align with the intuitively expected result because temperature is a measure of dynamic disorder in the crystal. Low temperatures mean the system is predisposed to the lower energy AF state and thus the required field to enforce ferromagnetic ordering is high and the dipoles undergo rapid relaxation once the field is removed

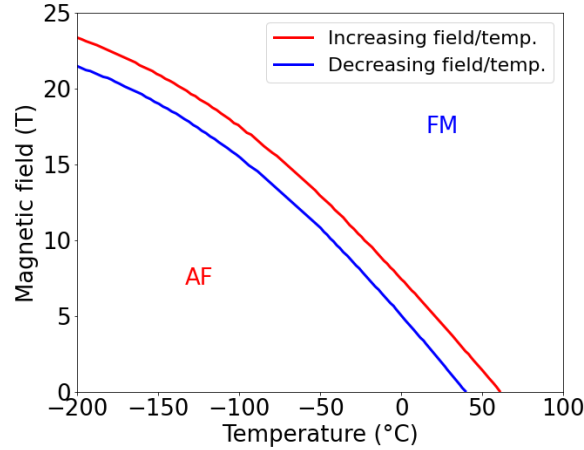


Figure 3.4: The phase diagram for equiatomic FeRh at a range of temperatures and external fields, adapted from the work of Swartzendruber^[30]. The application of an external field can clearly cause a significant reduction in the transition temperature and widening of the phase boundary.

hence exhibit a small hysteresis. On the other axis, the application of a strong field will predispose the system to an FM alignment so the dipoles will more readily switch once disorder enters the system and will relax slowly upon removal of the disorder, thus remaining aligned with the field longer and widening the hysteresis.

3.3 FeRh metamagnetic phase change properties

The α' and α'' phases both have a CsCl structure with the typical α'' lattice constant being 2.99 \AA ^[4;88;30] and the corresponding α' lattice constant being 3.00 \AA . Authors often provide this value to four significant figures, however the value is extremely dependent on measurement environment and film preparation to the extent that the fourth value is only valid for relative measurements on the same film. The Fe atoms carry a magnetic moment of $\pm 3.3\mu_B$ in the AF configuration which decreases to $3.2\mu_B$ in the FM configuration, whilst the rhodium atom exhibits no net moment in the AF configuration and $0.9\mu_B$ in the FM configuration^[89]. There is again some contention in these values, with other authors giving values that differ by up to $0.2\mu_B$ ^[90]. The FeRh unit cell in both magnetic configurations is shown in Figure 3.5 with relative dipole moment directions indicated.

The changing magnetic ordering induces a significant change in the electrical resistivity^[5] via magnetoresistance, discussed in Section 2.9.2. An example resistivity curve for a bulk sample of $\text{Fe}_{48}\text{Rh}_{52}$ is provided in Figure 3.6. The resistance drop in approximately equiatomic FeRh is unusually large with the figure showing a drop of 33% at 350 K. This is only marginally lower than the 37% predicted for idealised magnetoresistance, suggesting that the densities of states for each spin direction have very little overlap at the Fermi energy. The same hysteresis is observed as for the magnetisation in Figure 3.3, supporting

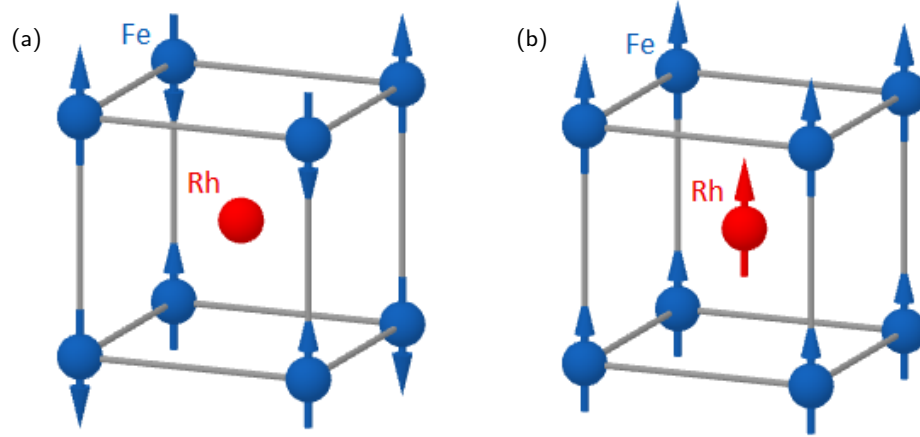


Figure 3.5: The FeRh unit cell in antiferromagnetic and ferromagnetic configurations. The blue atoms are iron and the red are rhodium, and the arrows indicate the relative dipole moment directions. (a) Antiferromagnetic FeRh. (b) Ferromagnetic FeRh.

the surmised causal relationship between the magnetic ordering and electrical resistivity. The curve away from the phase transition demonstrates a significant gradient arising from electron-phonon scattering, which was introduced in equation (2.98) of Section 2.9.2. The resistivity at room temperature is seen in Figure 3.6 to be $3.0 \times 10^{-8} \Omega \text{ m}$.

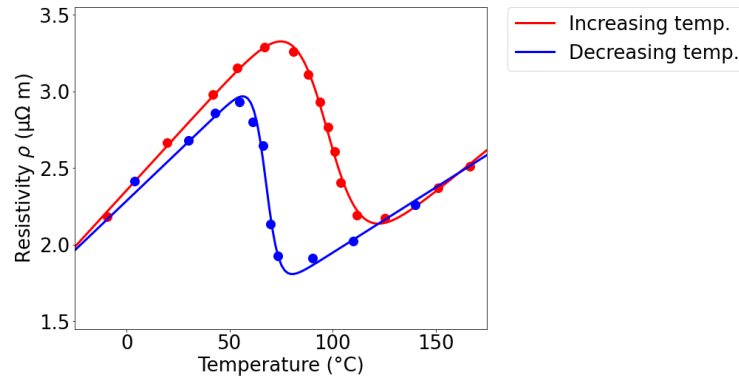


Figure 3.6: The temperature dependent resistivity of bulk equiatomic FeRh showing the phase transition hysteresis via the magnetoresistive effect. Figure adapted from Kouvel and Hartelius^[5].

Another crystal property affected by the metamagnetic transition is the lattice constant. In a bulk FeRh crystal the transition is accompanied by a $\sim 0.3\%$ homogeneous strain which increases the unit cell volume by $\sim 1\%$ ^[14]. This could be a consequence of Pauli repulsion arising from the parallel electron spin states, which are known from the magnitude of the magnetoresistance effect to be significantly unbalanced in FM-FeRh. The thin film strain is different due to the lateral pinning effect of the substrate crystal, and when grown on MgO(001) the result is instead a 0.7% strain in the [001] direction^[29]. This means that the FM-FeRh lattice forms the less common $P4mm$ tetragonal CsCl unit cell shown in

Figure 3.7.

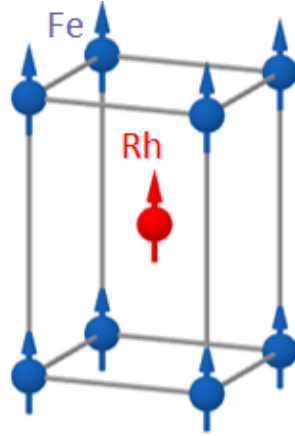


Figure 3.7: The $P4mm$ tetragonal FM-FeRh unit cell as observed in a thin film. The blue atoms are iron and the red are rhodium, and the arrows indicate the relative dipole moment directions.

The mechanical properties of FeRh have also been observed to change with magnetic ordering^[15], as predicted by the magnetoelastic effect introduced in Section 2.9.1. Figure 3.8 shows an example of the varying elastic modulus and Poisson's ratio for bulk $\text{Fe}_{50.5}\text{Rh}_{49.5}$ ^[15].

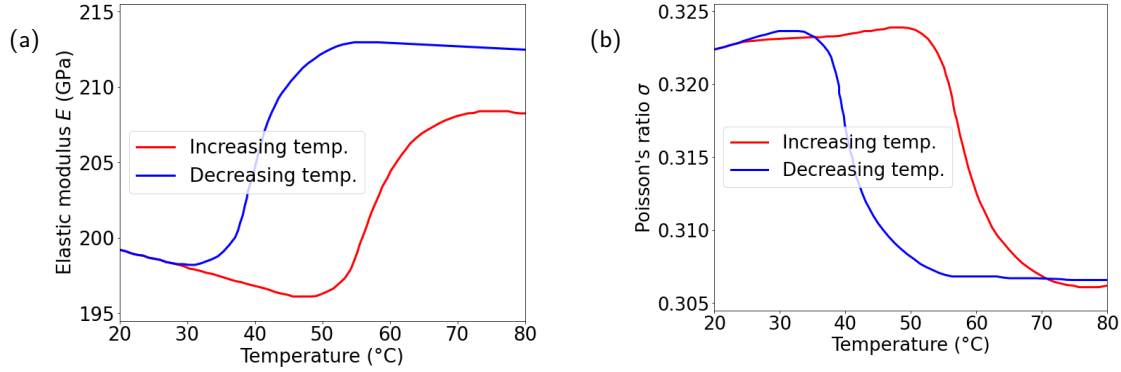


Figure 3.8: The temperature dependent mechanical properties of equiatomic FeRh showing the phase transition hysteresis via the magnetoelastic effect. Figures adapted from Palmer et al^[15]. (a) Elastic modulus. (b) Poisson's ratio.

The same hysteresis is observed as for the magnetisation in Figure 3.3 and resistivity in Figure 3.6, supporting the surmised causal relationship between the magnetic and mechanical behaviours. The relative change of each of the two properties was equal but with opposite sign, exactly as predicted in Section 2.9.1. Note however that this data was obtained using the small amplitude resonance technique^[15] and so much smaller changes will be seen if direct force measurements are attempted. The elastic modulus and Poisson's ratio at room temperature are seen in Figure 3.8 to be 198 GPa and 0.323 respectively.

No accepted theory has yet been established regarding the underlying mechanism of the FeRh metamagnetic exchange inversion. However, one proposal is that the rhodium magnetic moment is critical to the transition^[91]. The rhodium atom cannot simply be paramagnetically responding to the \vec{M} field from the aligned iron atom dipole moments because the paramagnetic susceptibility is several orders of magnitude too low. The theory postulates that the rhodium atoms possess two states: one with lower energy and zero-moment and the other with higher energy and non-zero moment $\sim \mu_B$ ^[91]. The rhodium atom is therefore raised to the magnetic state via thermal excitation and forms an FM exchange coupling with the neighbouring iron atoms which dominates the existing AF exchange coupling and creates a stable FM ordering for the FeRh crystal^[91].

This proposed phenomenon may be a contributor to the observed ferromagnetic stability, however it is now known that this cannot not be the sole mechanism. The metamagnetic transition is a consequence of lattice disorder^[6] and heating the FeRh crystal provides dynamic disorder in the form of thermal oscillations. Alternatively, static disorder may occur if crystal atoms are displaced from their intended sites and thus an indefinite ferromagnetic ordering is induced^[6;18]. This is the mechanism used in artificial multiferroics when using a piezoelectric substrate to control the magnetisation state of a metamagnetic film^[7], as mentioned in Section 2.14.

3.3.1 Potential applications

The magnetic transition is of great interest in spintronics, with one application being in the design of data storage memristors where it forms a thermally activated exchange layer as part of a multilayer stack^[16].

Memristors are considered the fourth basic electronic element, alongside resistors, capacitors, and inductors^[92], and just over a decade ago were created for the first time^[93]. They are effectively time dependent resistors with their name arising from the fact they ‘remember’ their electrical history. This memory effect is due to the constituent atoms rearranging when exposed to certain stimuli^[93] and in the case of FeRh this rearrangement is the magnetic dipole orientation direction.

A FeRh memristor may be used to create a magnetically stable binary bit for data storage^[16]: the data value stored in the bit is the antiferromagnetic magnetisation axis which may take two perpendicular positions within the plane of the film, and the value is read by applying a small bias across the width of the bit and measuring the current^[16]. The resistance will change between the AF magnetisation directions due to the magnetoresistance arising from dipole alignment, which is discussed in Section 2.9.2. Figure 3.9 shows this schematically. The writing process for the bit would be to heat it into the FM phase and apply a magnetic field to change the orientation then cool it back down^[16]. This results in a bit which is insensitive to stray magnetic fields and may be read without any risk of affecting the

value stored within.

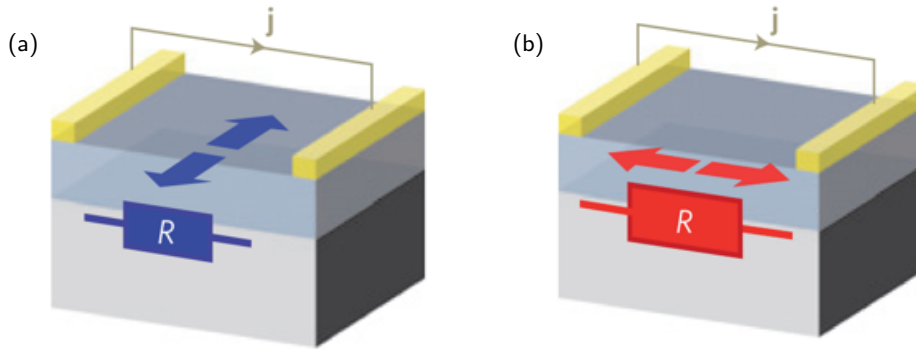


Figure 3.9: The reading process for a memristor using the magnetoresistance effect of an antiferromagnetic film. The arrows show magnetic dipole orientations and j denotes the measured current. Figures reproduced from^[16]. (a) Lower resistance due to the magnetisation axis being perpendicular to current direction. (b) Higher resistance due to the magnetisation axis being parallel to current direction.

It is important to consider that the use of FeRh in such applications is not necessarily suitable for mass production. Rhodium is a very expensive d-block metal, so in order to be economically viable as a replacement to existing consumer technology it must be used in minimal quantities in each device.

3.4 FeRh growth and patterning

3.4.1 Thin film growth optimisation

Thin films may be grown by sputter coating a substrate with atoms of the requisite elements, and this process will be briefly explained in Section 7.1.1. The growth parameters of FeRh thin films are dictated strongly by the requirement for the CsCl structure with α'' AF ordering. Single crystal MgO(001) is ideal for high-quality FeRh films due to the compatibility of the two crystal structures^[94]. MgO has a rock salt or NaCl prototype structure^[24] with a lattice constant of 4.212 \AA ^[95]. This structure is an $Fm\bar{3}m$ lattice with two atoms in the basis but may also be thought of as a simple cubic lattice with alternating vertex atoms and a lattice constant of 2.106 \AA ; essentially NaCl is the Heusler structure shown in Figure 2.16 without the X atoms.

The CsCl prototype being body-centred prohibits clean growth of FeRh on a NaCl crystal if the unit cells are aligned. However, rotating the CsCl structure by 45° about the $[001]$ axis resolves this conflict^[95] and provides each atom of the film with a corresponding atom in the substrate: Fe with Mg and Rh with O. The lattice constant of the film must therefore be similar to the diagonal between atoms in the substrate and for MgO(001) this would be 2.987 \AA , thus FeRh with a lattice constant of 2.99 \AA grows well on MgO(001) substrates. The lattice mismatch introduces a strain of just 0.65% which is

completely suppressed in films greater than 10 nm^[95]. The substrate must be heated during deposition to allow the Fe and Rh atoms to possess sufficient mobility to create the desired CsCl structure with minimal defects; this is finalised by annealing the film at an even higher temperature^[95].

3.4.2 Noble ion irradiation of FeRh

The metamagnetic phase transition parameters of FeRh may be modified through careful control of the film growth, including the ratio of iron to rhodium or doping with small percentages of other elements such as iridium. A simpler approach which permits locationally precise transition modification is to alter the crystal structure after the film has been grown. It has recently been shown that irradiation of the deposited film with energetic noble ions such as neon may be used to disrupt the lattice and cause ferromagnetic or even paramagnetic regions to form at room temperature, depending on the fluence used^[6;18].

There are two mechanisms by which the noble ions introduce disorder into the crystal structure^[18]. The first occurs for lower fluences and results in small displacements of crystal atoms from their intended sites which induces ferromagnetic ordering. The second occurs for higher fluences and involves the formation of monovacancies in the structure which induce paramagnetic ordering. It has been shown that maximal magnetisation for Ne⁺ ions with energy 25 keV occurs for a fluence of $7.5 \times 10^{13} \text{ cm}^{-2}$ ^[18] so this is the recommended value for work where room temperature ferromagnetic FeRh is required. The magnetisation curves for FeRh irradiated by a range of fluences are shown in Figure 3.10 where the high magnetisation values correlate with ferromagnetic ordering while the paramagnetic ordering exhibits much lower magnetisation due to the low paramagnetic susceptibility. A sufficiently thick resist, patterned with standard lithographic techniques, can be used alongside this ion irradiation process for precise creation of FM regions in a nominally AF crystal.

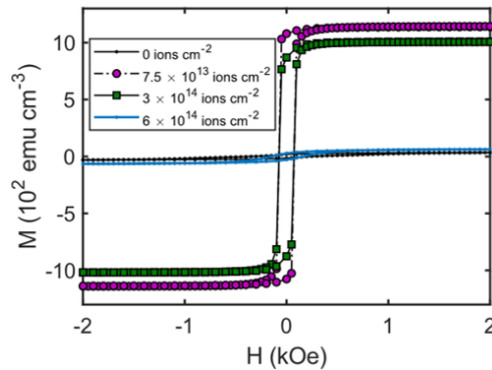


Figure 3.10: The metamagnetic curves for ion irradiated FeRh at a range of fluences. The maximum magnetisation occurs for a fluence of $7.5 \times 10^{13} \text{ cm}^{-2}$. Figure reproduced from Griggs et al^[18].

This work involves electrical resistivity measurements of ion irradiated FeRh and so the effect of the

bombardment on resistivity should be acknowledged. The ions themselves should not become implanted in a thin film because they have sufficient energy that they should pass through the film and enter the substrate^[96]. However, the defects may still have an effect. Significant resistivity increases of as much as $> 100\%$ have been observed in thin gold films irradiated by high fluences^[96]. Such significant changes should not occur in the irradiated FeRh films though, for multiple reasons which will now be explained. Firstly, the gold film was very thin at just 7 nm and so the relative current density through each defect was much larger than it will be through FeRh films of at least 40 nm. Secondly, the high fluences resulted in monovacancies with the displaced atoms forming debris on the surface^[96]. This provided many scattering opportunities to the conducting electrons that will not be present for a film which is merely disordered by small displacements. Finally, the baseline resistivity of FeRh is greater than of gold, so the same absolute resistivity change would produce a smaller relative change. Consequently, it is reasonable to assume that the irradiation process will not significantly increase the resistivity of the irradiated film.

3.5 FeRh oxide layer

Iron readily forms oxides in ambient conditions and these have also been observed for multiple thicknesses of FeRh films using X-ray reflectivity (XRR)^[18;97] and Rutherford backscattering spectrometry (RBS)^[98]. The oxide layer is not problematic in applications where a direct surface contact is not necessary or when the film is used as part of a stack deposited without exposure to ambient conditions, but an oxide layer will potentially disrupt any nanoscale measurements requiring electrical contact. This was not necessarily expected to be an issue for nanoscale measurements because preliminary macroscale measurements by multimeters and four-point probes used relatively large probes applied with relatively large forces and so easily penetrated the oxide; effects that are not important for macroscale measurements can become very significant on the nanoscale. A capping layer such as platinum may be used to minimise oxide formation^[99], however this would have the side effect of suppressing surface electrical or mechanical behaviours and so the sample investigated in this work will not be capped.

The exact composition of the oxide layer which forms is unknown, with Fe_3O_4 ^[97], $\alpha\text{-Fe}_2\text{O}_3$ ^[100], and FeRhO_3 ^[98] each being proposed in the literature. The uncertainty arises because XRR is only sensitive to the density of the crystal atoms whilst RBS is only sensitive to elemental content so can merely show that an oxide is present.

The oxide $\alpha\text{-Fe}_2\text{O}_3$ is also known as haemetite or iron(III) oxide and is an A-type antiferromagnet with spin canting via DMI so exhibits very weak ferromagnetic properties^[101]. It is a very poor conductor with reference resistivity $10^4 \Omega \text{ m}$ at 20°C ^[102]. The alternate iron oxide Fe_3O_4 is also known as magnetite or iron(II,III) oxide^[103] and is a strongly ferrimagnetic crystal. It possesses an unusually low resistivity for oxide

layers with an ambient value of $3.2 \times 10^{-5} \Omega \text{m}$ ^[103;104]. The final candidate of FeRhO_3 has not been well characterised in the literature so very few properties are known, however it does exhibit a strong ferromagnetic response with moment $7.7\mu_B$ ^[105]. The existence of accurate magnetic characterisation of the underlying FeRh film^[87;106;57] therefore suggests that this is not the oxide which naturally forms on FeRh films.

The typical oxide layer thickness when forming naturally on an exposed FeRh surface is between 1 nm and 2.5 nm^[18;97]. This oxide does not grow rapidly thus contact measurements may be made in ambient conditions provided the FeRh surface has not been exposed to air for any significant length of time prior to characterisation. Another issue to be aware of is that when performing electrical resistivity measurements in atmospheric conditions, or even clean room conditions, water will condense on the sample surface and the droplets will especially coalesce at any tip-sample contact^[107]. This does not usually present an issue, but on a readily oxidising film such as this the presence of water can accelerate the oxide formation.

3.6 Phase diagram of PMN-PT

The sample being investigated for its piezoelectric properties, as a potential substrate for artificial multiferroics, is formed from the solid solution of lead magnesium niobate and lead titanate with formula $\text{Pb} \left(\text{Mg}_{1/3} \text{Nb}_{2/3} \right)_{1-x} \text{Ti}_x \text{O}_3$, more commonly known by the initials PMN-PT^[28]. This crystal exhibits a stronger piezoelectric response than PZT, the current gold standard piezoelectric ceramic, so is of great interest for multiferroic applications^[22].

It has a perovskite structure ABX_3 where the primitive lattice (A sites) are occupied by Pb atoms with O atoms in the centre of each face (X sites). The centroid atom of each primitive cell (the B site) is either Mg, Nb, or Ti, which are distributed randomly in the respective ratios $(1 - x) : 2(1 - x) : 3x$, where x is the fractional content of PT in the PMN-PT solid solution.

PMN-PT is created by doping lead magnesium niobate (PMN) with lead titanate (PT) to specific concentrations x . Figure 3.11 shows the phase diagram for PMN-PT which was created using boundaries determined by Zekria et al^[28].

The diagonal lines dividing the phase diagram roughly in half describe the Curie temperature T_C , above which is the cubic structure $Pm\bar{3}m$ which is a paraelectric. The bottom left region of the phase diagram is labelled R and is the pseudocubic rhombohedral structure $R\bar{3}m$; in PMN-PT this region of the phase diagram acts as a relaxor. The regions denoted T are tetragonal $P4mm$ and the region at the right acts as a normal ferroelectric. The region in the middle is a hybrid of normal and relaxor ferroelectrics and was identified due to exhibiting some lattice change at its boundaries, but the structure is not certain

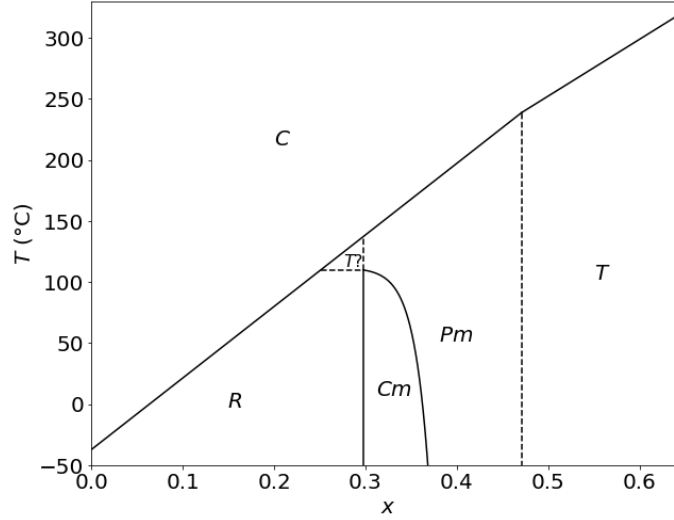


Figure 3.11: The PMN-PT phase diagram using boundaries calculated by Zekria et al^[28].

to be tetragonal.

The most interesting region is the morphotropic phase boundary between the PMN and PT properties, formed by the monoclinic regions Cm and Pm , where there is some overlap of behaviour. The region Pm was initially thought to be tetragonal and indeed is marked such on some older phase diagrams, but a transition is observed in the critical temperature line at $x = 0.45$ ^[28] and it was concluded that this region is an area of lower symmetry than tetragonal. It is very similar, however, because the lattice angle β tends towards 90° as x rises^[8] and thus the boundary is difficult to precisely identify, hence the dashed line in Figure 3.11. This agrees with the discussion in Section 2.13.2.1 regarding the rotation of the observed strain direction with rising PT concentration. Determining an accurate phase boundary is further complicated by a significant coexistence region where the two phases Pm and T overlap^[108].

The phase diagram of PMN-PT is contentious, with multiple slightly differing suggestions in the literature and some authors^[108;109] including an intermediary orthorhombic phase at some or all of the structural transitions discussed. The work in this thesis involves a PMN-PT substrate with a nominal PT concentration of $x = (0.29 \pm 0.01)$, so the only threshold of relevance is the R to Cm boundary. The argument follows that the eighth-order expansion of Landau-Devonshire theory prohibits a direct transition from rhombohedral to monoclinic lattice structures, and so an orthorhombic region must act as an intermediary and lies at approximately $0.30 < x < 0.31$ ^[108]. However, not all authors propose this intermediate phase^[28;109] and indeed only two lattices were observed for these substrates which are believed to be R and Cm ^[7]. Consequently the orthorhombic structure will be neglected in this work.

3.6.1 The rhombohedral boundary

The Curie temperature threshold is not the same value when crossing in each direction but is instead a hysteretic threshold^[28]. The hysteresis width of the Curie temperature differs significantly for compositions either side of the $R\text{-}Cm$ phase boundary and so may be used to determine its location. Zekria et al.^[28] state this to be at approximately $x \approx 0.295$ in their paper which was used to obtain the phase diagram shown in Figure 3.11. In an attempt to obtain a more precise value a sigmoid was fit to the thermal hysteresis width data provided and the values and fit are shown in Figure 3.12. The fit was unbounded and performed using non-linear least squares fitting via the Levenberg-Marquardt algorithm as implemented in the SciPy Python package^[110]. The calculated midpoint was $x = (0.298 \pm 0.001)$, which agrees with the approximate value stated.

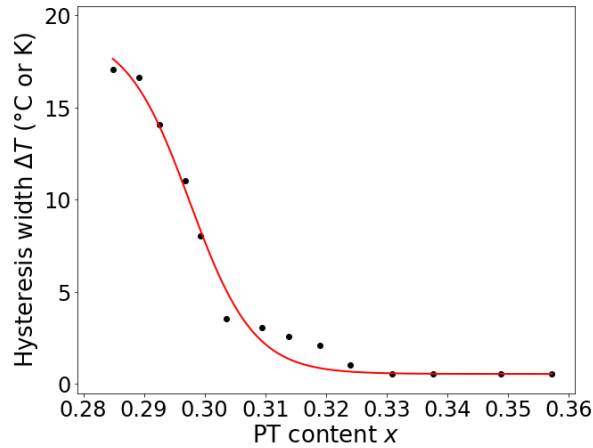


Figure 3.12: The thermal hysteresis of the Curie temperature of PMN-PT for a range of PT concentrations x . The data is taken from work by Zekria et al^[28] and the red line is the added sigmoid fit which has a midpoint of $x = (0.298 \pm 0.001)$.

3.7 Piezoelectric behaviour of PMN-PT

It was stated in Section 2.3.1 that a pseudocubic structure is one in which all lattice angles are approximately 90° and so the $R3m$ perovskite approximates the $m\bar{3}m$ point group. This lattice has inversion symmetry even though the true space group is not centrosymmetric, and so pseudocubic PMN has approximate inversion symmetry and any longitudinal piezoelectric behaviour will be suppressed.

On average the crystal atoms all occupy their intended sites^[111], however on a local basis the Pb, Nb, and Mg atoms are displaced by approximate root-mean-square displacements of 0.3 \AA , 0.19 \AA , and 0.11 \AA respectively^[111]. Mg displaces isotropically whilst Pb and Nb displace in an often correlated $\langle 111 \rangle$ direction. This is a result of the Pb and Nb atoms seeking to form stronger bonds with the crystal oxygen atoms via orbital hybridisation^[111] and is the origin of the polarisation which induces the strain

responsible for deforming the crystal from $Pm\bar{3}m$. This displacement of ions in a direction away from $[001]$ also provides the rotated dipoles responsible for shear piezoelectricity which shall be discussed in Section 3.7.1.

The piezoelectric response of rhombohedral PMN-PT is much larger than seen in other conventional or relaxor ferroelectrics such as PT or PZT. This is a consequence of the Pb, Ti, Nb, and O atoms displacing significantly in response to external stimuli in a similar manner to the zero-field displacements that were described for PMN^[22]. The response of these atoms is two to three times the magnitude seen for PT, while the Mg atoms have negligible displacements^[22].

3.7.1 Effect of PT ratio

The dependence of the OFF-field piezoelectric coefficient d_{33} on PT concentration x was investigated by Li et al.^[8] and the results from this investigation include the data shown in Figure 3.13. The figure shows that the response has a maximum at the R - Cm boundary with a smaller local maximum at the Cm - Pm boundary and only small values observed for Pm . It is reasonable to assume that a local maximum correlates to a crystal transformation thus the R - Cm boundary is expected to occur at the peak of the d_{33} against x curve. A scaled Lorentzian curve was fitted to this data using the same SciPy algorithm as used in Section 3.6.1 and determined the peak to be located at $x = (0.298 \pm 0.001)$. This is in agreement with the value obtained from the thermal hysteresis fit in Figure 3.12 and so for the purposes of this thesis the boundary will be taken to be located at $x = 0.298$.

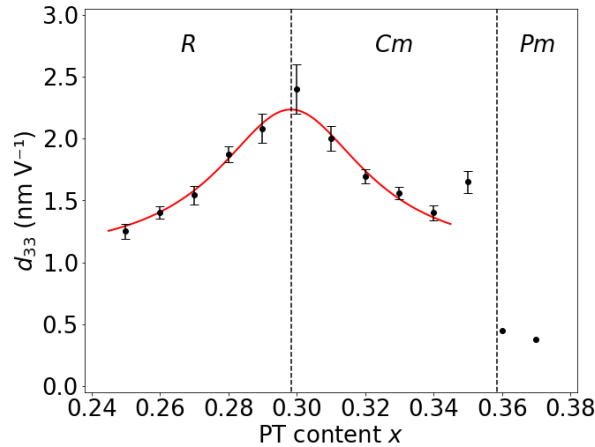


Figure 3.13: The piezoelectric coefficient of PMN-PT for a range of PT concentrations x . The data is taken from work by Li et al.^[8] and the red line is a scaled Lorentzian curve fit to the data with peak of $(2.24 \pm 0.09) \text{ nm V}^{-1}$ at $x = (0.298 \pm 0.001)$ and a vertical offset of $(1.02 \pm 0.12) \text{ nm V}^{-1}$.

There are two components to the piezoelectric response. The first is longitudinal piezoelectricity, which is the standard mechanism where the dipoles expand in the presence of a parallel electric field and

contract in the presence of an antiparallel field^[112]. This is the only mechanism present for tetragonal perovskites and thus also for the approximately tetragonal Pm structure.

The second mechanism is shear piezoelectricity, which is strain induced in the lattice by the applied field rotating the dipoles away from their spontaneous polarisation directions^[112] of $R3m$ to temporarily form the taller structure of Cm . The term shear is somewhat misleading because it does still produce a piezoelectric effect in the direction of the applied field, however it is a result of a shear transformation or rotation of the perovskite unit cell rather than the simple elongation of the longitudinal piezoelectric effect. The Gibbs energies of the two crystal phases are equal at the phase boundary^[112] which reduces the energy cost of reorienting the lattice and serves to enable the rhombohedral to monoclinic phase change to occur.

The free energy \mathcal{F} of the system may be written as^[112]

$$\mathcal{F} = \mathcal{F}_0 - \vec{P} \cdot \vec{E} \quad (3.1)$$

where \mathcal{F}_0 is the internal energy in zero external field, thus it can be seen that the system will seek to align \vec{P} to \vec{E} where possible. The rhombohedral crystal polarisation is in the $\langle 111 \rangle$ direction, so

$$\vec{P} \cdot \vec{E} \propto \begin{pmatrix} 1 \\ 1 \\ 1 \end{pmatrix} \cdot \begin{pmatrix} 0 \\ 0 \\ 1 \end{pmatrix} = \sqrt{3} \cos(\theta) \quad (3.2)$$

giving the polarisation angle relative to the field to be

$$\theta = \arccos\left(\frac{1}{\sqrt{3}}\right) \approx 54.7^\circ. \quad (3.3)$$

Meanwhile, the Cm polarisation is in the $[hhl]$ direction for $l > h > 0$, thus

$$\vec{P} \cdot \vec{E} \propto \begin{pmatrix} h \\ h \\ l \end{pmatrix} \cdot \begin{pmatrix} 0 \\ 0 \\ 1 \end{pmatrix} = \sqrt{2h^2 + l^2} \cos(\theta) \quad (3.4)$$

giving the polarisation angle relative to the field to be

$$\theta = \arccos\left(\frac{l}{\sqrt{2h^2 + l^2}}\right) \equiv \arccos\left(\frac{1}{\sqrt{2\left(\frac{h}{l}\right)^2 + 1}}\right) < \arccos\left(\frac{1}{\sqrt{3}}\right), \quad (3.5)$$

where the function is expressed in terms of some parameter $0 < h/l < 1$ giving $0^\circ < \theta < 54.7^\circ$. Lead titanate is naturally tetragonal^[28], thus higher x solid solutions will have a lower h/l ratio and consequently lower θ .

These results explain the peak at the R - Cm boundary in Figure 3.13: the free energy F seeks to align the polarisation to the field, which can be achieved by temporarily rotating some of the lattice cells

from $R3m$ to Cm . The reduced strain angle results in an increase in the cell height which induces a significant shear piezoelectric effect. The large peak size indicates a low ratio of h/l for Cm .

The second peak is due to the same mechanism. The Pm space group has a polarisation direction $[h0l]$ where $l > h > 0$, so

$$\vec{P} \cdot \vec{E} \propto \begin{pmatrix} h \\ 0 \\ l \end{pmatrix} \cdot \begin{pmatrix} 0 \\ 0 \\ 1 \end{pmatrix} = \sqrt{h^2 + l^2} \cos(\theta) \quad (3.6)$$

giving the polarisation angle relative to the field to be

$$\theta = \arccos\left(\frac{l}{\sqrt{h^2 + l^2}}\right) \equiv \arccos\left(\frac{1}{\sqrt{\left(\frac{h}{l}\right)^2 + 1}}\right), \quad (3.7)$$

where the latter is again in terms of some parameter $0 < h/l < 1$ giving $0^\circ < \theta < 45^\circ$. The relatively small size of the peak suggests there is less difference between Pm and Cm cell heights than between $R3m$ and Cm cell heights, which supports the conclusion that h/l is already low for Cm .

These peaks in the piezoelectric coefficient provide an uncommonly high piezoelectric response and as a result PMN-PT substrates with $x \approx 0.29$ are of greatest interest. The actual boundary of $x \approx 0.30$ would provide maximal macroscopic piezoelectric response but would also result in an equal split between $R3m$ and Cm cells on the nanoscale due to inhomogeneous stoichiometry. The slightly lower PT concentration of $x \approx 0.29$ provides a much more consistent nanoscale structure.

3.7.2 Ferroelectric coercive field dependence

The previous section showed how the polarisation angle from the z -direction decreases with rising PT concentration. This means the angle through which the electric dipole must rotate for polarisation reversal to occur rises with PT concentration and thus the coercive field would also be expected to rise. This is indeed observed and Skulski et al. recorded the coercive field for a range of values of PT concentration x ^[9]; this data is shown in Figure 3.14.

An empirical logarithmic fit was applied to the data with the form

$$E_c = A \log(x + B) + C \quad (3.8)$$

and the values were $A = (6.4 \pm 1.0) \text{ kV cm}^{-1}$, $B = (0.01 \pm 0.03)$, and $C = (16.2 \pm 0.6) \text{ kV cm}^{-1}$. The data point at $x = 0$ clearly did not match the trend so was excluded from the fit. Recall from Section 2.13.1 that the coercive field is strongly dependent on the crystal thickness so this fit must be scaled to be applicable to the sample under investigation. Skulski et al. used pelletised powdered PMN-PT so no crystal thickness was available, but it is known that the $\text{PMN}_{0.71}\text{PT}_{0.29}$ substrates under investigation in this work have a thickness of $250 \mu\text{m}$ and coercive field of approximately 2 kV cm^{-1} ^[7]. Using equation

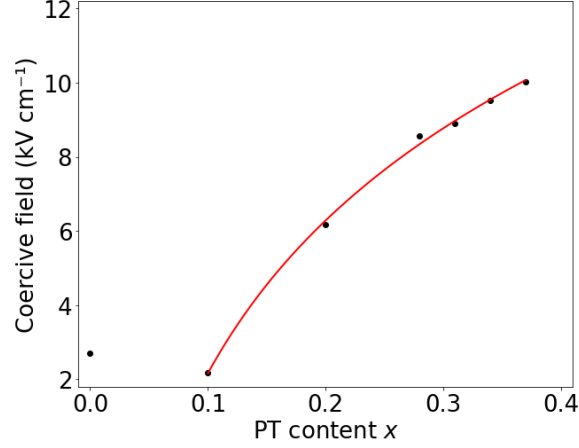


Figure 3.14: The coercive field of PMN-PT for a range of PT concentrations x . The data is taken from work by Skulski et al.^[9] and the red line is an empirical logarithmic curve fit to the data.

(2.128) and these values, the effective PMN-PT thickness used to generate Figure 3.14 is found to be approximately $28 \mu\text{m}$. Therefore the logarithmic fit obtained here may be scaled to describe any crystal of known thickness z_0 by multiplying A and C by the thickness correction factor

$$\left(\frac{z_0}{28 \mu\text{m}} \right)^{-2/3} \quad (3.9)$$

which is a consequence of equation (2.128).

3.8 PMN-PT observations

3.8.1 Effect of polishing PMN-PT

Prior to being polished a typical PMN-PT substrate has a rough striated surface and an example of this is shown in Figure 3.15a. The striations are due to the manufacturing process and result in a surface roughness of $\sim 3 - 4 \text{ nm}$ with no clear features of note. The substrates must be polished before use and this results in an interesting phenomenon.

Regardless of the polishing method, whether done in-house or commercially, the surface of PMN-PT forms two very clear terraces $\sim 3 - 4 \text{ nm}$ apart in height. An example of this is shown in Figure 3.15b. The terraces each occupy roughly half the surface and have a roughness of $\sim 0.5 - 1 \text{ nm}$, and are attributed to the ferroelectric domains at the time of polished^[113]. The up and down polarised domains have different reduction rates for both mechanical and acid based polishing so the surface forms a physical snapshot of the domain structure at the time of polishing^[113].

It is possible that these terraces are correlated to nanoscale PT distribution in some way, because a different structure can be readily expected to etch at a different rate. This is one of the motivations for

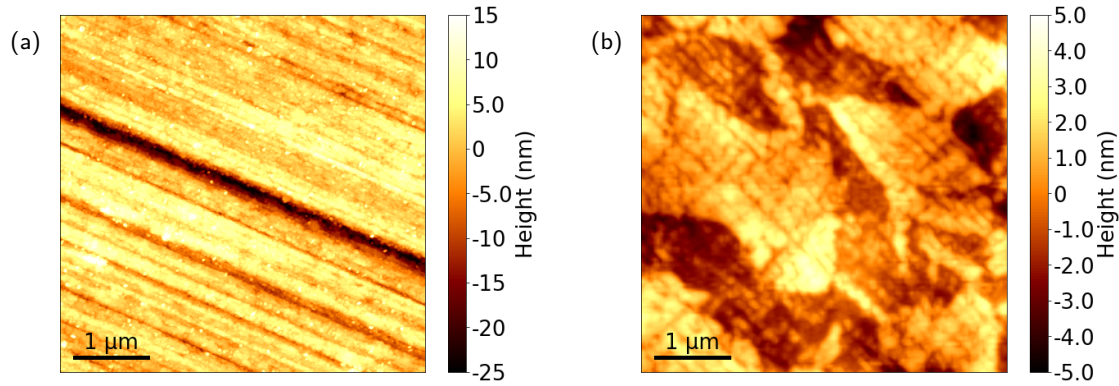


Figure 3.15: AFM images of the terraces formed by polishing PMN-PT crystal surfaces. (a) A typical surface prior to polishing showing striations. (b) A typical surface following polishing, demonstrating the two terraces.

the nanoscale characterisation of PMN-PT: to attempt to determine the rhombohedral and monoclinic regions and thus identify and explain any topographic correlation.

3.8.2 Weakness under strain

The PMN-PT substrates exhibit a proclivity for shattering when applying heat and external electric fields. This occurred during routine measurements and even during a field-cooling cycle with a very low ramp rate, chosen in an attempt to avoid shattering the crystal. The exact cause is unknown but cannot be easily investigated due to the substrates being too valuable to deliberately break. The hypothesis is that the thermal and piezoelectric expansion of the substrate is the cause, with the crystal either being constrained by the field electrodes or overloading internal crystal boundaries.

The thermal expansion coefficient of $\text{PMN}_{0.70}\text{PT}_{0.30}$ is $\sim 10^{-5} \text{ K}^{-1}$ [114] resulting in a strain of 0.1% arising from a change in temperature of 100 K, whilst the maximum piezoelectric coefficient in Figure 3.13 also yields a strain of 0.1% at the maximum applied field. This strain is too low for the electrode constriction to be problematic but these strains are certainly sufficient for crystal boundaries to fracture in response to unaligned expansions on either side.

3.9 Summary

The work presented in this thesis involves the analysis of equiatomic FeRh films and PMN-PT substrates as two components of an artificial multiferroic system. The properties of the materials therefore needed to be explained and this chapter aimed to provide a detailed introduction. The thermal phase diagrams for each material were discussed and the properties of interest introduced.

Chapter 4

Fundamental principles of atomic force microscopy

This chapter introduces atomic force microscopy and provides the groundwork for the advanced AFM techniques which are developed and used in this work. A detailed introduction to the fundamental principles of the atomic force microscope is provided, including a discussion of the scanning mechanism and the geometry and calibration of AFM probes. The multiple modes of operation used in this work are quantitatively explored in detail and the sample preparation process and thermal measurement stage are described.

4.1 Introduction to atomic force microscopy

The atomic force microscope (AFM) is a useful technique with a myriad of applications in nanoscale characterisation^[2;3;115;116]. It is commonly used simply as an efficient topography characterisation tool to verify deposition and lithography of structures prior to further analysis, but is a powerful instrument in its own right. In this work a Bruker Dimension Icon system was used, alongside a Bruker NanoScope V controller and Bruker NanoScope V9.4 control software. The system and its enclosure is shown in Figure 4.1.

The basic operation of an AFM is shown in Figure 4.2. A diode laser, typically red with a wavelength of 630 nm, is reflected off the back of the cantilever onto a quadrant photodetector^[117] (front view inset), whose position is calibrated such that the laser hits the centre for an undeflected probe. The probe is deflected by topographic features or other forces, even as small as femtonewtons^[1], and the deflection is measured using the photodetector. The difference in photodetector voltage between the top and bottom halves gives the vertical deflection whilst the horizontal difference gives the torsional rotation of the cantilever^[118]. The optical lever effect means that sub-nanometre deflection of the cantilever may be accurately detected using this arrangement.

The AFM probe consists of a sharp pyramidal tip attached to a long thin cantilever^[118], with the other

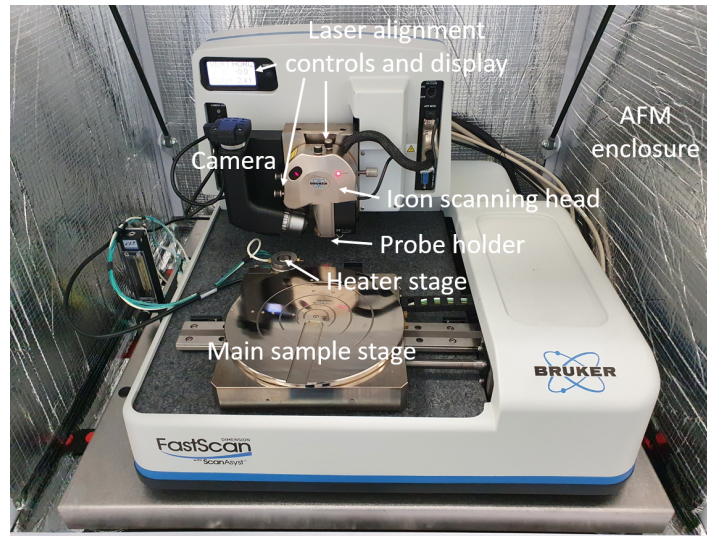


Figure 4.1: The Bruker Dimension Icon AFM used in this work with components labelled. The Dimension platform is shared by The FastScan and Icon scanning heads so the front of a Dimension AFM may feature either FastScan or Icon branding. This is just cosmetic and there is no functional difference.

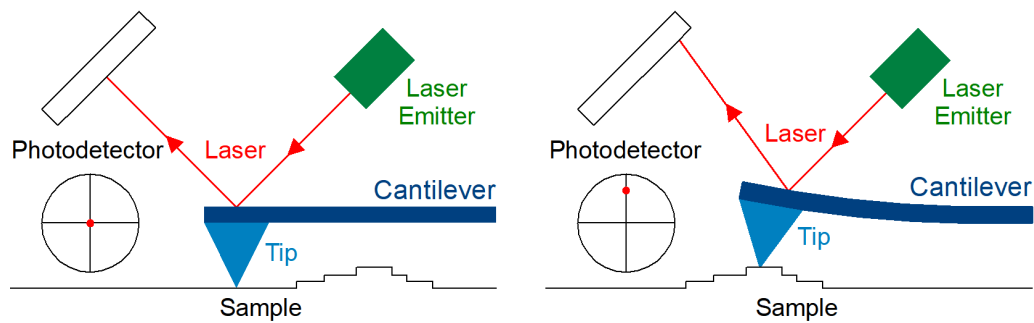


Figure 4.2: The basic operation of an AFM measuring the topography of a sample surface.

end attached to a small wafer called the probe substrate. The tip-apex is approximately spherical. AFM users generally use the terms 'probe' and 'tip' interchangeably, but for clarity this thesis shall use tip to mean the pyramidal region and probe to mean the tip and cantilever combination. AFM probes are usually manufactured from antimony doped silicon^[119], this n-type doping does not allow them to carry currents but does minimise electrostatic charge build-up at the tip which would cause artefacts in biased measurements. Some probes instead use silicon nitride in order to achieve lower spring constants without requiring impossibly narrow cantilevers^[118;119]. Prior to imaging the probe is mounted in a probe holder containing one or more piezoelectric crystals^[118] and these crystals are used to drive the probe accurately and precisely.

A thin reflective coating is often applied to the rear of the cantilever during manufacture to ensure specular reflection of the laser and thus maximum intensity at the photodetector. Functional coatings may

also be applied to the lower side of the cantilever, such as conductive layers for electrical measurements or ferromagnetic coatings for magnetic applications^[119]. The thickness of the coating is a lower bound to the tip radius, as may be seen by considering a locus of a fixed distance around the silicon tip, shown in Figure 4.3. This underlying tip typically has a near infinitesimally sharp point so the tip radius equals the coating thickness^[119]. Care must be taken when using coated probes for heated measurements, however, because mismatches in thermal expansion coefficients could induce strain which would result in artificial cantilever deflection.

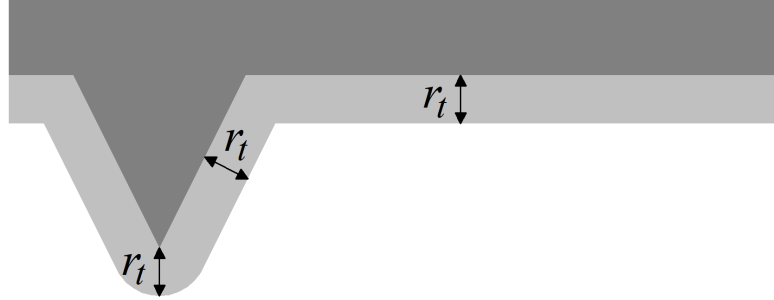


Figure 4.3: Schematic of a silicon probe (dark grey) with a thin functional coating (light grey). The thickness normal to the surface is the tip radius r_t in cases where the underlying silicon tip is infinitesimally sharp.

The scanner head is positioned above the sample using precise stepper motor control. The scanning process itself is beyond the precision of these motors so instead multiple piezoelectric actuators (piezos) are used. These are arranged inside the scanner head in a tube^[118], as shown in Figure 4.4. The opposing pairs of x and y piezos are used to raster the probe across the sample in a zig-zag pattern and each have a range of $\pm 45 \mu\text{m}$, whilst the z crystal is used to raise and lower the probe through a range of $6 \mu\text{m}$ ^[118]. The rastering occurs by oscillating the tube in the manner of a pendulum meaning the resulting measurement is bowed and must be corrected by the software^[118]. This correction is done as the first step in the data processing pipeline, which allows users to observe meaningful data during acquisition.

The first scan of the probe (the 'zig') is the trace line and the return scan (the 'zag') is the retrace line^[118]; this is shown in Figure 4.5a. A relatively low density of scan lines, as shown in the figure, will result in significantly skewed measurements, whilst a typical scan will have negligible skew. Figure 4.5b shows the relationship between number of scan lines and the resulting skew angles. Typically the data is captured using just one of the raster directions, but both can be used simultaneously to double the number of lines in the resulting AFM image. However, this doubling is not typically used because small line separations would result in double-measuring each line, while large line separations could result in image distortion resulting from the opposing skew angles between the trace and retrace measurements.

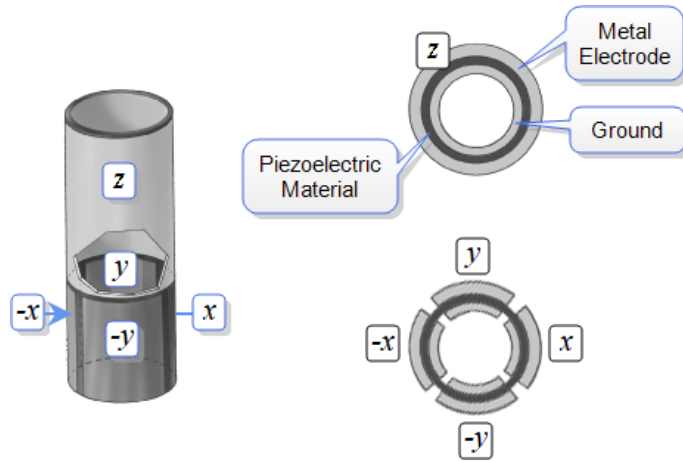


Figure 4.4: The geometry of the piezoelectric actuators within the Dimension Icon scanner head. Figure adapted from the *Piezoelectric Scanners* page of the NanoScope internal user guide.

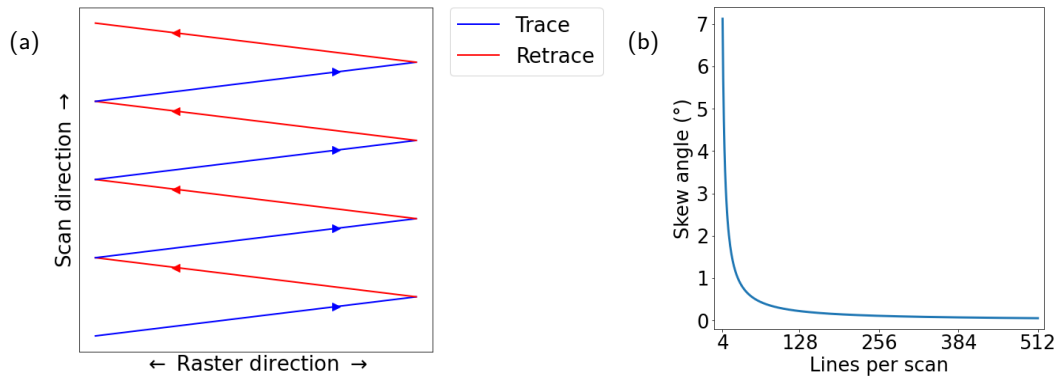


Figure 4.5: The skewed trace and retrace paths of the probe during typical AFM scans using the Dimension Icon scanner head. (a) The path drawn by the piezoelectric actuators during a standard AFM scan, the blue lines are the trace lines and the red lines are the retrace lines. (b) The skew angle of the actual trace and retrace rasters from the raster direction, depending on the requested number of lines per scan. This assumes a square scan area.

4.1.1 Tip geometry

The tip geometry is relevant for many AFM measurements and there are several distances that need to be defined. Figure 4.6 shows a diagram of the tip with key distances indicated.

The tip is formed from a skewed pyramid which is defined by its height and slope angles. The different angles are the front-angle α_f , side-angle α_s , and back-angle α_b , with the front being the edge furthest from the probe substrate. These are typically related as $\alpha_f \lesssim \alpha_s \lesssim \alpha_b$. The probe holder mounts the cantilever at an angle of $\sim 10^\circ$, meaning the back edge of the tip is near vertical and the front angle is shallower than one would expect^[118], and this is demonstrated in Figure 4.6a. One simplification that

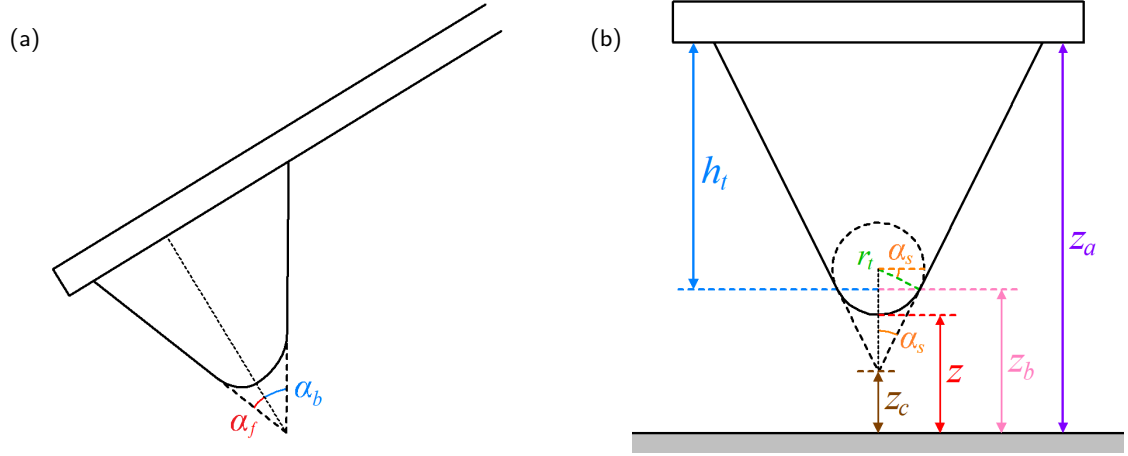


Figure 4.6: Schematic illustration of the tip geometry of an AFM probe. (a) The side of the probe showing the front-angle α_f and back-angle α_b , depicted at an angle to reflect the tilted mounting position. (b) The end of the probe above a sample surface showing the significant distances and the side-angle α_s .

may be made is to approximate the tip as a truncated cone with angle $\alpha = \alpha_s$ with the end rounded off by an approximately spherical cap of radius r_t , and this simplification is shown in Figure 4.6b. The radius of the truncated end of the cone is $r_t \cos(\alpha)$, which may be trivially derived by realising the slope of the cone forms a tangent to the cap meaning the two angles marked α are equivalent. The tip height h_t is usually used to refer to the full distance from the base of the cone to the furthest point of the spherical cap, but equations are simplified if the height of the truncated cone is taken instead. A typical tip height is of order $h_t \gtrsim 1 \mu\text{m}$ while the tip radius $r_t \lesssim 35 \text{ nm}$ and slope angle $\alpha \sim 20^\circ$, so this correction is minor in practice.

The height z is the distance between the lowest point of the tip and the sample surface and is the usual measure of tip-sample separation. The height z_b is the distance between the surface and truncated end of the cone, and may be derived to be

$$z_b = z + r_t - r_t \sin(\alpha) = z + r_t [1 - \sin(\alpha)] . \quad (4.1)$$

The distance z_a from the top of the cone to the surface is the sum of cone height and z_b , thus

$$z_a = z + h_t + r_t [1 - \sin(\alpha)] . \quad (4.2)$$

The height z_c is the distance between the surface and the location of the point of the cone were it not truncated, and is derived to be

$$z_c = z + r_t [1 - \sin(\alpha)] [1 - \cot(\alpha)] . \quad (4.3)$$

In electric field based experiments the distance of interest is from the tip to the second electrode so

these definitions become tip-electrode distances. If thick insulating materials such as substrates are the sample of interest then the definitions become tip-stage distances and due to the thickness of such a sample the approximations

$$z_b \approx z \quad (4.4)$$

and

$$z_a \approx z + h_t \quad (4.5)$$

may be used.

The AFM measures the distance z from some arbitrary baseline so the absolute values obtained do not describe any of the parameters in Figure 4.6. Instead it is the difference in measured height value between points on the sample surface that is of interest. The notation z' will be used for the raw height values recorded by the system.

The finite size of the AFM tip enforces a lower limit on the size of features that may be resolved^[118], as shown in Figure 4.7. This shows how if any region of the tip other than the apex makes contact with a feature then the cantilever will still be deflected, but the result is a measurement artefact representing the path the tip was forced to traverse rather than the true dimensions of the feature. Sharper probes mitigate this problem, but these are more difficult to manufacture and wear much faster, hence there is a compromise to be made when choosing a probe^[118].

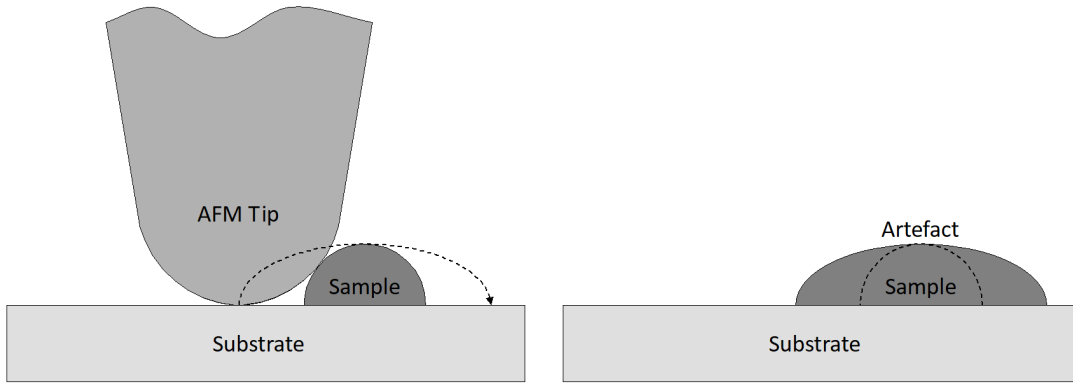


Figure 4.7: The measured artefact resulting from the path the finite tip was forced to traverse when passing over a small feature.

The default scan angle of 0° means the trace line is captured by the cantilever moving forwards and the retrace line is moving backwards. This coupled with the tip mounting angle shown in Figure 4.6a means that the trace line will show descending features more accurately whilst the retrace line will show ascending features more accurately. A scan angle of 90° means both the trace and retrace are captured with equal tip angles α_s and both ascending and descending features are equally affected on both passes.

4.1.2 Probe calibration

The AFM is only able to measure the deflection of a cantilever via the photodetector signal, which is arbitrarily scaled and measured in volts^[118]. In order to know the actual deflection or forces applied to the cantilever two conversion parameters must be calibrated. The first of these is the cantilever deflection sensitivity γ , which has units of nm V^{-1} and is the term which relates the photodetector output to the true cantilever deflection. The exact value depends on many factors, including the exact position of the laser spot on the rear of the cantilever, so must be calibrated every time a probe is loaded for accurate results^[118].

The deflection sensitivity of a probe may be calibrated by recording a deflection against height curve on a hard surface, typically a sapphire reference sample^[118]. This relates the piezo height to measured deflection and the gradient of the curve is then $1/\gamma$. The forces used are typically in the nN regime so a full nanomechanical treatment is not required when a hard sample is used.

The second parameter is the spring constant k of the cantilever, which simply relates the deflection to the corresponding force and remains constant for each individual probe^[120]. Typically this is given in units of N m^{-1} , but due to the vast majority of AFM forces being nN and deflections being nm this thesis will use the equivalent units nN nm^{-1} . This is considered to be more intuitive, especially in conjunction with the deflection sensitivity units of nm V^{-1} .

The spring constant is then determined in one of two ways. The first is a thermal tune technique, where the cantilever is allowed to oscillate freely and the elastic potential energy is related to the thermal energy via the equipartition theorem to yield^[120]

$$k \propto \frac{k_B \mathcal{T}}{\langle z_c^2 \rangle} \quad (4.6)$$

where $k_B = 1.380649 \times 10^{-23} \text{ J K}^{-1}$ is the Boltzmann constant^[36], \mathcal{T} is the surrounding temperature, and $\langle z_c^2 \rangle$ is the mean square cantilever displacement. The proportionality constant is a correction factor used to account for the differences between the idealised model and reality; the idealised model would have a constant of unity and equation (4.6) would become an equality. The correction factor for rectangular cantilevers is 0.817 but it is much more complex to determine for V-shaped cantilevers^[120]. This calibration technique is most suitable for cantilevers with low spring constant because this improves the signal-to-noise ratio of the measurement. However, the main source of error in this technique is that the calibration calculation requires the deflection sensitivity to be known, and consequently Ohler^[120] derived a typical total uncertainty in this technique of $\sim 8\%$. The other approach is known as the Sader method^[121], and allows direct calculation of the spring constant using cantilever dimensions, the resonance frequency, and the quality factor Q ; the latter two may be obtained accurately by fitting a Lorentzian curve to the ‘power spectral density’ (PSD) curve of the thermal oscillations. This is only

applicable to rectangular cantilevers but Ohler derived an uncertainty of 4% for this method, half that of the direct thermal method^[120].

The setpoint is a user-defined deflection value which the AFM controller will attempt to maintain via a feedback loop and allows control over the force exerted by the probe on the sample surface^[118]. The calibrated spring constant and deflection sensitivity allow the defined setpoint to be given in units of V, nm, or nN, the choice of which simply depends on which is most intuitive in context. The choice of probe allows these factors to be tailored to the application. The photodetector has a photovoltage measurement range of $\pm 12.3\text{ V}$ ^[118] with finite precision, so k and γ should be chosen such that the desired setpoint is comfortably within this range.

Low force setpoints will require small values of k and γ while higher forces will require larger values of these parameters. Typically, rectangular cantilevers are used for $k > 1\text{ nN nm}^{-1}$ and V-shaped cantilevers are used for $k < 1\text{ nN nm}^{-1}$ ^[120]. Setpoints between 1 V and 10 V have been found to be optimal for precise force control because they are large enough that the relative error in force is negligible whilst avoiding the end of the measurement range so that any larger forces which occur may be measured and controlled.

4.1.3 Lock-in amplifiers

Lock-in amplifiers (LIAs) are critical components of any AFM based measurement, however they are poorly understood and frequently considered as black boxes. They actually provide a rather elegant solution to screening out any components of an AC signal which are undesired, and may be used whenever a sinusoidal signal is to be applied to the sample with a sinusoidal response being measured^[122]. This initial signal is split into two identical branches: one connected to the experimental equipment and the other to the LIA. The measured response signal is then also fed to the LIA, where both signals are combined and the amplitude and phase of the measured signal may be reported.

Any AFM modes that do not use constant contact, such as TappingMode, PeakForce Tapping, and their derivatives, will involve an AC signal being directed to the tip drive actuator to oscillate the tip. In this case the measured tip response from the photodetector is the response signal, and in common with many other instruments the AFM uses an LIA to accurately extract the intended measurement from this, with a very low signal-to-noise ratio compared with direct measurement techniques^[122]. The Bruker NanoScope Controller V features three LIAs, two of which are high frequency devices with a frequency range of 1 kHz to 5 MHz while the third is a lower frequency device with a range of 5 Hz to 50 kHz^[123].

The LIA reports an output value of^[122]

$$X = A \cos(\theta) \quad (4.7)$$

where A is the amplitude of the response signal and θ is its phase. The value X is known as the in-phase component of the measured signal because it reports the oscillations in phase with the generated signal. In basic LIAs this may be the sole output, in which case a phase shift is applied to the reference signal before it enters the signal multiplier^[122] and is manually adjusted until X is maximal, meaning the applied phase shift matches the phase difference θ between the signals.

In more advanced systems, such as those in an AFM, a two-phase LIA is used^[123;122]. In this case two lock-in circuits are present: one receives the reference signal directly and the second receives the reference phase shifted by $\pi/2$ ^[122]. This second circuit outputs the value

$$Y = A \sin(\theta) , \quad (4.8)$$

which is known as the quadrature component of the measured signal and reports the oscillations $\pi/2$ out of phase with the generated signal. The name arises from the manner in which the amplitude may be calculated from the reported values, which is^[122]

$$A \equiv \sqrt{X^2 + Y^2} , \quad (4.9)$$

whilst the phase may be obtained using

$$\theta \equiv \arctan\left(\frac{Y}{X}\right) . \quad (4.10)$$

4.2 Contact and tapping AFM modes

Each AFM measurement technique is a 'mode' of operation and the simplest technique is contact mode. The tip is held against the sample with some set cantilever deflection, known as the deflection setpoint, and is then dragged across the surface. A feedback loop is used to actuate the z piezo and maintain the setpoint and the variation in z position is recorded as the 'Height' channel^[118]. However, the preferred height data channel for the Bruker system is the 'Height Sensor' channel^[118]. This is the change in z piezo size as measured by an external capacitor bridge circuit^[118].

Contact mode is conceptually the simplest but can lead to sample damage and tip wear, especially if the sample is soft or the tip is coated. One solution to this is tapping mode, which was the first mode to be developed for the AFM^[1]. The cantilever is driven at a frequency slightly below resonance using a piezoelectric actuator in the probe holder, and is then scanned across the surface where it only makes contact with the sample surface at the lower region of each oscillation^[1]. The force of this contact causes a shift in the cantilever resonance frequency and the amplitude and phase of the cantilever

oscillations will change accordingly. These parameters, measured in a modern system using LIAs^[118], may be used to maintain a constant value of 'amplitude error' by adjusting the scan height^[1;118]. The amplitude-frequency curve is symmetric in resonance frequency, so driving the cantilever slightly off-resonance means that the curve is locally monotonic and the direction of the resonance frequency shift is known. The resonance decreases slightly upon approach to the surface following calibration, so frequencies below resonance are used instead of above resonance to avoid this resulting in inadvertently driving the cantilever at the new resonance frequency^[118].

High amplitudes and low amplitude error setpoints result in higher forces and energy dissipation into the sample, but allow the cantilever to respond faster and more prominently to changes in sample surface height^[118]. Evidently the oscillation frequency must be much faster than the scan rate across any roughness variation in the sample, but AFM cantilevers have resonances from ~ 10 kHz^[124] to ~ 2 MHz^[119] so this is rarely an issue.

4.3 Magnetic force microscopy

Atomic force microscopes may also be used to measure the magnetic properties of a surface, and the ability to perform magnetic characterisation was the first mode developed after the initial tapping mode^[2]. This technique uses an interleave measurement in 'lift mode', where interleave simply means that a trace/retrace is performed twice at each row and different settings may be used for the 'main' and 'interleave' passes^[118]. A very useful tool for interleave techniques is the 'Rounding' setting in the NanoScope software, which configures the scanner to overscan each row. This allows the system to settle after the change in settings and reduces artefacts, for example if the cantilever drive settings for topography and lift mode measurements differ. The rounding setting value is the fraction to crop from the edges of the scanned area, so a value of 0.2 means only 80% of the rastered width is seen and the defined scan width is divided by 0.8 to obtain the applied raster width. During lift mode interleave the probe is raised to a set height above the surface and the z -piezo recreates the exact topographic surface recorded from the first pass^[118], as shown in Figure 4.8. This allows a measurement to be performed at an accurate height above the surface at every point. The short-range interatomic forces are far too weak to affect the probe whilst in lift mode^[2].

In magnetic force microscopy (MFM) the probe performs tapping mode whilst raised, and the force causing the amplitude and phase shifts of the oscillation is now the dipole-dipole magnetic force. The phase data typically yields higher contrast images than amplitude data^[118], and has a typical range of up to $\pm 3^\circ$ for a material with high saturation magnetisation M_s . The phase baseline is offset from zero by some arbitrary amount, so phase data is often normalised by subtracting the mean value of the phase data from every point. When carefully optimised, MFM is capable of resolving domains on the order

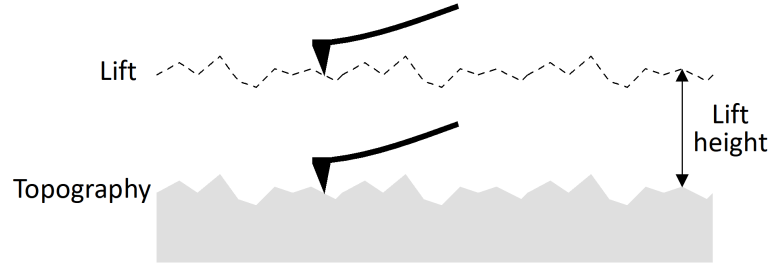


Figure 4.8: Schematic of a lift mode measurement being taken. The probe recorded the topography during the main pass then follows the dashed line during the lift mode interleave pass.

of 10 nm^[2]. MFM requires a tip to be magnetised as a single domain prior to measurement and this is done using a strong permanent magnet, with the dipoles in the tip usually aligned normal to the sample surface^[118]. A typical MFM probe has a magnetic moment of 10⁻¹³ emu^[119] and during measurement can perturb the magnetisation of magnetically soft materials^[125], so for these materials a low-moment (LM) probe should be used.

The force between two dipoles separated by r_{12} is the differential of the magnetic energy equation (2.36)^[2]. This is inversely proportional to r_{12}^4 and so the force acting on the tip varies with cantilever deflection, hence the important parameter for MFM is the force gradient $\partial F / \partial z$ which may be thought of as a spring constant. The phase shift $\Delta\phi$ is obtained from this gradient for a calibrated probe of Q-factor Q and spring constant k using^[126]

$$\Delta\phi = -\frac{Q}{k} \frac{\partial F}{\partial z} . \quad (4.11)$$

This MFM response depends strongly on the angle θ between each pair of dipole moments. If $\theta \approx 0^\circ$, meaning the sample is magnetised parallel to the tip magnetisation, then the attraction force gradient is positive and the probe is negatively phase shifted. If $\theta \approx 180^\circ$ then the attraction force gradient is negative and the probe is positively phase shifted. Significantly, if $\theta \approx 90^\circ$ then the force gradient is zero, meaning an MFM measurement may only interact with magnetic fields that do not lie entirely within the plane of the sample. If the sample magnetisation is mostly in-plane, as expected from observations in Section 2.8.1, then the MFM probe will only be able to interact with the stray fields emanating from domain walls^[2;118]. Figure 4.9 shows the phase shift experienced by an MFM probe as it crosses different domain walls, and the widths of these curves grow with domain wall width^[2].

The principal optimisation to consider for this mode is balancing lift height and interleave drive amplitude. The probe cannot be allowed to contact the surface during the lift measurement because this will obscure any magnetic effects, so the amplitude must always be less than the lift height. A lower lift height means stronger force but larger amplitude means a wider range of force gradients are sampled. Both of these

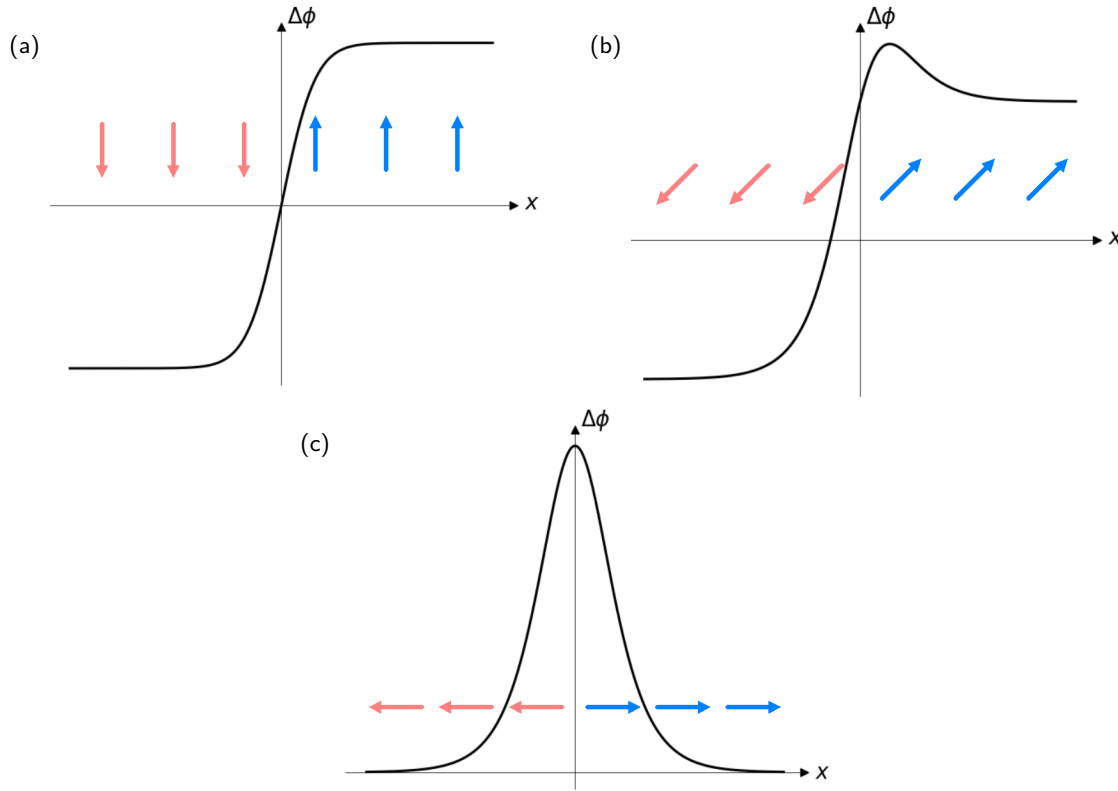


Figure 4.9: The phase shift $\Delta\phi$ experienced by an MFM probe as it crosses a domain wall between different orientations of magnetic domains, indicated by the arrows, where x is the lateral position of the tip relative to the domain wall. This is drawn for a tip magnetised such that the magnetisation points downwards, towards the sample surface. Figures adapted from Sáenz et al^[2]. (a) Domains magnetised perpendicular to the sample surface. (b) Domains magnetised at an angle of 45° to the sample surface. (c) Domains magnetised in-plane, the alignment most commonly encountered in thin films^[118].

aid magnetic domain detection, however the absolute force is ultimately more experimentally significant so lower lift heights should be prioritised where possible.

4.4 Quantitative nanomechanics

The forces experienced by a tip during contact with a surface provide a great deal of information about the mechanical properties of the sample. Once the tip reaches a critical distance z_{adh} from the sample, attractive intermolecular forces pull it downwards and it ‘snaps’ to the surface; this critical distance is typically in the range $3\text{ \AA} < z_{adh} < 6\text{ \AA}$ ^[127]. The magnitude of the force acting on the probe at this point is the adhesion force F_{adh} .

As the probe continues to be lowered the sample presses against the tip, deflecting the probe increasingly upwards. The equilibrium position where the cantilever is instantaneously experiencing no net

deflection is denoted z_0 . Simultaneously, following Newton's third law of motion, the tip also presses into the sample deforming them both. The elastic deformation of the sample is denoted δ_s and the tip deformation is denoted δ_t . Usually the tip is much harder than the sample under investigation, thus the tip deformation may be neglected and the total deformation $\delta = \delta_t + \delta_s$ is approximated as just being due to the sample deformation. Once the probe reaches the setpoint deflection $d_{set} \equiv F_{set}/k$ the downwards motion is halted.

When retracting from the surface the processes occur in reverse, with tip and sample returning to their original shapes and attractive forces holding the tip close to the surface until the elastic force of the deflected cantilever is stronger. The adhesion force on retraction from the surface is typically greater than on approach.

These forces experienced by a tip approaching a sample may be approximated by a Lennard-Jones function^[127]. This typically has the form

$$F(z) = 4F_{adh} \left[\left(\frac{z_0}{z} \right)^{12} - \left(\frac{z_0}{z} \right)^6 \right], \quad (4.12)$$

although for AFM purposes it is sometimes useful to rewrite equation (4.12) as the equivalent statement

$$F(z) = F_{adh} \left[\left(\frac{z_{adh}}{z} \right)^{12} - 2 \left(\frac{z_{adh}}{z} \right)^6 \right] \quad (4.13)$$

using the property that $z_{adh} = 2^{1/6} z_0$. The mechanical force F exerted on the tip by the sample points perpendicularly away from the sample surface. The tip-sample separation z is the separation between the sample and the position the tip would occupy if the cantilever were infinitely stiff and thus unbending. The form of the Lennard-Jones function is shown in Figure 4.10.

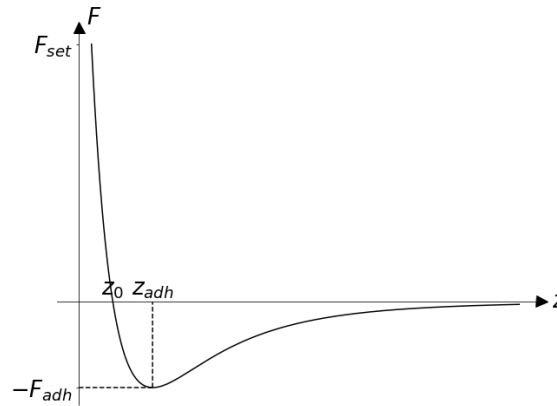


Figure 4.10: The Lennard-Jones function used to approximate AFM tip-sample interactions. The force setpoint F_{set} , adhesion force F_{adh} , adhesion deflection z_{adh} , and instantaneous equilibrium position z_0 are all labelled.

However, if the sample is very hard then the deformation effects are minimal and the observed potential

will appear to follow the linear piecewise function

$$F(z) = \begin{cases} 0 & \text{for } z > z_{adh} \\ k(z_{adh} - z) - F_{adh} & \text{for } z \leq z_{adh} \end{cases} \quad (4.14)$$

where k is the spring constant of the cantilever. This alternative form is shown in Figure 4.11.

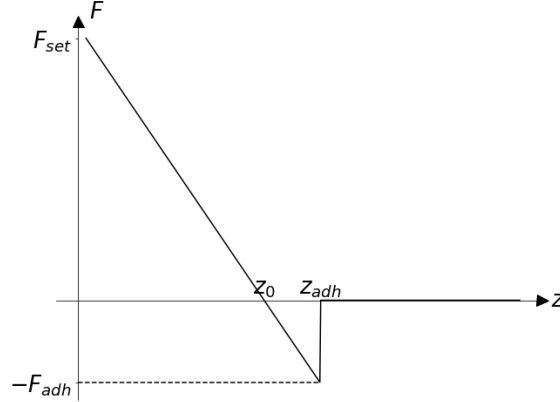


Figure 4.11: The linear piecewise function used to approximate AFM tip-sample interactions for hard samples. The force setpoint F_{set} , adhesion force F_{adh} , adhesion deflection z_{adh} , and instantaneous equilibrium position z_0 are all labelled.

The deformation effects are dominated by the elastic modulus E and the Poisson's ratio ν , which will be subscripted with t for tips and s for samples. It is often convenient to write these as the reduced elastic moduli

$$E_{s,t}^* \equiv \frac{E_{s,t}}{1 - \nu_{s,t}^2}, \quad (4.15)$$

with the reduced elastic modulus for the system as a whole given by^[128]

$$\frac{1}{E^*} \equiv \frac{1}{E_s^*} + \frac{1}{E_t^*} = \frac{1 - \nu_s^2}{E_s} + \frac{1 - \nu_t^2}{E_t}. \quad (4.16)$$

An AFM tip usually has elastic modulus much greater than the elastic modulus of the sample, in which case the tip contribution is negligible and $E^* \approx E_s^*$. However, in this work FeRh will be characterised which features similar elastic properties to those exhibited by solid-metal or metal-coated tips and thus the tip contribution is significant. The majority of literature on quantitative nanomechanics (QNM) makes the assumption that $E_t \gg E_s$, and as such the models they provide cannot be used directly to understand the tip-sample dynamics for mechanical measurement of FeRh thin films.

4.4.1 The Sneddon and Hertzian models

The definition of elastic modulus is well-known to be the ratio of mechanical stress to longitudinal strain, and the stress for both sample and tip will evidently be equal while the strain will be proportional to the

respective deformations. Thus, it may be deduced that the deformations are related as

$$\delta_s E_s = \delta_t E_t \quad (4.17)$$

where δ_s is the deformation of the sample and δ_t is the deformation of the tip. The strain is the ratio of deformation to equilibrium length, however this model considers infinitesimal deformations and so the strain will only affect a finite region of the tip or sample surface. Assuming that this finite depth is approximately equal in both the tip and the sample means that this depth cancels out along with the stress term. The relation given in equation (4.17) is not a robust treatment but is adequate for the purposes of the work reported in this thesis.

There are two common indentation models used for modelling the deformation arising from tip-sample interactions. In both cases the equations are in base SI units, however they are also compatible with a more intuitive set of units where distances are measured in nm, forces in nN, and elastic moduli in GPa.

The first model is the conical or 'Sneddon' model^[129], which is valid for sharp probes on soft samples such that the tip radius r_t is much larger than the maximal contact radius r_c . This model is shown in Figure 4.12a. In this case E_t^* may be neglected and the model states^[129]

$$F = \pi E_s^* r_c^2 \tan(\alpha) \quad (4.18)$$

where the half-angle of the tip is denoted α . It may be shown that the sample deformation δ_s relates to maximal contact radius as^[129]

$$\delta_s = \frac{\pi}{2} r_c \tan(\alpha) \quad (4.19)$$

giving

$$F = \frac{4E_s^* \delta_s^2}{\pi \tan(\alpha)}. \quad (4.20)$$

Equation (4.19) shows that the maximal contact radius r_c occurs at a depth of

$$\left(1 - \frac{2}{\pi}\right) \delta_s$$

below the sample surface, as labelled in Figure 4.12a.

The second model is the parabolic or 'Hertzian' model, so named because it follows the principles of elastic contact derived by Hertz. This is valid for larger probes on harder samples, and states that^[129]

$$F = \frac{4E^* r_{c,0}^3}{3r_t}. \quad (4.21)$$

where the terms are defined as in equation (4.18). This model is shown in Figure 4.12b and it may be derived that the maximal contact radius r_c for this model occurs at a depth of

$$\frac{1}{2} \delta_s$$

below the sample surface^[129].

Note the appearance of $r_{c,0}$ in equation (4.21). This is used because the expression is in terms of the contact radius if Poisson's ratio were zero. The true contact radius r_c may be deduced from the definition of Poisson's ratio to be

$$r_c = r_{c,0} \left(1 + \nu_t \frac{\delta_t}{r_t} \right). \quad (4.22)$$

This is not considered in the Sneddon model in equation (4.20) because, as stated previously, the elastic properties of the probe may be neglected in this case. In most AFM probes $\nu_t \frac{\delta_t}{r_t} \ll 1$, and as such the Poisson's ratio may be neglected and the approximation $r_c \approx r_{c,0}$ may be used.

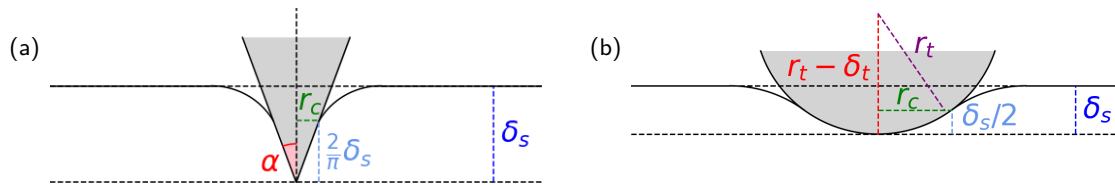


Figure 4.12: The Sneddon and Hertzian indentation models showing the resulting sample deformations and contact radii. (a) The Sneddon indentation model for a conical tip with half-angle α . (b) The Hertzian indentation model for a parabolic tip with radius r_t . The tip radius line in purple does not meet the end of the contact radius r_c marked in green due to the transverse deformation characterised by the Poisson's ratio ν_t .

4.4.2 Tip-sample contact area

Approximating the contact as perfectly flat and circular in the x - y plane, the contact area for the Hertzian model may be calculated as

$$A_c = \pi r_c^2 \quad (4.23)$$

which holds for $E_s \gtrsim E_t$. However, if $E_s \ll E_t$ then a more accurate model would consider a contact in the shape of a spherical cap. In this case the contact area is found, using standard expressions for a spherical cap, to be

$$A_c = \pi \left(r_c^2 + \frac{\delta_s^2}{4} \right). \quad (4.24)$$

The true probe is deformed via longitudinal strain and Poisson's effect so an oblate spheroid cap would be more appropriate. However, no neat analytical form exists for this case, which would lie between the bounds provided by the flat and spherical cases.

The resolution of a QNM measurement is limited to the contact diameter $2r_c$ and reflects an averaged mechanical response over the contact area A_c .

4.4.3 Characterising elastic modulus using AFM

During nanomechanical measurements the force is set and the maximal contact radius is the dependent variable. Consequently it may be beneficial to rewrite equation (4.21) as

$$r_{c,0} = \left(\frac{3Fr_t}{4E^*} \right)^{1/3} \equiv \left[\frac{3Fr_t}{4} \left(\frac{1-\nu_s^2}{E_s} + \frac{1-\nu_t^2}{E_t} \right) \right]^{1/3}. \quad (4.25)$$

It is shown in Appendix A.2 that the system deformation is described by

$$\delta_t + \frac{\delta_s}{2} = \frac{1}{2} \frac{r_{c,0}^2}{r_t}, \quad (4.26)$$

and equations (4.17) and (4.26) may be combined to obtain

$$\delta_s = \frac{1}{1 + 2E_s/E_t} \frac{r_{c,0}^2}{r_t}, \quad (4.27)$$

$$\delta_t = \frac{1}{2 + E_t/E_s} \frac{r_{c,0}^2}{r_t}, \quad (4.28)$$

$$\delta = \delta_s + \delta_t = \left(1 - \frac{1}{2 + E_t/E_s} \right) \frac{r_{c,0}^2}{r_t}. \quad (4.29)$$

As a sanity check, note that for $E_t \gg E_s$ equation(4.29) tends to $r_{c,0}^2/r_t$ while for $E_s \gg E_t$ it tends to $r_{c,0}^2/2r_t$. Both of these limits are in agreement with those for equation (4.26).

Equation (4.25) may be rearranged to give

$$\frac{r_c^2}{r_t} = \left(\frac{3F}{4E^*} \right)^{2/3} r_t^{-1/3}. \quad (4.30)$$

Using $r_c \approx r_{c,0}$ and equation (4.29), this becomes

$$\delta = \left(1 - \frac{1}{2 + E_t/E_s} \right) E^{*-2/3} \left(\frac{3F}{4\sqrt{r_t}} \right)^{2/3}, \quad (4.31)$$

which rearranges to give

$$F = \frac{4\sqrt{r_t}}{3} \times E^* \left(1 - \frac{1}{2 + E_t/E_s} \right)^{-3/2} \times \delta^{3/2}, \quad (4.32)$$

comprising a constant term, a modulus term, and a deformation term. The modulus term rises monotonically with sample modulus so mapping this term provides a qualitative map of sample modulus variation.

The AFM returns force curves as cantilever deflection d against arbitrary probe height z' . Deflection may be converted to total force using the spring constant k and deflection sensitivity γ of the cantilever. Nominal values of these will suffice when no calibration was performed. The arbitrary height z' axis is then converted to a calibrated height z axis by defining $z \equiv z_0 - z'$ and discarding any points where

$z < 0$; this retains only the region of curve where the sample is under load. This approach assumes $F_{adh} \approx 0$, but this is a reasonable simplification given the tip-sample adhesion in this work was observed to be negligible.

The deflection force experienced by the probe is

$$F = k(z - \delta) , \quad (4.33)$$

so the z axis may be converted to deformation using $\delta = z - F/k$ for each data point. The deflection force on the probe is equal to the tip-sample load force through Newton's third law. In systems with very soft samples $F \approx k\delta$ and the height z may be used directly in lieu of deformation. A linear fit may be applied to a plot of F against $\delta^{3/2}$ and the gradient of this fit gives a map of relative sample modulus.

4.4.4 The DMT and JKR models

The Hertzian model discussed so far in this section does not account for adhesion forces, which is permissible for measurements of FeRh but not necessarily in other cases. The Derjaguin, Muller and Toporov (DMT) model^[130] is an extension of the Hertzian model which handles adhesion forces explicitly. An alternative model to handle this is the Johnson, Kendall, and Roberts (JKR) model^[131]. The JKR model is appropriate for systems of large bodies and low modulus, and describes adhesion such that the contact area is non-zero when the two bodies detach^[128]. The DMT model is appropriate for systems with small bodies and higher modulus, and describes adhesion such that the two bodies detach from a point contact^[128]. Muller et al^[127] derived a quantitative parameter which uses system parameters to describe the behaviour of the contact, and thus objectively determine which model is most suitable.

The Bruker NanoScope Analysis software provides options for Hertzian, Sneddon, and JKR models to be used during analysis. The Hertzian model actually implements a DMT model since the DMT model is essentially the Hertzian model with adhesion considerations. The DMT model is appropriate for most AFM users because a standard probe has a small tip and high modulus. This means most elastic modulus data obtained using Bruker AFM systems will be labelled as DMT modulus data. The Hertzian model described in this section yields the same contrast map as seen in the NanoScope Analysis software, which supports the assumptions made here.

4.5 PeakForce and DataCube

PeakForce Tapping (PFT) modes are an implementation of rapid quantitative nanomechanics (QNM) where the probe height is ramped until the trigger, which is the QNM analogue of the setpoint, is reached^[117]. The ramp height at the trigger is recorded for a topography map and the force-distance

curve is used to produce contour plots of any requested QNM parameters such as DMT modulus or adhesion. The PeakForce family of modes feature precise force control allowing very soft samples to be accurately characterised without damage. They are also performed away from cantilever resonance and thus are less sensitive to noise while still providing the same avoidance of lateral friction observed for tapping mode^[117]. PeakForce ramp rates may be as high as 10 kHz^[117].

The ForceVolume AFM mode performs QNM ramps across the entire scan region but instead of just capturing the calculated maps the approach and retract force-distance curves are captured at each pixel, allowing for offline analysis of the data. Ramping across multiple sites is usually a very slow process, however the Bruker FastForce Volume (FFV) mode is an advanced implementation which permits ramp rates as high as 300 Hz and allows rapid QNM characterisation of a sample surface^[132].

This mode may be further enhanced by holding the probe at the trigger value for some defined period, and during this time one parameter is swept and a second measured^[132]. In common parlance the terms ramp and sweep may be used interchangeably, however in DataCube work the ramp is the approach and retract force spectra and the sweep is the hold spectrum. This thesis will therefore use 'ramp' for force-distance curves and 'sweep' for spectra obtained using a stationary probe.

There are DataCube variations of most electrical modes, such as TUNA and PFM^[132] which will be introduced in later sections. The main advantage of DataCube is that it is based on FFV so spectroscopy may be rapidly performed at many sites across the sample surface, allowing dynamics to be seen or functions to be fit to the spectral data in order to extract various local material properties^[132]. Slices may be taken from ramp or hold spectra and these are contour plots where the measured value is shown for a specific applied value at each pixel^[132]. For example, a slice from the ramp data shows the cantilever deflection at some fixed height above the surface, or a slice from I-V spectra would show the current produced by a particular bias at each pixel.

4.6 Measurements of electrical resistivity

A useful AFM technique is characterising the electrical resistivity of semiconducting samples^[3], which requires the use of conductive probes in a dedicated electrical measurements probe holder. This holder has a wire attached which is electrically connected directly to the main body of the AFM probe via a contact on the underside of the spring loaded clamp. The other end of the wire is plugged into an application module, a black box which contains sensitive electronic components to amplify and characterise current flow and which then communicates the measured values to the AFM controller using a data cable^[115]. A module is shown mounted on the AFM in Figure 4.13.

The sample itself must be grounded in some way^[118] to complete the resistivity characterisation circuit.

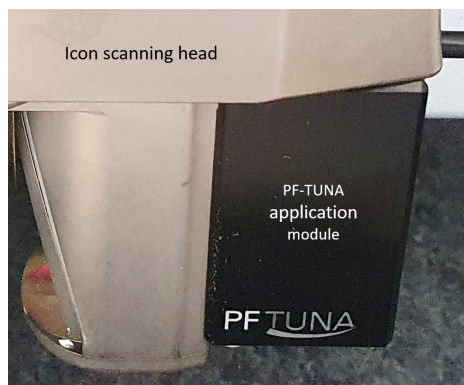


Figure 4.13: A PF-TUNA application module mounted onto a Dimension Icon scanning head.

Samples on non-conductive substrates may be grounded by mounting the substrate onto a steel puck and using conductive paint to electrically connect the sample surface to the puck^[118]. The puck then grounds through the AFM sample stage, or alternatively the stage may be biased and the tip serve as the ground^[118]. The sample must also be clean of contaminants such as oxides or debris to allow the tip to form a good electrical contact^[133]. If these conditions are met then the spatial resolution of AFM resistivity measurements is theoretically limited only by the tip-sample contact area^[133].

There are multiple implementations of conductive AFM techniques. The simplest is just called conductive AFM (C-AFM) and is a contact mode performed with a biased probe^[133]. A variant of this is tunnelling AFM (TUNA) which uses a more sensitive amplifier to detect lower currents^[133]. Spectroscopy may also be performed using C-AFM or TUNA, where the probe is held in a specific location and the bias is swept between two values, producing an I-V curve at that point^[133].

However, these modes suffer from some important drawbacks. The first is that the electrically conductive coating on the tip is highly susceptible to wear from the constant friction, or the sample itself could be damaged^[133]. The second is that the feedback loop responsible for maintaining tip-sample contact takes a finite time to respond, meaning the exact force applied, and thus the area of the contact, is not held constant^[134]. This has a significant effect on the measured resistance^[3], and can result in resistance values which vary by as much as 3 orders of magnitude^[134] when they should be largely constant.

One alternative to these issues is to use PeakForce Tapping to perform a force curve at each point and record the current at the trigger thus ensuring the contact force is consistent across the sample^[115]. This mode, developed by Bruker, is PeakForce TUNA (PF-TUNA). The advantage is that varying setpoint and tip wear are no longer major concerns, however PF-TUNA does have a significant flaw in certain samples. The bias is held constant throughout the measurement while the tip is approaching or retracting from the surface, so if the sample is highly conductive or the bias is high there will likely be arcing, which can lead to significant damage to an electrically conductive film.

The solution to this is to perform DataCube TUNA measurements (DCUBE-TUNA)^[116], where a bias is swept during the hold period of each force curve and the current is measured. The setpoint consistency from PF-TUNA is still present but the bias is kept to 0 V unless a sweep is being performed^[116], meaning arcing is not an issue. Additionally, each point of the image now produces an I-V curve rather than a single value, so it is easy to identify where ohmic contacts were made and where poorer Schottky tunnelling contacts were formed instead^[116], making it easier to identify and account for erroneous measurements.

Another approach is to use scanning spreading resistance microscopy (SSRM)^[133]. The small electrical contact between an AFM tip and a conductive sample is akin to a constriction^[3], which in a wire of radius r_c and resistivity ρ introduces a resistance^[135]

$$R = \frac{\rho}{2r_c} . \quad (4.34)$$

This is equally the sum of each half of the constriction

$$R = \frac{\rho}{4r_c} + \frac{\rho}{4r_c} , \quad (4.35)$$

which allows two materials of differing resistivities to be considered.

Equating this to an AFM measurement with contact radius r_c , one half of the contribution is from the tip and the other from the sample. The tip contribution may be neglected because the probe and system as a whole has some constant resistance and the tip constriction resistance is absorbed into this value. This just leaves the sample resistance, known as the spreading resistance^[3]

$$R_s = \frac{\rho}{4r_c} . \quad (4.36)$$

This technique requires good electrical contact and so SSRM is performed at high setpoints, typically between 1 and 100 μN ^[136]. The effective contact radius will be slightly larger than the true contact radius owing to tunnelling effects between the spherical tip and the conductive sample, reducing R_s relative to the theoretical value.

Standard C-AFM and TUNA modes are often used to produce a semi-qualitative resistivity map of semiconductor materials on electrically conductive substrates^[115], as opposed to quantitative resistance analysis, and as a result the spreading resistance need not be considered during these measurements. As with most AFM modes, these measurements are used to observe contrast between different regions of the sample rather than quantitatively characterise the surface, and so a quantitative characterisation is not required. SSRM mode uses a logarithmic amplifier^[137] to characterise the changing order of magnitude of the current signal across the surface and thus differentiate between regions such as semiconductors and high resistivity metallic conductors. The spreading resistance provides the localisation

of the measurement in such samples, while the rest of the current path between the contact site and ground will simply take the average of resistivities en route.

The Bruker C-AFM, TUNA2, and PF-TUNA application modules have a maximum measurable current of $1 \mu\text{A}$ ^[138] and the SSRM module has a maximum of $0.1 \mu\text{A}$ ^[138]. These current ranges are adequate for almost all uses because AFM is typically used to characterise semiconductors with measured resistances no lower than the megaohm regime. Indeed, it is thought that AFM cannot be used to characterise the electrical resistivity of metallic surfaces^[133] due to the low resistivities involved.

4.6.1 Resistive heating

The power dissipated by an ohmic device with constant resistance R and time varying current $I(t)$ is^[58]

$$\frac{\partial E}{\partial t} \equiv P(t) = I(t)^2 R \quad (4.37)$$

where E is dissipated energy and t is time. If the current is held constant over some period τ then the energy dissipated is

$$E = \int_{-\tau/2}^{\tau/2} I^2 R dt = I^2 R \tau. \quad (4.38)$$

If the bias is linear, sweeping from $-I$ to $+I$ over this period τ , then

$$I(t) = 2I \frac{t}{\tau} \quad (4.39)$$

so

$$E = \int_{-\tau/2}^{\tau/2} I(t)^2 R dt = \frac{1}{3} I^2 R \tau. \quad (4.40)$$

Thermal energy changes the temperature of an object with mass m and specific heat capacity c by^[58]

$$\Delta \mathcal{T}(t) = \frac{E(t)}{mc}. \quad (4.41)$$

The mass of the object may be calculated from the mass density ρ_m and volume \mathcal{V} giving the total temperature change from ambient conditions to be

$$\Delta \mathcal{T}(\tau) = \frac{I^2 \tau R}{\epsilon^2 \rho_m \mathcal{V} c} \quad (4.42)$$

where $\epsilon^2 = 1$ for constant currents and $\epsilon^2 = 3$ for linearly sweeping currents. The ratio I/ϵ represents an effective current for resistive heating purposes.

The resistance also has a temperature dependence seen in equation (2.98) which stated

$$R(t) = R_0 [1 + \alpha \Delta \mathcal{T}(t)] \quad (4.43)$$

where R_0 is room temperature resistance and α is the temperature coefficient of resistance. The period τ is chosen to be small enough that R may be considered constant over each period, but the thermal dependence must be considered over longer time scales. Due to the recursion between temperature and resistance the calculation is best solved iteratively, with the n^{th} iteration $\Delta\mathcal{T}_n$ being given by

$$\Delta\mathcal{T}_n = \Delta\mathcal{T}_{n-1} + \frac{I^2\tau R_0}{\epsilon^2\rho_m\mathcal{V}c} (1 + \alpha\Delta\mathcal{T}_{n-1}) \quad (4.44)$$

where $n \in \mathbb{N}$ and $\Delta\mathcal{T}_0 = 0$.

In a right prismatic conductor with reference resistivity ρ_0 this becomes

$$\Delta\mathcal{T}_n = \Delta\mathcal{T}_{n-1} + \frac{J^2\tau\rho_0}{\epsilon^2\rho_m c} (1 + \alpha\Delta\mathcal{T}_{n-1}) \quad (4.45)$$

where J is the current density.

This temperature change is Joule heating and means that there is a limit on the quantity and duration of scans which may be made during a single measurement session before pausing to allow some of the heat to dissipate and avoid the probe failing or the sample being excessively heated. This prohibits long sweep times τ , large current values I , or high numbers of sweeps n from being used. Lowering the ramp rate would extend the cool-down time between sweeps and hence extend the available scan duration, but AFM measurements drift with time and high resolution DataCube measurements take several hours even with relatively high ramp rates. Increasing the setpoint would reduce the risk of conductive probe failure, due to reducing the current density through the apex and increasing thermal contact area with the sample, however heating the sample is to be avoided where possible and the current density change is likely to be minimal without severe tip or sample deformation.

There are three heat dissipative mechanisms from media: radiation, conduction, and convection^[58]. All of these are dependent on external contact area, which is very small for an AFM probe, but the flat shape of a cantilever is beneficial due to the high surface area to volume ratio allowing efficient movement of heat energy to the surface. Radiative energy loss is limited by the very low emissivity of the platinum forming the tip and cantilever, which is just 3% of blackbody behaviour^[139]. Thermal conduction is limited by the small dimensions of the connection between the cantilever and tip, which will throttle the heat flow into the probe substrate or the sample. Convection requires currents in the surrounding fluid, in this case air, but the AFM enclosure is closed during measurements forming a sealed environment with minimal air movement. So while the probe has a high thermal conductivity and efficient surface area to volume ratio, the geometry of the system does not lend itself to rapid thermal dissipation and so Joule heating remains a limiting boundary on the values of several scan parameters.

The preceding discussion is difficult to quantify due to the multiple mechanisms at play, however the Preece equation may aid with this because it provides a quantitative expression for the fusing current

of an infinite wire^[140;141]. It is most suited to highly thermally and electrically conductive metals such as gold and platinum^[141] so is of interest when considering the failure of electrically conductive AFM probes. The equation was obtained by considering the limiting case^[140] where the dissipating electrical power

$$P = I^2 R \quad (4.46)$$

is equal to the thermal power loss

$$P = h A_s \quad (4.47)$$

where h is the thermal power per unit area through the wire wall and A_s is the exterior surface area of the wire. The relation for the resistance of a conductor with resistivity ρ , length l , and cross-sectional area A_c is^[58]

$$R = \frac{\rho l}{A_c} \quad (4.48)$$

so the fusing current I_f becomes

$$I_f = \sqrt{A_c} \sqrt{\frac{A_s}{l}} \sqrt{\frac{h}{\rho}}. \quad (4.49)$$

For a cylinder of radius r this yields

$$I_f = \frac{\pi}{2} \sqrt{\frac{h}{\rho}} (2r)^{3/2} \equiv B (2r)^{3/2} \quad (4.50)$$

which is the Preece equation where B is the Preece coefficient for the material. This does not necessarily apply to non-cylindrical conductors due to assuming uniform radial thermal dissipation but this will at least provide an order of magnitude estimate^[142]. Considering a cuboid with length l , width w , and thickness t , equation (4.49) becomes

$$I_f = \sqrt{8wt(w+t)} \frac{B}{\pi}. \quad (4.51)$$

Theoretical analyses have limited success when modelling resistive heating behaviour due to the complex dynamics of the system, and even finite-element-analysis will not perfectly represent the reality. The remaining solution is therefore to perform an empirical investigation, which was reported by Jiang et al.^[107] who investigated the failure process of metal-coated AFM probes due to resistive load. Figure 4.14 shows the I-V curves for repeated bias sweeps performed with a metal-coated probe on a 100 nm thick platinum film. It is not specified whether this was done using the PFTUNA or SCM-PIT-V2 probe, however both have a 25 nm PtIr coating^[119] so the difference is minimal.

The first curve initially displays the lowest resistance, however this conduction degrades during the first sweep once the current reaches 3.5 mA. This weakening without total failure suggests that the coating has thinned but remained continuous^[107]. The resistance then jumps to the M Ω regime where the probe remains stable, shown by the yellow curves. This stability is likely a result of the higher resistance

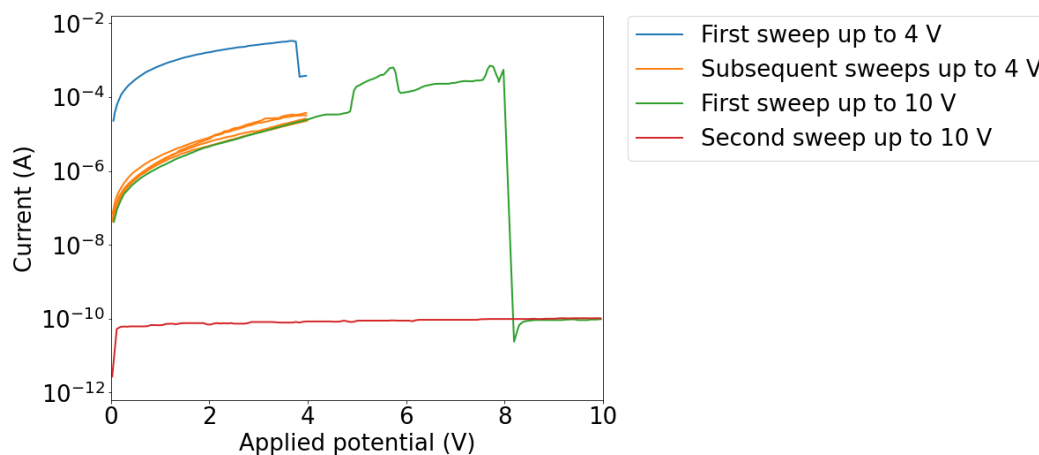


Figure 4.14: Repeated I-V curves performed over a metal-coated probe on a 100 nm thick platinum film^[107]. The blue curve shows the initial degradation to the coating during the first I-V ramp and the green curve shows the total failure of the electrically conductive coating at higher biases. Figure adapted from Jiang et al^[107].

significantly reducing the Joule heating due to $P = V^2/R$. The problem here is that the resistance measurement is purely an artefact of the damaged probe, obscuring the true values and providing misleading results^[107]. The contact still appears ohmic and so it is not obvious that the measurement has failed; indeed, ohmic curves with metal-coated probes were observed in the early stages of the work in this project and implied that the initial trial measurements were more successful than the reality.

The resistance increases slightly over consecutive sweeps, which is likely just the effect of gentle Joule heating as observed in all electrical conductors, but is otherwise stable within the swept range. The bias was then raised further until the degraded probe reached 510 μA and failed completely^[107], as seen in the green curve. The final red curve is measuring the poor electrical conductivity of the probe itself. These failure currents are far above the range of the usual measurement regime, with the Bruker application modules designed for sub- μA values, and so metal-coated probes are perfectly suited to standard electrical resistivity characterisation measurements. However, when measuring the higher currents arising during metallic film characterisation it is clear that metal-coated probes are inadequate and solid-metal probes must be used in their place.

4.7 Kelvin probe force microscopy

Kelvin probe force microscopy (KPFM) probes the electrostatic surface potential of a sample. An electrically conductive probe is used in TappingMode whilst an AC potential is applied to the probe or

sample stage. The AC potential has the form^[143]

$$V(t) = V_{AC} \sin(\omega t) + V_{DC} \quad (4.52)$$

where V_{AC} is the AC magnitude, ω is the AC angular frequency, t is time, and V_{DC} is some DC offset.

The capacitive force in the positive z -direction is derived from the differential of capacitive energy^[144]

$$F = \frac{\partial}{\partial z} \frac{1}{2} C(z) V^2 = \frac{1}{2} \frac{\partial C}{\partial z} [V_{cpd} + V_{AC} \sin(\omega_{AC} t)]^2 \quad (4.53)$$

rather than the naive consideration of Coulomb's law^[58]

$$F = -\frac{C(z)^2 V^2}{4\pi\epsilon z^2}, \quad (4.54)$$

because the energy considerations account for the geometry of the system whilst Coulomb's law assumes both capacitor electrodes may be approximated as point charges. The capacitance gradient is inherently always a negative value thus equation (4.53) is negative in the positive z -direction and hence attractive.

The cantilever therefore experiences a resultant force of^[143]

$$F = k\Delta z = \frac{1}{2} \frac{\partial C}{\partial z} \left[V_{cpd}^2 + \frac{1}{2} V_{AC}^2 \right] + \frac{\partial C}{\partial z} V_{cpd} V_{AC} \sin(\omega_{AC} t) - \frac{1}{4} \frac{\partial C}{\partial z} V_{AC}^2 \cos(2\omega_{AC} t) \quad (4.55)$$

and mechanical frequency shift^[143]

$$\begin{aligned} \Delta\omega &\approx -\frac{\omega}{2k} \frac{\partial F}{\partial z} \\ &= -\frac{\omega}{2k} \left\{ \frac{1}{2} \frac{\partial^2 C}{\partial z^2} \left[V_{cpd}^2 + \frac{1}{2} V_{AC}^2 \right] + \frac{\partial^2 C}{\partial z^2} V_{cpd} V_{AC} \sin(\omega_{AC} t) - \frac{1}{4} \frac{\partial^2 C}{\partial z^2} V_{AC}^2 \cos(2\omega_{AC} t) \right\}. \end{aligned} \quad (4.56)$$

Here C is capacitance, k is the cantilever spring constant, and V_{cpd} is the contact potential difference, which is a linear combination of the potentials and work functions of the tip and sample surface and represents the effective DC potential of the system.

These expressions have three main components: the **DC term**, the **ω term**, and the **2ω term**, which contribute towards **topography**, **potential**, and **capacitance** measurements respectively^[143]. The amplitudes of each of the oscillating terms are measured using lock-in amplifiers, and for the cantilever deflection Δz the amplitudes are

$$A_\omega = \frac{1}{k} \left| \frac{\partial C}{\partial z} V_{cpd} \right| V_{AC} \quad (4.57)$$

and

$$A_{2\omega} = \frac{1}{4k} \frac{\partial C}{\partial z} V_{AC}^2. \quad (4.58)$$

The latter is simply the root-mean-square of the AC potential $V_{AC} \sin(\omega t)$ and is equal to the **DC term** with $V_{cpd} = 0$.

4.7.1 Probe capacitance and capacitive forces

KPFM is not used in this work intentionally, but in any situation where an electrically conducting probe is not in contact with a grounded conductor, a capacitor is formed and the application of a potential will result in electrostatic charge build-up and thus the observation of electrostatic behaviour. This means that the term with frequency ω_{AC} will be picked up by lock-in amplifiers when performing any AC based measurement and the electrostatic contribution A_ω will be added onto any measured amplitude; when the total DC term V_{cpd} is negative the sign-reversal of the amplitude manifests as a phase shift of π . Strictly speaking the exact form of the terms provided is applicable solely to metallic systems, while for dielectric samples the contact potential difference is replaced by an expression considering electrostatic surface charge, but which still exhibits the phase shift of π when the net potential changes sign^[143].

The parallel plate capacitor equation gives the capacitance C for parallel plates with area A and separation z_0 to be^[58]

$$C = \frac{A\varepsilon}{z_0}, \quad (4.59)$$

but this is invalid here because it requires both lateral dimensions of each electrode to be much larger than the plane separation z_0 , which is evidently untrue for an AFM probe so a more specific treatment is required. The truncated cone and spherical apex of the AFM probe may be considered separately and summed as capacitors connected in a parallel circuit^[144]. The modelling of each component then extends this concept by considering each infinitesimal area of the tip to form a capacitor with the electrically conducting sample or stage^[144]. This model applies equally to metal-coated and solid metal-probes because charges within conductors migrate to the outer surface^[58], thus it is only the outer geometry which contributes to capacitance. The cantilever itself was neglected in this model.

The contribution of the tip-cone to the DC capacitive force of the tip-electrode system shown in Figure 4.6 is given for potential V and electric permittivity ε by^[144]

$$F_{\text{cone}}(z, V) = -\frac{\pi\varepsilon V^2}{\ln[\tan(\alpha/2)]^2} \left[\ln\left(\frac{z_a}{z_b}\right) + z_c \left(\frac{1}{z_a} - \frac{1}{z_b} \right) \right] \quad (4.60)$$

and in the large separation limit $z \gg r_t$ this becomes

$$F_{\text{cone}}(z, V) = -\frac{\pi\varepsilon V^2}{\ln[\tan(\alpha/2)]^2} \left[\frac{z}{z+h_t} - \ln\left(\frac{z}{z+h_t}\right) - 1 \right]. \quad (4.61)$$

The contents of the right-most square brackets have been written thus because the function $x - \ln(x) - 1$ is non-negative for all real x , and hence it is clear that the force is attractive. Using equation (4.53) the differential capacitance for the cone is

$$\frac{\partial C_{\text{cone}}}{\partial z} = \frac{2\pi\varepsilon}{\ln[\tan(\alpha/2)]^2} \left[\frac{h_t}{z+h_t} + \ln\left(\frac{z}{z+h_t}\right) \right] \quad (4.62)$$

which integrates to yield

$$C_{\text{cone}}(z) = \frac{2\pi\varepsilon z}{\ln[\tan(\alpha/2)]^2} \ln\left(\frac{z+h_t}{z}\right), \quad (4.63)$$

assuming ε to be approximately constant in z .

The contribution of the tip-apex to the capacitive force of the tip-electrode system shown in Figure 4.6 is given by^[144]

$$F_{\text{apex}}(z, V) = -\pi\varepsilon r_t^2 \frac{1 - \sin(\alpha)}{z \{z + r_t [1 - \sin(\alpha)]\}} V^2 \quad (4.64)$$

and in the large separation limit $z \gg r_t$ this becomes

$$F_{\text{apex}}(z, V) = -\pi\varepsilon \left(\frac{r_t}{z}\right)^2 [1 - \sin(\alpha)] V^2; \quad (4.65)$$

Using equation (4.53) the differential capacitance for the apex is

$$\frac{\partial C_{\text{apex}}}{\partial z} = -2\pi\varepsilon \left(\frac{r_t}{z}\right)^2 [1 - \sin(\alpha)] \quad (4.66)$$

which integrates to yield

$$C_{\text{apex}}(z) = 2\pi\varepsilon \frac{r_t^2}{z} [1 - \sin(\alpha)] = \frac{r_t}{z} \left(\frac{A_{\text{apex}}\varepsilon}{r_t} \right) = \frac{r_t}{z} C_{\text{self}}, \quad (4.67)$$

where C_{self} is the self-capacitance of a spherical cap with surface area A_{apex} . Again, ε was assumed to be approximately constant in z . The presence of the ratio r_t/z in the force and capacitive expressions highlights that the cone contribution dominates the apex contribution in the regime where $z \gg r_t$, which does make intuitive sense.

In contrast to a typical capacitor system, the AFM probe is free to move so will demonstrate the KPFM behaviour described in equation (4.55) in any situation in which an AC bias is applied and the tip does not make contact with a ground, especially when the insulating medium has a large relative permittivity. Electrostatic repulsion from induced surface charges will potentially raise the tip from the surface and allow the full cantilever oscillation to occur. This electrostatic contribution shall be considered empirically as it arises, thus in the following it shall be neglected and the DC potential will merely be the applied offset V_{DC} .

Over a sample of thickness $z_0 \gg r_t$ the electrostatic force acting on the cantilever may therefore be determined using equations (4.55) and (4.62) to be

$$F = F_{\text{cap,DC}} + kA_\omega \sin(\omega_{AC}t) + kA_{2\omega} \cos(2\omega_{AC}t) \quad (4.68)$$

where

$$\begin{aligned} F_{\text{cap,DC}} &= k\Delta z_{\text{cap,DC}} \\ &= \frac{\pi\varepsilon}{\ln[\tan(\alpha/2)]^2} \left[\frac{h_t}{z_0 + h_t} + \ln\left(\frac{z_0}{z_0 + h_t}\right) \right] \left(V_{cpd}^2 + \frac{1}{2} V_{AC}^2 \right) \end{aligned} \quad (4.69)$$

$$A_\omega = -\frac{2\pi\varepsilon}{\ln[\tan(\alpha/2)]^2} \left[\frac{h_t}{z_0 + h_t} + \ln\left(\frac{z_0}{z_0 + h_t}\right) \right] |V_{cpd}| V_{AC} \quad (4.70)$$

$$A_{2\omega} = -\frac{\pi\varepsilon}{2 \ln[\tan(\alpha/2)]^2} \left[\frac{h_t}{z_0 + h_t} + \ln\left(\frac{z_0}{z_0 + h_t}\right) \right] V_{AC}^2. \quad (4.71)$$

4.8 Piezoresponse force microscopy

Piezoresponse force microscopy (PFM) probes the piezoelectric behaviour of a sample and is a surface contact technique so the resolution of mechanical strain is confined to the tip-sample contact area and thus is highly localised. An electrically conductive tip is dragged along the surface while an AC potential is applied to the probe or sample stage, with form^[145]

$$V(t) = V_{AC} \sin(\omega_{AC}t) + V_{DC} . \quad (4.72)$$

The sample responds with an AC deflection^[145]

$$\Delta z(t) = A_s \sin(\omega_{AC}t + \phi_s) + \Delta z_0 \quad (4.73)$$

where A_s is the sample surface oscillation amplitude and ϕ_s is the corresponding phase. The values of A_s and ϕ_s are extracted using a pair of digital lock-in amplifiers.

However, this measurement is subject to the electrostatic contributions defined in Section 4.7, which means a more accurate expression for the measured response is

$$\Delta z(t) = A_s \sin(\omega_{AC}t + \phi_s) + \frac{1}{k} \left| \frac{\partial C}{\partial z} \right| V_{cpd} V_{AC} \sin(\omega_{AC}t) + \Delta z_0 . \quad (4.74)$$

A high k probe is typically used to suppress the deflection arising from the electrostatic term, but this cannot negate high potentials which require a more advanced technique as will be seen in Chapter 8.

4.8.1 PFM phase

The PFM phase is a measure of the electric dipole polarisation. The phase is zero when the the dipoles are parallel with the positive electric field direction and π when the dipoles are anti-parallel^[145]. The corresponding functional form is

$$\phi(E) = \frac{\pi}{2} \{1 - \tanh[a(E - E_c)]\} \quad (4.75)$$

which is a modification of the ferroelectric sigmoid expression in equation (2.129) and is again a theoretical Heaviside function which is smoothed by physical effects.

The sigmoid-like curve is inverted in samples with negative electrostriction coefficient Q_{33} , however the vast majority of materials have $Q_{33} > 0$ ^[146]. The phase follows the polarisation so also describes a hysteresis loop in ferroelectrics. The phase is a wholly intrinsic characteristic of the material so the value is the same however it is measured, in contrast to the amplitude.

In real experiments there will be some experimental offset which means the phase values do not lie neatly at $\phi_s = 0$ and $\phi_s = \pi$ ^[146]. This offset is dependent partially on the wiring in the AFM system

and especially on the resonance frequency of the cantilever being used^[146], and should be carefully accounted for due to the bounded nature of phase. The lock-in amplifiers return the phase on the domain $-\pi < \phi_s \leq \pi$, so a slight positive phase offset will push the $\phi_s = \pi$ values past the π domain limit and wrap it around to be just above $\phi_s = -\pi$, effectively inverting the loop^[146]. Figure 4.15 shows the same example data twice with different phase offsets.

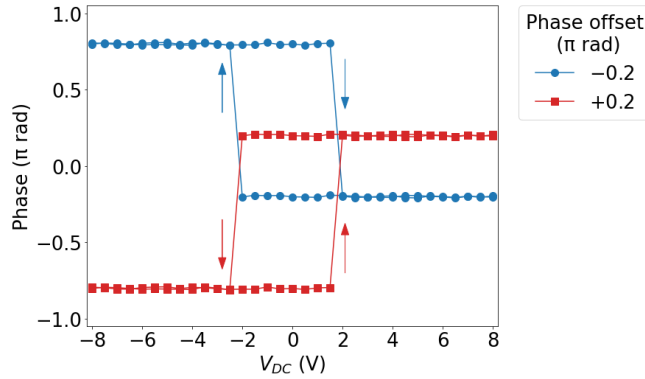


Figure 4.15: Two PFM phase curves for the same set of data points which have differing constant offsets.

The phase-wrapping effect means the phase shift appears to be reversed for one curve relative to the other^[146]. In wider transitions there will be data points during the transition process so any phase-wrapping will be clear, but in sharper transitions such as the example in Figure 4.15 context must be used to determine which phase shift is correct.

The absolute value of the phase is not as important as the magnitude and sign of the relative phase, and the unwrapped curve can just be shifted vertically to sit on the line $\phi_s = 0$. As a rule of thumb, if the offset is negative then the curve should not have been inverted because it should have simply been shifted downwards and thus not passed a domain limit, while if the offset is positive then some values of the curve will have been pushed past the $\phi_s = \pi$ threshold and inverted. This inversion should be straightforward to correct by simply displaying the data on the range $0 < \phi_s \leq 2\pi$ instead of the recorded $-\pi < \phi_s \leq \pi$. This does not work in all instances but is a very good starting point.

There are two possible approaches to quantitatively account for this inversion. The easiest is to use a sample with known sign of Q_{33} and perform PFM far above and below the switching potential^[146]. The mean phase of each scan can be taken and using the known sign of Q_{33} it can be determined which scan should have a phase of zero: the higher potential for $Q_{33} > 0$ and the lower potential for $Q_{33} < 0$. The recorded mean phase for this scan is the experimental phase offset^[146].

However, Q_{33} is not known for all materials, especially when they are formed into structures and stacks; in these cases the AFM experimental phase offset must be calibrated. One way to do this is to positively

polarise the sample, then determine the phase far from sample resonance for a range of cantilevers and produce a plot of measured phase against cantilever resonance frequency^[146]. A straight line may be fit which provides a function by which the phase offset for a specific cantilever may be calculated. This is specific to each particular AFM system, however an example for what this would look like is provided in Figure 4.16^[146].

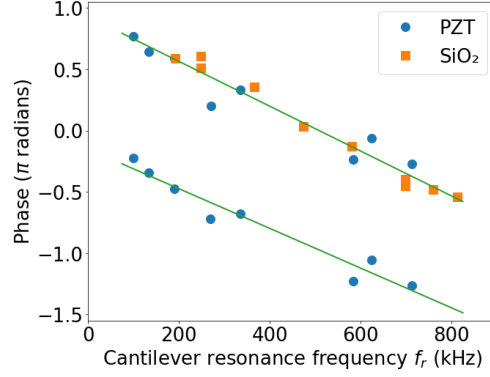


Figure 4.16: An example calibration plot for phase offset due to measuring equipment, using data for SiO₂ and PZT. The PZT results form two bands offset by π radians, which correspond to opposite ferroelectric polarisation directions. The phases have been unwrapped hence the range of the phase-axis is larger than 2π . Figure adapted from Neumayer et al^[146].

4.8.2 PFM amplitude

The amplitude of the oscillation is the range over which the substrate deforms during the PFM measurement and the exact value of this is somewhat extrinsic because it depends on the magnitude of the applied AC potential and on the difference between drive and resonance frequency. The off-resonance amplitude is half of the total change in deformation, so for a potential dependent deformation $\Delta z(V)$,

$$A_s = \frac{1}{2} |\Delta z(V_{DC} + V_{AC}) - \Delta z(V_{DC} - V_{AC})|. \quad (4.76)$$

If V_{AC} is small,

$$A_s \approx \frac{1}{2} |\Delta z(V_{DC} + 2V_{AC}) - \Delta z(V_{DC})| = V_{AC} \left| \frac{\Delta z(V_{DC} + 2V_{AC}) - \Delta z(V_{DC})}{2V_{AC}} \right|, \quad (4.77)$$

and using l'Hôpital's rule

$$A_s \approx V_{AC} \left| \frac{\partial \Delta z}{\partial V_{DC}} \right| = V_{AC} \left| \frac{\partial \Delta z / z_0}{\partial V_{DC} / z_0} \right| \quad (4.78)$$

where z_0 is the substrate thickness. The vertical strain is $S_3 = \Delta z / z_0$ and the applied field is $E_3 = V_{DC} / z_0$ so

$$A_s \approx V_{AC} \left| \frac{\partial S_3}{\partial E_3} \right| \equiv V_{AC} |d_{33}|. \quad (4.79)$$

Hence any variation in measured amplitude is proportional to a variation in piezoelectric coefficient d_{33} .

However, this only applies to fine samples such as powders or thin films. PFM measurements are sensitive to a depth of $1.7 \mu\text{m}$ ^[147] in most materials but cannot resolve any contrast below this depth. This limit is a consequence of strain dissipation effects, similar to those observed for FeRh grown on MgO(001) substrates in Section 3.4.1, which arise because the majority of the crystal is not exposed to the field and thus does not change in size. The strain is therefore calculated over a different thickness to the field, and equations (4.78) and (4.78) become

$$A_s \approx V_{AC} \left| \frac{\partial \Delta z / z'_0}{\partial V_{DC} / z_0} \right| = V_{AC} \left| \frac{\partial S_3}{\partial E_3} \right| \frac{z'_0}{z_0} \equiv V_{AC} |d_{33}| \frac{z'_0}{z_0} \quad (4.80)$$

where the characterisation depth z'_0 has value

$$z'_0 = \begin{cases} z_0 & \text{for } z_0 < 1.7 \mu\text{m} \\ 1.7 \mu\text{m} & \text{for } z_0 \geq 1.7 \mu\text{m} \end{cases} \quad (4.81)$$

The resulting amplitude curve for an exemplar piezoelectric sample with piezoelectric coefficient $d_{33} = 2 \text{ nm V}^{-1}$ and drive amplitude $V_{AC} = 0.5 \text{ V}$ is shown in Figure 4.17. The response has a constant amplitude of 1 nm for thin films, but decreases rapidly for thicker samples and for $250 \mu\text{m}$ the amplitude is just 6.8 pm . This demonstrates that a consequence of the characterisation depth is that thick samples exhibit substantially smaller amplitudes than fine ones, and thus using PFM to characterise samples such as PMN-PT substrates will be much more difficult than for the thin films typically characterised using AFM techniques.

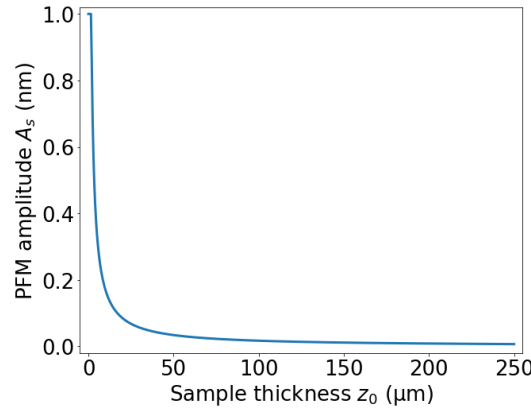


Figure 4.17: The theoretical dependence of PFM amplitude on sample thickness for an exemplar piezoelectric sample with piezoelectric coefficient $d_{33} = 2 \text{ nm V}^{-1}$ measured using a drive amplitude of $V_{AC} = 0.5 \text{ V}$.

Significantly, the existence of this characterisation depth also means that PFM does not specifically provide a characterisation of the sample surface, which is highly unusual for a scanning probe technique. This is a consequence of PFM being an active measurement technique, meaning that the sample response

to external stimulus is being characterised, in contrast to the majority of AFM techniques which passively measure surface properties without directly stimulating the sample.

4.8.3 Piezoelectric resonance

The resonance frequency of the system may be determined by sweeping the drive frequency and recording the amplitude of the sample response while $V_{DC} = 0\text{ V}$ ^[146], so that electrostatic contributions are negligible and the amplitude is simply $A_s = \Delta z$. The resulting amplitude curve is a Lorentzian centred at the resonance frequency f_r ^[146]. The resonance frequency depends on the local crystal structure of the sample and so it is useful to determine how the resonance frequency varies across the surface, because inhomogeneity in this parameter could introduce artefacts into the PFM data when imaging near resonance^[146]. This is not solely dependent on the resonance of the sample itself, but also depends strongly on measurement parameters such as the probe used, and thus will vary significantly between measurements even when using similar probes on the same sample.

Imaging with the drive frequency f_{AC} near resonance has advantages and disadvantages and a decision must be made regarding which to choose. The resonance provides an enhancement to the measurement signal amplitude which improves the signal-to-noise ratio^[146] and enhances the contrast of the phase map. However, the amplitude is now a convolution of sample response and the difference between drive and resonance frequencies, and the resonance frequency varies across the sample surface meaning the amplitude may no longer provide meaningful values^[146].

4.8.4 High-voltage PFM

High-voltage PFM (HV-PFM) can be performed by using the high-voltage line on the Dimension Icon system to increase the applied potential and hence electric field strength, especially over thicker samples. This line increases the potential range from the standard $\pm 12\text{ V}$ to $\pm 220\text{ V}$ and should only ever be applied to the probe rather than to the stage for safety reasons. However, throughout this work it was observed that performing HV-PFM resulted in significant surface degradation, by seemingly ablating or depositing material to form craters, peaks, or even raising the entire scan area, with the consequence that the topography is obscured and piezoelectric contrast is lost to the degraded surface. This was observed and explained by Chung et al.^[148] for polymethyl methacrylate (PMMA) and it is believed that this phenomenon will affect all insulating materials. Spectroscopic sweep-based measurements produce peaks at individual sites whilst contact based measurements disrupt the entire surface. This limits the repeatability of HV-PFM scans because the sample will be poorer condition following measurement, and limits the resolution of spectroscopic measurements because the pixels must be separated by a distance larger than the degradation radius.

In the study on PMMA this was a consequence of the very high field adjacent to the probe acting on an insulating crystal^[148]. This field is of the order 10^9 V m^{-1} to 10^{10} V m^{-1} so is able to sever the localised electrons from their orbitals and attract them towards the tip, resulting in extreme Joule heating occurring and a nanoscale portion of the sample becoming a nanofluid^[148]. The probe is repulsed by forces within the fluid and the fluid rises with it then cools to form the peaks^[148]. Multiple peaks may be formed if the tip-apex is sufficiently large and rough to feature multiple field maxima. The peak forming process is more significant for softer probes such as PFTUNA than for stiffer probes such as SCM-PIT-V2 due to the deflection size being governed by the cantilever spring constant.

In the literature nanodots with height up to 8 nm and diameter up to 150 nm were formed on polymethylmethacrylate (PMMA) for potentials in the range 10 – 30 V^[148]. Increasing the potential to the 30 – 60 V range produced Taylor cones^[148], which feature a central cone of height 50 nm and full width at half maximum 150 nm surrounded by a moat with diameter 2 μm and depth 60 nm. Both of these features are shown in Figure 4.18a. The time over which the potential is applied is also significant, with the Taylor cone rising with time until it completely ablates leaving only the moat which now forms a crater, this is shown in Figure 4.18b.

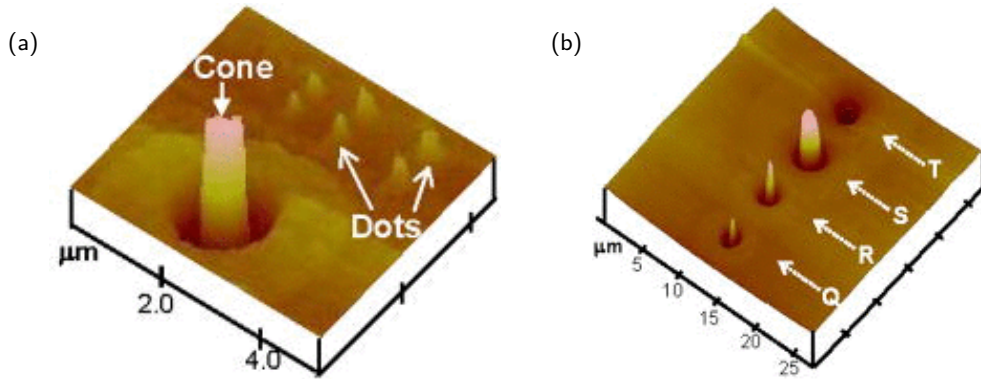


Figure 4.18: The structures produced by applying high potentials to AFM probes in contact with insulating crystals. Figures reproduced from Chung et al^[148]. (a) Six nanodots produced at 10 – 30 V and a Taylor cone with height 50 nm formed by applying 40 V for 16 s. (b) Three Taylor cones *Q*, *R*, *S* and one crater *T* formed by applying 50 V for 6 s, 10 s, 14 s, and 22 s respectively.

Alternatively, atoms may also be manipulated by temporarily bonding lattice ions to an AFM tip and then depositing the ion at a new site^[149]. This is aided significantly by high electric fields being present, for example when using a high-voltage conductive AFM probe. However, this is less likely to produce the distinctive features observed for the PMN-PT sample, which more closely replicate the Taylor cones seen in the study on PMMA^[148]. It should be noted though that the cause of the surface disruption of the PMN-PT sample under high fields is only speculated upon in this work, and the precise origin of this remains an open question.

4.8.4.1 Signal access module

The high-voltage line is not available on the standard NanoScope Controller and instead must be accessed using the ANA2 (HV) connection on a signal access module (SAM). Each NanoScope Controller is only compatible with the same generation SAM unit because the signals in use are altered between controller generations. Hence the SAM-V was the module used in this work and is shown in Figure 4.19. The SAM is a large breakout box which connects between the microscope and the controller and features pairs of BNC connectors for every input and output signal on the system. These allow the signal to be redirected to an external device or be replaced by the signal from an external device to allow advanced control and analysis; both connectors may be used simultaneously to perform a real-time modification of the signal. In this work the SAM will be somewhat underutilised because the only BNC connection being used is the ANA2 (HV) output.



Figure 4.19: The signal access module for the NanoScope Controller V system with a BNC cable attached to the ANA2 (HV) connection. The red caps are safety covers for unused high-voltage outputs.

4.9 The nanoscope Python package

Analysis of the files captured by the Bruker NanoScope software is typically performed using the proprietary NanoScope Analysis software. This provides a wide range of processing tools however was inherently too inflexible for use in the advanced metrological development work in Chapters 5 and 8 of this thesis. Instead, the official nanoscope Python package^[150] was used to import the captured data values into Python where multiple files were able to be compiled into a single data set and numeric analysis such as functional fits could be performed.

The package was only publicly released in April 2021 however a beta version of the package was provided by Bruker in November 2018 due to the requirements of this work. All AFM data obtained and presented in this thesis has been extracted using this package and processed and plotted using Python.

4.10 Sample preparation for AFM measurements

The preparation required before imaging a sample using an AFM is minimal which is why AFM is such a flexible and useful technique. The predominant requirements are simply that the sample surface be free from contaminants, and have features smaller than the tip height or the $6\text{ }\mu\text{m}$ range of the z piezo. There are a wide range of possible types of contaminants from loose debris and particles to grease or oils on a mishandled sample, and it is important to avoid unnecessary exposure to air outside of cleanroom environments for samples intended for AFM analysis.

There are two types of solvents categorised by the presence or absence of electric dipoles: polar and non-polar^[151]. These may only dissolve contaminants with the same properties so both types should be used for a comprehensive clean, however the majority of surface contamination is simply loose debris which may be readily removed with any cleaning liquid. Acetone is typically the initial solvent to be used because it features both polar and non-polar bonds within the molecule^[151] thus is an effective cleaning agent for most contaminants. Plastics are susceptible to non-polar solvents due to being formed from long chain non-polar polymers^[151] and so samples must be free of residual acetone before being replaced in a plastic sample box; polar solvents have no such effect. Acetone readily evaporates from surfaces however may leave behind a residue when it does so.

A second cleaning step is thus performed using isopropanol (IPA) which is a polar solvent that evaporates cleanly. Nitrogen guns are used to aid with drying samples when available but often the solvent must be left to evaporate naturally. The cleaning occurs by submerging the sample in the solvent of choice then placing the beaker inside an ultrasonic cleaner where the vibrations provide a scrubbing effect. On occasion some well-adhered debris will not be removed with this technique so a cleanroom swab or wipe may be carefully used with some solvent to physically clean the surface, although this can lead to damage including scratches so should be avoided where necessary. In addition to the rapid evaporation, both of these solvents are used because the small amounts required mean that if used in a ventilated room the dermal and inhalation exposures will be orders of magnitude below safe working limits^[152;153].

In certain cases it is required to mount the sample onto a steel puck prior to characterising on the AFM. These are discs with thickness $0.5 - 1.0\text{ mm}$ and diameter 15 mm and allow the use of magnetic mounts or performance of electrical resistivity measurements. The latter requires a continuous path from the surface to the AFM stage and this is often achieved through the use of silver conducting paint (SCP). The SCP cannot be applied to the stage nor could it reasonably be reapplied for every measurement, and these limitations are especially pertinent given the requirement to anneal SCP to $120 - 150^\circ\text{C}$ for $5 - 10\text{ min}$ to achieve the maximum electrical conductivity of 10^5 S m^{-1} ^[154].

The use of a puck allows an electrically conductive path to be made from the surface to the puck and be annealed once, and then the puck forms a conductive contact with the stage wherever it is placed. The mounting process requires an adhesive that is strong enough to prevent any movement, is thermally stable to permit heated measurements, yet may be easily removed when the sample is to be unmounted. Conveniently, SCP has good adhesive properties, is stable up to at least the annealing temperature, and is readily removed using acetone. Thus the samples were mounted and conductive paths were drawn using the same medium. The SCP was applied to the puck using a pointed plastic tool supplied with the bottle and the sample was pressed down onto this and gently wiggled to ensure a clean contact. The conductive path was then added using the same tool before annealing the mounted sample at 135 °C for 10 min using a standard hotplate.

The Dimension Icon sample stage can accommodate samples up to a maximum circular diameter of 200 mm and maximum thickness of 16.5 mm^[118] which makes it a highly versatile system. The main stage consists of a circular rotating chuck of diameter 200 mm which features a small hole through which a vacuum may be applied to hold the sample in place, allowing for rapid loading and unloading of samples by simply placing them over this hole and activating the vacuum^[118]. Alternatively the thermal measurement stage features a magnet upon which the samples may be placed but this stage is much smaller and requires the sample be first mounted on a steel puck.

4.11 Thermal measurement stage

The characterisation abilities of an AFM may be further enhanced by controlling the environment of the sample such as raising the temperature or applying a magnetic field. The AFM has an attached thermal measurement stage using a thermal applications controller (TAC) and a heater stage capable of applying temperatures up to 250 °C, which enables measurements at a wide range of temperatures to be performed. Figure 4.20 shows the heater stage itself which is 15 mm in diameter and features a metallic surface covering a magnet and heating element. This magnet produces a field of 150 mT immediately above the surface^[155]. The metallic surface is electrically connected to the main stage allowing the full range of electrical measurements to be performed on the heater stage. However, it was observed that potentials above ~ 7 V caused significant errors in the thermocouple feedback resulting in complete loss of control of the heater stage temperature. Regardless, the high-voltage line is unavailable when the heater stage is in use because the NanoScope Controller uses the same channel to communicate with the TAC and the high-voltage source.

A typical sample is thin and so should heat up very quickly, however in practice there are substantive thermal losses and several minutes should be allowed. If the sample has not equilibrated then the changing temperature of the sample and probe makes it difficult for the AFM to maintain good surface

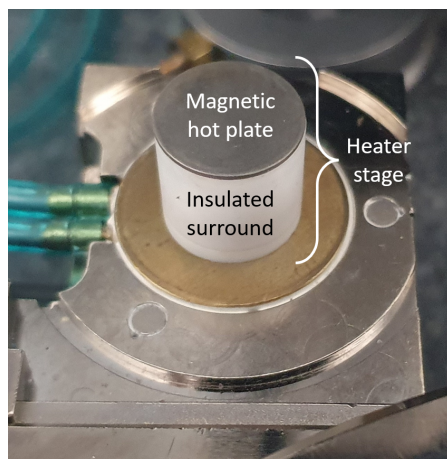


Figure 4.20: The heater stage on the Dimension Icon system.

contact. Upon engaging the probe at least one scan should be performed prior to capturing any data, this improves the captured data quality due to allowing the probe and tip to equilibrate. The temperature should only be changed whilst the probe is withdrawn from the surface to prevent damage so an engage is regularly required during thermal measurements. There is often micrometre scale sample drift following a change in temperature and so the first equilibrating scan after engaging on the surface is useful in locating the movement of some reference point and correcting the x and y piezoelectric actuator offsets prior to data capture.

The TAC reports temperatures to a precision of $\pm 0.1^\circ\text{C}$ however this is not realistically achieved. The sample surface and the thermocouple are sufficiently separated that the two will not remain in equilibrium, especially at higher temperatures where the surface will be losing heat more rapidly through radiation and convection. The *TAC Panel Control* page of the NanoScope internal user guide presents a calibration table measured for a generic sample and this is plotted in Figure 4.21.

This little-known error in temperature is significant, and has manifested in the literature when comparing thermal measurements obtained using an AFM with those from a second characterisation methodology. Warren et al.^[57] recently reported measurements of the magnetisation of a 40 nm film of equiatomic FeRh during a heating and cooling cycle. This was measured over a $5\text{ }\mu\text{m}$ square of the surface using MFM as well as for the sample as a whole using a vibrating sample magnetometer (VSM). There was an offset between the two hysteresis loops, as seen in Figure 4.22a, which was tentatively attributed to a calibration error in the AFM thermocouple. Converting the temperature axis of the MFM data using the generic calibration data in Figure 4.21 yields Figure 4.22b, where the two hysteresis loops now align almost perfectly, demonstrating the importance of considering this calibration.

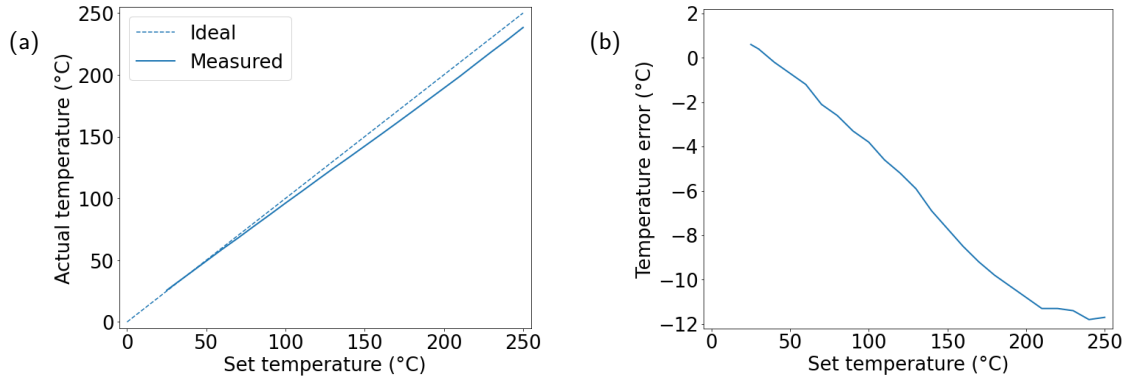


Figure 4.21: A comparison of applied and measured temperatures for the heater stage using values from the calibration data in the NanoScope internal user guide. (a) The measured values plotted against set values with ideal curve included. (b) The difference between the measured and applied temperatures.

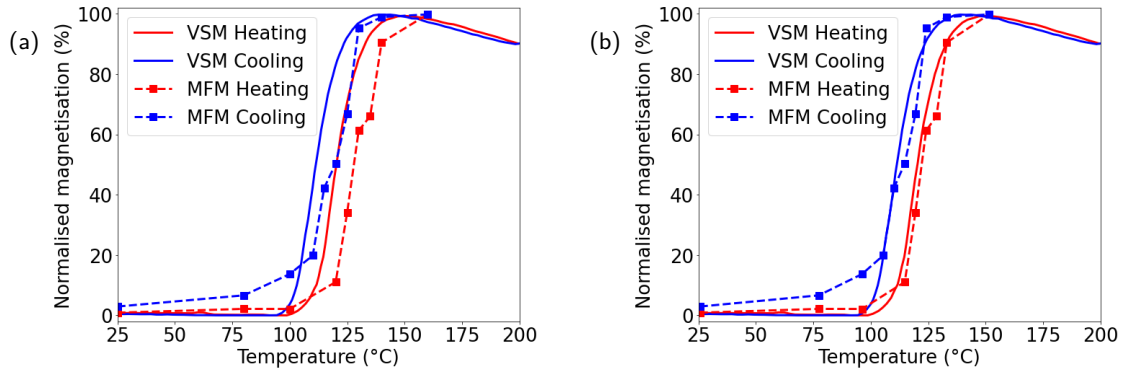


Figure 4.22: Measurements of the normalised magnetisation for thermally cycled equiatomic FeRh as measured using MFM and VSM by Warren et al^[155]. (a) The data as-reported, with an offset between the two hysteresis loops. (b) The data with a corrected MFM temperature axis, without offset.

4.12 Summary

The established techniques used in the atomic force microscopy characterisation of the samples of interest in this work have been explained in detail, providing the groundwork for understanding any new methodologies developed as part of the project in later chapters. The underlying principles of atomic force microscopy have been provided and the geometry and composition of the AFM probe itself was considered. This was followed by an in-depth discussion of all AFM modes used or referred to in this thesis, and the chapter concluded with descriptions of the sample preparation process and the thermal measurement stage.

Chapter 5

Metallic resistivity characterisation on the AFM

The ability to perform metallic resistivity measurements on the nanoscale is a technique missing from the arsenal of currently available AFM modes. The work in this thesis involved comprehensive characterisation of a FeRh metallic film and so the methodology to perform such measurements was required to be developed and implemented. This chapter will begin by considering all of the sources of resistance in an electrical measurement and how they may be exploited to achieve highly localised resistive characterisation. The phenomena which may impede accurate measurement will be discussed in detail including Joule heating and surface contaminants. The chapter will end by explaining the design and development of the fledgling AFM technique for characterising the local electrical resistivity of metallic surfaces.

5.1 Motivation and aims

Conductive AFM techniques have been available for semiconducting surfaces for over two decades^[3], but nanoscale resistivity characterisation of metallic surfaces is a missing technique that leaves a hole in the spectrum of AFM abilities. This work seeks to address this gap in available nanoscale characterisation techniques.

Characterising magnetic domains using MFM is a long established^[2] technique which may be performed on any AFM system equipped with phase detection capability and a magnetised ferromagnetic tip, however the interaction of stray fields and the finite size of the tip can result in the distortion of fine structures. Recall from Section 4.6 that electrical resistance characterisation is a highly localised technique due to depending entirely on tip-sample contact rather than any stray fields, so the measurement resolution is limited only by the effective contact radius.

The local resistivity of an electrically conductive surface is an ideal candidate for characterising metallic thin films, and so there is a need for nanoscale characterisation of the electrical resistivity of metallic

surfaces which has so far remained unfulfilled. The aim of this work is to develop a methodology by which a commercial AFM may be used to perform this characterisation with minimal modification.

The film under investigation is a 40 nm equiatomic FeRh film which has been magnetically patterned with alternating 100 nm wide stripes of ferromagnetic (FM) and antiferromagnetic (AF) ordering. The resistive properties vary alongside this patterning through density of states induced magnetoresistance as discussed in Section 2.9.2, providing a sample with a strong resistance contrast to characterise. This type of magnetoresistance produces regions which share the same order of magnitude of resistance thus the metallic characterisation technique has been developed with the aim of being sufficiently sensitive to distinguish these.

5.2 Sources of resistance

There are many possible sources of resistance which must be considered when quantifying electrical AFM measurements and the seven main contributors are shown in Figure 5.1 and summarised in Table 5.1. Standard electrical resistance methodologies on the AFM, such as those introduced in Section 4.6, are used to characterise samples with high resistances and thus any system resistances are negligible. However, these must be quantified when exploring metallic samples, including contributions from the electrical conduction properties of the probe itself which depend on whether the probe is metal-coated or solid metal. The exemplar probes considered during the development of this work are the Bruker SCM-PIT-V2^[119], a PtIr coated probe which is a workhorse of electrical measurements, and the RMN-25PT300B^[124], a lesser-used solid platinum probe. In the interests of clarity it should be established that any references to a solid metal probe refer jointly to the tip and cantilever; this class of probe contains no silicon whatsoever. The definitions of tip, cantilever, and probe, will continue to be used as defined in Section 4.1.

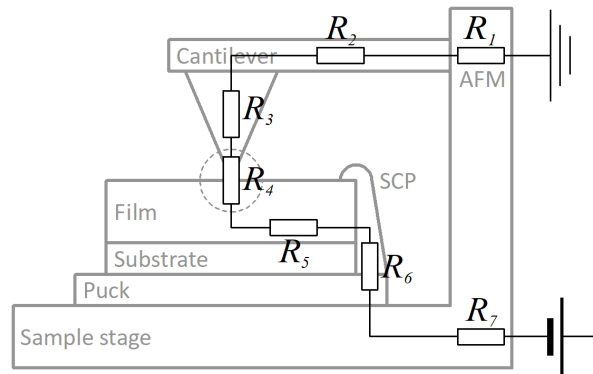


Figure 5.1: The main sources of resistance in an electrical AFM measurement, overlaid onto a simplified schematic of the system. Silver conducting paint (SCP) is used to create a conducting path from the film to the puck. These resistances are summarised in Table 5.1.

Label	Summary
R_1	Negligible resistances within the AFM system itself.
R_2	Cantilever resistance.
R_3	Tip resistance.
R_4	Total resistance of tip-sample interface.
R_5	Macroscopic sample resistance.
R_6	Total resistance of the conductive paint, puck, and interfaces thereof.
R_7	Negligible resistances within the AFM system itself.

Table 5.1: The main sources of resistance in an electrical AFM measurement. The corresponding diagram is shown in Figure 5.1.

Negligible system resistances R_1 and R_7

The contributors R_1 and R_7 represent resistances within the AFM system itself, accounting for all wiring and connections to the cantilever and sample stage. These cannot be measured or modified directly due to the majority of these being internal AFM components but are known to be negligible.

Cantilever resistance R_2

The resistance of the cantilever is R_2 , which is simple to calculate for rectangular cantilevers but less so for triangular ones because of the varying cross-sectional area. The resistance for a rectangular cantilever with length l , thickness t , width w , and resistivity ρ , is^[58]

$$R_2 = \frac{\rho l}{wt} . \quad (5.1)$$

The RMN-25PT300B platinum probe is quoted to have full length $1300 \mu\text{m}$, width $110 \mu\text{m}$ ^[124], thickness $4.5 \mu\text{m}$ ^[156], and resistivity $1.0 \times 10^{-7} \Omega \text{m}$ ^[63], so for this probe $R_2 \approx 0.3 \Omega$. The SCM-PIT-V2 probe is quoted to have length $225 \mu\text{m}$, width $35 \mu\text{m}$, and tip radius (and thus coating thickness) 25nm ^[119]. The specific ratio of PtIr used for the coating is not stated, but $\text{Pt}_{90}\text{Ir}_{10}$ has resistivity $2.5 \times 10^{-7} \Omega \text{m}$ ^[63] so using this value the cantilever resistance is found to be $R_2 \approx 64 \Omega$.

Tip resistance R_3

R_3 is the resistance of the physical tip which can be approximated as the sum of two components. The first is a truncated cone with resistance

$$R_{3,\text{con}} = \frac{\rho}{\pi r_t \sin(\alpha)} \quad (5.2)$$

which is derived in the Appendix in Section A.3. The expression for the coating of an insulating probe is derived in a similar way in Section A.3.1 to be

$$R_{3,\text{con}} = \frac{\rho}{2\pi r_t \sin(\alpha)} \ln \left[\frac{2h_t \sin(\alpha)}{r_t \cos^2(\alpha)} \right]. \quad (5.3)$$

The second component of R_3 is the resistance of the spherical cap at the end of the tip, given by

$$R_{3,\text{sph}} = \frac{\rho}{\pi r_t} \left\{ \tanh^{-1} \left[1 - \left(\frac{r_c}{r_t} \right)^2 \right] - \tanh^{-1} [\cos(\alpha)] \right\}, \quad (5.4)$$

which is derived in the Appendix in Section A.4.

The setpoint needs to be kept low to ensure a large spreading resistance, as shown in Section 4.6, so during testing various setpoints were trialled and it was discovered that the RMN-25PT300B probe exhibited stable current measurements for biases as low as ~ 1 V. This setpoint is also optimal for the photodetector because it lies in the ideal range specified in Section 4.1.2. Figure 5.2 shows the contact radii in the vicinity of this setpoint for both of the exemplar probes which were calculated for an AF-FeRh surface using equation (4.25). Platinum has an elastic modulus of 171 GPa and a Poisson's ratio of 0.39^[63] and PtIr has an elastic modulus of 210 GPa and a Poisson's ratio of 0.38^[157]. The RMN-25PT300B and SCM-PIT-V2 probes have tip radii of 20 nm^[124] and 25 nm respectively.

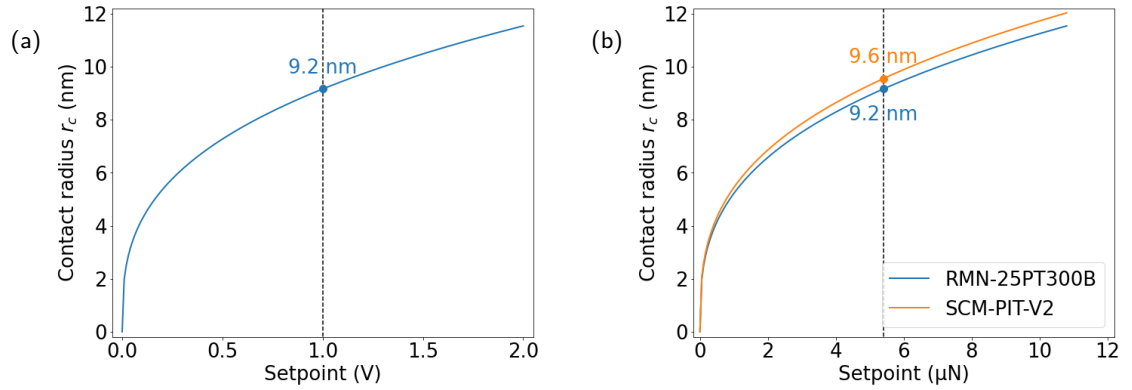


Figure 5.2: The contact radius for the two exemplar probes, the solid platinum RMN-25PT300B probe and the PtIr coated SCM-PIT-V2, on AF-FeRh in the vicinity of the optimal setpoint value which is marked with the dashed line. (a) The radius of the RMN-25PT300B for setpoints on the photodetector voltage scale. (b) The radius of both probes for setpoints on a force scale which was calibrated using nominal values.

The same applied surface pressure should be able to penetrate any contamination and establish stable connection for any probe. Both probes have similar tip radii and at the same force have similar contact areas thus the pressure will be approximately equivalent, so this shows that forces no larger than 5.4 μ N should be necessary and thus the contact radius for any electrical resistivity measurements should be $\lesssim 10$ nm. The maximal value of $r_c = 10$ nm will be used for the exemplar values in this chapter because

this corresponds to the lowest and thus worst-case spreading resistance. The RMN-25PT300B probe has side-angle 20° ^[124] so for this probe $R_3 \approx 3 \Omega$. The SCM-PIT-V2 probe has tip height $12.5 \mu\text{m}$ and the same side-angle so using the expression for a hollow cone $R_3 \approx 18 \Omega$.

Tip-sample interface resistance R_4

R_4 is the tip-sample resistance which has three components: constriction of the tip-apex $R_{4,\text{tip}}$, spreading within the sample $R_{4,\text{sam}}$, and impurity contact resistance $R_{4,\text{imp}}$. The constriction and spreading resistances are explained in the context of SSRM in Section 4.6. The impurity contribution $R_{4,\text{imp}}$ is not able to be directly characterised because it is due to surface contamination such as impurities and the condensation of water molecules, and also contains a contribution from the effect of the heterojunction formed from the different work functions of the tip and sample surface^[133]. Equation (4.36) may be used for each probe to give $R_{4,\text{tip}} \approx 3 \Omega$ for the RMN-25PT300B probe and $R_{4,\text{tip}} \approx 6 \Omega$ for the SCM-PIT-V2 probe. Equation (4.36) may also be used for $R_{4,\text{sam}}$, using the room temperature AF-FeRh resistivity of $3.0 \times 10^{-6} \Omega \text{m}$ from Figure 3.6 and calculating an approximate corresponding FM-FeRh resistivity of $2.0 \times 10^{-6} \Omega \text{m}$ using the magnetoresistive induced drop of 33% also observed in Figure 3.6. This yields a spreading resistance of $R_{4,\text{sam}} \approx 75 \Omega$ for AF-FeRh and $R_{4,\text{sam}} \approx 50 \Omega$ for FM-FeRh. This difference provides the localisation of the measurement and demonstrates how a modified SSRM approach may be used to characterise electrically conductive films.

Macroscopic sample resistance R_5

R_5 is the resistance of the current paths through the sample itself and for thin films is calculated from the sheet resistance. The bulk resistivity may be calculated for a sample of thickness t using^[158]

$$\rho = \frac{V}{I} t \frac{\pi}{\ln(2)} F, \quad (5.5)$$

where V/I is the observed ohmic bulk resistance R_5 and F is some geometric correction factor^[158]. The factor F tends to unity for samples which have thickness much less than the other two dimensions and so in thin films this may be neglected^[158]. This yields

$$R_5 = \frac{\ln(2)}{\pi} \frac{\rho}{t} \approx \frac{\rho}{4.5t}, \quad (5.6)$$

which is similar to the spreading resistance equation (4.36) suggesting that thin film resistance is akin to a lateral spreading resistance. The corresponding values for 40 nm thick FeRh are therefore $R_5 \approx 17 \Omega$ for AF-FeRh and $R_5 \approx 11 \Omega$ for FM-FeRh. A hybrid film HY-FeRh features equal areas of regions of both magnetic orientations so the resistivity and hence resistance would be the mean and thus $R_5 \approx 14 \Omega$.

Conductive paint and puck resistance R_6

Finally, R_6 is the resistance of the conductive paint, the puck, and the interfaces between film, paint, puck, and sample stage. This was measured using a standard handheld multimeter to be $R_6 \lesssim 1 \Omega$.

5.2.1 Discussion of values and comparison of probes

In all cases R_1 , R_6 , and R_7 may be neglected because these are found to be collectively $\lesssim 1 \Omega$. This leaves the total system resistance to be

$$R_{\text{total}} = (R_2 + R_3 + R_{4,\text{tip}}) + R_5 + R_{4,\text{imp}} + R_{4,\text{sam}} \equiv R_{\text{probe}} + R_5 + R_{4,\text{imp}} + R_{4,\text{sam}} . \quad (5.7)$$

The sample configuration will not be changing during the measurement, so R_5 is a constant term and as long as the force setpoint is consistent and impurities are minimised the only variation should be from the local resistivity in sample spreading resistance. More specifically, the resistance is

$$R_{\text{total}} = R_{\text{quant}} + R_{\text{contact}} \quad (5.8)$$

where R_{quant} is the quantified resistance of the system and $R_{\text{contact}} \equiv R_{4,\text{imp}}$ is the resistance due to impurities in the tip-sample contact.

In a high resistivity sample such as those typically investigated by C-AFM, TUNA, or SSRM, R_{probe} and R_{contact} may be ignored because they will be negligible alongside $R_{4,\text{sam}}$ and R_5 . However, on a metallic surface these parameters are highly relevant. The RMN-25PT300B probe has been found to have $R_{\text{probe}} \approx 6 \Omega$ and the SCM-PIT-V2 probe to have $R_{\text{probe}} \approx 88 \Omega$. The sample used in this work is a hybrid film with $R_5 \approx 14 \Omega$ and the estimated tip radius is 10 nm. This means that when using RMN-25PT300B, $R_{\text{quant}} \approx 95 \Omega$ for AF-FeRh compared with $R_{\text{quant}} \approx 70 \Omega$ for FM-FeRh, a drop of $\sim 25 \Omega$, and when using SCM-PIT-V2, $R_{\text{quant}} \approx 177 \Omega$ for AF-FeRh compared with $R_{\text{quant}} \approx 152 \Omega$ for FM-FeRh. These values are summarised in Table 5.2. Budget Sensors reported R_{total} in the regime of 300Ω for their platinum coated probes on a platinum film^[133] so assuming a similar value is valid here it may be concluded that both probes could theoretically be used to observe the drop in resistance, although the solid platinum RMN-25PT300B probe is ultimately superior to the PtIr coated SCM-PIT-V2 probe.

Probe	R_{quant} on AF-FeRh	R_{quant} on FM-FeRh	Relative decrease
RMN-25PT300B (platinum)	95 Ω	70 Ω	26%
SCM-PIT-V2 (PtIr coated)	177 Ω	152 Ω	14%

Table 5.2: The quantifiable resistance R_{quant} for each of the probes and FeRh magnetic ordering of interest.

It is important to consider the thermal dependence of probe resistance when confronted with the dissipation of electrical energy in the narrow probe. The thermal dependence of resistance is stated in

equation (2.98) to be $R = R_0 (1 + \alpha \Delta T)$, where R_0 is the resistance at the reference temperature of 20°C ^[63], α is the thermal coefficient of resistance, and ΔT is the change in temperature from the reference temperature. Platinum has a coefficient of $\alpha = 0.0039\text{ K}^{-1}$ ^[63] so a $1\ \Omega$ change in the calculated resistance of $6\ \Omega$ for the RMN-25PT300B probe requires a temperature change of 43 K . PtIr has a much lower coefficient of $\alpha = 0.0013\text{ K}^{-1}$ ^[63], but the much larger reference resistance R_0 means that a $1\ \Omega$ change in the calculated resistance of $88\ \Omega$ for the SCM-PIT-V2 probe requires a temperature change of just 8.7 K .

This demonstrates that the solid platinum probe exhibits a much smaller absolute change in resistance with temperature, and so Joule heating will have far less effect on the measured resistance. There will possibly still be drift of $\sim 1\ \Omega$ whilst using this probe but this is far below the expected change in $R_{4,\text{sam}}$ for even relatively high setpoints on FeRh. Consequently, the thermal resistance effects will just slightly reduce the percentage change and thus marginally impede the contrast of later measurement traces in the scan.

There is an additional significant complication that has hitherto remained unconsidered. The observed resistance change with a contact radius of 10 nm has a theoretical magnitude of $25\ \Omega$ and will be less if a higher contact setpoint is applied, as will be shown in Section 5.4. This means that any variation in contaminants across the film surface would need to result in much less than 10% variation in a $300\ \Omega$ contact resistance else the transition would disappear under the noise of the contaminants. The film must therefore be cleaned very carefully prior to investigation.

5.2.2 Limitations of existing electrical resistivity characterisation techniques

The measurement regime of metallic conduction is outside the capabilities of existing electrical modes on commercially available AFM systems. The Bruker application modules were stated in Section 4.6 to service currents of μA or less so the system resistance order of magnitude $100\ \Omega \lesssim R_{\text{total}} \lesssim 1000\ \Omega$ necessitates either very low applied voltages or very high induced currents.

The bias values produced and measured by the Bruker NanoScope V controller are discretised in steps of $\sim 0.4\text{ mV}$ due to the resolution of the analogue-to-digital converters (ADCs). More specifically, the bias inputs record data in increments of $375.011 \dots \mu\text{V}$, which provides a maximum voltage of $\pm 12.3\text{ V}$ when utilising a 16-bit ADC. The value $\pm 12.3\text{ V}$ may be familiar to users of the Icon system as these are also the limits of the deflection signal from the quadrant photodetector; the same specification ADCs are used throughout the system. A smooth I-V curve is required for accurate and precise analysis due to errors being inherently large when fitting continuous functions to discretised data where the discretisation is of similar order of magnitude to the expected features; as a result applied biases should ideally have a range no less than around $\pm 500\text{ mV}$ to $\pm 1\text{ V}$. Using lower values means that the conducting electrons

have insufficient energy to tunnel through thin impurities and this has a notable impact on the number of failed sweeps where no conduction was observed. The application of higher voltages would permit tunnelling through thicker impurities and would increase the absolute change in current arising from the change in resistivity, however the ensuing higher current density through the tip-apex has been observed to cause the probe to fail before a measurement scan has completed. This will be discussed further in Section 5.3.

A bias of up to 1 V and resistance $100\ \Omega \lesssim R_{\text{total}} \lesssim 1000\ \Omega$ means that ohmic currents will lie in the range $10\ \text{mA} \gtrsim I \gtrsim 1\ \text{mA}$. This is beyond the specifications of the Bruker application modules so clearly they cannot be used here and an alternate measurement setup must be used.

One possibility to re-enable the use of an application module would be to use a large shunt resistor with $R \geq 1\ \text{M}\Omega$ to produce the requisite low currents. This was considered and trialled, however the percentage change in sample resistance is below the noise floor due to the shunt resistance, necessitating at least five significant figure precision in the ohmic fit. The ammeters and linear fits do not have the precision to do this. The low resistance and high currents are therefore unavoidable characteristics of this measurement.

5.3 Resistive heating of the AFM probe

It was suggested in Section 4.6.1 that in general coated probes are unsuitable for high-current measurements due to their small cross-sectional area. This will now be revisited for the specifics of this work. The coating only forms $\sim 1\%$ of the cantilever thickness meaning the cross-sectional area of the electrically conductive region will be 1% of the area of a similar solid metal probe, and the RMN-25PT300B probe is both wider and thicker than a typical coated silicon probe. The result is that a particular current will result in current densities differing by a factor of over 500 between the two types of probe. The expected resistance of $100\ \Omega \lesssim R_{\text{total}} \lesssim 1000\ \Omega$ will produce electric currents in the milliamp regime, which will be close to the maximal current densities supported even by such mesoscale structures as solid metal AFM probes.

5.3.1 Simple modelling of Joule heating

The Joule heating of the RMN-25PT300B probe in the absence of thermal losses can be simulated using equation (4.45). The sweeps will be taken as part of a DataCube ramp and sweep cycle as detailed in Section 4.5, so consider the discretised time period $\tau = \tau_c$ which is the period of the entire approach/sweep/withdraw process. The settings used for the model are ramp rate $f_r = 30\ \text{Hz}$ and hold

time $\tau_h = 150$ ms. The cycle period τ_c is given by

$$\tau_c \approx \tau_h + \frac{2}{f_r}. \quad (5.9)$$

The factor of 2 is because the system cannot always ramp at the specified rate and occasionally requires extra time to stabilise certain ramps, but note that this factor is just estimated from experimental observation. The factor grows with ramp rate so it is still faster to use the setting of $f_r = 30$ Hz with the approximate factor of 2 than $f_r = 15$ Hz where the factor is reduced. The effective-current correction factor ϵ used in equation (4.45) is multiplied by τ_c/τ_h in order to take a weighted average of energy dissipation over the period τ_c , giving $\epsilon = 13/9\sqrt{3}$ for these settings.

The probe has known parameters of width $w = 110 \mu\text{m}$ ^[124], thickness $t = 4.5 \mu\text{m}$ ^[156], reference resistivity $\rho_0 = 1.0 \times 10^{-7} \Omega\text{m}$, thermal coefficient of resistance $\alpha = 0.0039 \text{K}^{-1}$, mass density $\rho_m = 2.15 \times 10^4 \text{kg m}^{-3}$, and heat capacity $c = 133 \text{J kg}^{-1} \text{K}^{-1}$ ^[63]. The example current has a maximum of $I = 5$ mA. Figure 5.3 shows the resulting curve from using these values to iteratively calculate equation (4.45).

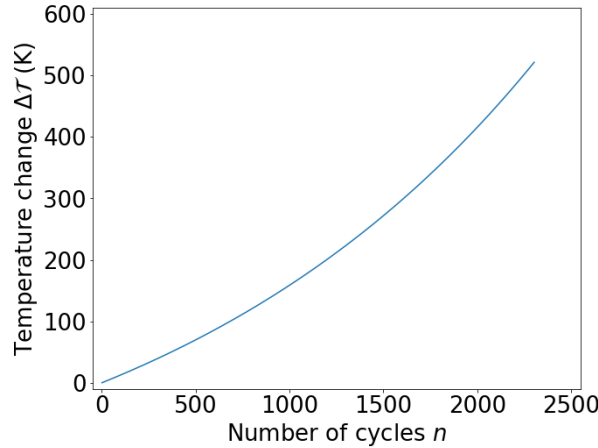


Figure 5.3: The simulated Joule heating of the RMN-25PT300B AFM probe over 2304 DataCube cycles. Thermal losses have been neglected so this is a significant overestimate and not a true representation, however the probe is not optimised for such losses and so this does serve to demonstrate the severity of the resistive load.

The number of cycles used relates to a single scan with resolution of $48 \text{px} \times 48 \text{px}$. The temperature grows very rapidly and in the absence of heat loss would reach 100°C within just 700 cycles. However, it is important to remember that this basic model does not account for radiative, conductive, or convective losses so is not a true description of the system, but is instead a significant overestimate. It was explained in Section 4.6.1 that the probe geometry and composition are not conducive to such losses though, so this simplistic model does at least serve to demonstrate the severity of the resistive load experienced by the mesoscale probes during these measurements.

5.3.2 Preece equation applied to an AFM probe

The Preece equation was introduced in Section 4.6.1 and the Preece coefficient B for platinum is $0.057465 \text{ A mil}^{-3/2} \approx 4.5 \times 10^5 \text{ A m}^{-3/2}$ [140]. Using equation (4.51) with the RMN-25PT300B cantilever dimensions gives a maximum sustainable current of $I_f = 96 \text{ mA}$, which is an order of magnitude beyond the expected current so the cantilever itself should not fail unless biases of $\sim 10 \text{ V}$ are applied. Note however that this equation is not intended for long-term resistive loads [142] and assumes idealised heat dissipation from the conductor. Note also that this assumes a room temperature environment, but the loss mechanisms in a heated environment will be reduced thus I_f would be significantly decreased.

The approximately conical tip is much narrower than the cantilever. Equation (4.50) rearranges to give the minimum radius r_f for some current I to be

$$r_f = \frac{1}{2} \left(\frac{I}{B} \right)^{2/3}. \quad (5.10)$$

Considering a current of up to 5 mA and using $\epsilon = 13/9\sqrt{3}$ as determined in Section 5.3.1 yields $r_f = 1.3 \mu\text{m}$. Assuming a constant side-angle of 20° this radius occurs at a height of $3.6 \mu\text{m}$ above the apex. This lower region is at risk of failure, however the rest of the probe is much wider so will be at a lower temperature, and the high thermal conductivity of platinum [63] should allow this dissipated energy to readily flow into the rest of the probe. This is assumed to be the reason that the apex and surrounding material of the platinum probe does not appear to melt during use despite electric current densities far exceeding the supposed maximum limit.

5.3.3 Discussion of resistive heating and choice of probe

Recall from Section 4.6.1 that Jiang et al. [107] empirically investigated the failure of coated probes due to Joule heating. The probe degradation provides a shunt resistance and allows the existing application modules to produce ohmic I-V curves, but large shunt resistances have already been stated to obscure the measurement of interest. The values presented in that section make it very clear that a coated probe such as SCM-PIT-V2 will not survive the resistive loads of the measurement discussed in this chapter. Instead, a solid metal probe must be used, and even then overloading the probe remains a real concern.

The significant Joule heating precludes the use of the heater stage for heated measurements, for example to characterise changing resistance with heating, because this would exacerbate the thermally strained tip which is already operating far beyond the limit predicted by the Preece equation. Cooled measurements on the heater/cooler stage could be performed though, and may even be superior to ambient measurements due to the enhanced thermal gradients between the probe and the environment resulting in expedited energy dissipation.

There are multiple solid platinum probes available commercially [124] so it was possible to select one

which best matched the required parameters. Spring constants of 10 to 20 nN nm^{-1} typically result in the setpoint range of the AFM photodetector aligning with the SSRM regime of 1 to $10 \mu\text{N}$, but this is of course also dependent on deflection sensitivity which is inherently variable. Additionally, shorter probes are preferred, hence the use of RMN-25PT300B over the similar but longer RMN-25PT400B^[124], because this minimises cantilever resistance and ensures the Joule heated probe is as close as possible to the heat-sink formed by the probe substrate.

Adama Innovations manufacture doped diamond probes which provide an alternate source of uncoated electrically conductive probes^[159] and would be more stable under resistive load than platinum. However, the resistivity of this doped diamond is $4 \times 10^{-5} \Omega \text{ m}$ ^[159] as opposed to the $1.0 \times 10^{-7} \Omega \text{ m}$ of platinum, and that extra order of magnitude would decrease the percentage change in R_{total} below the noise floor of the measurement.

5.4 Setpoint and spatial resolution

The choice of setpoint is an important decision. A larger setpoint is useful to puncture any debris or contamination layers and form a good ohmic contact with the surface, while setting the setpoint too high can compromise the contrast in the measured resistance or even damage the tip. Equation (4.36) states that

$$R_{4,\text{sam}} \propto \frac{1}{r_c} \quad (5.11)$$

and equation (4.21) gives

$$F \propto r_c^3 \quad (5.12)$$

so

$$R_{4,\text{sam}} \propto F^{-1/3} \quad (5.13)$$

and more importantly

$$\Delta R_{4,\text{sam}} \propto F^{-1/3}, \quad (5.14)$$

where $\Delta R_{4,\text{sam}}$ is the difference between the spreading resistances of AF-FeRh and FM-FeRh. Thus the setpoint must be small enough that $\Delta R_{4,\text{sam}}$ remains a significant percentage of R_{total} .

A resistance change of at least $\Delta R_{4,\text{sam}} \sim 10 \Omega$ is the target for this methodology because this would provide a change of at least 1% even for the upper predicted limit of $R_{\text{total}} \sim 1000 \Omega$, and three significant figure precision is feasible to achieve. Equation (4.36) gives the required contact radius for $\Delta R_{4,\text{sam}} \geq 10 \Omega$ to be $r_c \leq 7.9 \text{ nm}$. The correlating setpoint may then be found using equation (4.21), the AF-FeRh elastic modulus $E = 198 \text{ GPa}$ and Poisson's ratio $\nu = 0.32$ ^[15], and the platinum parameters $E = 171 \text{ GPa}$ and $\nu = 0.39$ ^[63], to be $F \leq 3.5 \mu\text{N}$. Another consideration is the malleability

of platinum: excessive forces on the tip could damage it, significantly increasing r_c , or even attach small pieces of debris which would impede the electrical conduction.

The elastic modulus defect was introduced in Section 2.9.1 and implies an increased contact radius for the same setpoint on FM-FeRh compared with AF-FeRh, which could result in a resistivity change through artefact rather than measurement. However, under AFM measurement conditions the defect is expected to be a fall of $\sim 1\%$ ^[39] corresponding to a $< 0.3\%$ rise in contact radius. The resulting fall in spreading resistance is therefore $< 0.3\%$ while the resistivity drops by $> 30\%$, so the modulus defect will have no noticeable effect on measured resistance.

5.4.1 Spatial resolution of the measurement

The observed spatial precision of SSRM on silicon is $\sim 20\text{ nm}$ ^[160] with the use of setpoints as high as $10\text{ }\mu\text{N}$, which demonstrates that spreading resistance is essentially localised to the contact diameter $2r_c \sim 10 - 20\text{ nm}$ plus an adjacent small oblate hemispheroid within the sample where the spreading resistance occurs. The resolution of the silicon results suggests this spreading distance r_s is of similar order or less than the contact radius. Indeed, it is reasonable to assume that $r_s \sim \lambda$ where λ is the mean free path of conduction electrons.

The non-zero spreading region volume $\mathcal{V}(r_s)$ will result in an averaged effective resistivity of the region under the tip, such as

$$\rho_{eff} = \frac{1}{\mathcal{V}} \int_{\mathcal{V}} \rho d\mathcal{V}. \quad (5.15)$$

This averaging effect will show any changes in resistivity in the correct locations, albeit with sigmoidal edges meaning the cross-section of a striped sample with pitch near the resolution limit would appear somewhat sinusoidal rather than square wave.

The small contact radius and evidenced small spreading distance suggests that SSRM on metallic surfaces can readily resolve features below 100 nm . However, this is not quite as low as can be achieved with C-AFM or TUNA on semiconductor surfaces which exhibit no spreading effects.

5.5 Surface contamination and oxide layers

The cleanliness of the surface is much more important for electrical resistance measurements than other AFM modes. For example, magnetic measurements may be affected by pieces of debris but uniform contamination should not affect the lift mode interleave measurement beyond a slight reduction in contrast.

A small contact resistance R_{contact} is required for maximal percentage change $\Delta R_{4,\text{sam}}/R_{\text{total}}$, so dirt

and debris must be cleared to permit a clean tip-sample contact. This includes residual lithography resist or even native oxide layers. The first step is to clean the sample as described in Section 4.10, using polar and non-polar solvents in an ultrasonic cleaner, and following this minimise any exposure to atmospheric conditions outside of a cleanroom environment.

A 4 nm platinum cap is sometimes used to prevent oxidising of FeRh films^[57], but care must be taken when using capping layers on samples intended for electrical resistivity characterisation. The metallic resistivity characterisation is enabled by the initial scattering of conduction electrons upon encountering the sample surface so the platinum cap must not scatter the conduction electrons before they enter the underlying film. This requires ballistic or quasi-ballistic transport through the capping layer which occurs for thicknesses $t \lesssim \lambda$ ^[161]; in platinum $\lambda = 2.8 \text{ nm}$ ^[162] meaning the cap ideally cannot be thicker than $\sim 2 \text{ nm}$. This is around 10 atomic layers of platinum which has an approximate lattice constant of 0.39 nm and an $Fm\bar{3}m$ structure^[63], plus films over 1.5 nm demonstrate continuous conduction^[163] and thus must form a continuous film, so it is reasonable that a consistent platinum film could be deposited at this thickness. Precise rate testing would be required before deposition due to the strict limits of $1.5 \text{ nm} < t < 2.0 \text{ nm}$ imposed. The cap would have the positive effect of reducing R_5 by providing an additional path with a ρ/t ratio $4.5\times$ that of the existing 40 nm HY-FeRh film, but the sheet resistance R_5 is so low relative to R_{contact} that the benefit is negligible.

Unusually, the oxide layer formed on FeRh has electrically conductive properties. Recall that in ambient conditions the resistivity of single-crystal Fe_3O_4 is $3.2 \times 10^{-5} \Omega \text{ m}$ ^[103;104] and the oxide thickness formed on the FeRh surface is typically between 1 nm and 2.5 nm ^[18;97]. The mean free path of electrons in Fe_3O_4 is between 0.5 nm and 0.8 nm ^[164] so the spreading resistance will occur within the oxide. This means the contrast will be lost, but ohmic behaviour will still be seen via a shunted signal. An estimate of the magnitude of the shunt resistance term may be made, by modelling the contact as a simple disc of thickness equal to the oxide thickness $\sim 2 \text{ nm}$ and of approximate area πr_c^2 where $r_c \approx 10 \text{ nm}$. This gives a resistance of 200Ω , which is a similar order of magnitude to the total expected resistance and so significantly increases the measured resistance value. The consequence is that the measurement will still produce an ohmic resistance signal but with no indication that contrast has been blocked other than a higher R_{contact} . Care must be taken to identify and avoid this effect. Alternatively, the formation of $\alpha\text{-Fe}_2\text{O}_3$ would result in an effectively insulating barrier between the probe and the film and so no current signal will be detected.

The oxide $\alpha\text{-Fe}_2\text{O}_3$ has an elastic modulus of $E = 359 \text{ GPa}$ and Poisson's ratio $\nu = 0.12$ ^[165] and Fe_3O_4 has an elastic modulus of $E = 175 \text{ GPa}$ and Poisson's ratio $\nu = 0.37$ ^[165]. The RMN-25PT300B probe is used with a setpoint of $1 \text{ V} \sim 5.4 \mu\text{N}$ in this work and the deformation of a bulk oxide under this load may be calculated using equations (4.25) and (4.27) to give 0.83 nm for Fe_3O_4 and 0.48 nm for Fe_2O_3 .

These are much less than the expected oxide thickness so a conducting probe is unable to puncture the oxide in normal operation, not even enough to achieve ballistic conduction, so the presence of the oxide will completely prohibit accurate electrical resistivity measurements at oxidised sites.

Loose debris may be removed from the sample surface by performing a large area contact mode scan with a generic AFM probe prior to using the electrical measurement probe. This will either push the debris to the edges of the scan area or the debris will stick to the tip, clearing the way for the electrical probe. If the debris were to adhere to the electrical measurement tip instead the contact quality would be impeded and electrostatic effects could occur due to potential capacitive behaviour involving the debris. The oxide layer may be thinned or removed at the same time if a probe of sufficient hardness and spring constant is chosen and scanned at a high setpoint.

Material hardnesses are measured using multiple metrics but the Vickers metric is one of the most commonly used^[166] and will be considered here. Confusingly this uses two unit systems: SI units and hardness units. The hardness units are written HV or omitted entirely and equate to kg mm^{-2} or kgf mm^{-2} . The unit kgf is kilogram-force and is related to SI units as $\text{kgf mm}^{-2} \equiv g^{-1}\text{MPa}$ where $g = 9.80665 \text{ m s}^{-2}$ ^[36] is the standard acceleration due to gravity.

The oxide $\alpha\text{-Fe}_2\text{O}_3$ ranges in hardness from 10,000 MPa to 11,000 MPa^[167] while Fe_3O_4 ranges from 6678 MPa to 7767 MPa^[168]. Platinum has a hardness of just 549 MPa^[169], so it is not possible to erode either oxide layer using the RMN-25PT300B probe. This is not surprising given platinum is known to be a relatively soft metal. The alternatives for hard-tipped AFM probes with high spring constants include the silicon probe RTESPA-300 from Bruker^[119] and the diamond-tipped probe AD-40-AS from Adama Innovations^[159], both with nominal spring constant 40 nN nm^{-1} . The hardness of silicon is known to be between 9,000 MPa and 10,200 MPa^[170] while the hardness of synthetic diamond is inherently difficult to measure but has been estimated to be 80,000 MPa^[171]. These are both significantly higher than for Fe_3O_4 and thus either will theoretically be adequate as Fe_3O_4 erosion tools, however only the diamond probe will be able to erode $\alpha\text{-Fe}_2\text{O}_3$ assuming the oxide forms a single crystal. It should be noted that these are the macroscopic hardnesses for these materials. Hardness is highly dependent on penetration depth below $1 \mu\text{m}$ ^[172] so the stated values are not strictly accurate on these length scales. However, they still serve as a good guide to the likely result.

In practice there are additional parameters to consider. The density of scan lines must be sufficient that every point on the surface is covered, and penetration must be sufficient that the cumulative eroded depth over multiple cycles is greater than the oxide layer thickness. The eroding scans are performed at a high setpoint of 10 V and both probes (RTESPA-300 and AD-40-AS) have a nominal deflection sensitivity of 80 nm V^{-1} , as determined from the AFM software defaults and considering the averages of previous calibrations. This gives a force setpoint of $32 \mu\text{N}$. $\alpha\text{-Fe}_2\text{O}_3$ has an elastic modulus

of $E = 359$ GPa and Poisson's ratio $\nu = 0.12$ ^[165], Fe_3O_4 has an elastic modulus of $E = 175$ GPa and Poisson's ratio $\nu = 0.37$ ^[165], silicon has a typical elastic modulus of $E = 160$ GPa and Poisson's ratio $\nu = 0.27$ ^[170], and diamond will be assumed to have $E \rightarrow \infty$ and $\nu \rightarrow 0$ for the purposes of calculating E^* . The RTESPA-300 probe has a nominal tip radius of 8 nm^[119] and the AD-40-AS probe has a nominal tip radius of 10 nm^[159]. The Hertzian contact radius and sample deformations may be calculated from these values using equations (4.25) and (4.27) with results given in Table 5.3.

Probe	Oxide	Contact radius (nm)	Sample deformation (nm)
RTESPA-300 (silicon)	$\alpha\text{-Fe}_2\text{O}_3$	12	3.2
RTESPA-300 (silicon)	Fe_3O_4	13	6.3
AD-40-AS (diamond)	$\alpha\text{-Fe}_2\text{O}_3$	8.7	7.6
AD-40-AS (diamond)	Fe_3O_4	11	11

Table 5.3: The Hertzian contact radius and sample deformation for each combination of probe and oxide at a force setpoint of 32 μN .

Both probes have sufficient hardness, penetrate deeper than the oxide layer, and have mostly similar contact radii, so the number of scan lines required for each are the same; hence on a theoretical basis either will be suitable for Fe_3O_4 . However, there are some practical considerations which favour a particular type of probe. Specifically, the results in Chapter 6 will show that the AFM was unable to maintain the setpoint contact with the diamond tip on the surface during the eroding scans, and the topography measurements captured during these scans just show severe noise. On the other hand, the RTESPA-300 probe maintains clean contact throughout and the channels show much cleaner images. This consistency is essential to guarantee that the oxide and other surface contamination will be uniformly removed from the film. A practical note is that the RTESPA-300 probes are much cheaper^[119] and are commonly already found in AFM laboratories, due to being a popular choice for tapping mode topography measurements.

The oxide removal process is performed by setting the AFM to perform continual high setpoint scans at the same site, then capturing a wider scan at a low setpoint to verify the success of the oxide erosion. A very wide-area contact mode scan, typically 20 μm , is then recorded at a low setpoint and serves two purposes. The first is that any debris from the eroded oxide will have been piled up around the scan site and this contact scan will push that away from the scan area. The second is to provide a reference image to aid relocating the site.

The AFM can be set to return to the original coordinates after changing over probes. However this will not be completely accurate due to small differences in tip position on the cantilever and the mechanical tolerance of the AFM stage positioning mechanism. The microscope camera is used to manually perform

fine adjustment of the stage position with respect to visible features on the sample surface. Wide-area scans may then be taken using this probe and compared with the previous wide-area images to correlate any specific features and offsets may then be applied to the x and y scanning piezos to adjust the precise location of the measurement region and complete the realignment. Initially engaging within $10 - 15 \mu\text{m}$ of the original site is considered a successful relocation, necessitating the wide-area scans and meaning the oxide erosion sites should be chosen to be near distinctive features to aid with relocation. The eroded site itself is difficult to resolve at the high scan rates required to image multiple exploratory $20 \mu\text{m}$ squares in a reasonable time frame, so prominent neighbouring features are helpful in minimising the time required.

5.6 Measuring the electrical resistance of metallic surfaces

The fundamental measurement is performed by using DataCube-TUNA to undertake bias sweeps at each image pixel and record the response. The resistance $R_{4,\text{sam}}$ cannot be characterised using a voltmeter connected in parallel because the only feasible connections for such a device would have to be before R_2 and after R_6 . The result is that all non-negligible resistances would be in parallel to this device and so the observed voltage drop would simply be the applied bias. Instead, the measurement device must measure current and be connected in series. This has the additional benefit that it need only connect to a single location of the circuit and thus is simpler to connect and disconnect from the system.

The connection of additional components is made possible by using a 'dummy' application module with BNC connection, as shown in Figure 5.4. Application modules were introduced in Section 4.6 and contain sensitive measurement circuitry which characterises the incoming signal from the probe. The application modules with BNC connections are referred to as dummy modules by Bruker because they are just the outer shell containing a single wire between probe connection and BNC, with no other components present. This particular device is a modified scanning capacitance microscopy (SCM) module on loan from Bruker so does contain SCM measurement components but these are superfluous and shall remain unused; purpose built dummy modules are available to purchase on request. The cable permanently attached to the module is the data cable for the SCM functionality and is not used in this work.

One of the gold sockets at the base of the module is routed directly to the central pin of the BNC connection, with the outer sheath of the BNC being pathed to ground via the module shell and the Icon scanning head. The other connects to the SCM measurement components which would characterise the sample capacitance and send a data signal along the application module cable. Standard electrical measurement probe holders such as the DTRCH-AM^[119] are compatible with these sockets, meaning the central BNC pin may be electrically connected directly to the AFM probe and thus tip. The dummy

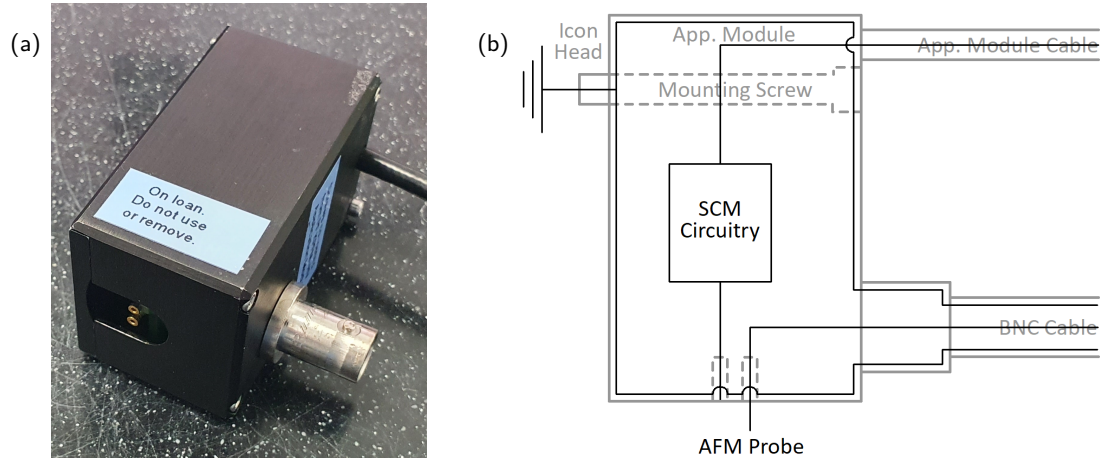


Figure 5.4: The dummy application module used to directly connect BNC components to the AFM probe. (a) A photo of the module. (b) A schematic representation of the circuitry within the module. The casing is metal and the back and top faces are in direct contact with the grounded Icon scanning head, but the mounting screw was chosen to be labelled as ground because it forms the strongest mechanical contact.

module and any components attached to the BNC cable replace the ground in Figure 5.1 so either a return current must be passed along the outer sheath of the BNC cable or the component must provide a replacement ground. The return current is not a suitable option for larger currents than those used in standard TUNA, i.e. $> 1 \mu\text{A}$, because the current will have to pass through the Icon head itself which would disrupt the scanning piezos and possibly even damage the sensitive control electronics. Consequently, the outer sheath of the BNC cable must be isolated from the measurement circuit to avoid the Icon head being used as this ground.

Multiple approaches were considered in detail when determining how to measure the current flowing through the system. Direct measurement of the current was thoroughly explored through the use of a Keithley 2410 SourceMeter source measure unit^[173] (SMU) as an ammeter. The internal buffer of the 2410 SMU is only capable of storing 2500 source-measure values locally so real-time data transfer was performed via a GPIB-USB adapter and the PyVISA^[174] Python package running on a PC. However, the requisite short sweep time of the DataCube measurement at each pixel means that the sampling rate of the SMU was inadequate. Another problem with this technique was that the Keithley 2410 SMU constantly attempted to counter the potential difference using its floating ground, because it was supplying 0V and so tried to maintain 0V across its connections, and as a result it frequently reported very low or zero current. The BNC input connections of the Bruker NanoScope controller feature sampling rates of up to 50 MHz^[118], and so the 2410 SMU was therefore replaced by a voltage divider which connected to one of these high rate connection. This has further advantages because the AFM

then records the measured curves for each pixel within the standard capture file and provides real-time data to the user.

A voltage divider is a simple low-noise device wherein a voltmeter measures the voltage drop over a reference resistor with known resistance, and this may be used to determine the resistance of a second unknown resistor connected in series. Figure 5.5 shows the voltage divider circuit applied to the AFM. It works because the relative voltage drop over components of a series circuit equals the relative resistance, so

$$\frac{V_{\text{div}}}{V_{DC}} = \frac{R_{\text{div}}}{R_{\text{total}} + R_{\text{div}}} \quad (5.16)$$

where V_{DC} is applied voltage, V_{div} is the voltage drop over the divider resistor R_{div} , and R_{total} is the total resistance of the AFM measurement system defined in equation (5.7). Equation (5.16) may be rearranged to yield

$$R_{\text{total}} = R_{\text{div}} \left(\frac{V_{DC}}{V_{\text{div}}} - 1 \right) \quad (5.17)$$

which is dependent entirely on configurable or measurable parameters.

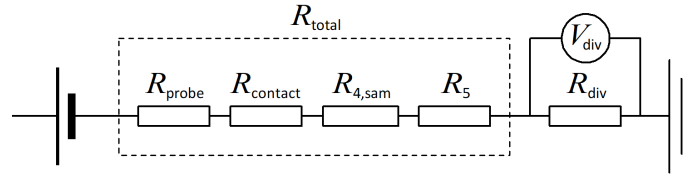


Figure 5.5: The constituent resistances of the system as part of a voltage divider circuit, wherein a voltmeter is used to measure the voltage drop over a resistor of known resistance R_{div} .

The process to implementing a DC circuit using BNC components is not immediately obvious. Figure 5.6 shows the resulting voltage divider design. The T-junction component connects all three inner pins to one another and also connects all three outer sheaths together, meaning the devices connected to each branch are in parallel. One branch was connected to the NanoScope V Controller port Input1, which provided the voltmeter and the ground, while a BNC terminator was connected to the other branch. The impedance of standard BNC components is 50Ω meaning when used in a DC circuit a terminator provides a very convenient 50Ω resistance between the outer and inner contacts of the junction. The outer sheath of the cable was isolated using a pair of BNC to 4 mm banana plug adapters, which only provide a conductive path for the inner BNC pin and not the outer sheath.

The signal access module (SAM) described in Section 4.8.4.1 initially appears to provide an alternative to the custom BNC application module, where the voltage divider would instead connect to the Tip Bias or Sample Bias BNC connections. However, this requires a direct and unimpeded conductive path between the BNC connections on the SAM and the tip or sample, and testing with a multimeter determined that no such path exists. This is not surprising because BNC electronics are designed for

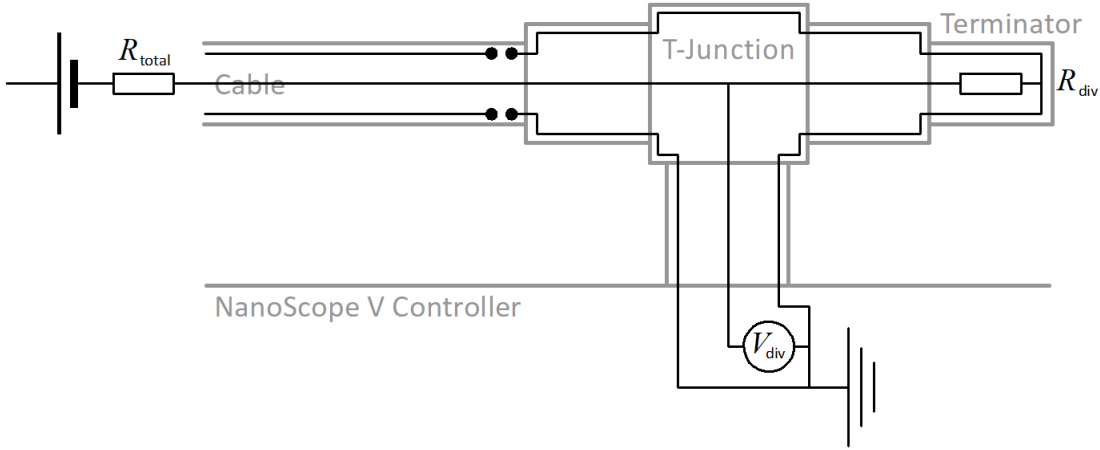


Figure 5.6: The voltage divider circuit from Figure 5.5 overlaid onto a simplified schematic of the components. The inner and outer conductors of the BNC components are connected only by the terminator resistance and the controller voltmeter. The outer conductor of the cable is electrically isolated from the T-junction to prevent the current from returning towards the AFM head.

communication of potentials rather than DC conduction.

The relative voltage drop over the sample should be as high as possible so that any change in measured resistance is maximised. However, in order for any effects to be measured the drop over the divider resistor needs to be as high as possible so that the change in curve gradient is clear. Qualitatively this suggests the optimal configuration for this system is to have $R_{\text{div}} \approx R_{\text{total}}$, or at the very least be within an order of magnitude. This may be shown quantitatively by maximising the change in gradient m_V of the measured voltage drop V_{div} as a function of applied voltage V_{DC} for different AFM resistances R_{total} . The different possible values of AFM resistance will be labelled $R_{t,i}$ with corresponding divider voltages $V_{d,i}$ and gradients $m_{V,i}$. The change in gradient is therefore

$$\Delta m_V \equiv m_{V,1} - m_{V,2} = \frac{V_{d,1}}{V_{DC}} - \frac{V_{d,2}}{V_{DC}} = \frac{R_{\text{div}}}{R_{\text{div}} + R_{t,1}} - \frac{R_{\text{div}}}{R_{\text{div}} + R_{t,2}} \quad (5.18)$$

where equation (5.16) has been used. This is maximised by setting the derivative equal to zero giving

$$\frac{d}{dR_{\text{div}}} \Delta m_V = \frac{R_{t,1}}{(R_{\text{div}} + R_{t,1})^2} - \frac{R_{t,2}}{(R_{\text{div}} + R_{t,2})^2} = 0 \quad (5.19)$$

which rearranges to yield maximal voltage divider sensitivity when

$$R_{\text{div}} = \sqrt{R_{t,1} R_{t,2}}. \quad (5.20)$$

The recommended reference resistance is therefore the geometric mean of the two AFM resistance values and for small changes in resistance these are approximately equal so $R_{\text{total}} \approx R_{t,1} \approx R_{t,2}$ and $R_{\text{div}} \approx R_{\text{total}}$. This means that the terminator resistance of 50Ω is adequate, although in future work an

approximately $200\ \Omega$ resistor could be soldered to BNC connectors and included between the terminator and T-junction to potentially improve precision and thus contrast.

The heater stage was used for the electrical resistivity measurements despite no heating being applied. This is because it exhibits less drift than the vacuum mount on the main sample stage, and because placing the sample on a raised column allows the short wire between the probe holder and the application module to curve freely. The current carrying cantilever lies parallel to the surface and Section 4.11 explained that the heater stage uses a magnetic field normal to the surface to secure the puck to which the sample is affixed. This means that a Lorentz force will be acting on the cantilever, with force^[58]

$$\vec{F} = I\vec{l} \times \vec{B} \quad (5.21)$$

where I is the magnitude of the current, \vec{l} is the vector along the cantilever length in the direction of conventional current flow, and $|\vec{B}| = 150\text{ mT}$ ^[155] is the field from the stage. These vectors are normal to each other so the resulting intensity of distributed load q may be written as

$$q \equiv \frac{F}{l} = IB. \quad (5.22)$$

The resulting deflection at the end of a cantilever of length l , width w , thickness t , and elastic modulus E is^[175]

$$d = \frac{ql^4}{8EI}, \quad (5.23)$$

where the moment of inertia in the direction of the deflection is^[176]

$$\mathcal{I} = \frac{w^3t}{12} \quad (5.24)$$

giving

$$d = \frac{3BIl^4}{2Ew^3t}. \quad (5.25)$$

A RMN-25PT300B probe of free length $300\ \mu\text{m}$ ^[124] carrying $I = 5\text{ mA}$ would therefore have a maximum deflection of $d = 8.9\text{ pm}$. This demonstrates that using the magnetic mounting does not affect the accuracy of the results obtained.

5.7 Postulated alternative approach

An alternative concept was considered which involves tailoring the sample to the existing electrical modes on commercially available AFM systems. A thin insulating film could be placed between the film under investigation and a grounded conductive film to act as a tunnel barrier. This would require lithographically preparing the sample stack such that the conductive film protrudes in such a way as to allow an electrical connection to be formed with the puck, as shown in Figure 5.7.

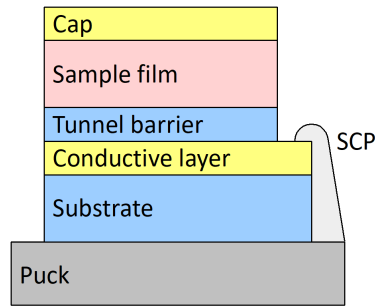


Figure 5.7: The multilayer stack required for the alternative approach.

The tunnel barrier would ensure highly localised measurements could be made, with the tunnelling probability being maximal at the point directly below the probe. The advantage of this approach is that sheet resistance is mitigated and $R_{4,sam}$ becomes negligible with R_5 being the characterisation resistance, and thus a capping layer may be used. Additionally, the tunnelling resistance adds a shunt resistance which enables the use of standard probes and application modules.

However, the inclusion of a shunt resistance has been discussed in Section 5.2.2 to be unsuitable for metallic characterisation, because the relative change in measured resistance would be below the noise floor of existing electrical measurement modes. Additionally, any pinholes or inhomogeneities in the tunnel barrier would result in incorrect tunnelling sites or even shorts which would permit high current flow and overload the coating on a standard probe, losing electrical continuity. Most significantly of all, only specially deposited stacks could be characterised using this technique, whilst the voltage divider approach proposed in this chapter is applicable to any conductive film.

5.8 Summary

In this chapter the different sources of resistance were outlined and the spreading resistance was identified as the localisation mechanism for nanoscale resistivity measurements. The limitations of the existing hardware were explained, with the low resistance and discretised bias requiring currents beyond the abilities of coated probes or existing Bruker application modules. Resistive heating was acknowledged through power considerations and the Preece equation. The choice of probe and possible spatial resolution of the measurement were discussed, and the motivation and process for surface cleaning and oxide removal were also explained. The development process for the voltage divider measurement system was presented and the final design explained. An alternative approach to enable existing hardware to be used on specially designed samples was considered but rejected. The developed characterisation methodology appears to be sound and may now be used to perform characterisation of a patterned FeRh film.

Chapter 6

Electrical and mechanical characterisation of FeRh

The developed electrical resistivity measurement system for metallic surfaces must now be evaluated by applying it to a high-contrast metallic sample. This chapter will begin by introducing the motivation and experimental procedure for doing so on magnetically patterned FeRh. The results from the proof-of-concept electrical resistivity measurements performed using the technique will be analysed in detail and the changes between each measurement explained. Nanomechanical results will also be demonstrated and the reasons for the lack of contrast will be explored. A method to unify the electrical, magnetic, and mechanical measurements will be introduced and the limitations when applying it to this sample will be acknowledged. Finally, to attempt to resolve some of these limitations the development of a new metal probe with ferromagnetic properties will be postulated and left open for future research.

6.1 Introduction

The previous chapter details the design and development of a system and accompanying methodology to enable electrical resistivity characterisation on the nanoscale. This system now needs to be tested on a metallic film with contrasting electrical resistivity in order to prove the concept and verify its viability as a new measurement technique. Additionally, the use of DataCube-TUNA presents an interesting opportunity to begin to amalgamate the different characterisation modes of magnetic, electric, and nanomechanical measurements into a single correlated operation.

The sample under investigation is an equiatomic FeRh film of thickness 40 nm on an MgO(001) substrate. This film was magnetically patterned using noble ion irradiation, which will be described more thoroughly in Section 7.1.2, yielding a metallic sample with regions of differing electrical resistivity. The dynamics of the patterned film will be investigated more thoroughly via magnetic measurements in Chapter 7, but for the purposes of this chapter it serves as an ideal test sample for the electrical resistivity measurement technique developed in Chapter 5.

6.2 Experimental procedure

The measurement process commences with the oxide erosion described in Section 5.5, with either the RTESPA-300 or the AD-40-AS probe being used. Both probes feature a nominal spring constant of $k = 18 \text{ nN nm}^{-1}$ [119;159] and nominal deflection sensitivity of $\gamma = 80 \text{ nm V}^{-1}$, meaning a defined setpoint of 10 V applies a force of approximately $32 \mu\text{N}$. The erosion was carried out at a scan angle of 90° meaning the probe was moved side-to-side and experienced torsional frictional deflection, rather than moving forwards and backwards where the resulting vertical deflection would have altered the applied force. Following the erosion each site was imaged with a wider scan size and lower setpoint to verify the success of the procedure. The depth was determined by fitting a top-hat function, defined as the product of two symmetric sigmoids, to a cross-section of the scan. This fit was especially useful given the surface roughness is on occasion a similar scale to the erosion depth, making accurate depth determination by eye difficult. The fit was unbounded and performed using non-linear least squares fitting via the Levenberg-Marquardt algorithm as implemented in the SciPy Python package [110].

The electrical resistivity measurements were performed using an uncalibrated RMN-25PT300B probe which has a nominal spring constant $k = 18 \text{ nN nm}^{-1}$ [124] and nominal deflection sensitivity $\gamma = 300 \text{ nm V}^{-1}$. This means a defined setpoint of 1 V is approximately $5.4 \mu\text{N}$, with a theoretical contact radius $r_c \approx 9.2 \text{ nm}$ and corresponding predicted maximum change in spreading resistance $\Delta R_{4,\text{sam}} \approx 27 \Omega$. The lack of calibration is not significant because the spring constant and deflection sensitivity will be the correct order of magnitude, so a calibration would simply scale all $\Delta R_{4,\text{sam}}$ or DMT moduli by a small scale factor close to unity and would not significantly affect contrast. The resistance sources described in Section 5.2 are not quantifiable with sufficient precision to measure quantitative local electrical resistivities, so this is inevitably a purely qualitative measurement. This is standard across AFM modes, with MFM being a prime example of a qualitative mode which is extremely difficult to directly quantify [125].

The data shown in this chapter is the first data taken with this newly developed AFM mode, so contrast is expected to be low and noisy until refinements can be made in future work; this is very much a proof-of-concept at this stage. The regular patterned stripes of alternating resistivity proved to be extremely useful in cutting through the noise to demonstrate the underlying success. The sample was always aligned so that the stripes would run vertically in the scanned image, so the mean value for each column was taken and the resulting curve plotted as a mean cross-section. This served to reduce the noise-related randomness present in the cross-sections and clarified any underlying pattern. The curve was then passed through a Savitzky-Golay filter [177] to reduce noise and aid the visualisation of the plotted data, while a sinusoidal fit was also applied to the original curve. This was another unbounded non-linear least squares fit and both the fit and filter were implemented using SciPy.

An additional tool that may be used to demonstrate the success of the measured signal is the fast Fourier transform (FFT)^[178], which provides rapid Fourier transform calculations and is also included in SciPy. The Fourier transform is a representation of any function as a summation of sinusoids and the resulting plot of the sinusoidal amplitude for each frequency shows peaks at significant periodicities in the pattern; the stripe pitch of 200 nm should result in a peak at $5\text{ }\mu\text{m}^{-1}$. The image must be equal to a whole number of half wavelengths so the Fourier transform is discretised into allowed frequencies of multiples of $1/2l$ where l is the image size, so larger images have higher precision FFT curves. The FFT curves provided in this thesis are typically capped at $20\text{ }\mu\text{m}^{-1}$ to crop away superfluous values and allow the region of interest to be clearly seen. The lower frequency values for each FFT curve are also discarded because the curve grows exponentially as frequency approaches zero. The FFT was applied in two ways: in one case it was applied to each row individually and the mean amplitude of each frequency was taken, and in the other case the FFT was simply applied to the mean cross-section.

It would be remiss not to acknowledge the caveat here: it is important to use judgement when using these tools to enhance and identify periodic behaviour. Images may have regular noise or other features on a similar frequency which can also result in an FFT peak. The mean cross-section should ideally remove this noise but this is not guaranteed. However, DataCube modes are inherently largely insensitive to scanning noise and surface artefacts so on this occasion the peaks and cross-sections are predominantly trustworthy.

The full characterisation process including oxide erosion was carried out at three locations on the surface of the magnetically patterned FeRh sample. All three of these will be discussed in the following sections, and these sites will be referenced as A, B, and C in chronological order.

6.3 Analysis of erosion procedure

6.3.1 Erosion of site A

The first resistivity characterisation to be carried out following the implementation of the oxide erosion procedure into the workflow was located at site A, and this was the first to exhibit stable metallic conduction behaviour.

The erosion was performed using an RTESPA-300 probe at a setpoint of $10\text{ V} \sim 32\text{ }\mu\text{N}$. Ten scans were carried out over a square of side length of $2.2\text{ }\mu\text{m}$ with 512 pixels per side and the result is shown in Figure 6.1. The scan rate was 1.0 Hz giving a scan speed of $4.4\text{ }\mu\text{m s}^{-1}$. The scan size was chosen to enable an electrical resistance measurement over a $2\text{ }\mu\text{m}$ square, however the emergence of a large feature in the corner meant that instead a $1\text{ }\mu\text{m}$ square was chosen to avoid the compromised area. The resolution was simply the default used for high-resolution imaging due to powers of 2 being recommended for AFM

scan sizes, and gives a pixel size of 4.3 nm which is approximately $1/3$ of the estimated contact radius of 12 – 13 nm given in Table 5.3. The scan speed was chosen experimentally: the highest value that allowed the tip-sample contact to remain stable was used.

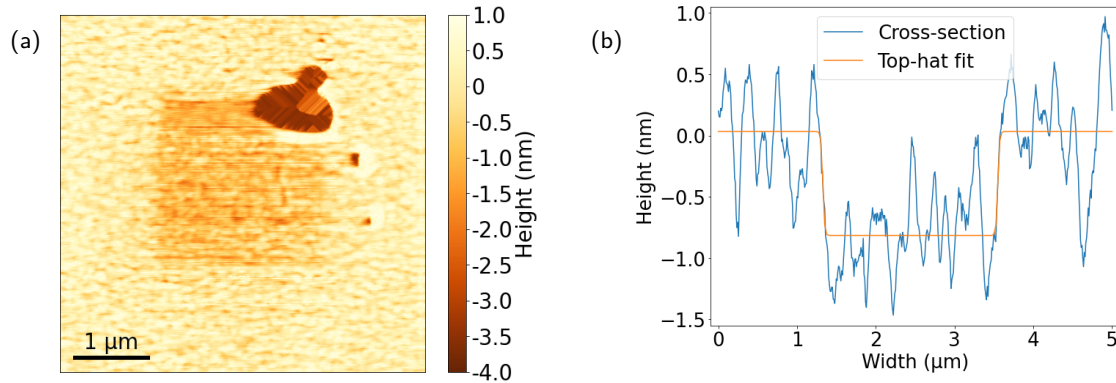


Figure 6.1: The topography of site A following oxide erosion, captured at a scan size of 5 μm . The eroded square clearly be seen in the topography image and its cross-section. (a) The topography contour of the eroded site. Contrast is impeded by the feature in the corner skewing the colour scale. The feature has been artificially reduced in size in this plot to allow the eroded square to be visible and the striations on this feature are artefacts of this reduction. (b) A cross-section through the eroded site with top-hat fit, giving the depth to be (0.85 ± 0.03) nm.

The top-hat function demonstrates that this is a cleanly defined erosion of nearly a nanometre depth, which is shallower than hoped. The fact the electrical resistance measurement succeeded regardless suggests ballistic conduction still occurred through the oxide which consequently cannot have been more than ~ 1.6 nm thick prior to erosion, placing it at the lower end of the range mentioned in Section 3.5. The success of the erosion with the silicon probe suggests that the oxide layer formed had stoichiometry Fe_3O_4 .

The scale of the cross-section plot makes it appear that the surface is extremely jagged, but this is simply because one axis is in μm and the other in nm, and it is much smoother in reality. The surface does have roughness, just not to the apparent exaggerated extent in the plot. The roughness is a similar frequency to the stripe pitch, which should raise suspicions regarding data validity despite the sensitivity of DataCube to such features. Upon closer inspection this frequency is seen to be sufficiently different to that of the stripes that it cannot falsely produce the measured electrical resistance pattern via artefacts.

6.3.2 Erosion of site B

The process was repeated to perform a second erosion at site B. This time the AD-40-AS diamond tipped probe was trialled to investigate whether the higher hardness would be beneficial compared to

the results obtained with the silicon probe used previously. The same setpoint of $10\text{ V} \sim 32\text{ }\mu\text{N}$ was used. Again, ten scans were carried out, but this time over a square of side length $3\text{ }\mu\text{m}$ to enable a $2\text{ }\mu\text{m}$ electrical resistance measurement even if the previous issue reoccurred. The result is shown in Figure 6.2. The resolution of 512 pixels was retained because it gives a pixel size of 5.9 nm which is $\sim 1/2 - 2/3$ of the estimated contact radius of $8.7 - 11\text{ nm}$ given in Table 5.3. The scan speed had minimal effect on stability for this probe so the frequency of 1.0 Hz was reused.

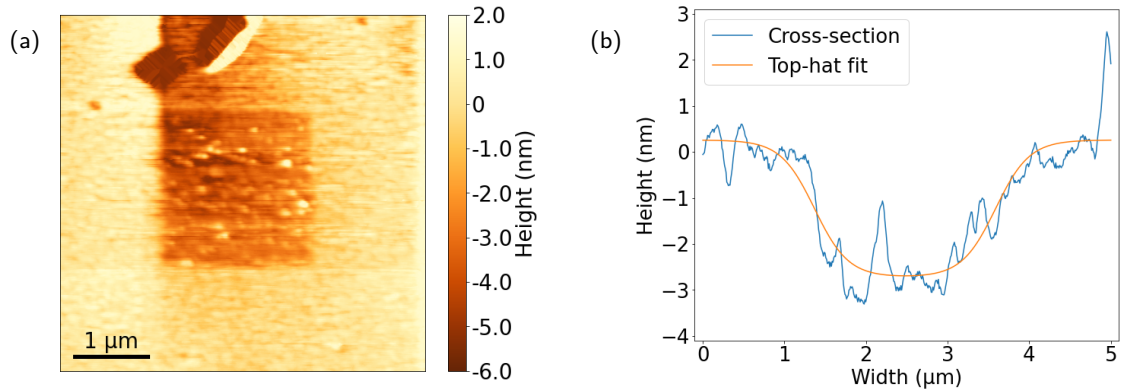


Figure 6.2: The topography of site B following oxide erosion, captured at a scan size of $5\text{ }\mu\text{m}$. The eroded region can clearly be seen in the topography image and its cross-sections. (a) The topography contour of the eroded site. Contrast is again impeded by a feature at the top but it is clear that the cleaning process was not as successful as in Figure 6.1. (b) A cross-section through the eroded site with top-hat fit, giving the depth to be $(2.98 \pm 0.09)\text{ nm}$.

The AD-40-AS was very unstable during the cleaning process and the AFM was unable to maintain good tip-sample contact despite refining all scan settings. This is reflected in the lower quality erosion which contains large peaks and is very sloped at one side; the sigmoids used in the top-hat fit are much wider than those fit to Figure 6.1b. However, the positive note to observe here is the depth of the erosion, which is larger than the expected oxide thickness and is likely due to the extreme hardness of diamond.

6.3.3 Erosion of site C

The poor quality of the erosion at site B is reflected in the corresponding resistivity measurements, which will be discussed in section 6.4.2. Consequently, the RTESPA-300 probe was reintroduced for the erosion of site C.

The same setpoint of $10\text{ V} \sim 32\text{ }\mu\text{N}$ was used and this time nine scans were done due to the increased duration arising from larger scan size. The eroded region was a square with side length $7\text{ }\mu\text{m}$ to enable a $5\text{ }\mu\text{m}$ electrical resistance measurement. The result is shown in Figure 6.3. The resolution was increased to 1024 px giving a pixel size of 6.8 nm which is approximately $1/2$ of the estimated contact radius of

12 – 13 nm given in Table 5.3. A scan rate of 0.66 Hz was used in an attempt to compromise between duration and stability, resulting in a scan speed of $9.2 \mu\text{m s}^{-1}$.

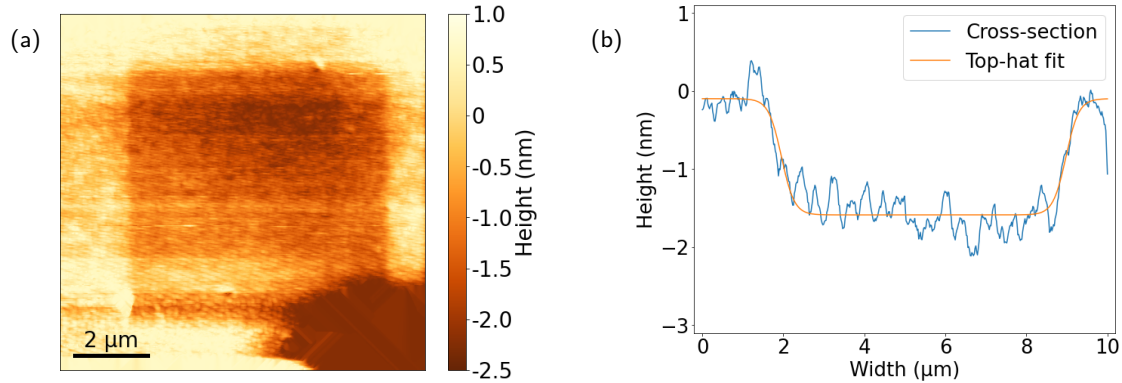


Figure 6.3: The topography of site C following oxide erosion, captured at a scan size of $10 \mu\text{m}$. The eroded region can very clearly be seen in the topography image and its cross-sections. (a) The topography contour of the eroded site. Contrast is again impeded by a feature, this time at the bottom. Compensation was difficult so the image is purely a qualitative indication and the whole square was in fact all eroded evenly. (b) A cross-section through the eroded site with top-hat fit, giving the depth to be $(1.49 \pm 0.03) \text{ nm}$.

The RTESPA-300 probe was far more stable than the AD-40-AS probe, even with the higher scan speed. The sides of the site are marginally sloped at the edges but not unduly so, and the roughness is lower than the previous silicon probe erosion shown in Figure 6.1. This erosion is deeper than that figure too, comfortably deep enough that any remaining oxide should exhibit ballistic conduction.

6.3.4 Erosion summary

The observations show that the RTESPA-300 silicon probe is an excellent candidate for oxide removal, suggesting the oxide stoichiometry to be Fe_3O_4 . Oxide erosion was most successful when carrying out approximately ten scans at a setpoint of $10 \text{ V} \sim 32 \mu\text{N}$, and with pixel spacing of up to 7 nm . The higher scan rate of the erosion at site C compared with site A is believed to have degraded the quality of the removal because the resistivity data in Section 6.4.3 was poorer than expected. Therefore the maximum recommended scan speed is approximately $4.4 \mu\text{m s}^{-1}$.

However, it should be noted that this removal may only be used for films consisting of a single metal, and is a destructive technique so certainly cannot be used on structures. Unfortunately, resistivity measurements are not possible through oxide layers so only structures formed from metals which do not oxidise may be characterised using the resistivity measurement methodology developed in Chapter 5.

6.4 Characterisation of surface resistivity

6.4.1 Resistivity of site A

The resistivity characterisation of site A following erosion is shown in Figure 6.4.

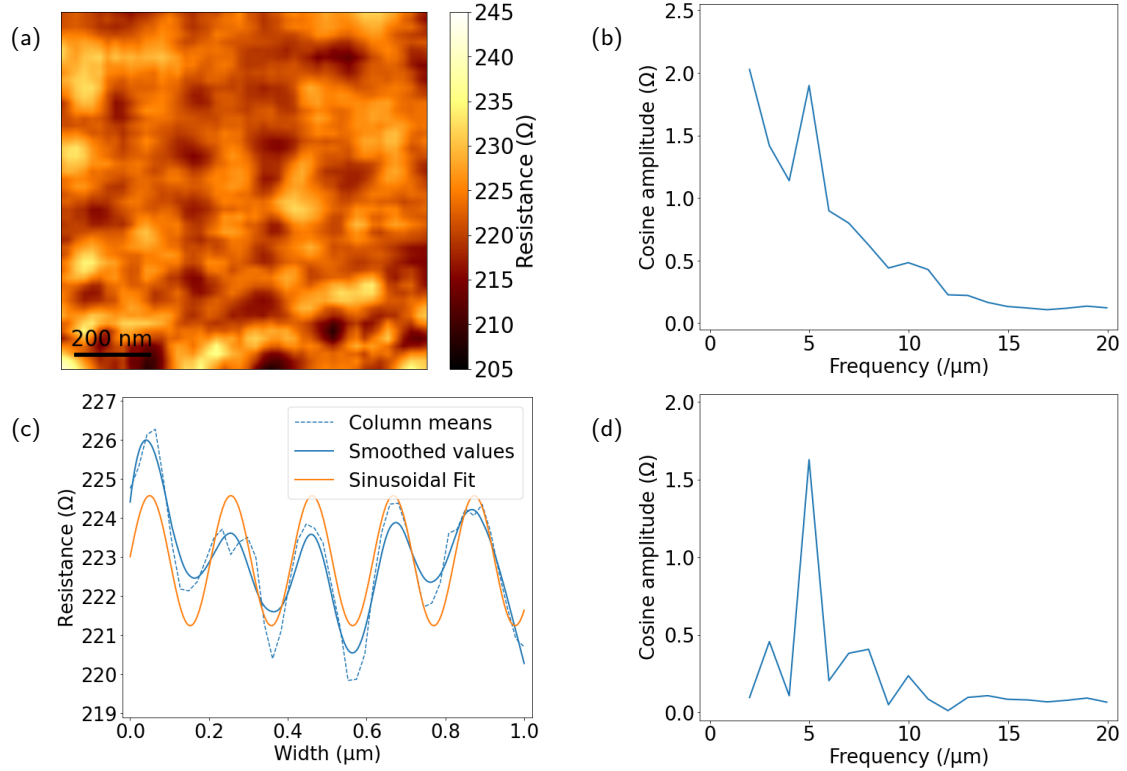


Figure 6.4: The resistivity characterisation of site A, carried out over a square with a side length of $1\mu\text{m}$ and 48 pixels per side. The ramp rate f_r was 30.5Hz and the hold time τ_h was 150ms giving an estimated cycle time of $\tau_c \sim 210\text{ms}$. The sweep range was $-1\text{V} \leq V_{DC} \leq 1\text{V}$ and setpoint was $1\text{V} \sim 5.4\mu\text{N}$. (a) The resistance contour calculated from the measurement showing the patterned stripes of alternating resistivity. (b) The mean row-by-row FFT curve for the resistance contour showing a clear peak at $(5.0 \pm 0.5)\mu\text{m}^{-1}$. (c) The mean value of each column along with filtered values to reduce noise and a sinusoidal fit. The fit has a pitch of $(206.1 \pm 0.9)\text{nm}$ and exhibits a resistance drop of $(3.33 \pm 0.12)\Omega$ or $(1.49 \pm 0.05)\%$. (d) The FFT curve for the resistance means showing a very clear peak at $(5.0 \pm 0.5)\mu\text{m}^{-1}$.

The contour in Figure 6.4a shows the stripes arising from the magnetic patterning. The resolution is low so it is actually easier to see the stripes in a smaller version of the image. The low pixel density was used to minimise Joule heating and reduce the time taken to run the scan in the event of multiple iterations of refinements being required; fortunately the methodology was sound and this measurement worked on the first attempt. The FFT curve in Figure 6.4b has a clear peak in the correct location,

although the small scan size has resulted in limited frequency precision. The stripes are especially clear when the means of each column are taken, shown in Figure 6.4c. The curve immediately shows the sinusoidal behaviour expected and the smoothed and fit curves match the original data very closely. The FFT curve in Figure 6.4d also supports this with a very large peak present at $5\text{ }\mu\text{m}^{-1}$.

The sinusoid fit does give an incorrect pitch of 206 nm, but there are only five peaks with fuzzy edges so the uncertainty in the fit is a significant understatement in context. Considering this, the determined value is satisfactorily close to 200 nm. The interesting values are the absolute resistance: the overall resistance $R_{\text{total}} \approx 223\text{ }\Omega$ which is less than the $\sim 300\text{ }\Omega$ expected. This suggests a very clean contact between tip and sample. However, the expected drop $\Delta R_{4,\text{sam}}$ was $25\text{ }\Omega$ which was not observed, with the resistance drop being just an eighth of that expected.

The most likely cause is a corresponding increase in contact radius. This could be due to the high setpoint deforming the platinum tip-apex, or possibly the tip picking up some conductive debris. This increased radius hypothesis is supported by the lower few lines of Figure 6.4a, which were the first to be recorded and show resistance values as low as $20\text{ }\Omega$ below the scan average in some stripes. A high contact radius would also aid in reducing R_{contact} , and would be expected to produce a noisier and very sinusoidal pattern, exactly as shown here.

Therefore, this first scan has been a very successful proof of concept. The stripes were resolved, especially in the mean cross-section, and the FFT plots have very large peaks. The contact resistance was lower than expected as was the change in resistance, but a reasonable hypothesis has been proposed. The small scan size and resolution meant that the measurement took less than 15 minutes to complete, so larger scans may now be considered.

6.4.2 Resistivity of site B

The resistivity characterisation of site B following erosion is shown in Figure 6.5.

The resistance contour map in Figure 6.5a is very poor quality showing no clear evidence of any vertical stripes. There do appear to be stripes running horizontally across the image but these are likely due to gaining or losing debris from the probe. The horizontal lines are known to be somewhat random and thus artefacts because the standard analysis of the mean cross-section and FFT curves were applied to the columns, in addition to the usual rows, where they just revealed randomness. The FFT curve in Figure 6.5b also does not show much of significance except for a small peak at $4\text{ }\mu\text{m}^{-1}$, but this is within the general noise amplitude of the FFT curve so cannot be attributed to anything physical.

The mean cross-section plot in Figure 6.5c offers a marginal improvement. There is some clearly periodic behaviour present and a sinusoid of expected pitch does correlate. The use of an unbounded fit lends

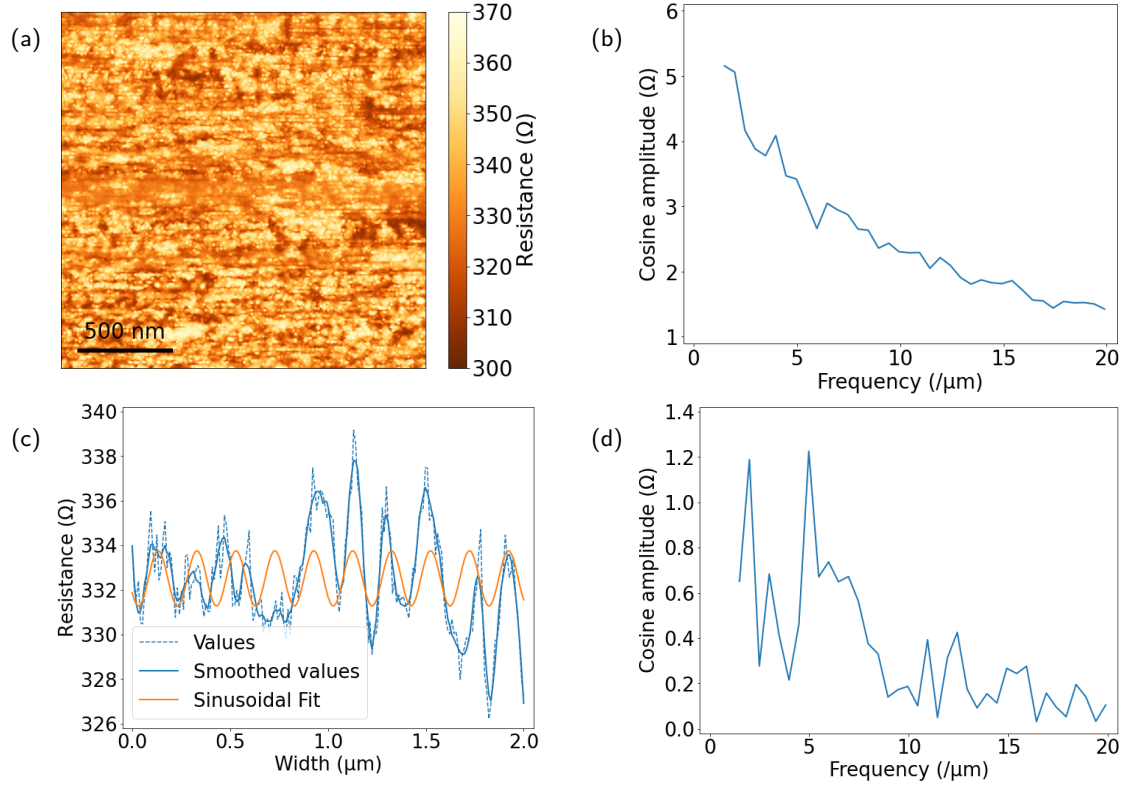


Figure 6.5: The resistivity characterisation of site B, carried out over a square with a side length of $2\mu\text{m}$ and 192 pixels per side. The ramp rate f_r was 30.5 Hz and the hold time τ_h was 150 ms giving an estimated cycle time of $\tau_c \sim 210\text{ ms}$. The sweep range was $-1\text{ V} \leq V_{DC} \leq 1\text{ V}$ and setpoint was $1\text{ V} \sim 5.4\mu\text{N}$. (a) The resistance contour calculated from the measurement showing no clear contrast. (b) The mean row-by-row FFT curve for the resistance contour showing a slight peak at $(3.98 \pm 0.25)\mu\text{m}^{-1}$. (c) The mean value of each column along with filtered values to reduce noise and a sinusoidal fit. The fit has a pitch of $(198.9 \pm 1.9)\text{ nm}$ and exhibits a resistance drop of $(2.5 \pm 0.4)\Omega$ or $(0.75 \pm 0.13)\%$. (d) The FFT curve for the resistance means showing a peak at $(4.97 \pm 0.25)\mu\text{m}^{-1}$.

credence to the correlation and suggests this is in fact driven by the stripes. The corresponding FFT curve in Figure 6.5d shows a strong peak at the expected frequency $5\mu\text{m}^{-1}$ and has amplitude equal to the fit sinusoid. The peak has quite a wide sub-peak to the side and this reflects the noise in the mean cross-section data.

The absolute resistance numbers are higher than the previous data in Figure 6.4 suggesting the contact was poorer. The sinusoid amplitude is again much smaller than would be expected but the data amplitude does rise towards the right-hand side of the data, which lies in the sloped region of the cross-section shown in Figure 6.2b. This side of the signal is cleaner in general, possibly meaning the deeper region was damaged by the erosion process.

This measurement is very poor and this can be attributed to the use of the diamond probe for erosion. The instability and extreme hardness appears to have resulted in an inconsistently eroded and possibly damaged surface. The contour and corresponding FFT curve show nothing of significance, and while the mean cross-section does show correlating periodic behaviour this is also very noisy and features a poor quality fit.

6.4.3 Resistivity of site C

Once erosion of this site was complete and confirmed a large scale characterisation was attempted over a square of size $5\text{ }\mu\text{m}$ and with resolution 512 px . The bias sweep resistance signal only survived for around 10 rows before becoming patchy, then failing completely after another 10 rows. This failure cannot be related to Joule heating because the number of successful bias sweeps was below that shown in the previous measurement in Figure 6.5, and had similar spacing between measurement sites. Additionally, temporarily doubling the setpoint and bias restored the probe to electrically conducting behaviour, suggesting that debris of some kind had accumulated at the tip-apex. High-resolution scans over a large area were not reattempted because these take ~ 26 hours to complete, and due to time constraints tinkering with such lengthy scans was not a feasible task. Instead, the probe with restored conduction was used on a smaller $2\text{ }\mu\text{m}$ area of the eroded site and the data generated by this characterisation is shown in Figure 6.6.

Once again the resistance contour map in Figure 6.6a is very poor quality with no evident stripes. However, it was noticed that the image thumbnail does faintly show vertical lines, so they are observable if the image is zoomed out beyond the noise limit. The noise is too severe to reliably remove from the full-size image though. As before, there appear to be lines running horizontally across the image, likely due to gaining or losing debris from the probe. The FFT in Figure 6.6b shows a small peak at $5\text{ }\mu\text{m}^{-1}$ which is above the noise floor of the curve and is most likely physical, showing an improvement over Figure 6.5b.

The sinusoid also exhibits a much improved fit in Figure 6.6c when compared with Figure 6.5c, with very consistent frequency and amplitude. The fit period is approximately 200 nm as expected and correlates to the data very well. The resistance drops by the same percentage as Figure 6.4c, suggesting the measurement was similar to the successful first attempt, except with some unidentified shunt resistance causing a smaller voltage than intended to be applied to the probe-sample system, and thus a seemingly higher resistance to be measured. This also ties into the observed baseline resistance being much higher than seen in the previous measurements. The corresponding FFT curve for this data is shown in Figure 6.6d to have a very strong peak at $5\text{ }\mu\text{m}^{-1}$, reinforcing the observed periodicity.

The faint stripes and clear mean cross-section behaviour makes it clear this measurement was able

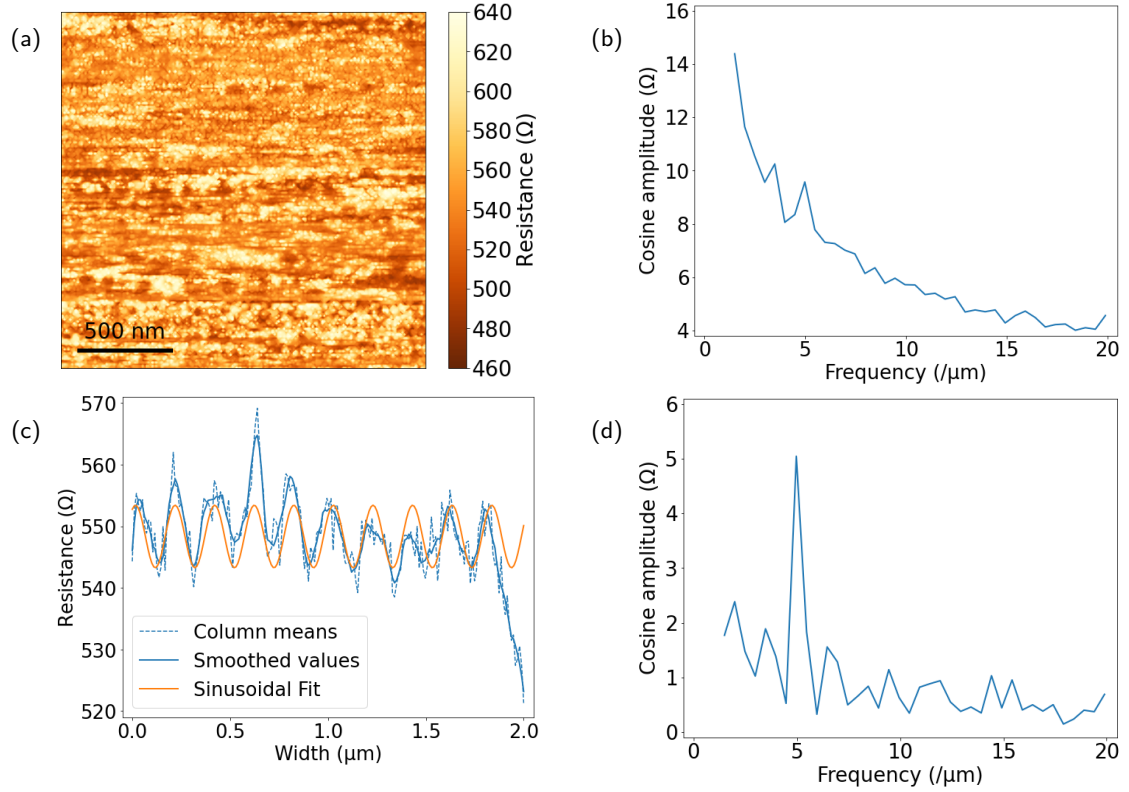


Figure 6.6: The resistivity characterisation of site C, carried out over a square with a side length of $2\mu\text{m}$ and 192 pixels per side. The ramp rate f_r was 30.5 Hz and the hold time τ_h was 150 ms giving an estimated cycle time of $\tau_c \sim 210$ ms. The sweep range was $-1\text{ V} \leq V_{DC} \leq 1\text{ V}$ and setpoint was $1\text{ V} \sim 5.4\mu\text{N}$. (a) The resistance contour calculated from the measurement showing no clear contrast. (b) The mean row-by-row FFT curve for the resistance contour showing a small peak at $(4.97 \pm 0.25) \mu\text{m}^{-1}$. (c) The mean value of each column along with filtered values to reduce noise and a sinusoidal fit. The fit has a pitch of $(202.2 \pm 1.3) \text{ nm}$ and exhibits a resistance drop of $(10.2 \pm 1.2) \Omega$ or $(1.8 \pm 0.2) \%$. (d) The FFT curve for the resistance means showing a very clear peak at $(4.97 \pm 0.25) \mu\text{m}^{-1}$.

to detect the undulating resistivity of the sample. The erosion scan was performed at over twice the previous speed due to time but this may have resulted in a poorer surface. The noise appears to be driven by the horizontal lines dominating the signal, which are likely caused by debris acquisition and loss at the apex of the tip. This could be due to an imperfect erosion or to general contamination present. Regardless, the oscillating resistivity was very clearly observed despite the high noise levels.

6.4.4 Resistivity summary

The data in this section provides proof-of-concept for the resistivity measurement methodology developed for metallic surfaces in Chapter 5. The data does not exhibit high contrast at this stage of development

but the resistivity variation of a metallic surface has been reliably and robustly observed with adequate precision to identify changes of $< 1\%$ or $< 3\ \Omega$. The resistance change is also very slight due to the order of magnitude of the resistivities being equal, and samples containing metals with a ratio of resistivities greater than 10 would show much improved contrast.

The fact that any periodicity was observed at all at site B is notable given the relatively poor quality erosion, and is indicative of a robust measurement methodology. Additionally, the survival of electrical conduction throughout the measurement highlights that Joule heating will likely not disrupt measurements for scans of resolution of at least $192\text{ px} \times 192\text{ px}$.

6.5 Mechanical measurements of magnetically patterned FeRh

Given the use of the FFV derived DataCube mode to obtain the electrical resistance data in Section 6.4 it would be remiss not to consider the use of mechanical data for enhanced sample surface characterisation. The data taken alongside the presented electrical resistance measurements is unfortunately unusable for these purposes due to the low elastic modulus of platinum dominating the value of E^* , although using a harder probe for mechanical characterisation may be able to demonstrate the modulus defect on this striped sample, ideally concurrently with other properties. It was stated in Section 2.9.1 that the magnetoelastic effect responsible is expected to be very small, on the order of $\sim 1\%$, due to use of direct force curve measurements^[39] in lieu of the more optimal resonance method used to characterise bulk FeRh^[15].

An ideal probe for mechanical characterisation would be the diamond AD-40-AS probe, because the hardness of diamond means any observed modulus will be the reduced modulus of the surface alone. This was trialled in the simple ForceVolume mode, which has no DataCube hold period, and the results shown in Figure 6.7. The oxide was not removed prior to measurement because the diamond tip should negate the influence of the oxide at high setpoints. The applied setpoint was $5\text{ V} \sim 16\ \mu\text{N}$ and the deformation may be calculated using equations (4.25) and (4.27) as per Table 5.3 to yield an expected deformation of 4.8 nm into pure $\alpha\text{-Fe}_2\text{O}_3$ or 7.0 nm into pure Fe_3O_4 . This is two to four times the oxide thickness so the underlying FeRh should still contribute significantly to the observed E^* , although would certainly be suppressed if the oxide layer is $\alpha\text{-Fe}_2\text{O}_3$.

The contour in Figure 6.7a shows no clear stripe pattern, just an array of varying modulus. The corresponding FFT curve in Figure 6.7b does show a peak in the correct place but this is fairly wide. The mean cross-section in Figure 6.7c manages to produce a somewhat periodic pattern, but the amplitude is extremely minor and the pitch of the sinusoid is slightly off with the correlation of certain peaks being rather poor. This is further evidenced by the extra peaks in the corresponding FFT curve in Figure 6.7d.

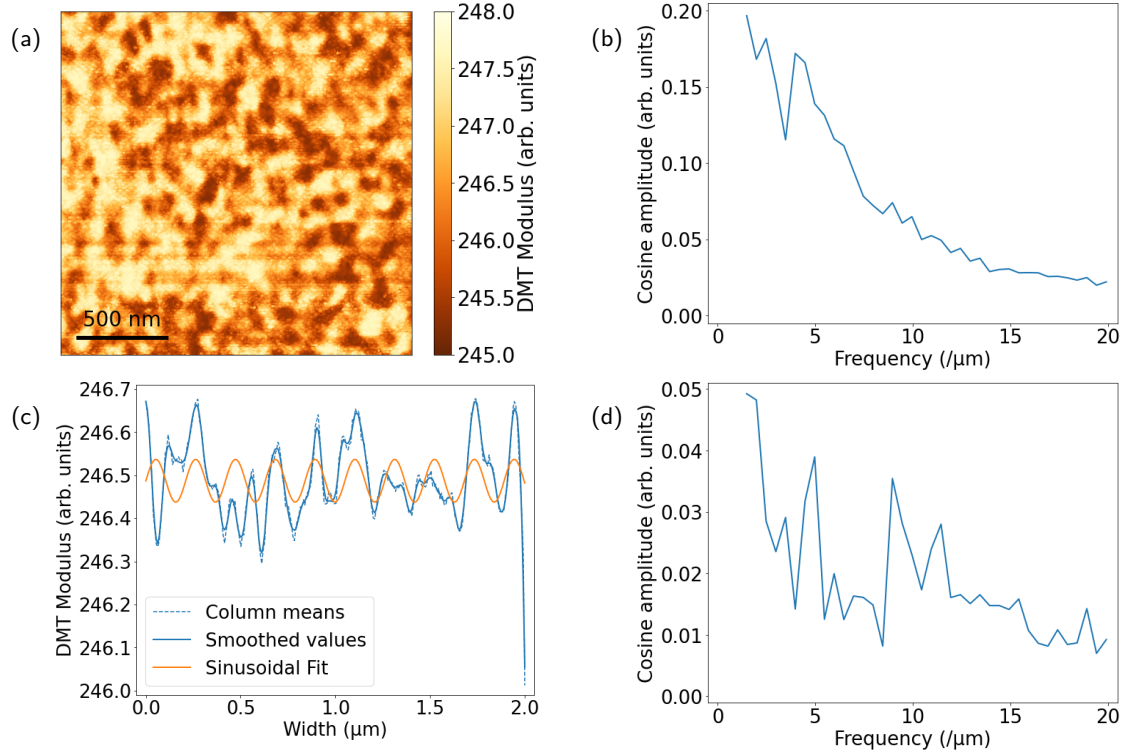


Figure 6.7: The DMT modulus data for the ForceVolume measurement using a diamond probe, taken over a square with size $2\text{ }\mu\text{m}$ and 256 pixels per side. The ramp rate was 30.2 Hz and setpoint was $5\text{ V} \sim 16\text{ }\mu\text{N}$. (a) The DMT modulus contour calculated from the measurement showing no stripe effects. (b) The mean row-by-row FFT curve for the DMT modulus contour showing a peak at $(4.48 \pm 0.25)\text{ }\mu\text{m}^{-1}$, although the point at $(4.98 \pm 0.25)\text{ }\mu\text{m}^{-1}$ is not much lower. The dip immediately to the left is the result of the peak being located on the rapidly decreasing portion of the baseline FFT curve, so is legitimate. (c) The mean value of each column along with filtered values to reduce noise and a sinusoidal fit. The fit has a pitch of $(210.1 \pm 1.8)\text{ nm}$ and implies a modulus defect of $(0.040 \pm 0.005)\%$. (d) The FFT curve for the resistance means showing a very clear peak at $(4.98 \pm 0.25)\text{ }\mu\text{m}^{-1}$, but also a pair of peaks near $10\text{ }\mu\text{m}^{-1}$.

These results are not unexpected because FeRh films exhibit strong saturation magnetisation in-plane with out-of-plane being a hard axis, so any magnetic rotation along the direction of the stressing force will be minimised even further than the low response already expected for stress-strain measurement of the elastic modulus.

Recall the caveat in Section 6.2 regarding this row-based analysis. The features in the contour in Figure 6.7a are around 100 nm in size, which means any cross-section based analysis will likely observe some periodicity from these alone. Consequently, no conclusions may be drawn from the presence of ensuing FFT peaks and this data instead appears to exhibit no magnetoelastic contrast of any kind. This is a

prime example of how the analysis methods used must be contextualised.

6.5.1 Unification of techniques

The three avenues of interest for characterising such a sample as this are the magnetic, electrical, and mechanical properties. These all probe the same magnetic dipole configuration via three of the resulting phenomena: stray field, magnetoresistance, and the magnetoelastic effect. These all have advantages and disadvantages, and combining all three into a single directly correlated measurement would be ideal.

The possibility of combining electrical and magnetic measurements using DataCube was discussed with Dr Vishal Panchal at Bruker and the result was the custom mode termed DCUBE-MFM-TUNA. This is similar to DataCube-TUNA, albeit using a magnetic probe which is driven near amplitude. A lock-in amplifier tracks the amplitude and phase shift of the cantilever and the approach and retract curves at each pixel result in a pair of 3D arrays of phase data across and above the surface. A slice taken from this data yields the relative phase across the surface at some fixed height. There is no interleaving here, and so the approach curves are calibrated based off the height of the previous pixel whilst the retract curves are based off the current pixel; for locally smooth samples this should only have a minimal effect on the slice values. The approach data is higher quality, despite the lack of direct height control, due to ringing in the retract curve. This ringing is the result of the sudden release of the adhesion force from the deflected cantilever which induces a diminishing oscillation at resonance. This second resonance signal introduces noise into the MFM phase data.

The mechanical characterisation of the surface of the FeRh film in Section 6.5 was not successful with a diamond probe, so is unlikely to succeed with a metal-coated or solid-metal probe as part of a more complex analysis. Additionally, the standard MESP-V2 probe used for MFM imaging is not suitable for performing electrical resistivity characterisation on metallic surfaces. This is due to the conduction path being provided by the 35 nm thick CoCr coating^[119], and it was explained in Section 4.6.1 that probe coatings will fail at milliamp currents. Consequently, unification of the magnetic, electrical, and mechanical characterisations into a single measurement is not currently possible for metallic samples using AFM. Electrical and magnetic modes are unable to be combined using commercially available AFM probes, however there is no evidence to suggest that these techniques could not be unified using a specially designed probe.

6.5.2 Custom probe requirements

The unification of electrical and magnetic measurements requires a probe which does not exist at this time. The immediate candidate is a nickel duplicate of the RMN-25PT300B probe. This is a ferromagnetic metal which does not readily oxidise, both of which are essential properties for this application.

The elastic modulus is slightly higher than that of platinum, at 199.5 GPa, with corresponding Poisson's ratio of 0.312^[63]. These are approximately equal to FeRh elastic properties so a nickel probe would still be too small for good mechanical analysis but would form a more robust tip-sample contact. The Vickers hardness is slightly higher too, with a value of 638 MPa rather than the 549 MPa of platinum^[169], but still low enough that an alternate probe must be used for oxide erosion.

The electrical resistivity of nickel is also lower than platinum, at $6.2 \times 10^{-8} \Omega \text{ m}$ as opposed to $1.0 \times 10^{-7} \Omega \text{ m}$ ^[63], meaning the nickel probe resistance would decrease by 40%, to 12 Ω , along with the energy dissipated into the probe via Joule heating. Additionally, the thermal conductivity of nickel is $91 \text{ W m}^{-1} \text{ K}^{-1}$ up from $71 \text{ W m}^{-1} \text{ K}^{-1}$ for platinum^[179], allowing enhanced heat dissipation and further reducing the current limiting effects of Joule heating. This would permit larger biases to be used which would aid the current in tunnelling through thin contaminants and increases the absolute change in observed voltage drop over the reference resistor of the voltage divider, which aids measurement precision.

The development of such a probe is a substantial project in and of itself, and is beyond the scope of this work. The ideal probe would be a solid non-oxidising ferromagnet with a high elastic modulus for the mechanical measurements, whilst also being highly thermally and electrically conductive to minimise Joule heating which would in turn maximise the allowed biases or even enable the use of the heater stage. Nickel appears to be the best candidate from the elements, however there may be alloys or allotropes which are even more suited to this application.

6.6 Summary

This chapter introduced the experimental procedure for putting the system developed in Chapter 5 into practice and evaluated the results. These demonstrations have shown that the underlying electrical resistivity pattern may be observed even for two resistivities with the same order of magnitude. Additionally, the local resistivity of FeRh thin films has been empirically confirmed to change as a result of the magnetic patterning process. The prototype demonstrated here serves as an excellent proof-of-concept which was the primary aim of this work. In future developments the system could be refined into a dedicated bespoke device rather than the prototype constructed here. A methodology for mechanical erosion of the oxide layer was trialled with mixed results, suggesting that a chemical oxide-removal technique would be more suitable where possible. Nanomechanical characterisation of FeRh was attempted but no contrast was observed. The DCUBE-MFM-TUNA mode to unify two or three measurement techniques into one was introduced, but is not suitable for metallic surfaces using commercially available probes.

Chapter 7

Magnetic characterisation of noble ion irradiated FeRh

The size and composition of magnetically patterned stripes on an FeRh film will now be magnetically characterised. The film growth and patterning procedure will be explained and the expected domain structure will be introduced along with the corresponding expected MFM signal. Magnetic images of the stripes in ambient conditions will be shown and the magnetic structure discussed and contrasted with XMCD-PEEM results. The expected stripe widths will be discussed and the MFM data analysed to determine if they were patterned to the dimensions intended. The periodicity of the stripes will be considered for a range of scan sizes and the topography will be checked for unintended patterning effects. The robustness of the stripes will be verified and the effect of external fields on the ferromagnetic regions will be considered. The boundary of the patterned region will be inspected to verify the precision of the patterning. The effects of heating and cooling the FeRh film will be considered with regards to the survival of the pattern and to the behaviour of magnetic domains.

7.1 Preparation of magnetically patterned FeRh thin films

7.1.1 Deposition of FeRh thin films

The FeRh sample investigated in this work is an uncapped FeRh film of thickness 40 nm deposited on an MgO(001) substrate. This film was grown by Dr William Griggs using an eleven-target AJA International ATC 2200-V magnetron sputtering system. The sputtering system consists of a vacuum chamber with a substrate mounted facing the sputtering targets^[180]. The 'targets' are solid blocks of the material to be deposited and are covered by shutters when not in use. During sputtering a negative DC potential is applied to conductive targets whilst an AC bias is applied to insulating targets to avoid electrostatic charge build up, argon gas is added to the chamber and this applied potential ejects electrons from the target structure which collide with nearby argon atoms and liberate their outer shell electrons. The now charged Ar^+ ions are attracted to the negative potential in the form of a plasma which ablates atoms

from the target^[180], which drift across the chamber and deposit onto the substrate. A magnetron system uses a magnetic field to trap the jettisoned electrons in a loop above the target surface to maximise argon collisions and allow lower argon pressures to be used; reducing the argon pressure results in an increase of the mean free path of the ablated atoms and thus improves efficiency^[180]. The substrate may be heated using radiative heating halogen lamps located behind the substrate mounting position.

The thickness of the growing film is not able to be measured in situ on this system so the magnetron power and duration must be calibrated to produce the desired thickness from a particular target. A higher power results in a more rapid sputtering so is suited to growing thicker films, whilst lower power allows more precise thickness control due to slower growth and is required for growing ultrathin films^[180]. The thickness depends linearly on time so once a suitable power has been identified the film thickness is controlled by the duration of deposition. This is calibrated by depositing a series of films over different lengths of time and determining the thickness for each film using X-ray reflectometry (XRR) on a Rigaku SmartLab X-ray diffractometer (XRD). A linear fit is then applied to the resulting data and this function may be used to calculate the deposition time for a particular film thickness.

The procedure for growing good quality equiatomic FeRh films on this sputter system was developed by Dr Craig Barton^[95]. Section 3.4.1 describes this process which involves heating the substrate and then annealing in order to achieve the requisite magnetic ordering. The deposition occurred with the substrate heated to 650 °C at a pressure of 4×10^{-6} bar using DC magnetron sputtering with a magnetron power of 100 W. After sputtering for the calibrated time the substrate was heated to 750 °C and annealed for two hours in situ. The vertical distance between the substrate and the 2 inch diameter Fe₅₀Rh₅₀ target was 27 cm.

7.1.2 Magnetic patterning

Section 3.4.2 explains how noble ion irradiation may be used to transition equiatomic FeRh from antiferromagnetic to ferromagnetic ordering at room temperature. This has been demonstrated for irradiating whole films^[6,18], but utilising this phenomenon requires that it be localisable and to investigate this the equiatomic FeRh sample was patterned with parallel stripes of irradiated regions. A 500 nm positive resist was applied to the film surface and stripes were patterned into this by Dr Fredrik Schedin using electron beam lithography. The substrate and hence film is a square of side length 10 mm and the patterned region was a square of side length 8 mm leaving a completely unpatterned border of width 1 mm. The stripes were 100 nm wide with a pitch of 200 nm.

The sample was then shipped to Dr Rantej Bali at HZDR in Dresden, Germany, for ion-irradiation. The parameters for this were determined from the initial work by Griggs et al.^[18] which is discussed in Section 3.4.2. This was performed using a Model 1050 40 kV ion implanter manufactured by Danfysik

A/S, which used a 10 mm diameter rastering beam of Ne^+ ions to supply the $7.5 \times 10^{13} \text{ cm}^{-2}$ fluence to the film held at 2×10^{-6} mbar and room temperature. The resist was removed using isopropanol and acetone and the surface was characterised using XMCD-PEEM at BESSY II in Berlin; XMCD-PEEM will be explained in Section 7.2.1.

The expected shape of the stripes within the film was simulated by R. Bali for an irradiation density of $7.5 \times 10^{13} \text{ ions cm}^{-2}$ and the result is shown in Figure 7.1. The stripes are expected to reach full magnetisation however there is some over-spill into the nominally AF regions due to scattering effects within the film. The width of the stripe exhibiting at least 90% magnetisation is $\sim 115 \text{ nm}$ but magnetisation falls off rapidly beyond this point. Within a few nanometres of the surface the stripe is very well behaved with negligible over-spill, and surface characterisation techniques are only sensitive to a few nanometres of depth therefore the patterned wire width of 100 nm should be observed. Measures of the whole sample using techniques such as vibrating sample magnetometry could be used to investigate the total percentage of the volume which was converted to FM ordering.

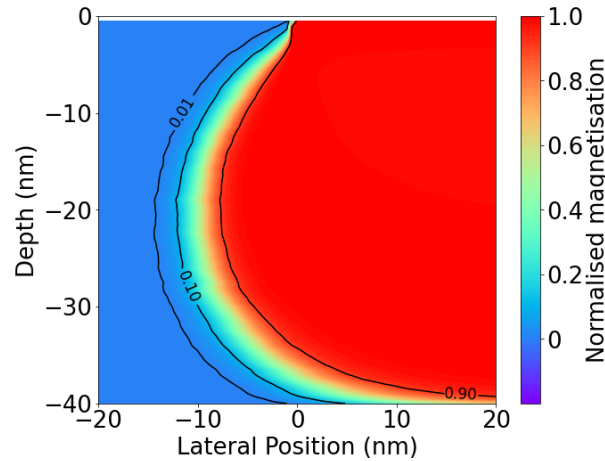


Figure 7.1: The normalised magnetisation expected within the film at the stripe edge for a flux of $7.5 \times 10^{13} \text{ ions cm}^{-2}$. The red region is maximally magnetised whilst the blue region exhibits no magnetisation. The 1%, 10%, and 90% isolines are shown giving the width of the stripe exhibiting at least 1% magnetisation to be $\sim 135 \text{ nm}$.

The characterisation work reported in this thesis is the first to be performed on the sample in order to minimise the possibility of surface damage. The future characterisation will involve vibrating sample magnetometry which requires a circular disc to be cut from the film. This could result in inadvertent damage to the film so was delayed until after the work presented here.

7.1.3 Expected domain structure

These patterned stripes must now be characterised to investigate the patterning dynamics. This requires magnetic studies at ambient and heated conditions over a wide range of areas, and magnetic force microscopy (MFM) is an ideal tool for such analysis.

The stripes should disappear when the film is heated above the AF-FM transition temperature of the AF regions and reappear once the film is cooled back below the FM-AF transition temperature. In MFM phase contour plots the AF regions should be featureless and all share some arbitrary phase value, while the FM stripes should have phase values a few degrees above and below this value. Recall that films such as FeRh form in-plane domains which cannot be observed directly, instead only the stray field from the domain walls may be measured. This means that it is possible that no contrast will be observed if the domains are arranged as shown in Figure 7.2.

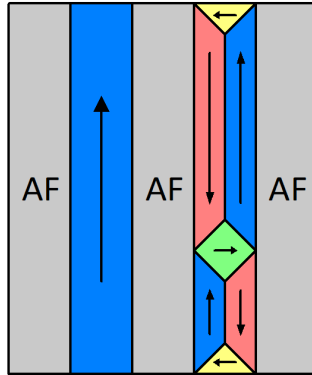


Figure 7.2: Possible domain orientations in the stripes which would not exhibit the stray field required for characterisation using MFM.

If the stripes form single domains then any stray field will be at the edges of the patterned region, rather than in the centre where the characterisation will be taking place. Alternatively, the right-hand stripe shows how cyclical domains may form closed loops of various sizes, as seen in Section 2.8.2. This possible lack of domain walls which provide contrast is a downside to MFM characterisation, but this may be addressed via AC demagnetisation which would scramble the domains and form a mesh of domain walls and thus stray field for the probe to detect. Fine domain structure would be lost but overall AF vs FM contrast would be enhanced.

The sample is mounted on the heater stage for most measurements and as a result the sample is subject to a constant 150 mT field normal to the surface. This could, in certain circumstances, reorient the dipoles into a vertical position pointing towards the probe, and as a result produce a majoritarily negative phase shift.

7.2 Initial XMCD-PEEM characterisation of the sample

7.2.1 Introduction to XMCD-PEEM

X-ray magnetic circular dichroism (XMCD) may be applied to photoemission electron microscopy (PEEM) to form XMCD-PEEM. In this technique the sample is illuminated by circularly polarised X-rays which release electrons via the photoelectric effect and the resulting current is measured. The contrast in the image is a map of the local absorption coefficient of the sample and magnetic images are obtained due to the absorption coefficient being dependent on the orientation of local magnetisation relative to the polarisation of the incident X-rays. This is a surface dependent technique penetrating only ~ 1 nm into the surface^[181] while demonstrating a resolution of as good as 10 nm, but more routinely 50 nm is achieved^[181]. XMCD-PEEM requires a synchrotron and beamline and thus cannot be performed ad hoc using tabletop apparatus unlike MFM.

The L -edge is a series of absorption maxima in the energy spectrum observed as a result of a second shell orbital being raised to the incomplete d orbital^[182]. The label L is a legacy from the X-ray notation which denoted the electron shells as K , L , M , etc. The L_1 peak is the excitation of a $2s$ electron which is high energy due to the stability of the lower shell, while the L_2 and L_3 peaks are excitations of $2p$ electrons which are split into two levels due to spin-orbit coupling^[182]. L_2 has a longer decay time and so a less intense signal is seen while L_3 is a lower energy peak with high intensity^[182]; the size of the L_3 peak makes it the absorption edge of choice for XMCD-PEEM characterisation of magnetic films^[183].

The L_3 currents are recorded for both right and left circular polarisations which may only excite up or down spin electrons respectively^[184], with the relative currents being indicative of the relative densities of states of spin up and spin down electrons which are offset in magnetised materials as shown in Figure 2.33 in Section 2.9.2. The polarisation with highest current relates to the spin direction which is not responsible for magnetisation and equal currents mean no net magnetisation is observed^[184]. An XMCD-PEEM image is formed from ratios which are calculated using these currents. One approach is to simply take the ratio of currents^[183], which is simply the ratio of absorption coefficients and returns a log scale with zero magnetisation occurring for a ratio of 1. A second approach is to take the ratio of the difference between currents to their sum^[87], this returns a linear scale with limits ± 1 and zero magnetisation occurring for a ratio of 0.

7.2.2 XMCD-PEEM characterisation results

XMCD-PEEM may be used to characterise the magnetisation of the magnetically patterned FeRh film by mapping the spin distribution across an FM surface, using the relative quantum efficiencies of photoelectrons of each spin. Heated XMCD-PEEM was performed on the BESSY II synchrotron in Berlin

following noble ion irradiation of the film and prior to returning the patterned film to Manchester. This characterisation was carried out by a team at HZDR led by Dr Rantej Bali. Images above and below the AF-FM transition temperature are provided in Figure 7.3.

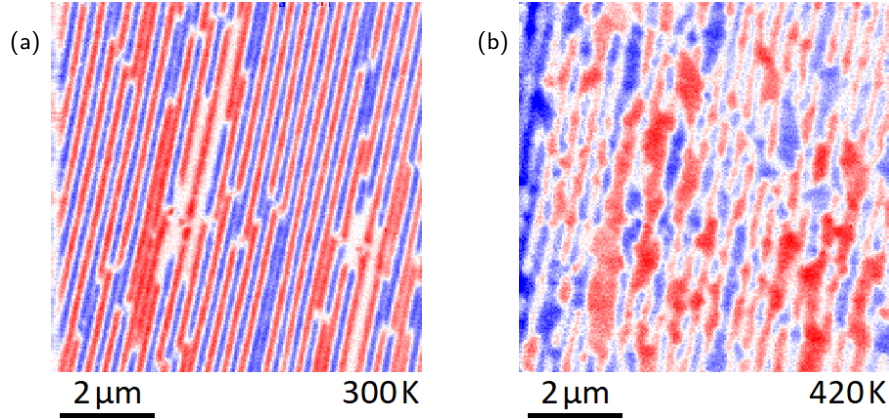


Figure 7.3: XMCD-PEEM images of size $8\text{ }\mu\text{m}$ obtained above and below the AF-FM transition temperature, captured at the same site with only minor drift. White regions are AF and blue and red regions are FM domains of opposite spin. (a) Spin distribution below the transition temperature. (b) Spin distribution above the transition temperature.

Figure 7.3a shows the patterning was overall successful, except for a few small white regions where no photocurrent difference was observed. The FM stripes appear to be much wider than the AF counterparts, although the image resolution precludes quantitative interpretations of this. The spin distribution shows that neighbouring stripes are typically of opposite spin state, albeit with frequent exceptions. This will likely be due to some form of weak coupling through the unirradiated regions of the film; this cannot be strong coupling due to the width of the AF regions and the observed exceptions. Upon heating the film Figure 7.3b shows that the clean AF borders disappear and the spin domains become more naturally shaped, although the overall distribution is preserved.

The advantage of this XMCD-PEEM data is that the spin states of the domains may be observed and this alternating spin coupling detected. However, this technique is inconvenient for frequent or ad hoc characterisation due to the need to use a beamline facility such as BESSY. MFM provides a far more convenient tool for frequent and rapid imaging of domain structures, although it cannot directly observe the spin of the electrons forming the magnetic dipole moments.

7.3 Ambient MFM characterisation

The MFM characterisation shall initially be performed in ambient conditions, with heated characterisation to follow in Section 7.4. The periodic nature of the sample parameter under investigation meant

that a scan speed of $10 \mu\text{m s}^{-1}$ could not be used during this work. This is because an imperfectly shielded AFM may sometimes inadvertently overlay noise from the mains electricity supply onto the measured data. The UK mains frequency is 50 Hz, so imaging at $10 \mu\text{m s}^{-1}$ would result in image noise with frequency $5 \mu\text{m}^{-1}$, which very clearly would present issues.

The sample was cleaned and mounted onto a steel puck as described in Section 4.10 then placed onto the AFM with no specialised preparation. A series of MFM scans were taken at various scan sizes, and two of these are shown in Figure 7.4.

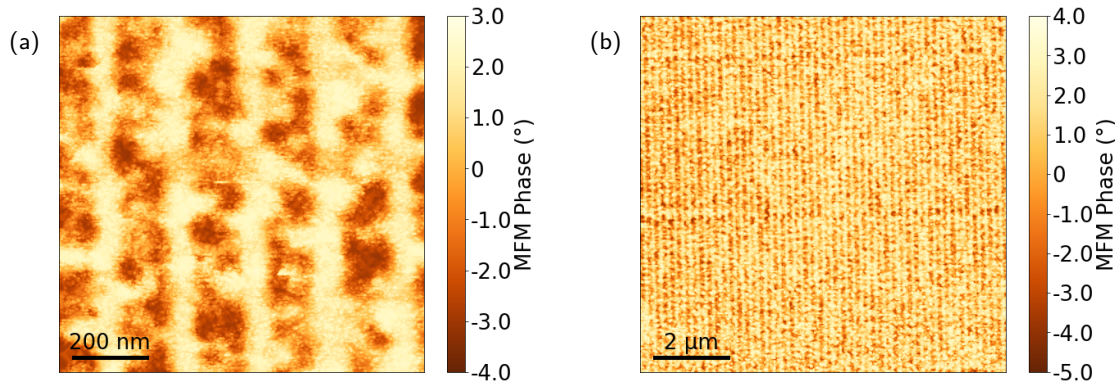


Figure 7.4: The normalised magnetic phase data for two scans at a lift height of 10 nm, each with a resolution 256 pixels per side. The scan rate was 1.0 Hz and the rounding value was 0.1. The sample was loaded onto the heater stage and imaged using a Bruker MESP-V2 probe. (a) Data for a square of side length $1.0 \mu\text{m}$, pixel size of 3.9 nm, and scan speed of $2.2 \mu\text{m s}^{-1}$. (b) Data for a square of side length $10 \mu\text{m}$, pixel size of 39 nm, and scan speed of $22 \mu\text{m s}^{-1}$.

These images show the patterned stripes very clearly, duplicating the patterning success seen in the XMCD-PEEM data. The wider FM lines are once again observed, but Figure 7.4a shows much finer detail than seen previously. There is clearly some interesting magnetic structure within the FM stripes which was not demonstrated in the XMCD-PEEM data. Any domains formed from in-plane dipoles should exhibit zero phase over their area, while the ends should show equal and opposite phase shifts from the stray field looping around. The absence of any phase shifts greater than the AF value suggests that no in-plane domains exist, although it is possible that the ends of an in-plane domain which should show positive phase shifts are lost to the stronger neighbouring dipole moments. The structure seen within the FM stripes is thus either due to an incomplete transition of the irradiated regions or to partially rotated domains. The horizontal lines seen in Figure 7.4b appear in all MFM images and have pitch $\sim 5 \mu\text{m}$; they are believed to be a magnetic artefact of the rasters of the lithographic or irradiation process.

The XMCD-PEEM and MFM techniques were both used to obtain $25 \mu\text{m}$ scans to compare the capa-

bilities over relatively large areas. The MFM scan is captured at the same site as Figure 7.4 and the resulting images are shown in Figure 7.5.

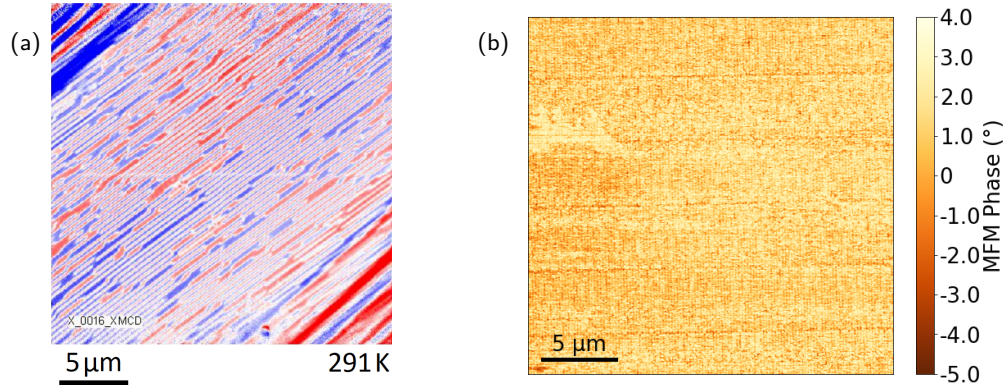


Figure 7.5: Magnetic images obtained using XMCD-PEEM and MFM over a square with side length $25\text{ }\mu\text{m}$. (a) The spin distribution over the surface as measured using XMCD-PEEM at BESSY II. (b) The normalised magnetic phase data captured at a lift height of 10 nm , with a resolution of 512 pixels per side giving a pixel size of 49 nm . The scan rate was 1.46 Hz and the rounding value was 0.1 giving a scan speed of $81\text{ }\mu\text{m s}^{-1}$. The sample was loaded onto the heater stage and imaged using a Bruker MESP-V2 probe.

The stripes can be clearly seen in both images, however the XMCD-PEEM data in Figure 7.5a struggles to resolve the top-left and bottom-right corners, with significant smearing of the measured values occurring. The MFM image in Figure 7.5b has no such issue. The presence of a 5 nm surface contaminant, likely to be residual resist, can be seen near the top-left of Figure 7.5b, but even so the stripes are cleanly resolved throughout. The MFM measurement is therefore superior over larger measurement areas. The precision of this technique, even at a scan speed of $81\text{ }\mu\text{m s}^{-1}$, can be demonstrated by comparing the central $5\text{ }\mu\text{m}$ square of Figure 7.5b with the $5\text{ }\mu\text{m}$ MFM measurement taken at the same site. These are shown in Figure 7.6.

The high scan speed and low resolution of Figure 7.6a is very clear to see, however the stripes are clearly resolved and even the presence of some underlying pattern in the FM stripes is visible. The slower speed scan in Figure 7.6b shows much improved resolution and is definitely the superior image, but these images demonstrate that even high-speed and low-resolution scans over large areas may still resolve small features throughout, unlike XMCD-PEEM. Note also that this was captured with mostly default settings, making the preparation time significantly less than for XMCD-PEEM, even excluding the need to travel to a synchrotron.

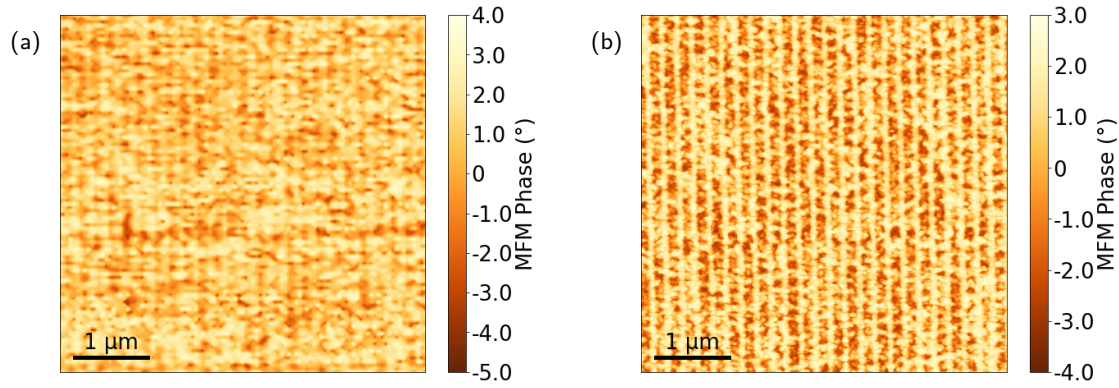


Figure 7.6: The normalised magnetic phase data for two scans of the same site at a lift height of 10 nm, each with a side length of 5 μm . (a) The data cropped from the 25 μm scan with a pixel size of 49 nm and scan speed of 81 $\mu\text{m s}^{-1}$. (b) The data from a 5 μm scan with a pixel size of 20 nm and scan speed of 11 $\mu\text{m s}^{-1}$.

7.3.1 Edge of the patterned region

The success of the patterning does not solely lie with the efficacy of induced magnetisation, but also with the precision of the edges of the patterned region. To investigate this the corner of the patterned region was located and imaged with the result shown in Figure 7.7.

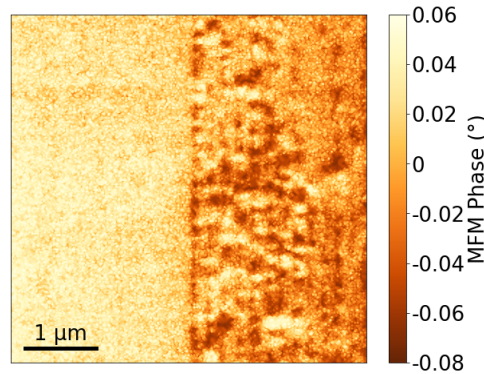


Figure 7.7: The normalised magnetic phase data for the corner of the patterned region. This was captured using a scan size of 5 μm at a lift height of 10 nm. The resolution is 248 pixels per side giving a pixel size of 20 nm. The image is cropped down from 5.5 μm and used a scan rate of 1.0 Hz and a rounding value of 0.2 giving a scan speed of 14 $\mu\text{m s}^{-1}$. The sample was loaded onto the heater stage and imaged using an NT-MDT MFM10 probe.

The corner of the irradiated region lies at the midpoint of the image, with the bottom-right quadrant of the scan overlapping the 8 mm square ion irradiated region. The left-hand side of the image demonstrates that the patterning was very clean parallel to the stripes. No magnetic contrast is visible in this region,

showing that the resist protected this area from ion irradiation and also that no rogue ferromagnetic domains were induced beyond the patterning boundary as a result of stray field from the FM stripes. The top-right quadrant is supposedly outside the irradiated region and this is why it is not as consistently patterned as the bottom-right. The reason for the existence of this patterning is unclear, but the most likely reason is the lithography extending beyond the originally intended border. The magnetic domains are certainly not consistent with ion scattering within the film, and magnetically formed rogue domains would be expected to occur in all directions so would have also been observed in the AF region to the left of the figure.

7.3.2 Stripe widths

In Section 7.1.2 it was shown that simulations predict a resist mask with 100 nm openings to form stripes of width 135 nm. Indeed, both the MFM phase data and the XMCD-PEEM data appear to observe that the AF and FM regions are not equally wide. Ideally, when all phase is below the AF baseline, the cross-section of the MFM phase data perpendicular to the stripes would form a square-wave between the two magnetisation regions. Instead, the cross-sections show the boundaries to occur over a gradient, which is sometimes constant and other times rounded off in an almost sinusoidal appearance. The result is a mismatch between what the eye sees in the contour images and the reality.

The 1 μm scan in Figure 7.4a will be used as an example due to the high resolution of the image. A typical cross-section is shown in Figure 7.8 and has lower phases (FM) of ~ 100 nm wide, slopes spanning ~ 20 nm, and upper phases (AF) ~ 60 nm wide. The highest visual contrast in images is between the higher regions and the rest of the image, giving an apparent ~ 60 nm AF region and ~ 140 nm FM region. The usual characterisation of gradated transitions is to consider the midpoints of the slope, and this threshold gives ~ 120 nm for the FM region and ~ 80 nm for the AF region. This is closer but still exhibits some mismatch between patterning and observation.

The subtlety here is that the FM is an active measurement and AF is a passive measurement, because AF is observed through the lack of magnetic field rather than a signal in its own right, meaning the midway point is not the correct point to consider. Instead, due to the nature of this measurement, the point at which the phase *begins* to change from the FM value is the critical point. This reflects the tip moving away from being directly over the FM region and the diminishing stray field produces the interim phase values between the FM and AF limits. The width of these FM regions turns out to be 100 nm, as shown in Figure 7.8, demonstrating that the patterning appears to have been accurately applied and the difference is a measurement artefact.

The measurement artefact in the MFM case will be the interaction between the stray field and the finite tip size. The cantilever motion will be influenced by the magnetic stray field for as long as an appreciable

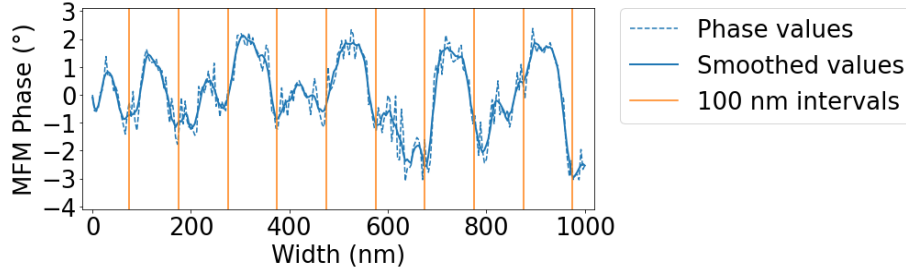


Figure 7.8: A cross-section taken from 30% of the way down Figure 7.4a. The data has been smoothed using a Savitzky-Golay filter for clarity. Lines have been marked at 100 nm intervals to highlight the correlation between lower phase regions and the expected periodicity.

magnetic mass is in proximity to the FM region. The 20 nm slopes are approximately equal to half the tip radius, suggesting that the interaction is no longer significant once $\frac{3}{4}$ of the the tip passes beyond the stripe boundary.

This also serves to explain the inconsistent width of the AF stripes, and even the apparent nonlinearity seen in small scan sizes such as the 500 nm image shown in Figure 7.9. The AF stripes appear to oscillate rather than progress linearly. The points where the AF stripe appears to be narrow or curve are located beside a particularly dark region. This is further from baseline than other regions and indicates a stronger stray field is located at this point. This stronger field then has a larger sphere of influence than other points and so the probe is still being affected further into the AF region than it would otherwise be. One such region with a strong field may be seen at approximately 700 nm in Figure 7.8.

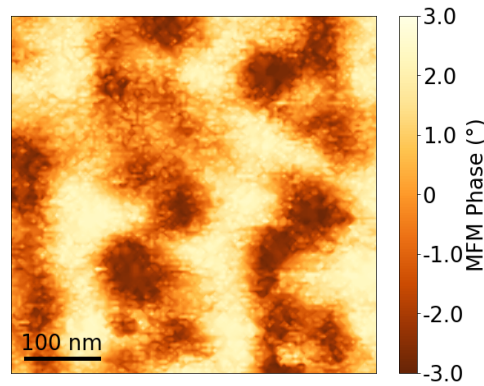


Figure 7.9: The normalised magnetic phase data for a scan size of 500 nm captured at a lift height of 10 nm. The resolution is 128 pixels per side giving a pixel size of 3.9 nm. The scan rate was 1.0 Hz and the rounding value was 0.1 giving a scan speed of $1.1 \mu\text{m s}^{-1}$. The sample was loaded onto the heater stage and imaged using a Bruker MESP-V2 probe.

The XMCD-PEEM data shows perfectly straight lines but with the FM stripes much wider than the AF

counterparts. The resolution of this technique was stated in Section 7.2.1 to be of similar order to the gradated width, and so a similar effect occurs to MFM where the measurement is still influenced by the FM region even when the centre of the measurement site is located within the passive AF region. The linearity of the stripes is preserved because this implementation of XMCD-PEEM is influenced by spin density-of-states rather than stray fields, and so is insensitive to the particular orientation of dipoles. However, the particular problem here is that this is a ratio driven technique, so the two photocurrents being at reduced intensity had no net effect and there is no way to distinguish between the regions where the imaging area slightly overlaps the FM region and where it wholly lies within the FM stripe.

7.3.3 Stripe periodicity

The resolution of the imaging technique is critical when characterising small structures, especially when stray field effects are so prominent. The XMCD-PEEM images are particularly significant for having low density of pixels relative to feature sizes, due to the large imaging radius. MFM performs better here because its analogue nature means the influence of any sample dipole is weighted by a function of its distance from the tip, so the strongest contributor to the signal at any time is directly below the probe. Thus as long as any rogue stray field is accounted for MFM is able to produce higher resolution images than XMCD-PEEM.

The choice of scan size and number of pixels must be considered together if quantitative analysis is to be performed on the data. The pixel size must be small enough that any features of importance can be rendered. This is a particular problem in the larger scans seen in Figures 7.4b and 7.5b which have pixel sizes of 39 nm and 49 nm respectively. This allows only two or three pixels per stripe and is larger than the gradated region meaning these scans cannot be used to characterise the stripe widths. However, these scans are still perfectly valid for characterising the strip periodicity.

All of the MFM plots shown in this chapter thus far, with the exception of the scan at the edge of the patterning presented in Figure 7.7, were recorded in a single measurement session at the same site, along with an additional $2.5\text{ }\mu\text{m}$ scan with resolution 256 px and scan speed $5.6\text{ }\mu\text{m s}^{-1}$. Due to the dipole orientation being such that all FM phases are lower than AF phases, mean row-by-row FFT curves may once again be used to determine the periodicity. These curves for the MFM phase data are shown in Figure 7.10.

The peak is very cleanly at $5\text{ }\mu\text{m}^{-1}$ in all scans, with the uncertainty falling with increasing scan size to give $(4.95 \pm 0.02)\text{ }\mu\text{m}^{-1}$ for the $25\text{ }\mu\text{m}$ scan. This minor offset from $5.00\text{ }\mu\text{m}^{-1}$ corresponds to the image being tilted at 8° from the vertical, which may be seen visually in the contour plots. The second peak at $10\text{ }\mu\text{m}^{-1}$ is quite prominent and appears in all scans. This simply relates to there commonly being two features per stripe, and is a consequence of the non-magnetic components of the FM regions

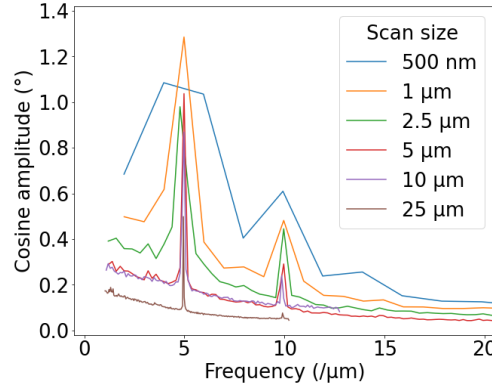


Figure 7.10: The mean row-by-row FFT curves for multiple scan sizes of MFM phase data which were captured at the same site during a single session. The values are limited to $< 20 \mu\text{m}^{-1}$ so that only relevant points are shown.

observed in the contour images. It bears noting that taking an FFT of magnetic phase data is somewhat ironic in that the amplitude is measured using degrees and the frequency using μm . The FFT was also applied to the topography data from these scans and unexpectedly there were some peaks in this data too. The FFT curves from the topography data are shown in Figure 7.11.

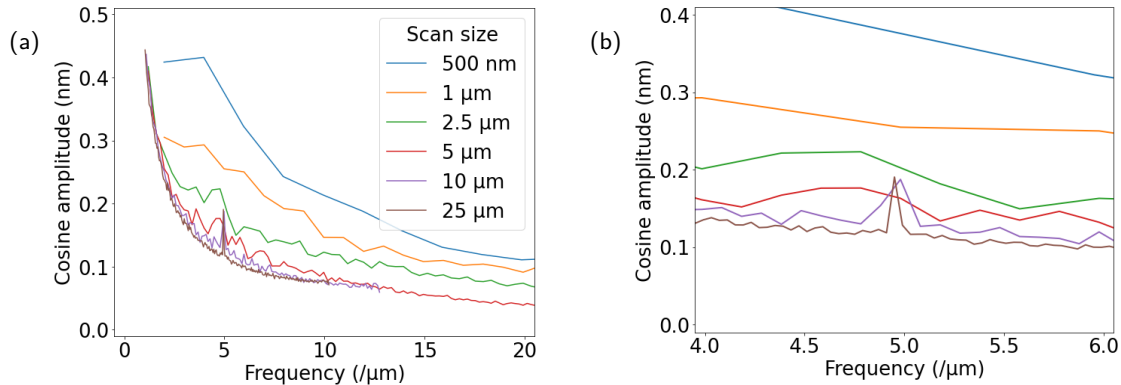


Figure 7.11: The mean row-by-row FFT curves for topographic data captured alongside the MFM measurements. (a) The full range of values up to the standard limit of $20 \mu\text{m}^{-1}$. (b) A cropped version of the FFT curves showing only $(5 \pm 1) \mu\text{m}^{-1}$.

Most of the height curves in Figure 7.11a show the generally monotonic curve of a non-periodic function. However, as seen in Figure 7.11b, the $10 \mu\text{m}$ and $25 \mu\text{m}$ scans exhibit periodic behaviour in their Height Sensor channels. This cannot be a true representation of the surface because the other scans did not show the peak and the ion irradiation should not affect the surface morphology. Notably, these are the scans with the highest scan speeds of $22 \mu\text{m s}^{-1}$ and $81 \mu\text{m s}^{-1}$ respectively. This suggests that the cantilever feedback control was not fast enough to compensate for the magnetic forces acting on the tip during the topography pass at such high scan speeds, and so a magnetic shadow appeared in the

topography data.

7.3.4 Persistence of the magnetic structure

The next aspect of the patterning to consider is the persistency over time and during exposure to low level magnetic fields, such as the field produced by the heater stage. Figure 7.12 shows a series of $2\ \mu\text{m}$ MFM scans of the same site on the surface taken over a total time of 5.5 hours.

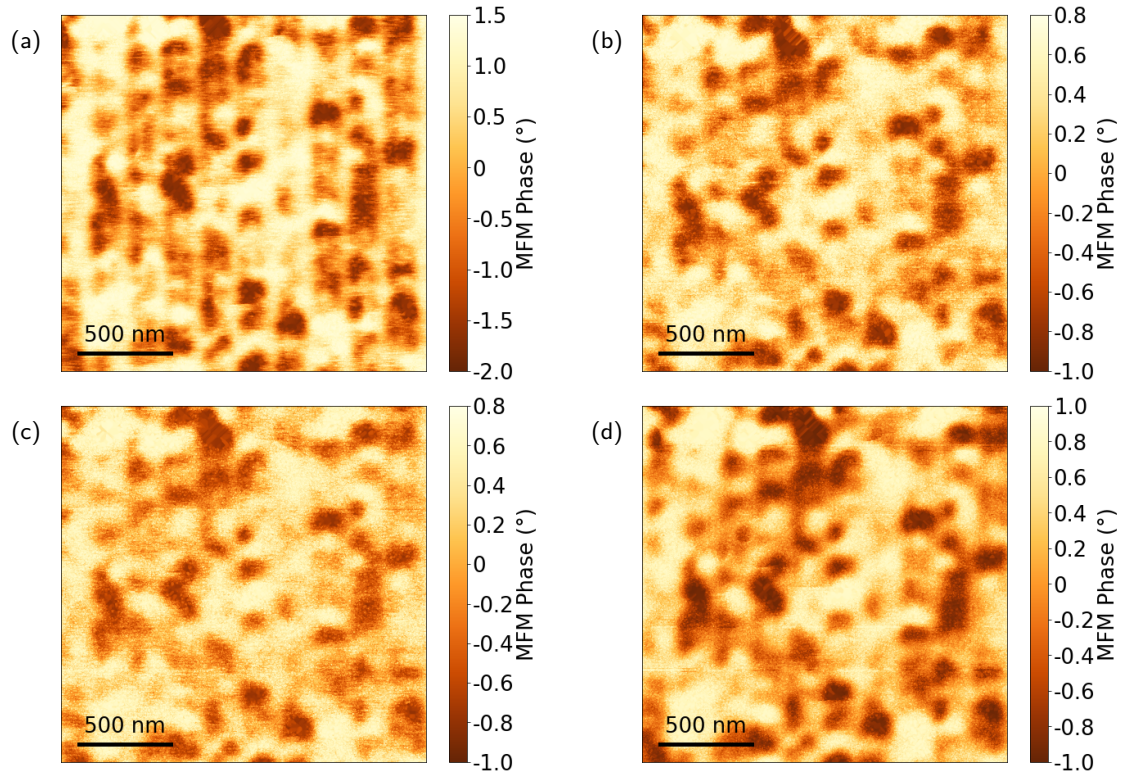


Figure 7.12: The normalised magnetic phase data for a series of scans of size $2\ \mu\text{m}$ captured at a lift height of $30\ \text{nm}$. The resolution is 518 pixels per side giving a pixel size of $3.9\ \text{nm}$. The images are cropped down from $2.1\ \mu\text{m}$ to improve drift compensation, and used a scan rate of $1.0\ \text{Hz}$ and a rounding value of 0.2 giving a scan speed of $5.3\ \mu\text{m s}^{-1}$. The sample was imaged using a Bruker MESP-V2 probe. (a) Initial scan captured on the heater stage. (b) Scan captured on the main sample stage 40 minutes after the previous image. (c) Second scan captured on the main sample stage 3.5 hours after the previous image. (d) Final scan captured on the heater stage 5.5 hours after the initial image.

The magnetic pattern observed for in all four of the figures is consistent, showing that the local magnetic structure does not change over time. Additionally, this shows that the heater stage does not unduly affect the dipole orientations, with the contrast being enhanced by stronger phase shifts observed for the heater stage. All channels of the heater stage images are higher contrast than the vacuum chuck images, and this is attributed to a more secure hold on the puck and thus reduced noise. The heater

stage will therefore be favoured during this work, including for ambient measurements.

7.3.5 Effect of external fields

The effect of strong external fields is of interest to observe how the magnetic properties of the stripes are affected. The MFM characterisation was carried out at remanence following removal of the field. The main sample stage was necessarily used for these images due to the steel puck being inherently incompatible with the strong magnetic fields involved.

During the application of the external magnetic field the FeRh sample was placed inside a clear plastic sample box for protection, and was then held between the poles of an electromagnet by hand. No stand or clamp was used because non-magnetic materials were required and the human hand provides a very versatile yet magnetically insensitive support, and the short time frames meant very little movement was likely to occur. The electromagnet was disabled and the field measured to be 0 Oe prior to inserting or removing the sample, in order to avoid any flux of the wrong orientation being applied and also minimise any electromotive force from the sudden and uncontrolled change in flux density. The field was ramped in a controlled manner so that the time dependence of flux density was constant and small. The MFM data captured in this section used small topographic features to realign the scan sites as closely as possible prior to capture, and wider scans were then captured than are shown here to allow additional post-processing realignment.

The first field to be applied was $|\vec{H}| = 20 \text{ kOe}$ parallel to the stripes; this is applied in air with $\mu_r \approx 1$ so $|\vec{B}| \approx 20 \text{ kG} = 2 \text{ T}$. The field was held at this value for 30 s. The before and after MFM scans are shown in Figure 7.13.

These figures were cropped down to $1.5 \mu\text{m}$ rather than the intended $2.0 \mu\text{m}$ due to the size of the offset between the captured images. Comparing the figures it may be seen that some of the dark spots have remained, whilst the dark/light pairs have often changed. This suggests these pairs are indeed the ends of in-plane domains and so they rotated readily to align with the applied field. Clearly though neighbouring domains did not perfectly align because this would have resulted in a single larger domain demonstrating no observed phase due to the lack of domain walls. The dark spots without lighter counterparts are likely to be out-of-plane domains as discussed previously, and these seem to have a local easy-axis in the out-of-plane direction thus did not remain aligned with the field direction after removal due to it being energetically favourable to revert back. The AF stripes were completely unaffected, as expected.

The next field direction to be considered is again in-plane but now applied first perpendicular to then parallel to the stripes. The field strength was $|\vec{H}| = 20 \text{ kOe}$ or $|\vec{B}| \approx 20 \text{ kG} = 2 \text{ T}$ and was held for 30 s

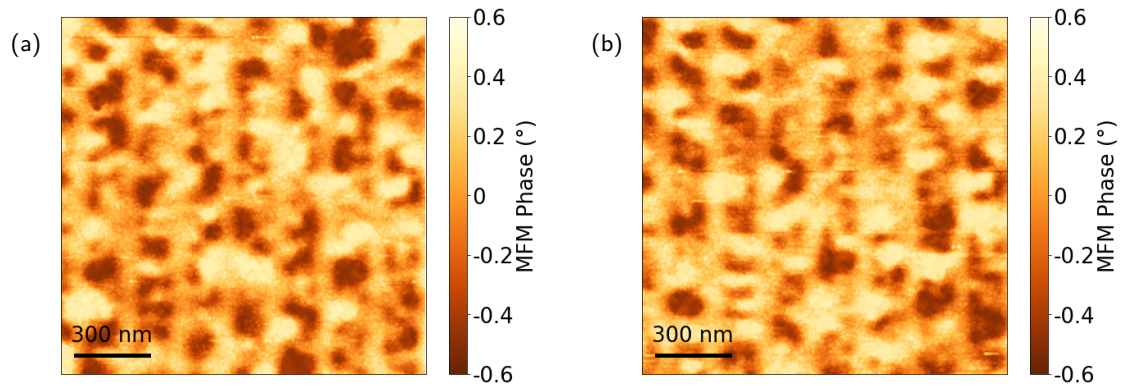


Figure 7.13: The normalised magnetic phase data before and after a field of 2 T was applied parallel to the stripes. The scan size is $1.5\text{ }\mu\text{m}$ captured at a lift height of 15 nm. The resolution is 195 pixels per side giving a pixel size of 7.7 nm. The images are cropped down from $2.1\text{ }\mu\text{m}$ and used a scan rate of 1.0 Hz and a rounding value of 0.2 giving a scan speed of $5.3\text{ }\mu\text{m s}^{-1}$. The sample was loaded onto the main sample stage and imaged using a Bruker MESP-V2 probe. (a) Measurement before applying the field. (b) Measurement after applying the field.

each time. The before and after MFM scans for each field direction are shown in Figure 7.14.

The perpendicular field induced a significantly distorted domain pattern, seen in Figure 7.14b. This is the result of the 100 nm wide stripe forming a particularly high-energy domain structure in the perpendicular direction, due to this magnetisation direction having an extremely short and wide aspect ratio. The dipoles will have sought the lowest energy compromise for the system and this will have resulted in a significant out-of-plane component, the direction of which may have been influenced by a slight tilt in the sample holder or simply be the preferred direction of one of the dominant domains which encouraged other domains to align in roughly similar directions. The ability of MFM to characterise this type of domain structure is very poor. The parallel field restored the domains in a similar manner to Figure 7.13, as shown in Figure 7.14c. The domain structure is still somewhat messy following the perpendicular effects but the stripes have been restored and now exhibit higher contrast than was seen in the initial scan in Figure 7.14a.

The MFM phase pattern degraded over long time periods due to the dipoles beginning to align, likely aided by perturbations from magnetic and thermal effects during measurements. This meant the stripes could no longer be observed on the MFM so the domains were required to be broken up using AC demagnetisation. This is the process described in Section 2.7.1 by which an oscillating magnetic field of decaying amplitude is applied to the sample with each domain ceasing to reverse once the local coercive field is no longer being achieved. The result is a large domain being fragmented into many smaller domains creating a mesh of domain walls to provide MFM contrast. The LabView Virtual Instrument

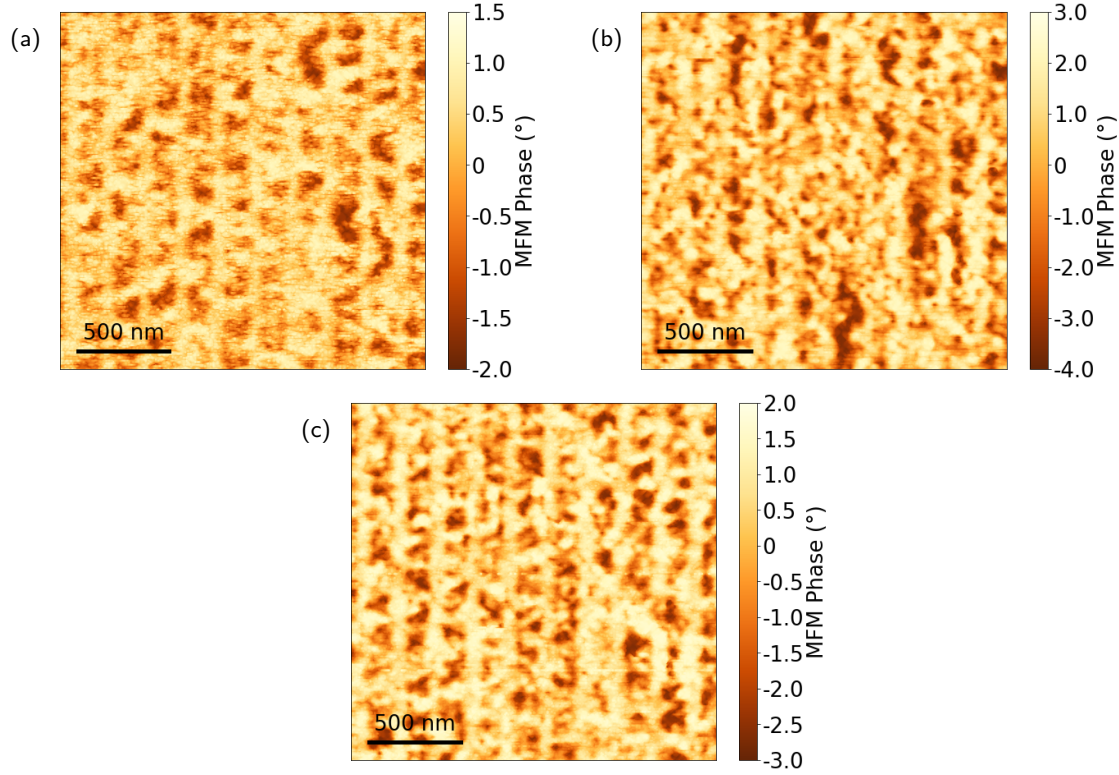


Figure 7.14: The normalised magnetic phase data before and after a field of 2 T was applied first perpendicular to then parallel to the stripe direction. The scan size is $2\mu\text{m}$ captured at a lift height of 15 nm. The resolution is 260 pixels per side giving a pixel size of 7.7 nm. The images are cropped down from $2.1\mu\text{m}$ and used a scan rate of 1.02 Hz and a rounding value of 0.2 giving a scan speed of $5.4\mu\text{m s}^{-1}$. The sample was loaded onto the main sample stage and imaged using a Bruker MESP-V2 probe. (a) Measurement before applying the fields. (b) Measurement after applying the perpendicular field. (c) Measurement after applying the parallel field.

file controlling the electromagnet was configured to perform AC demagnetisation automatically so this was a straightforward process. The field was applied parallel to the stripes and an initial starting field of $|\vec{H}| = 1\text{ kOe}$ or $|\vec{B}| \approx 1\text{ kG} = 0.1\text{ T}$ was used because this is larger than the easy-axis coercive field of an ion irradiated FeRh film^[18]. The heater stage provides a larger field than this but in a hard-axis direction so does not rotate all dipoles to form out-of-plane ferromagnetic ordering in the FeRh film. The demagnetisation decay factor was chosen to be 0.99 meaning each applied field was $-0.99 \times$ the previous value. The cut-off value was 1 Oe meaning the last value to be applied was 1.0031 Oe after 687 values.

Many attempts to recover the signal by remagnetising the probe and optimising various settings were trialled, including changing probe completely to an NT-MDT MFM01 probe^[185], before it was concluded that the domains had truly aligned and the sample demagnetisation was required. Representative images

from before and after for this process is shown in Figure 7.15; the sites differ but both are representative of the sample as a whole.

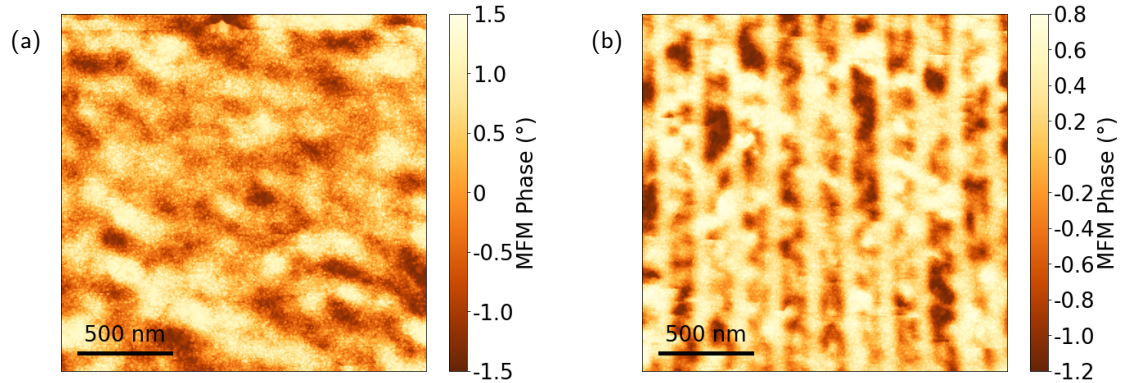


Figure 7.15: The normalised magnetic phase data before and after an AC demagnetisation was performed parallel to the stripes. The scan size is $2\mu\text{m}$ captured at lift heights of 40 nm and 10 nm respectively. The resolution is 256 pixels per side giving a pixel size of 7.8 nm. The scan rate used was 1.0 Hz alongside a rounding value of 0.2 giving a scan speed of $5.0\mu\text{m s}^{-1}$. The sample was loaded onto the main sample stage and imaged using an NT-MDT MFM01 probe. (a) Before demagnetisation. (b) After demagnetisation.

The stripe pattern can faintly be seen in Figure 7.15a although the precision is so poor that the AF stripes have disappeared completely. Figure 7.15b shows the success of the demagnetisation with the AF stripes now being very clearly resolved. This demagnetisation technique enables further MFM characterisation to be performed on samples even after the dipoles have begun to align in-plane.

7.4 Heated MFM characterisation

The behaviour of the stripes upon heating and cooling is of great interest and this can be characterised by performing MFM measurements on the heater stage. The data discussed here was initially intended as preliminary data, hence the limited resolution and selection of temperatures. However, the MFM struggled to maintain coherent magnetic measurements on this particular sample later on in the work due to poor surface tracking resulting in inaccurate lift mode heights. This issue is very curious and was unfortunately never resolved. The use of MFM01 and especially MFM10 probes provided an improvement for some unidentified reason to do with subtleties in the probe dynamics, however these probes were far less stable than the MESP-V2 probe when the sample was heated and they could not be used for thermal measurements.

The thermal characterisation was done by heating the sample in steps from room temperature to 160°C and then cooling back to room temperature again, with MFM measurements captured at each applied

temperature. The applied temperatures were adjusted using the generic calibration values from Section 4.11, and the stated values are the expected values of the FeRh film rather than the value measured by the thermocouple in the heater stage. The resulting set of images is provided in Figure 7.16. The scans were carefully realigned after each re-engagement by completing at least two scans in tapping mode and adjusting the x and y piezo offsets until the topography data aligned with that previously captured. Ideally the cantilever should be retuned at each temperature due to a slight thermal dependence in the resonant frequency, however the signal did not degrade here and so the extra steps involved were not considered an efficient use of time.

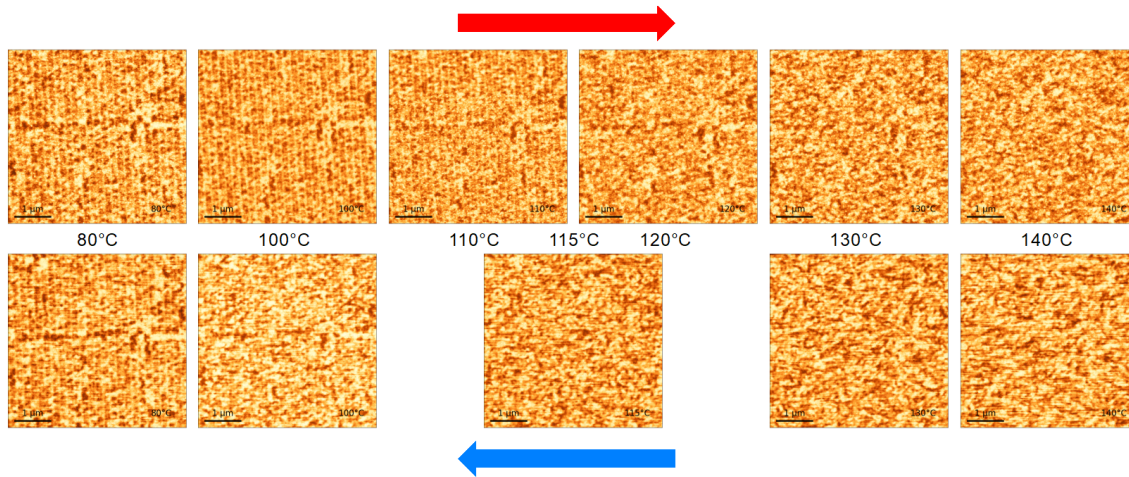


Figure 7.16: The normalised magnetic phase data for a series of scans of size $5\text{ }\mu\text{m}$ captured at a lift height of 15 nm . The resolution is 248 pixels per side giving a pixel size of 20 nm . The images are cropped down from $5.5\text{ }\mu\text{m}$ and used a scan rate of 1.0 Hz and a rounding value of 0.2 giving a scan speed of $14\text{ }\mu\text{m s}^{-1}$. The sample was loaded onto the heater stage and imaged using a Bruker MESP-V2 probe. The temperature was raised to $160\text{ }^{\circ}\text{C}$ between the scans captured at $140\text{ }^{\circ}\text{C}$.

The thermal data in Figure 7.16 shows the stripes are highly robust to thermal cycles. The clean stripes dissolve into FM domains as the sample is heated past the transition temperature and reappear as it is cooled, demonstrating that the irradiated regions remain FM throughout whilst the as-grown regions transition from AF to FM and back, just as equiatomic FeRh would be expected to.

Importantly, the domain structure within each irradiated FM stripe is preserved during the thermal cycle, with no reorientations occurring due to the increase in thermal energy or as a result of magnetically coupling to the transitioning stripes. The contrast between the two $80\text{ }^{\circ}\text{C}$ scans in Figure 7.16 is almost entirely unchanged, with the majority of differences attributable to measurement noise; these scans are shown side-by-side in Figure 7.17. This demonstrates that not only are the FM stripes very robust, but their specific magnetic domain structure persists throughout heating and cooling past the FM-AF transition temperature.

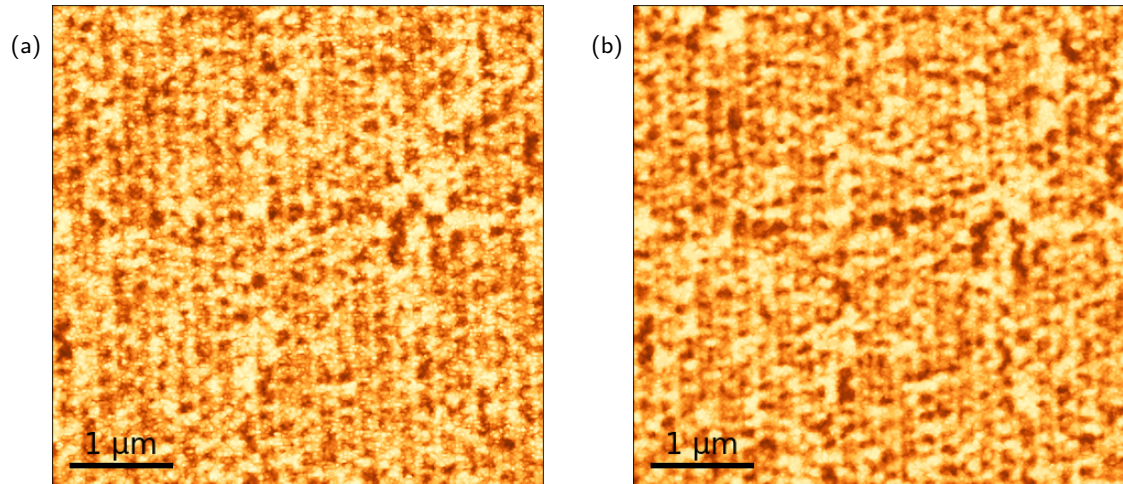


Figure 7.17: The 80 °C scans from Figure 7.16. The contrast is almost entirely unchanged, with the majority of differences attributable to measurement noise. (a) The MFM phase before heating past the transition temperature. (b) The MFM phase after cooling back past the transition temperature.

This persistency is shown more clearly in Figure 7.18, where a 500 nm wide region is compared for each of the scans in Figure 7.16. There is some consistency in the domain structure visible throughout the whole cycle, such as the magnetic feature highlighted by the red box. The persistency of the FM domains may be shown quantitatively by considering the mean row-by-row FFT curve of one of the 140 °C images, shown in Figure 7.19.

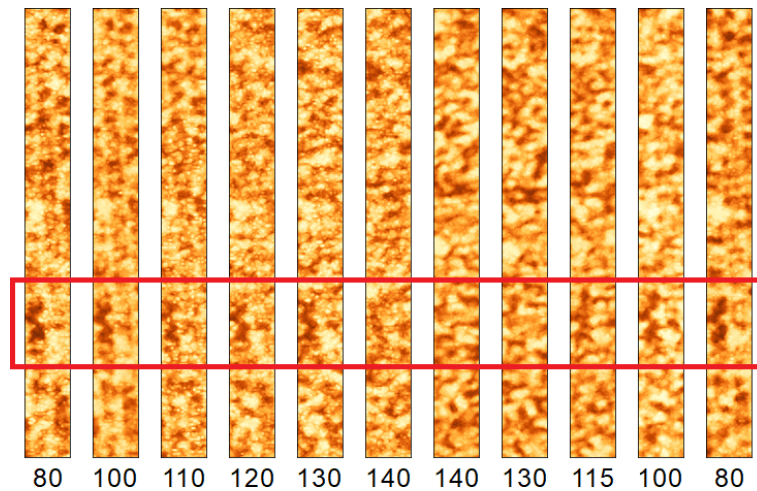


Figure 7.18: A 500 nm wide region compared for each of the MFM phase measurements in Figure 7.16. The temperature in Celsius is given at the base of each plot. The red box highlights a particularly clear and persistent feature. Recall that the temperature was raised to 160 °C between the scans captured at 140 °C.

The FFT curves in Figure 7.19 are highly significant because they demonstrate that the periodicity

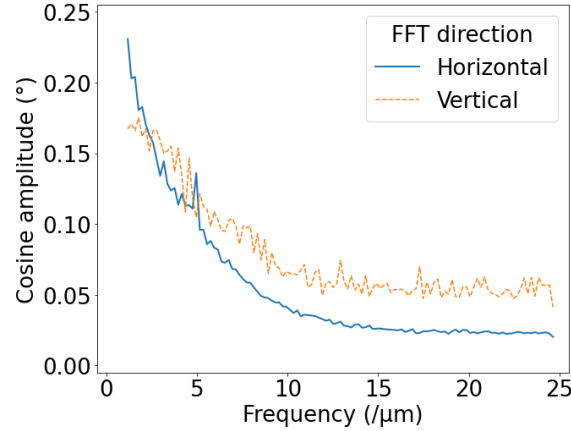


Figure 7.19: The mean row-by-row and column-by-column FFT curves for the second 140 °C scan in Figure 7.16. The values are limited to $< 20 \mu\text{m}^{-1}$ so that only relevant points are shown. The peak occurs at $(4.97 \pm 0.10) \mu\text{m}^{-1}$.

remains even after the sample is wholly FM. This is because the patterned stripes are very stable and do not interact significantly with the AF stripes during transition, with the result that the AF and FM stripes feature independent domains and thus continue to exhibit the stripe periodicity. The column-by-column FFT was taken from vertical slices of the data and showed that there is no peak at all in this direction, thus it is unlikely that the peak is purely an artefact of 100 nm domain structures because freely forming domains would produce a peak for both FFT directions. This stability likely also stems from the ion irradiation disrupted lattice structure forming a lattice boundary at the AF-FM interface, which disrupts the long-range magnetic ordering required to form coherent FM domains across the threshold.

The transition hysteresis may be observed qualitatively by considering the relative contrast in the scans in Figure 7.16. The heating transition occurs over the 100 °C to 120 °C range and is shown in Figure 7.20, while the cooling transition occurs over the 115 °C to 80 °C range and is shown in Figure 7.21.

The contours and their corresponding FFT curves clearly show a transition between sharp and faded stripes which corresponds to the metamagnetic transition of the unirradiated regions. These place the transition temperatures at ~ 110 °C and ~ 100 °C, yielding a hysteresis of ~ 10 °C, and these three values agree with those expected for FeRh^[57]. This suggests that the transition temperature and hysteresis width of the unirradiated regions is not significantly altered by the patterning process.

It may be observed that the amplitudes of the FFT peaks for the decreasing temperature data are approximately half of the size of the peaks seen in the increasing temperature data, but this is simply an artefact of the measurement. The heating process alters the resonance properties of the MFM probe and so the resonance frequency drifts away from the drive frequency, thus producing lower contrast

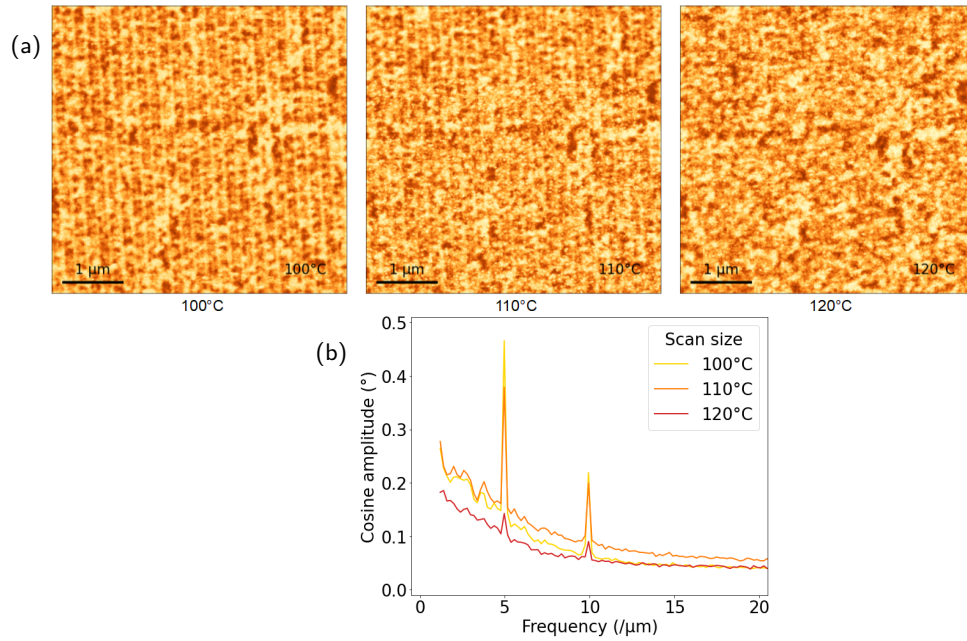


Figure 7.20: The series of scans from Figure 7.16 spanning the heating transition. The transition temperature appears to be $\sim 110^\circ\text{C}$. (a) The MFM phase scans for the transition. (b) The mean row-by-row FFT curves for each of the three scans.

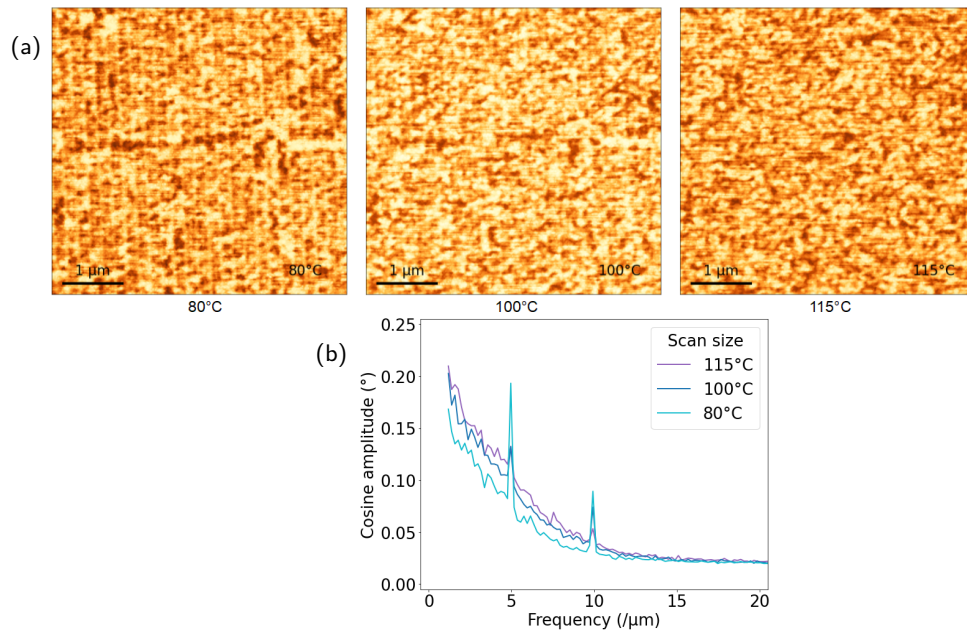


Figure 7.21: The series of scans from Figure 7.16 spanning the cooling transition. The transition temperature appears to be $\sim 100^\circ\text{C}$. (a) The MFM phase scans for the transition. (b) The mean row-by-row FFT curves for each of the three scans.

imagery. The image contrast may be preserved by regularly recalibrating the probe, however this adds a significant amount of time onto the measurement and was not necessary to capture the required data on this occasion.

7.5 Summary

This chapter discussed the MFM characterisation of magnetically patterned FeRh and compared the results with those from XMCD-PEEM. The deposition and patterning process for the ion irradiated FeRh films has been described, and the expected domain structure present in the film was explained along with how it is expected to manifest in MFM scans. Ambient MFM characterisation was used to demonstrate the success of the patterning and to characterise the resulting magnetic domain structures. The patterned FeRh film was heated and cooled past the metamagnetic transition temperatures, and MFM measurements captured during this temperature cycle demonstrate the persistence of the ferromagnetic domains, as well as the expected hysteresis in the transition.

Chapter 8

Nanoscale characterisation of PMN-PT ferroelectric substrates

Substrates for use in composite multiferroics must have predictable and ideally homogeneous ferroelectric properties such as piezoelectric coefficient and coercive field, and investigating this requires nanoscale characterisation of these properties to be carried out. This chapter will discuss such characterisation for a PMN-PT ferroelectric substrate with a PT concentration of $x = 0.29$. Models will be developed for the stoichiometric distribution of PT, and thus the distribution of key ferroelectric properties, across the surface of a PMN-PT substrate and the resulting models will be compared with results in the literature. Further models will be developed to consider the atypical piezoelectric behaviour of relaxor ferroelectrics, including the field-dependence of the inverse piezoelectric effect and the capacitive forces acting on the probe. These properties cannot be measured directly so spectroscopy must be performed. However, the thickness of the substrates poses a challenge that has not been addressed in the literature. Two measurement methodologies will be developed and trialled to resolve these challenges, one performing repeated sweeps across the sample surface and the other performing repeated scans, and the results of the characterisations will be evaluated. These will be compared with the derived models and the wider implications will be discussed in the contexts of advanced AFM metrology and of ferroelectric substrates for composite multiferroics.

8.1 Motivations and aims

PMN-PT is of great interest at present as a potential substrate material for use in composite multiferroics^[7]. It has been shown by Griggs and Thomson^[7] that substrates with a PT concentration of $x = 0.29$ feature both rhombohedral and monoclinic structures, and that these appear to exhibit piezoelectric coefficients d_{33} which differ by at least one order of magnitude. This difference needed to be investigated further, especially on the nanoscale, because such differing responses have significant consequences for the magnetoelectric coupling. Composite artificial magnetoelectric multiferroics are mediated through piezoelectric strain, thus the local piezoelectric coefficient d_{33} and coercive field $E_{c,3}$

of the surface at the interface directly affect the coupling between the ferroic materials, and hence understanding the local surface distribution of PT concentration is critical. This is not a simple characterisation to perform due to the thickness of the sample, and as a result is not commonly discussed in the literature. The purpose of this chapter is therefore to investigate how and why the ferroelectric properties of PMN-PT substrates vary as a consequence of local stoichiometry, through developing and evaluating novel metrological methodologies and applying these to a PMN-PT substrate from the same batch as that used in the initial macroscopic characterisation published by Griggs and Thomson^[7]. This substrate was manufactured by JFE Mineral Co., Ltd and has thickness 250 μm with a nominal stoichiometry of $x = (0.29 \pm 0.01)$. A gold film of thickness $\sim 1 \mu\text{m}$ was applied to the back surface to provide a consistent electrode and to negate measurement artefacts which could arise from imperfect contact with the sample stage.

Standard PFM amplitude and phase measurements as described in Section 4.8 are not suitable for characterising such substrates. Equation (4.80) shows that the difference in amplitude with varying piezoelectric coefficient will be of the order of picometres and hence below the measurement precision. Additionally, the phase contrast is not a suitable metric either because this does not correlate to x , d_{33} or $E_{c,3}$. Consequently, the PT concentration must be characterised by using field-spectroscopy to observe the reversal and determine the coercive field $E_{c,3}$ at each image site. Due to the sample thickness the coercive field is much higher than may be applied within the 12 V limit available from the AFM, thus high voltage PFM (HV-PFM) is required to be used. Here, the dummy application module introduced in Section 5.6 is used to connect the probe to a high-voltage connection on the signal access module (SAM). This spectroscopic approach involving sweeping high voltages requires the development of theoretical models prior to characterisation, including the expected field dependence of piezoelectric characteristics and the unusual capacitive forces acting on the AFM probe.

This chapter will begin by developing a model to reconcile the apparent conflict between the observed d_{33} dependency on stoichiometry and the relations in Sections 3.7.1 and 3.7.2. A theoretical model will then be developed to consider the field dependence of the piezoelectric properties of relaxor ferroelectrics, such as electrical permittivity and piezoelectric coefficients. The capacitive properties of a HV-PFM system will be considered and used to determine the optimal AFM probe to be used. An additional series of theoretical models will be produced to characterise the expected AFM probe response to the piezoelectric and electrostatic forces acting during measurements. Two distinct spectroscopic approaches will then be introduced and trialled, and the results discussed to attempt to characterise the PMN-PT surface whilst also evaluating the feasibility of using AFM based techniques to perform spectroscopic characterisation of thick samples.

8.2 Distribution of piezoelectric properties

X-ray diffraction (XRD) measurements have been recorded at a range of applied electric fields for the PMN-PT sample under investigation in this work and have been published by Griggs and Thomson^[7]. The measured XRD curves were plotted against twice the diffraction angle θ at each field to provide histograms of lattice spacings, and an example is provided in Figure 8.1. A homogeneous stoichiometry would result in a very narrow single peak at the lattice spacing corresponding to the configuration predicted by the phase diagram. However, this idealised case is rarely observed and so the local PT content ratio x will vary across the structure^[108]. This may broaden the histogram peak, and potentially introduce additional peaks if there are any phase transitions, and hence different lattice spacings, within the PT distribution range. The sample under investigation features a nominal PT concentration of $x = 0.29$, which is expected to be rhombohedral but lies very close to the monoclinic boundary of $x_{rm} = 0.298$ stated in Section 3.7.1. This means that a varying local distribution of x will likely result in the formation of monoclinic regions which feature a different lattice spacing, thus two peaks are expected to be observed in the XRD data for this crystal, and indeed this is shown for zero applied field in Figure 8.1. The lattice spacing is the only crystal property discussed in this chapter which is expected to show two peaks in its distribution, with other parameters such as coercive field and piezoelectric coefficients smoothly varying with x across the phase boundary.

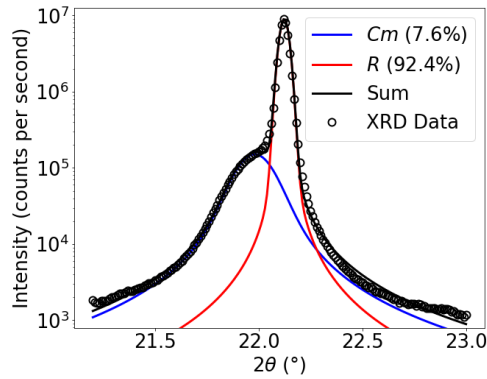


Figure 8.1: The XRD intensity data for the PMN-PT sample under no applied field shown on a logarithmic scale. The sum of two Voigt curves was fitted and is shown in black. These two curves are shown as the blue and red curves and the relative area under each is provided in the legend, normalised to sum to 100%. The XRD data is reproduced from Griggs and Thomson^[7].

The XRD data is shown by the circular markers in Figure 8.1. Voigt behaviour is expected^[7] and so the function fitted to the data was the sum of two such curves. The data and function were logged prior to fitting because the Cm peak was too small relative to the R peak for a good fit to both on a linear scale. The fit was unbounded and performed using non-linear least squares fitting via the Levenberg-Marquardt algorithm as implemented in the SciPy Python package^[110]. The individual peaks were integrated over

all values using SciPy, which uses Fourier integrals, and these areas were normalised to sum to 100%. These values provide the approximate relative volume of each crystal phase within the PMN-PT sample and suggests the crystal phases are in approximately a 9 : 1 ratio. This is not an exact method because the error in the fit is of the order of 1%, and in principle the structure factors for X-ray scattering will be slightly different for the two phases^[7].

Most ferroelectric parameters such as $E_{c,3}$ and d_{33} have been shown to vary smoothly with x , including across the phase boundary, as introduced in Section 3.7.1. However, two parameters are expected to demonstrate discontinuities at this boundary, and these are the unit cell dimensions and polarisation angle. It was explained in Section 3.7.1 that the crystal structure is a result of the polarisation direction of the perovskite cell, meaning a change in structure results in a change in polarisation direction and thus in the component of saturation polarisation parallel to the field, $P_{\text{sat},3}$. The peaks of the fits in Figure 8.1 are located at $2\theta_m = 21.98^\circ$ and $2\theta_r = 22.12^\circ$ for the monoclinic and rhombohedral phases respectively. Bragg's law^[58] provides that the ratio of monoclinic lattice spacing d_m to rhombohedral spacing d_r is

$$\frac{d_m}{d_r} = \frac{\sin(\theta_r)}{\sin(\theta_m)} \approx 1.006 \quad (8.1)$$

and it follows geometrically that this is also the ratio of sines of polarisation angles, thus the rhombohedral angle of 54.7° only decreases to 54.3° in the monoclinic cells, and any change in $P_{\text{sat},3}$ will be entirely negligible.

The inhomogeneity of the stoichiometry demonstrated in Figure 8.1 means that the linear piezoelectric coefficient $d_{33,0}$ will also be varying across the sample. The XRD measurements for the series of applied fields were recorded by Griggs and Thomson^[7] and these are reproduced in Figure 8.2. The peak positions provide the modal lattice spacing of each crystal system in the sample under that field, thus the dependence of peak position on applied field is indicative of the piezoelectric coefficient d_{33} for each lattice system. The peaks are symmetric so these modal values are also equal to the mean lattice spacing in each case. The series of curves show a significant difference in response, with the larger $R3m$ peak moving substantially more than the Cm peak, suggesting the monoclinic piezoelectric coefficient is much smaller than its counterpart for the rhombohedral phase.

This initially seems to suggest that the two phases intrinsically have very different piezoelectric coefficients, and thus nanoscale measurements should be performed to characterise these. Additionally, this result appears to be incompatible with the symmetric peak for piezoelectric coefficient in Figure 3.13, so further investigation of this property is clearly required.

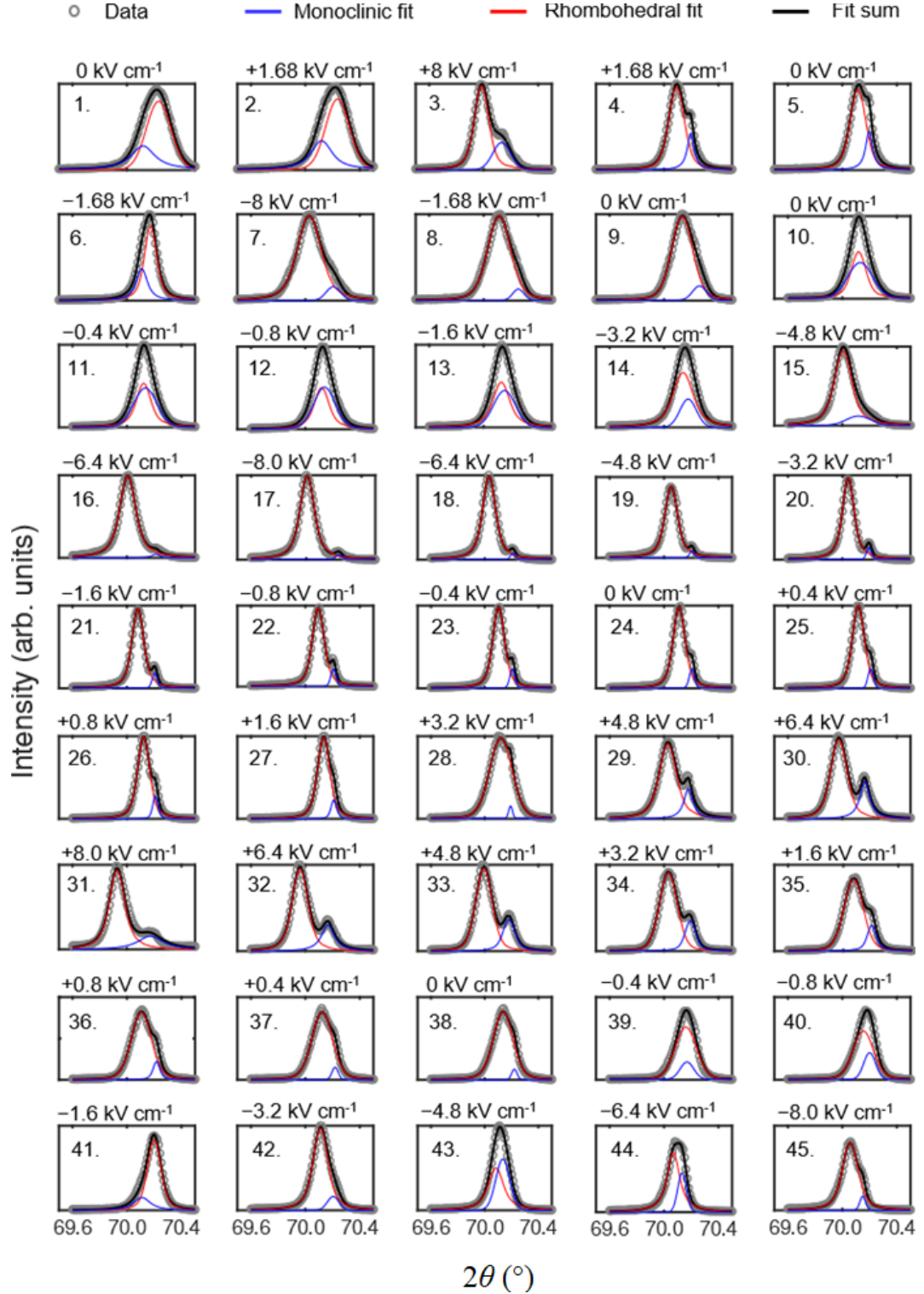


Figure 8.2: The XRD data for the PMN-PT sample at a range of potentials, measured in the $[001]$ direction. The red curves correspond to the rhombohedral ($R3m$) phase, the blue to the monoclinic (Cm) phase, and the black to their sum. Figure reproduced from Griggs and Thomson^[7].

8.2.1 Effective piezoelectric response

The stochastic distribution of PT concentration x within the sample may be assumed to follow a Gaussian distribution

$$g(x; \bar{x}, \sigma) = \frac{1}{\sigma\sqrt{2\pi}} \exp\left(-\frac{(x - \bar{x})^2}{2\sigma^2}\right) \quad (8.2)$$

with mean \bar{x} and standard deviation σ . The standard deviation of this distribution describes the degree of inhomogeneity within the crystal and may be obtained from the fit to the data in Figure 8.1. The nominal value for this crystal is $\bar{x} = 0.29$, with the threshold between phases being at 0.298 and the fraction of the crystal having rhombohedral ordering being 0.924. Thus the standard deviation satisfies

$$0.924 = \int_{-\infty}^{0.298} \frac{1}{\sigma\sqrt{2\pi}} \exp\left(-\frac{(x - 0.29)^2}{2\sigma^2}\right) dx \quad (8.3)$$

which may be solved to give

$$\sigma = \frac{0.298 - 0.29}{\sqrt{2} \operatorname{erf}^{-1}(2 \times 0.924 - 1)} = 0.00558... \approx 0.006, \quad (8.4)$$

where the inverse error function erf^{-1} was calculated using the SciPy implementation of this function. This is consistent with the manufacturer stated value of $x = (0.29 \pm 0.01)$ approximately being the 2σ range, describing 95% of all x values present within the sample.

Therefore, the distribution of values of x may be modelled as the Gaussian distribution

$$g(x; 0.29, 0.006), \quad (8.5)$$

which is shown in Figure 8.3a overlaid on the curve $d_{33}(x)$ that was fit to the OFF-field piezoelectric coefficient data in Figure 3.13. This shows that the majority of the perovskite cells are rhombohedral and clustered near the peak of the $d_{33}(x)$ curve, thus all have high piezoelectric coefficient, whilst the remaining rhombohedral cells and all of the monoclinic cells are spread over a range of PT concentrations x which have a lower average piezoelectric response. This concentration of rhombohedral cells at a particular x value also serves to explain why the XRD curves observed in Figure 8.1 show a much broader peak for the monoclinic data than the rhombohedral data.

The effective coefficient in each crystallographic phase is therefore obtained by taking the weighted average of $d_{33}(x)$ for each crystal phase. For the rhombohedral phase this yields

$$\int_{-\infty}^{0.298} d_{33}(x) g(x; 0.29, 0.006) dx \approx 1.9 \text{ nm V}^{-1} \quad (8.6)$$

and for the monoclinic phase this yields

$$\int_{0.298}^{\infty} d_{33}(x) g(x; 0.29, 0.006) dx \approx 0.2 \text{ nm V}^{-1}, \quad (8.7)$$

where the integrals were again resolved numerically in SciPy using Fourier integrals. These values differ by an order of magnitude and consequently serve to explain the apparent discrepancy between the functional form of $d_{33}(x)$ and the behaviour of the peaks observed via XRD measurements.

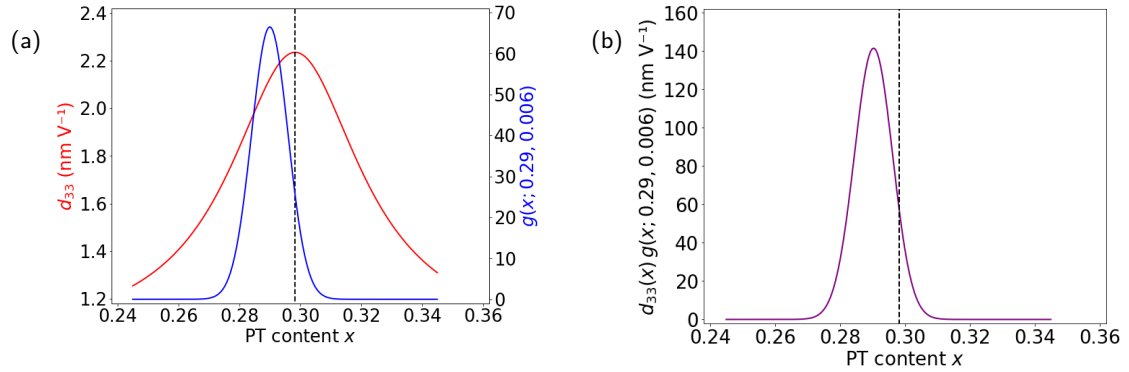


Figure 8.3: The scaled Lorentzian piezoelectric coefficient function fit to the data in Figure 3.13 overlaid by the proposed Gaussian distribution in x , with the boundary between rhombohedral and monoclinic ordering indicated by the black dashed line. (a) The two distributions on the same x -axis. (b) The product of the two distributions, where the areas under the curve on each side of the black dashed line provide the effective piezoelectric coefficient for each crystal phase of PMN-PT.

Infinite limits were used in equations (8.6) and (8.7) in lieu of the physical limits of 0 and 1. The peak is far from the limits thus the curve will be negligible for $x < 0$ and $x > 1$ and so the difference is negligible. More significantly, Figure 3.13 shows that above $x = 0.34$ the true behaviour of OFF-field $d_{33}(x)$ strays from the fitted functional form, and instead climbs towards a local maximum at the $Cm-Pm$ boundary. However, setting the upper integration limit to 0.34 only affected the 10th decimal place of the result due to the value of the Gaussian being negligible for such stoichiometries. Consequently, these physical limits need not be accounted for in the mathematical treatment.

8.2.2 Theoretical distribution of ferroelectric parameters

The Gaussian distribution determined in Section 8.2.1 may be used to model the expected distributions of the coercive fields $E_{c,3}(x)$ and piezoelectric coefficients $d_{33}(x)$ observed across the PMN-PT sample surface. The coercive field distribution may simply be determined by plotting the Gaussian distribution in x against the corresponding coercive field values using the logarithmic dependence of $E_{c,3}$ on x discussed in Section 3.7.2. The normalised distribution of the coercive field assuming a modal value of $E_{c,3} = 2 \text{ kV cm}^{-1}$ is shown in Figure 8.4

The half-width at half maximum of the log-normal coercive field distribution is 0.03 kV cm^{-1} to one significant figure and the crystal phase boundary is located at 2.04 kV cm^{-1} . These values and the figure itself show that only minimal variation is expected in the coercive field and thus very precise

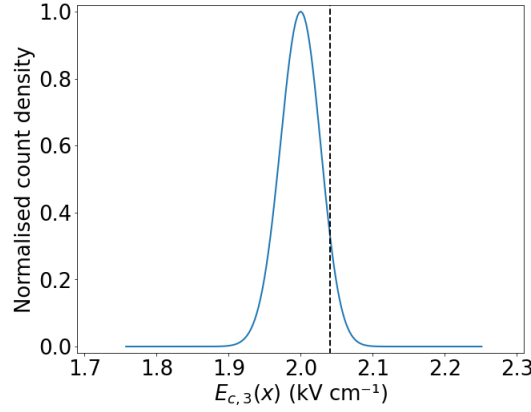


Figure 8.4: The expected distribution of coercive field $E_{c,3}$ within the PMN-PT sample, with only minor skewing of the Gaussian such that the tail to the left is marginally longer than the tail to the right. The black dashed line corresponds to the phase boundary x_{rm} and is located at 2.04 kV cm^{-1} .

measurements must be made to characterise the sample surface.

The distribution of the OFF-field piezoelectric coefficient $d_{33}(x)$ may also be modelled but is complicated by the lack of a monotonic relation between d_{33} and x , due to the peak at $x = x_{rm}$. The histogram may be obtained by reflecting the Gaussian density distribution in this line and adding it to the unreflected distribution. It is known that reflecting a general function $f(x)$ in the line $x = x_0$ yields $f(2x_0 - x)$, thus the histogram of $d_{33}(x)$ follows the distribution

$$g(x; 0.29, 0.006) + g(2x_{rm} - x; 0.29, 0.006) \quad (8.8)$$

and transforming the x -axis into d_{33} using the scaled Lorentzian fit produces the distribution shown in Figure 8.5.

The figure shows that the distribution is predominantly rhombohedral, although there is expected to be a significantly higher occurrence of the larger $d_{33}(x)$ values due to the monoclinic contribution. However, this histogram can not be produced by simply performing standard PFM amplitude measurements because the amplitude when the field is driven using $V_{AC} = 1 \text{ V}$ is small enough that even a 9% variation is predicted by equation (4.80) to just be $\sim 1 \text{ pm}$. This is below the measurement precision of the system, and driving at resonance does not resolve this issue because variation in resonance frequency may also affect observed amplitude contrast. Furthermore, the drive amplitude can not be set to higher values such as $V_{AC} = 10 \text{ V}$ because the AFM is unable to sweep this voltage at the requisite frequency for characterisation. As a result the sample must be characterised through coercive field values obtained using field-spectroscopy, as stated in Section 8.1.

There will only be significant variation in coercive field $E_{c,3}(x)$ and piezoelectric coefficient $d_{33}(x)$ if

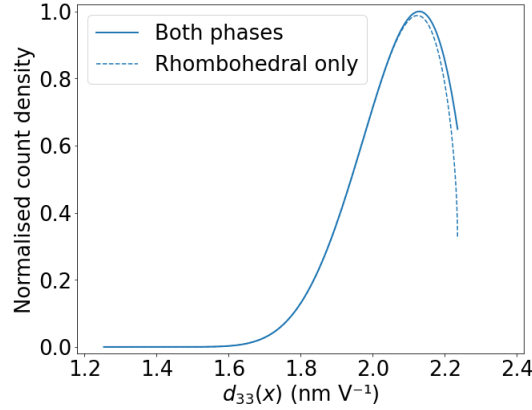


Figure 8.5: The expected distribution of OFF-field piezoelectric coefficient d_{33} within the PMN-PT sample up to the maximum value of 2.24 nm V^{-1} . The modal value is 2.13 nm V^{-1} with a half-width at half maximum of 0.19 nm V^{-1} or 9% of the mode. The dashed line is solely the unreflected distribution and describes the rhombohedral contribution.

the PT concentration x forms distinct ‘domains’ of constant value. Inhomogeneity and crystallographic domains are known to exist due to the twin peaks seen in Figure 8.1, because monoclinic regions may only form where the local average value of x is above the x_{rm} threshold over a sufficiently large area that the rhombohedral regions do not enforce rhombohedral ordering through lattice strain. The existence of these constant domains is not surprising given the binary nature of being either rhombohedral or monoclinic. However, d_{33} and $E_{c,3}$ depend on x continuously thus any contrast is expected to be much more subtle.

Recall from Section 4.8.2 that PFM measurements of these ferroelectric parameters are averaged over the $1.7 \mu\text{m}$ PFM characterisation depth^[147], and thus if the variation in x occurs over a distance significantly smaller than this depth then the surface will appear to be ferroelectrically homogeneous. Alternatively, if the characterisation depth is instead mostly constant in x then domains will appear in the $E_{c,3}(x)$ data, from which the distribution of x and $d_{33}(x)$ may be derived. This means that PFM can determine whether or not there is variation over a distance greater than $\sim 100 \text{ nm}$, but cannot differentiate between short-range variation and homogeneity. However, the lattice strain on such length scales is likely to be sufficient that any variation in local piezoelectric response would be significantly suppressed. This means that if no contrast is observed via PFM then variation in local PT concentration is not likely to be a concern for composite multiferroics grown upon PMN-PT substrates, provided that the surface distribution is the same as the depth distribution.

The high-voltage measurements required to perform field-spectroscopy over a sample of this thickness are not simple to perform and require new methodologies to be developed and evaluated. This is further compounded by the high electrical permittivity of relaxor ferroelectrics which result in significant

capacitive forces acting on the AFM probe. Theoretical models must now be developed regarding the field-dependence of ferroelectric properties of the sample and the ensuing capacitive contributions, and these must then be considered in the context of AFM probe dynamics prior to the experimental work being performed.

8.3 Theoretical electrostatic probe dynamics for homogeneous relaxors

Section 4.7 introduced the electrostatic forces acting on an AFM probe due to the capacitor formed by the tip and sample stage. This is particularly significant when working with high potentials or high capacitive gradients, and the latter occurs whenever dielectrics have high electrical permittivity. The result is that any high field measurements or characterisation of relaxor ferroelectrics will result in notable electrostatic effects.

8.3.1 Polarisation and relative electrical permittivity

The expression for ferroelectric polarisation was given as equation (2.129) in Section 2.13.1 to be

$$P_3(E_3) = P_{\text{sat},3} \tanh[a_3(E_3 \mp E_{c,3})]$$

where the weighting constant a_3 was given in equation (2.132) to be

$$a_3 = \frac{1}{E_{c,3}} \operatorname{arctanh}\left(\frac{P_{r,3}}{P_{\text{sat},3}}\right).$$

The saturation ($P_{\text{sat},3}$) and remanence ($P_{r,3}$) polarisation values in the literature for PMN-PT with $0.28 < x < 0.30$ have approximate ratio^[186;9]

$$\frac{P_{r,3}}{P_{\text{sat},3}} \approx 0.75 \quad (8.9)$$

which means that for the PMN-PT sample under investigation,

$$a_3 \approx \frac{1}{E_{c,3}}. \quad (8.10)$$

This implies that electric dipoles may begin to reverse as soon as the applied field opposes the polarisation direction, which is not an unexpected result. In order to simplify the data analysis the value of a_3 was allowed to fit as a free parameter rather than fitting the more physical $P_{r,3}$. The PMN-PT sample under investigation in this work has a coercive field of $E_{c,3} \sim 2 \text{ kV cm}^{-1}$ ^[7] and so the theoretical normalised polarisation

$$\frac{P_3(E_3)}{P_{\text{sat},3}} = \tanh[a_3(E_3 \mp E_{c,3})] \quad (8.11)$$

is shown in Figure 8.6.

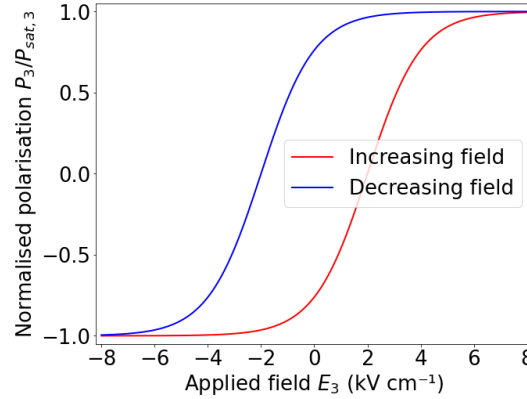


Figure 8.6: The theoretical normalised polarisation for the PMN-PT sample under investigation.

A significant consequence of this is the distinctly non-linear relative electrical permittivity, which was given in equation (2.130) of Section 2.13.1 to be

$$\varepsilon_{r,33}(E_3) = \frac{a_3 P_{\text{sat},3}}{\varepsilon_0} \text{sech}^2[a_3(E_3 \mp E_{c,3})] + 1.$$

The electrical permittivity will feature prominently in this analysis and so this behaviour must be considered. The saturation polarisation $P_{\text{sat},3}$ is unknown but typical values for relative electrical permittivity are $\varepsilon_{r,33}(0) \sim 5000$ ^[113;186;9] for PMN-PT with coercive field $E_{c,3} \sim 10 \text{ kV cm}^{-1}$ so $P_{\text{sat},3} \sim 0.1 \text{ C m}^{-2}$. This is not a rigorous determination, but does provide a value for modelling work and for the fitting algorithm as an initial estimate. Using this value the theoretical relative electrical permittivity was plotted in Figure 8.7.

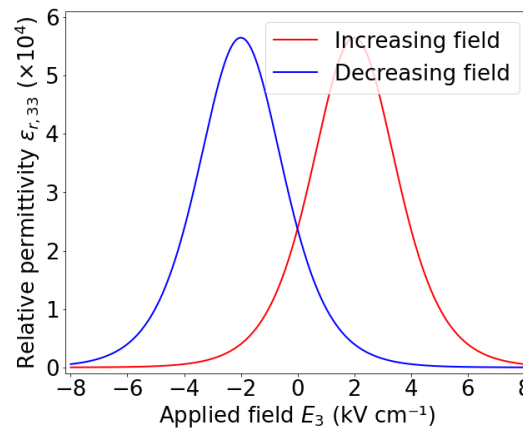


Figure 8.7: The ferroelectric dependence of the relative electrical permittivity of the PMN-PT sample on applied electric field.

These peaks show unusually large electrical permittivities close to the coercive field, meaning the many functions which depend on electrical permittivity will be directly dependent on the past and present values of the applied field via polarisation direction. One such function is electrostriction and hence

PMN-PT has an unusually large electrostrictive response to an applied field. Additionally, this response is highly dependent on polarisation direction which is notable because electrostriction is usually observed to be independent of the polarisation direction. Thus the observed electrostrictive behaviour manifests as a restoration of the longitudinal piezoelectric effect which was suppressed due to the pseudocubic centrosymmetry of PMN-PT.

The total piezoelectric effect $d_{33} = d_{33}^Q + d_{33}^S$ may also be modelled by using the approximate electrostriction coefficient $Q_{33} = 0.033 \text{ m}^4 \text{ C}^{-2}$ ^[187] and the expression for d_{33}^Q in equation (2.126) to yield

$$d_{33} = 2Q_{33}P_3\varepsilon_0 (\varepsilon_{r,33} - 1) + d_{33}^S, \quad (8.12)$$

where superscript Q denotes the electrostrictive contribution and superscript S denotes the shear contribution. The shear coefficient d_{33}^S is expected to tend to zero away from the phase boundary, thus the peak seen for d_{33} against x in Figure 3.13 is likely formed from a Lorentzian curve for d_{33}^S and some baseline for d_{33}^Q . Equation (2.126) is shown for the PMN-PT sample with $x = 0.29$ and a range of field values in Figure 8.8a. This shows hysteretic piezoelectric behaviour which falls off with electrical permittivity, because it describes the ability of a medium to support polarisation and the electrostriction-originated longitudinal piezoelectric effect may only manifest in strongly poled crystals. Figure 8.8b shows the dependence of OFF-field electrostriction on the PT content x , where $a = 1/E_{c,3}$ was used thus both $E_{c,3}$ and a varied with x . This does not show exact agreement with the constant baseline of the fit to Figure 3.13, which was found to be $(1.02 \pm 0.12) \text{ nm V}^{-1}$, but this is not concerning because the data that were fitted to do not show the baseline behaviour either side of the Lorentzian peak thus the assumption of a constant value may not necessarily be accurate. Additionally, the model and the fit both produce similar values for d_{33}^Q .

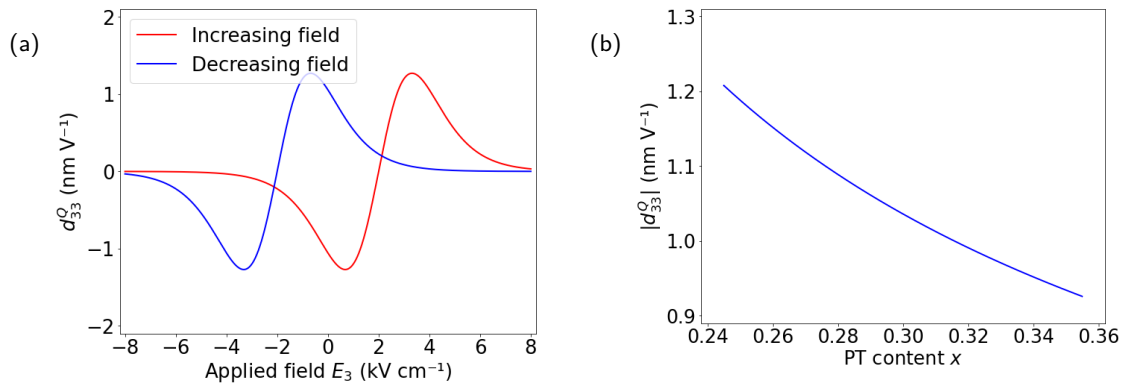


Figure 8.8: The derived distribution of the electrostriction originated longitudinal piezoelectric effect d_{33}^Q . (a) The hysteretic dependence of d_{33}^Q on applied field E_3 . (b) The dependence of the absolute value of d_{33}^Q on PT concentration x ; the sign of d_{33}^Q depends on the relative polarisation direction.

The functional form for d_{33}^S was determined empirically using data from Turik et al.^[68] for a PMN-PT

sample with $x = 0.30$ which is shown in Figure 8.9a. The initial ansatz was that due to the polarisation dependence the strain equation would use a sigmoid of amplitude $d_{33,0}^S$, yielding

$$S_3^S = d_{33,0}^S \tanh[a_3(E_3 \mp E_{c,3})] E_3 \quad (8.13)$$

with corresponding differential shear piezoelectric coefficient

$$d_{33}^S = d_{33,0}^S \tanh[a_3(E_3 \mp E_{c,3})] + d_{33,0}^S a_3 E_3 \operatorname{sech}^2[a_3(E_3 \mp E_{c,3})] . \quad (8.14)$$

This was modelled against applied field for the PMN-PT sample and it was observed that rather than removing the peaks from Figure 8.8a which did not match the data in Figure 8.9a, they were instead made larger. This was attributed to the second term of equation (8.14) so the sign between the terms was reversed to yield

$$d_{33}^S = d_{33,0}^S \tanh[a_3(E_3 \mp E_{c,3})] - d_{33,0}^S a_3 E_3 \operatorname{sech}^2[a_3(E_3 \mp E_{c,3})] . \quad (8.15)$$

and the resulting piezoelectric model becomes

$$d_{33} = 2Q_{33}P_3\varepsilon_0(\varepsilon_{r,33} - 1) + d_{33,0}^S \tanh[a_3(E_3 \mp E_{c,3})] - d_{33,0}^S a_3 E_3 \operatorname{sech}^2[a_3(E_3 \mp E_{c,3})] . \quad (8.16)$$

Substituting in equations (2.129) and (2.130) yields the full piezoelectric model of

$$\begin{aligned} d_{33} = & 2Q_{33}P_{\text{sat},3}^2 a_3 \tanh[a_3(E_3 \mp E_{c,3})] \operatorname{sech}^2[a_3(E_3 \mp E_{c,3})] + d_{33,0}^S \tanh[a_3(E_3 \mp E_{c,3})] \\ & - d_{33,0}^S a_3 E_3 \operatorname{sech}^2[a_3(E_3 \mp E_{c,3})] \end{aligned} \quad (8.17)$$

which is shown in Figure 8.9b. The fit to Figure 3.13 gave $d_{33}(x = 0.29) = 2.12 \text{ nm V}^{-1}$ and the electrostriction model in Figure 8.8b gave $d_{33}^Q = 1.06 \text{ nm V}^{-1}$, so for the sample under investigation the predicted value of $d_{33,0}^S$ is 1.40 nm V^{-1} . Figure 8.9 shows that the derived model for piezoelectric coefficient d_{33} very closely reflects the values and shape of the results in the literature which suggests the functional form and the relative weighting of contributors are reasonable. Approximating the model for $d_{33}^Q(x)$ in Figure 8.8b with a horizontal line, thus approximating $d_{33}^Q(x)$ as constant over $0.25 < x < 0.35$, yields a predicted baseline of $(1.04 \pm 0.07) \text{ nm V}^{-1}$ for the Lorentzian fit, which agrees extremely well with the fit obtained here. This result suggests that the model is accurate and the values of $P_{\text{sat},3}$, Q_{33} , and a_3 used here are close to the true values of the sample, as well as supporting the relation between $E_{c,3}$ and x determined in Section 3.7.2 including the correction for sample thickness.

The functional form shown in Figure 8.9 suggests that using field-spectroscopy to measure d_{33} via strain characterisation may allow the local coercive field to be determined despite the electrostatic effects. The curve displays a clean single feature centred at the coercive field with exact shape dependent on the relative magnitudes of Q_{33} and $d_{33,0}^S$. A relatively large electrostriction coefficient produces a curve similar to a single period of a sinusoid whilst a relatively small value produces a curve similar to a sigmoid.

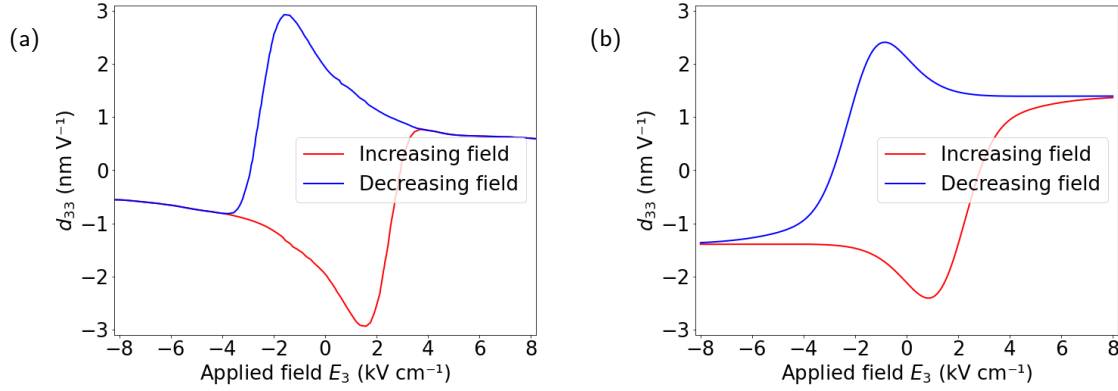


Figure 8.9: The ferroelectric dependence of the total piezoelectric response d_{33} of PMN-PT on applied electric field E_3 . (a) Measured piezoelectric coefficient of PMN-PT with nominal $x = 0.30$, adapted from Turik et al^[68]. (b) The derived model for $x = 0.29$ generated using values from the literature.

8.3.2 Field between probe and ground

In all prior discussions it has been assumed that the electric field E_3 between the electrically conducting AFM tip and the grounded sample stage at some potential V_{DC} over an insulating sample of thickness z_0 is the constant value

$$E_3 = \frac{V_{DC}}{z_0} \quad (8.18)$$

as observed for parallel field lines such as in a parallel plate capacitor^[58]. However, this has not been justified for this system and due to the probe size and distance from the stage it is tempting to replace this with the divergent Coulomb field from an isolated point charge which is^[58]

$$E_3(z) = \frac{CV_{DC}}{4\pi\epsilon_{33}z^2} \quad (8.19)$$

and is further complicated by the strong recursive dependence of electrical permittivity on electric field.

Fortunately, in this situation the naive assumption proves to be the correct one. The surface charge density of a biased tip produces an electric field perpendicular to its surface which induces an opposing charge density distribution in the sample stage. The locally-homogeneous charge distribution of the stage, which is a large flat conductor, then produces a corresponding electric field of parallel lines perpendicular to the surface. These sum to the diverging field lines from the probe to form approximately parallel lines within the sample which only curve to the surface of the tip locally. However, the field lines further from the apex will not be parallel due to the divergence of the field emanating from the tip becoming non-negligible. The tip-stage field lines are shown schematically in Figure 8.10. The parallel field expression given in equation (8.18) may be used to describe the field directly below the apex where the local geometry is approximately flat. Any effects which raise the probe from the surface by deflections $\Delta z \ll z_0$ would not have a significant effect on electrostatic behaviour, especially near

the coercive field, because the electrical permittivity of the air is up to four orders of magnitude smaller than the electrical permittivity of PMN-PT rendering the contribution of the air to be negligible.

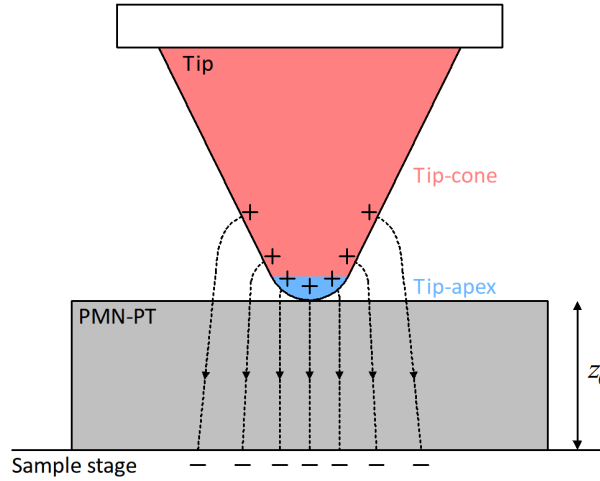


Figure 8.10: The schematised electric field lines passing through PMN-PT between a positively charged tip and negatively charged stage. The field lines close to the apex are parallel, however the divergence of the tip field means that the tip-stage field lines away from the apex maintain residual curvature throughout. The conical region (tip-cone) and spherical apex (tip-apex) of the tip are indicated, and the sample thickness z_0 is labelled. The induced surface charges within the PMN-PT sample have been omitted.

While the field lines are approximately parallel directly below the tip, the diverging field lines further away from the apex means that the probe will be affected by the electrical permittivities of regions adjacent to the image site. However, the increased path length decreases the field strength, which reduces the electrostatic forces and ensures that the strongest field remains focussed directly below the probe. A more pressing concern arising from the capacitive forces is the fact that the electrical permittivity is being averaged across the $250\text{ }\mu\text{m}$ sample thickness, thus the capacitive response will inherently be centred at the mean coercive field of the whole sample rather than centring at the particular coercive field of the surface.

8.3.3 Capacitive probe deflection

Section 4.7.1 discussed the capacitive forces experienced by a biased AFM probe located above a grounded conducting surface. The dependence of the relative electrical permittivity of a ferroelectric on the applied field was then introduced in Section 8.3.1, and these two concepts must now be combined to consider the probe dynamics when the capacitor dielectric is a ferroelectric medium, instead of air. The response of four different probes will be considered throughout this section and the spring constants and geometries of these are summarised in Table 8.1. The PMN-PT parameters used for the theoretical

model have already been established in this chapter, and are $P_{\text{sat},3} \approx 0.1 \text{ C m}^{-2}$, $1/a_3 = E_{c,3} = 2 \text{ kV cm}^{-1}$ and $z_0 = 250 \mu\text{m}$. The typical AC potential applied during measurement is $V_{AC} = 0.5 \text{ V}$ and in these figures the electric field E_3 is being increased while applied to a negatively polarised crystal; the plots may be mirrored in the zero field axis to yield the reverse configuration. These models will also neglect the fine detail of the contact potential difference V_{cpd} and instead approximate it with the applied DC potential V_{DC} .

Name	Composition	k (nN nm ⁻¹)	h_t (μm)	r_t (nm)	α (°)
AD-40-AS ^[159]	Boron doped diamond	40	12.5	10	22.5
RMN-25PT300B ^[124]	Platinum	18	80	20	20
SCM-PIT-V2 ^[119]	PtIr coated silicon	3.0	12.5	25	20
PFTUNA ^[119]	PtIr coated silicon nitride	0.4	5.25	25	17.5

Table 8.1: The spring constant k , tip height h_t , tip radius r_t , and tip side-angle α of each of the four electrically conductive probes which shall be considered in this section.

The first consideration is the capacitance of the tip-stage system. The capacitances of the conical region (tip-cone) and spherical apex (tip-apex) of the tip were provided in Section 4.7.1 as equations (4.63) and (4.67) respectively, and evaluating these at $z = z_0$ with electrical permittivity calculated using equation (2.130) yields Figure 8.11. These show that the capacitance and thus the charge stored on the probe becomes negligible away from the coercive field, and that perhaps unsurprisingly the apex contribution is always negligible when considered alongside the contribution of the tip-cone.

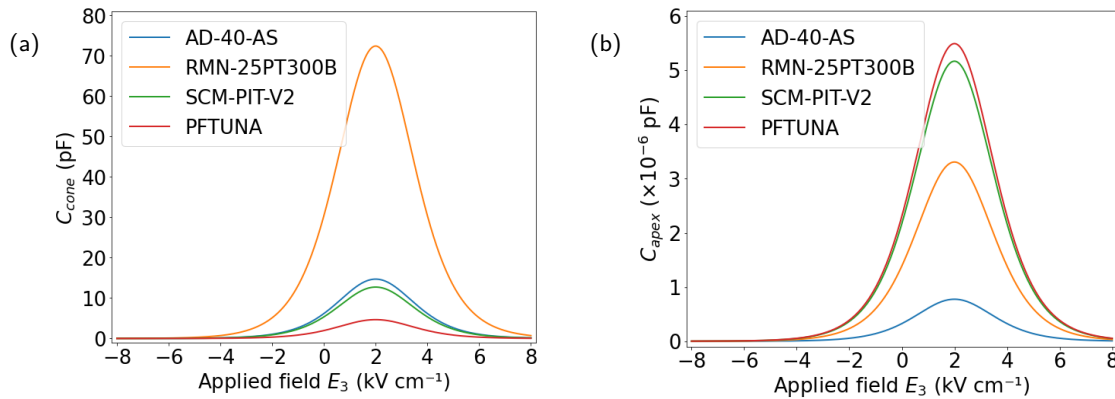


Figure 8.11: The dependence of tip-stage capacitance on applied field for four AFM probes. (a) The tip-cone contribution. (b) The tip-apex contribution.

A more relevant measure for force considerations is the capacitance gradient of the tip-stage system evaluated at the tip-sample contact. This may be obtained by evaluating equations (4.62) and (4.66) at $z = z_0$ which yields Figure 8.12. These values are negative, as expected, and show the apex contribution

to once again be negligible whilst the cone contribution is clearly strongly dependent on its height, even more so than the absolute capacitance.

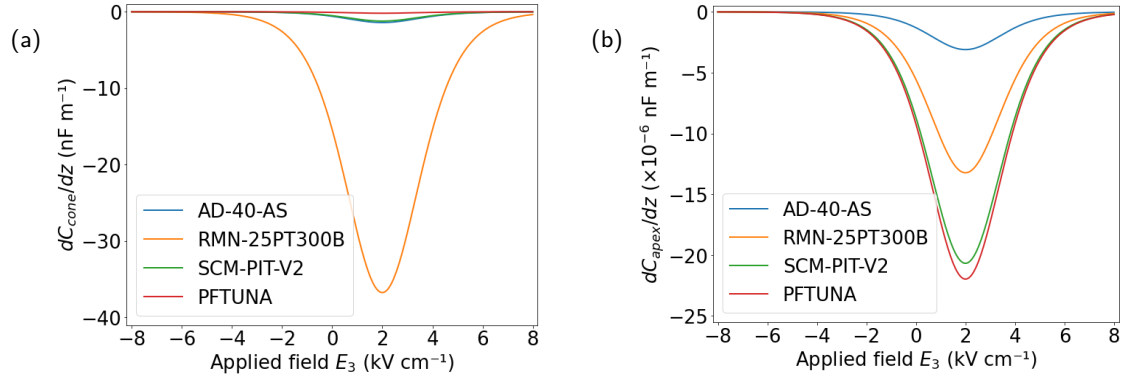


Figure 8.12: The dependence of tip-stage capacitance gradient on applied field for four AFM probes. (a) The tip-cone contribution. (b) The tip-apex contribution.

The constant force on the tip and the resulting probe deflection may be determined using the capacitance gradient of the cone and evaluating equation (4.69) at $z = z_0$ to yield Figure 8.13. The force in Figure 8.13a is clearly strongest for the RMN-25PT300B probe due to the particularly large cone height, but the large spring constant reduces the induced deflection seen in Figure 8.13b to a more comparable value. Capacitive forces are required to be minimised during PFM characterisation because of the resulting averaging of the measurement over the full sample thickness meaning there may potentially be a different coercive field for piezoelectric and capacitive terms.

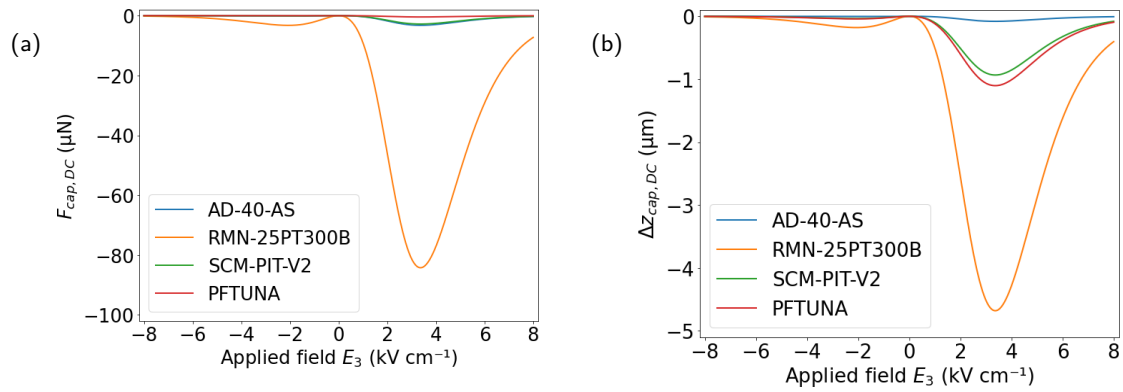


Figure 8.13: The dependence of the DC electrostatic force on applied field for four AFM probes. (a) The DC electrostatic force acting on the probe. (b) The resulting cantilever deflection calculated using the spring constant.

However, the deflections in Figure 8.13b assume the probe is able to move freely. The probe is instead in contact with the surface of the PMN-PT film and so the deformation of the sample must be considered rather than simply using the spring constant. This is calculated using the Hertzian model equations

(4.25) and (4.27) in Section 4.4. The elastic modulus and Poisson's ratio for the sample and the four probes considered in this section are provided in Table 8.2 and the resulting deformations shown in Figure 8.14.

Name	Composition	Elastic modulus (GPa)	Poisson's ratio
PMN-PT	$x = 0.30$ and $x = 0.33$ respectively	56 ^[188]	0.47 ^[189]
AD-40-AS	Boron doped diamond	Infinite	0
RMN-25PT300B	Platinum	171 ^[63]	0.39 ^[63]
SCM-PIT-V2 ^[119]	PtIr coated silicon	210 ^[157]	0.38 ^[157]
PFTUNA ^[119]	PtIr coated silicon nitride	210 ^[157]	0.38 ^[157]

Table 8.2: The elastic modulus and Poisson's ratio of PMN-PT and the four electrically conductive probes considered in this section. The elastic properties of PMN-PT vary significantly with PT concentration x and are rarely discussed in the literature, however the provided values are adequate for order of magnitude demonstrations. The values for diamond are assumed to be negligible relative to PMN-PT so are approximated as in Section 5.5.

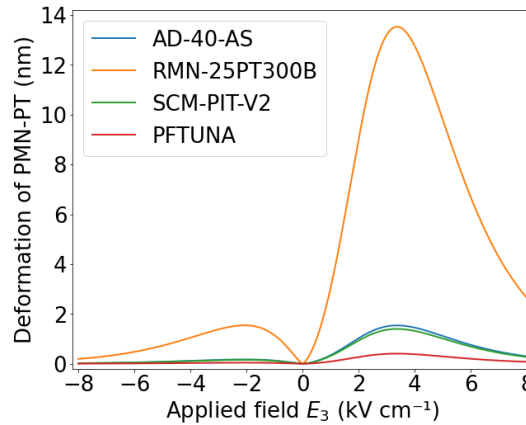


Figure 8.14: The dependence of nanomechanical deformation of a PMN-PT sample on applied field for four AFM probes.

The resulting model shows that the expected capacitive effect on the probe is of the order of nanometres, which is much smaller than Figure 8.13b suggested and so should be small enough that piezoelectric effects are still visible. However, this is just the case of a static field. The AC component of the PFM measurement induces additional forces on the probe, and stiff cantilevers or large tip-heights are likely to not show clear responses as a result.

There is also an AC electrostatic force acting on the probe due to the AC applied field, producing an oscillating deflection described by equation (4.70). This is evaluated for $z = z_0$ and shown in Figure 8.15. This response evidently has the same frequency as the piezoelectric response and thus the lock-in

amplifier cannot remove this signal, meaning this AC signal provides interference which may not even be in phase with the piezoelectric response. Additionally, the phase reverses at $V_{DC} = 0$ so if the AC electrostatic force dominates the piezoelectric response, then the phase data will just show a reversal at the origin rather than at the sample coercive field.

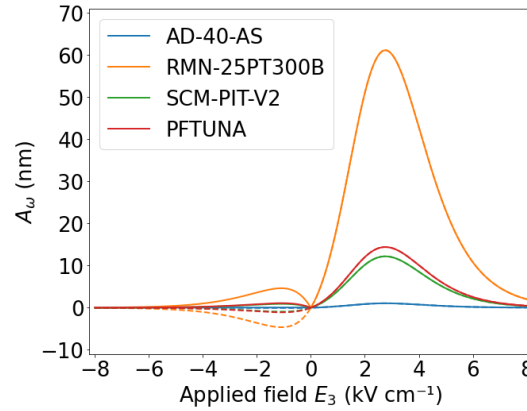


Figure 8.15: The dependence of AC electrostatic deflection on applied field for four AFM probes with a drive amplitude of 0.5 V. The solid line shows the deflection amplitude A_ω while the dashed line shows the full capacitive AC deflection term including phase; the amplitude being positive by definition forces a phase reversal at the origin.

The AD-40-AS probe appears to be an ideal candidate for PFM due to the high k and modest h_t both suppressing the electrostatic forces from having a significant effect on cantilever dynamics. However, in practice this probe is unable to even measure piezoelectric resonance peaks. This is attributed to the spring constant being too high as alluded to in the preceding discussion of sample deformation. The SCM-PIT-V2 and PFTUNA probes both exhibit extremely similar electrostatic deflections, and it is possible that Bruker deliberately calculated the relative spring constants and tip heights for these probes to achieve this. Both of these probes are able to observe resonance peaks, however the SCM-PIT-V2 probe records smaller resonance amplitudes and this is again attributed to the spring constant.

The electrostatic influences should be suppressed for accurate piezoelectric characterisation. Typical measurements are performed over thin samples using lower potentials, and the resulting capacitive deflections are small enough that the spring constant of a rectangular cantilever, such as in the SCM-PIT-V2 probe, may be used to mitigate them. The PMN-PT sample has an unavoidably large capacitive gradient due to the substantial thickness so the spring constant alone cannot solve this, thus small spring constants are ideal to maximise the piezoelectric contribution to the measurement.

Considering the plots in this section does reveal a solution, however: the electrostatic influences are minimal when the DC potential is zero and OFF-field measurements may be used to exploit this. These are measurements where the DC poling field and AC measurement field are split into two distinct steps

as shown in Figure 8.16. A series of DC potential values are applied in turn and reverse some fraction of the electric dipoles each time, which then remain poled when the field is removed thus the polarisation state is the same as if the field were applied. An AC potential may then be used to measure the PFM amplitude and phase whilst the electrostatic force contributions are reduced or removed by the absence of the DC component. The disadvantage of these OFF-field measurements when compared to conventional ON-field measurements is that it is more discretised than just sweeping the applied field smoothly. Switching spectroscopy PFM (SS-PFM) is able to do this automatically at each measurement pixel^[190], but this functionality was only introduced with NanoScope Controller 6. This methodology is analogous to direct current demagnetisation (DCD) measurements of remanence magnetisation.

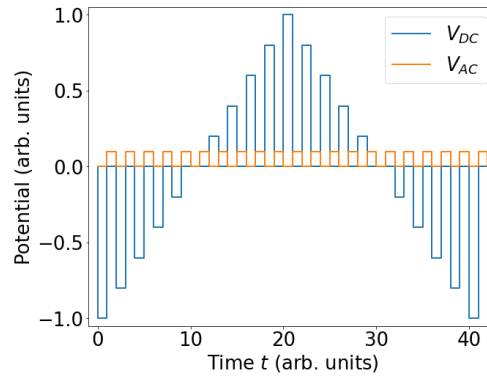


Figure 8.16: DC and AC potentials against time for OFF-field PFM measurements, commencing at an extreme DC value to ensure the sample has a uniform initial polarisation.

Alternatively, it may be possible to record the height of the probe against applied field and fit a modified version of the d_{33} model in equation (8.17) to the result. Electrostatic effects would still be significant and be difficult to quantify, however this method is simpler to automate using either the DataCube PFM mode (DCUBE-PFM) or the Point-and-Shoot tool on the AFM. The latter tool allows a defined sweep to be performed at a series of defined points and saved as individual files, and is an adequate alternative when the more specialised DCUBE-PFM is unavailable. A third approach that was briefly investigated was to characterise the ferroelectric switching current I_{fe} introduced in Section 2.13.1.1. However, the high voltage line is not available in any of the electrical conduction AFM modes which use the PFTUNA application module, and the current is too small to measure using the voltage divider technique developed in Chapter 5.

8.4 Residual surface charges induced by potentials

Following the discussion of capacitance dynamics, other causes of electrostatic interference should also be considered. A simple experiment was performed to determine whether pockets of trapped charges are likely to be induced in the sample surface due to the proximity of the significantly charged tip of the

AFM probe. This involved performing five scans of a $5\text{ }\mu\text{m}$ square area of the surface of the PMN-PT sample using an SCM-PIT-V2 probe with a 6 V DC potential applied, equivalent to 0.24 kV cm^{-1} . The potential was chosen because previous measurements at this value demonstrated anomalies which were believed to be electrostatic in origin.

A PFM measurement was performed prior to the biased scans and the amplitude data is shown in Figure 8.17. The mean amplitude here is $A_s = (14 \pm 6)\text{ pm}$ and thus equation (4.80) may be used to determine the PFM characterisation depth to be $z'_0 = (1.6 \pm 0.7)\text{ }\mu\text{m}$ which agrees very well with the $1.7\text{ }\mu\text{m}$ value in the literature^[147].

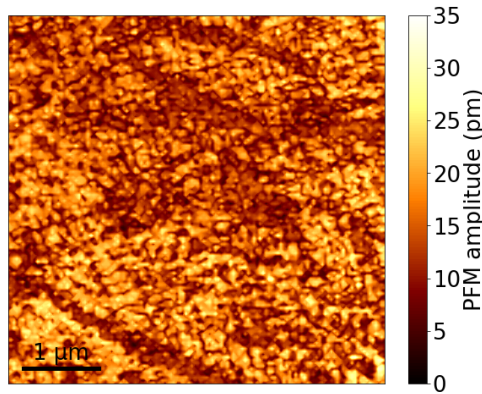


Figure 8.17: Piezoelectric amplitude data obtained using PFM over a square with side length $5\text{ }\mu\text{m}$, with a resolution of 128 pixels per side giving a pixel size of 39 nm . The scan rate was 1.0 Hz and the rounding value was 0.0 giving a scan speed of $10\text{ }\mu\text{m s}^{-1}$. The piezoelectric drive amplitude was 1.0 V at a calibrated drive frequency of 286.1 kHz . The sample was imaged using a Bruker SCM-PIT-V2 probe at a setpoint of $0.10\text{ V} \sim 24\text{ nN}$ yielding a Hertzian contact radius of 1.7 nm .

Following the five scans the potential was removed and a PFM measurement was performed over a $7\text{ }\mu\text{m}$ area to identify any effects with the results shown in Figure 8.18. There was a profound difference in the amplitude data with a distinct square formed at the biased scan location, but no such feature appeared in the topography data thus this is electrostatic in origin. The mean baseline amplitude was determined from the areas surrounding the square to have been marginally raised to $(17 \pm 8)\text{ pm}$, which is essentially unchanged. The charged area is relatively uniform in amplitude value with the only features correlating to topographic artefacts. This means that this charging phenomenon is not likely to be related to the local PT concentration x and thus cannot be leveraged as an alternative characterisation methodology.

The potential from the induced charges may be determined by equating the mean observed amplitude of $(38 \pm 10)\text{ pm}$ from Figure 8.18b to the difference between the electrostatic amplitude from equation (4.57) and the baseline piezoelectric amplitude $(14 \pm 6)\text{ pm}$ from Figure 8.17. The difference is taken rather than the sum due to the two amplitudes being 180° out of phase. This was solved numerically

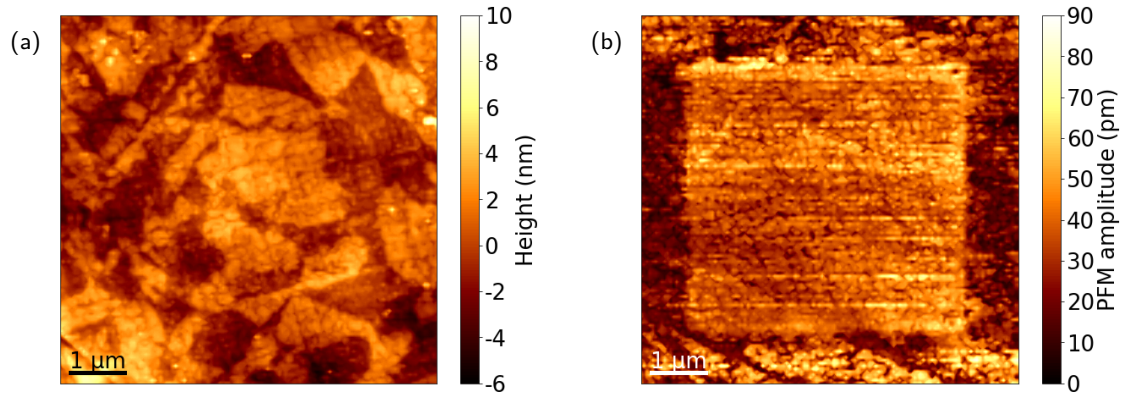


Figure 8.18: Topographic and piezoelectric amplitude data obtained using PFM over a square with side length $7\text{ }\mu\text{m}$, with a resolution of 128 pixels per side giving a pixel size of 55 nm . The scan rate was 1.0 Hz and the rounding value was 0.0 giving a scan speed of $14\text{ }\mu\text{m s}^{-1}$. The piezoelectric drive amplitude was 1.0 V at a calibrated drive frequency of 286.1 kHz . The sample was imaged using a Bruker SCM-PIT-V2 probe at a setpoint of $0.10\text{ V} \sim 24\text{ nN}$ yielding a Hertzian contact radius of 1.7 nm . (a) The topography data. (b) The piezoelectric amplitude data.

because an analytical calculation was not possible due to the combination of polynomial and hyperbolic terms in the expressions, and the result was an induced potential of $(0.30 \pm 0.09)\text{ V}$. The exact value of the calculated injected potential depends on the polarisation direction of the sample via the electrical permittivity, however both polarisation directions yield the same value in this case to the precision provided. This induced potential is low but not negligible, especially for the relatively low applied potential of 6 V , and demonstrates that the surface does indeed become charged when measurements are performed with an applied potential. This phenomenon could offset the measured coercive field values, and during ON-field measurements in particular this mechanism could result in an additional electrostatic term that further obscures the features of interest.

8.5 Strain behaviour of relaxor ferroelectrics during ON-field HV-PFM

It was established in Section 8.3.3 that ON-field measurements will be dominated by capacitive force effects and thus the measured amplitude and phase will not be an accurate representation of the local ferroelectric properties. However, the strain curve may instead be considered because the differential d_{33} shown in Figure 8.9 should still show a prominent feature at the coercive field as discussed in Section 8.3.1. Ideally the strain curve would describe the bow-tie shape shown in Figure 2.37 with the corresponding d_{33} following Heaviside functions, but aside from the homogeneity of the coercive field of the dipoles below the tip there are additional factors such as electrostatic forces and the significant

field dependence of electrical permittivity which prevent this from occurring.

The issue here is that the strain curve is not directly meaningful due to the electrostatic deflections of the AFM probe being unrelated to the strain, a measure of proportional change in probe position. Instead the absolute change in probe height should be considered, and where piezoelectric coefficient curve d_{33} would be obtained by differentiating the strain curve, the differential of the probe height will be analysed instead. Probe height is still not a perfect metric because the true position of the tip would be determined from the sum of probe height and cantilever deflection from this point, with height only being accurate once the feedback loop has adjusted the probe to restore the setpoint value. The deflection error was not able to be captured and so there will be an inherent error in the probe position. The most significant effect is that the field may be swept faster than the height can be adjusted to restore the setpoint, with the result that the height channel simply shows the probe ‘chasing’ the correct position, and this is believed to be partially responsible for the empirical parabolic term which is introduced into the model.

The piezoelectric model for d_{33} in equation (8.17) may be used alongside the definition of piezoelectric coefficient in equation (2.119) to obtain the piezoelectric contributions to height-change and differential height-change to be

$$\begin{aligned} \Delta z_{\text{piezo}} = & -z'_0 Q_{33} P_{\text{sat},3}^2 \text{sech}^2 [a_3 (E_3 \mp E_{c,3})] - \frac{z'_0 d_{33,0}^S}{a_3} \ln \{ \text{sech}^2 [a_3 (E_3 \mp E_{c,3})] \} \\ & - z'_0 d_{33,0}^S E_3 \tanh [a_3 (E_3 \mp E_{c,3})] \end{aligned} \quad (8.20)$$

and

$$\begin{aligned} \frac{\partial \Delta z_{\text{piezo}}}{\partial E_3} = & 2z'_0 Q_{33} P_{\text{sat},3}^2 a_3 \tanh [a_3 (E_3 \mp E_{c,3})] \text{sech}^2 [a_3 (E_3 \mp E_{c,3})] + z'_0 d_{33,0}^S \tanh [a_3 (E_3 \mp E_{c,3})] \\ & - z'_0 d_{33,0}^S a_3 E_3 \text{sech}^2 [a_3 (E_3 \mp E_{c,3})] \end{aligned} \quad (8.21)$$

respectively, where the terms are defined alongside the equations in Sections 2.12.1 and 8.3.1.

The capacitive contribution may be determined by modifying equation (4.69) using equation (2.130), $V_{DC} = z_0 E_3$, and $V_{DC} \gg V_{AC}$, to obtain

$$\Delta z_{\text{cap}} = -\phi \{ a_3 P_{\text{sat},3} \text{sech}^2 [a_3 (E_3 \mp E_{c,3}/2)] + \varepsilon_0 \} E_3^2 \quad (8.22)$$

where

$$\phi \equiv \frac{\pi z_0^2}{k \ln [\tan (\alpha/2)]^2} \left[\frac{h_t}{z_0 + h_t} + \ln \left(\frac{z_0}{z_0 + h_t} \right) \right] \quad (8.23)$$

only contains constant system properties and for simplicity is treated as a single fit parameter. The division of $E_{c,3}$ by 2 is an empirical observation whose origins are not well understood, but is attributed to the complex manifestation of electrostatics across the sample thickness. This contribution differentiates

to yield

$$\begin{aligned} \frac{\partial \Delta z_{\text{cap}}}{\partial E_3} = & 2\phi \left\{ (a_3 E_3)^2 P_{\text{sat},3} \tanh [a_3 (E_3 \mp E_{c,3}/2)] \operatorname{sech}^2 [a_3 (E_3 \mp E_{c,3}/2)] \right. \\ & \left. - a_3 E_3 P_{\text{sat},3} \operatorname{sech}^2 [a_3 (E_3 \mp E_{c,3}/2)] - \epsilon_0 E_3 \right\}. \end{aligned} \quad (8.24)$$

Additional modifications made to these expressions to aid with fitting include treating the term $Q_{33}P_{\text{sat},3}^2$ as a single parameter, and reversing the decreasing-field data so that $-E_{c,3}$ may be fit to all curves rather than handling $\mp E_{c,3}$.

An empirical contribution must also be added to the model, which is a parabolic term dominating the height data obtained via sweeping high potentials. The exact origin of this is not clear, but is likely to be a consequence of phenomena such as charged nanofluid being formed from the high potentials, as discussed in Section 4.8.4, or the probe chasing effect described earlier in this section. This term simply contributes

$$\Delta z_{\text{para}} = \frac{1}{2} \beta E_3^2 \quad (8.25)$$

and

$$\frac{\partial \Delta z_{\text{para}}}{\partial E_3} = \beta E_3 \quad (8.26)$$

to the observed dynamics, where β is some empirical constant.

The expressions for these three contributors are summed to provide the functions Δz and $d\Delta z/E_3$ to be fit to the data. It was explained in Section 8.3.3 that the capacitive contribution will depend on average electrical permittivity of the whole sample below the AFM tip, so the $E_{c,3}$ from the capacitive terms will almost certainly be the mean of the histogram, independent of the surface properties. This means that accurate measurements of the surface may only be achieved when the capacitive contribution is not significant relative to the piezoelectric contribution. It was also explained that the downwards forces acting on the probe are limited by the deformation of the sample surface, so any negative height changes from the capacitive contribution will be smaller than the model suggests. This does not need to be handled directly because the fitting algorithm may simply adjust the value of ϕ to compensate.

Figure 8.19 shows the height-change and differential height-change models derived in this section, plotted over the range of interest. The three contributors are shown for reference, along with the two combinations which are expected to occur. The red curve shows the ideal situation where the capacitance contribution is negligible and demonstrates the need for differentials. The red Δz curve in Figure 8.19a describes a skewed parabola and this shape results in a poor fit due to the lack of distinct features to fit to. However, the differential version in Figure 8.19b features a distinct linear component of gradient β but also a feature akin to a single period of a sinusoid, which is centred at the coercive field and this feature results in a much improved fit. The purple ‘Piezo. & cap. & para.’ curve also benefits from reducing the parabola to a linear term because again the differential accentuates the coercive feature

and improves the fit accuracy. Consequently, when considering the height-change results in this chapter, all data is numerically differentiated prior to analysis and the differential form of the function is used.

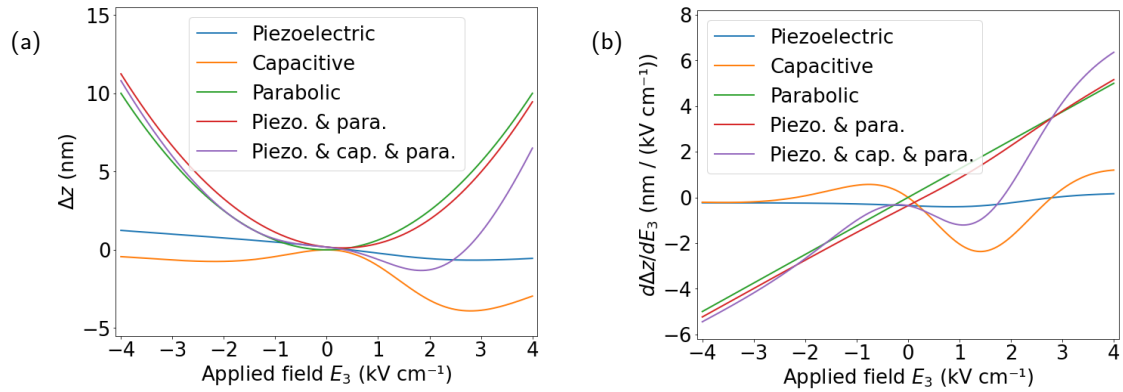


Figure 8.19: Models of the height-change and differential height-change for HV-PFM measurements of PMN-PT. These were calculated using parameter values from the literature, although ϕ was scaled and β was calculated to provide curves which are similar to those measured. (a) The height-change models. (b) The differential height-change models.

8.6 Point-and-Shoot Spectroscopy (PSS)

Spectroscopy measurements performed via Point-and-Shoot will be referred to as Point-and-Shoot Spectroscopy (PSS) for brevity. This methodology involved an automated process whereby the AFM performs a frequency or field sweep at every point of a defined grid and saves the response at each site as an individual file. A Python program is then used to import all of these data into a 3D array using the nanoscope package^[150] and to iterate the analysis over each measured sweep. The DCUBE-PFM mode could do the measurement more efficiently and save the results as a single file, which would also expedite the import into the 3D Python array, however the licence key for this mode was unavailable and the PSS technique serves as an adequate alternative. The number of measurement sites across the grid will be described as the spatial data point density and the number of points per spectroscopy curve will be described as the spectral point density.

The PSS approach has the advantage over scan-based techniques that no drift will occur during the sweep and a high density of spectral data points may be obtained. However, the requirement to lift the probe between measurement sites means that the spatial density is accompanied by a significant time penalty, so grids of just 128 sweeps per side take over 7 hours to complete.

8.6.1 Resonance characterisation

The first characterisation that must be performed on the PMN-PT sample is the resonance frequency f_r . If this is approximately constant across the surface then the drive frequency of the following field-spectroscopy may be set to the piezoelectric resonance frequency in order to maximise the response. The amplitude measurement during ON-field field-spectroscopy is not expected to show piezoelectric behaviour, however setting the drive frequency to resonance frequency does increase the possibility of some piezoelectric feature being observed in the amplitude curve at the coercive field. Alternatively, if the resonance frequency is not constant then this indicates some significant variation in local mechanical properties which would most likely be the consequence of significant variation in x .

The resonance characterisation was performed over a square with side length $5.0\text{ }\mu\text{m}$, with a density of 64 sweeps per side giving a pixel separation of 79 nm . The field drive amplitude was 0.02 kV cm^{-1} and was swept from 100 to 500 kHz and back again at a rate of 1.5 sweeps per second. The spectral measurements were captured over 512 data points which were thus spaced every 0.8 kHz . The AFM probe used was a Bruker PFTUNA probe at a setpoint of $0.10\text{ V} \sim 4.0\text{ nN}$ yielding a Hertzian contact radius of 1.0 nm .

Figure 8.20 shows a pair of example amplitude curves obtained for increasing and decreasing drive frequencies. The quality of the peaks may be improved by decreasing the sweep rate whilst increasing it degrades the curves. There is a lag in the response at higher sweep rates, as seen by the difference in peak positions in Figure 8.20, which disappears for lower sweep rates and increases for higher sweep rates. However, it was observed that the lag is equal in both sweep directions and thus the midpoint of the two peaks is the location of the true resonance. This observation allow higher speed sweeps to be used whilst preserving the reliability of the result, thus the chosen sweep rate was an optimisation between total measurement time and peak quality. A scaled Lorentzian curve was fit to each peak using SciPy and the peak positions were $(218.26 \pm 0.17)\text{ kHz}$ and $(214.31 \pm 0.12)\text{ kHz}$ yielding a midpoint of $(216.25 \pm 0.10)\text{ kHz}$.

The resonance frequency of each measurement point was determined by fitting a Lorentzian peak to all captured amplitude curves and calculating the midpoint of the two peaks at each site, with the resulting values shown in Figure 8.21; a Lorentzian function was chosen rather than a Gaussian because it provided a better fit to the data. The contour plot shows a constant resonance frequency with no contrast visible across the surface, whilst the histogram very clearly displays a single peak and a Lorentzian fit to it yields a peak position of $(218.389 \pm 0.007)\text{ kHz}$ and half-width at half maximum (HWHM) of $(0.347 \pm 0.011)\text{ kHz}$. A useful metric to summarise the histogram data is to combine the two values, using the HWHM as a measure of distribution, to obtain $(218.4 \pm 0.3)\text{ kHz}$. This narrow variation of $\pm 0.14\%$ across the PMN-PT surface demonstrates an approximately constant resonance

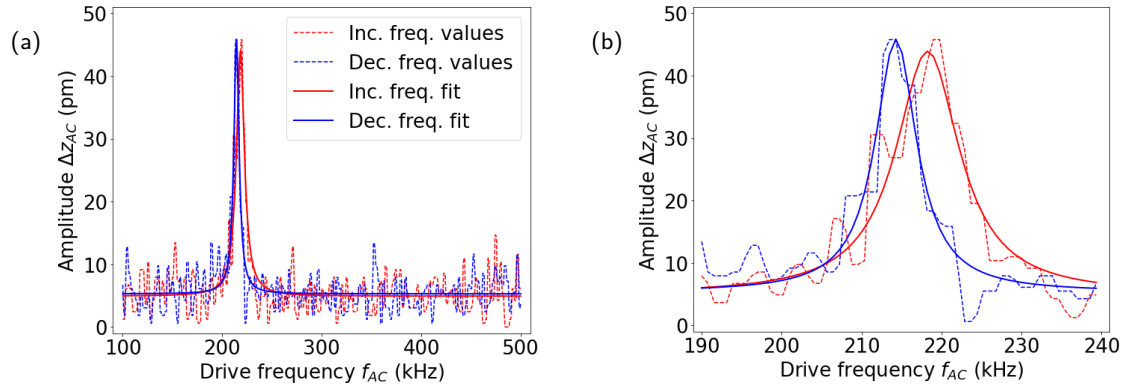


Figure 8.20: Example piezoelectric resonance curves obtained by sweeping the drive frequency from 100 to 500 kHz and back. (a) The full resonance measurement. (b) The results cropped to show the details of the peaks.

frequency, and the complete lack of contrast implies minimal variation in PT concentration x . The asymmetry in the peak implies that a slight bimodality may be present, however the resolution of the data is too poor to conclude anything regarding this.

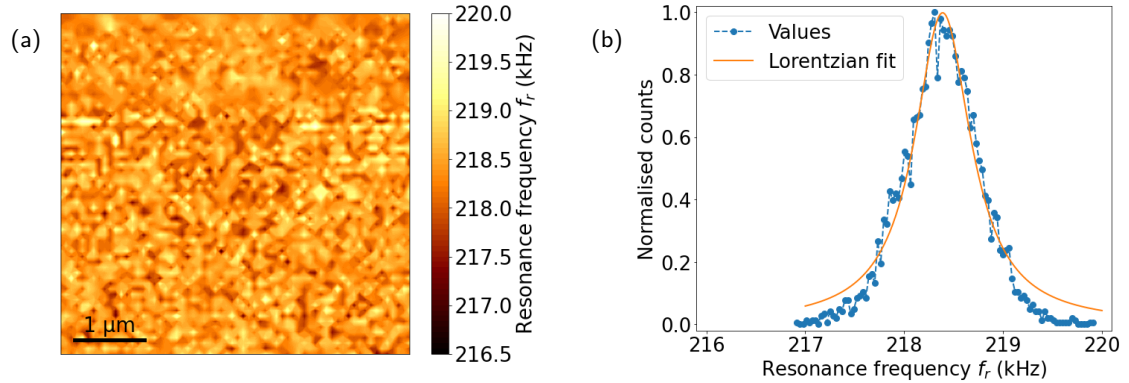


Figure 8.21: PSS characterisation of resonance frequency over a 5 μm square of the PMN-PT sample. (a) Contour map of the resonance frequency across the surface. (b) Histogram of the results with Lorentzian fit.

8.6.2 Coercive field characterisation

Following the successful implementation of PSS on the simpler resonance curves the field-spectroscopy measurements were carried out. The methodology was similar to the frequency-spectroscopy performed in Section 8.6.1 except the swept parameter is now the applied DC field E_3 . The data were imported into Python and each curve was numerically differentiated by fitting a straight line to each rolling group of 21 data points and allocating the gradient to the midpoint; 21 was an optimisation between processing time and the accuracy of the differentiation and does mean that the first and last 10 data points are

lost. The function derived in Section 8.5 was fitted to these results using literature values as initial estimates, with the exception of the ϕ estimate, which was scaled as in the model; the β estimate, which was obtained by first fitting a straight line to the data; and the $E_{c,3}$ estimate, which was set to 0 kV cm^{-1} to ensure that any non-zero values of $E_{c,3}$ were the result of real features.

Two field-spectroscopy characterisations were performed and analysed using PFTUNA probes, and the sites used will be labelled site A and site B. At both sites the DC field was swept over the range $-3.67 \text{ kV cm}^{-1} \leq E_3 \leq 3.67 \text{ kV cm}^{-1}$, chosen because the limits are approximately double the expected coercive field. The sweep can not start at 0 kV cm^{-1} because the sample is initially unpoled and so the region being characterised must be poled at the start of each sweep.

The characterised area at site A was a square with side length $5.0 \mu\text{m}$, with a sweep density of 72 sweeps per side giving a separation of 70 nm between each measurement. The piezoelectric drive amplitude was 0.02 kV cm^{-1} at a calibrated drive frequency of 222 kHz and the DC field was swept at a rate of 1.0 sweep per second. The measurements were captured over 512 data points which were thus spaced every 0.014 kV cm^{-1} and recorded every 2.0 ms , which is much larger than the switching time. PMN-PT has a mass density of $8.0 \times 10^3 \text{ kg m}^{-3}$ ^[191] so the expected forward-growth time is given by equation (2.134) to be $t_{fg} \approx 69 \text{ ns}$ and thus the side-growth time of $t_{sg} \sim 1 \mu\text{s}$ remains dominant. Switching occurs when $E_3 + E_{AC} \sin(2\pi f_{AC}t) > E_{c,3}$ for longer than the switching time, but $E_{c,3} \sim 2 \text{ kV cm}^{-1}$ and $E_{AC} = 0.02 \text{ kV cm}^{-1}$ so any error in the determined coercive field due to the oscillating field will be less than 1%, which is below the uncertainty in the measurement.

The characterisation at site B mostly used the same settings, however was carried out at the increased spatial density of 128 sweeps per side of the square, giving a sweep separation of 39 nm . The piezoelectric drive frequency for this probe was calibrated to 233 kHz and the DC field sweep rate was increased to 1.4 sweeps per second due to time, so the data points were recorded every 1.4 ms . The setpoint was raised to $1.5 \text{ V} \sim 60 \text{ nN}$ yielding a Hertzian contact radius of 2.4 nm in the absence of capacitive forces.

An example sweep from site A is shown in Figure 8.22. The capacitive contribution is negligible in this case resulting in a skewed parabola in the height-change data as seen in Figure 8.22a. This demonstrates the need for differentiating the curves, because in Figure 8.22b the increasing-field curve shows a feature at approximately 2 kV cm^{-1} where none is visible in Figure 8.22a.

Two example sweeps from site B are shown in Figure 8.23. The capacitive contribution is no longer negligible, and Figure 8.23a demonstrates the empirical $E_{c,3}/2$ term in Δz_{cap} due to the spike being located at $\sim 1 \text{ kV cm}^{-1}$. The capacitive response of the first sweep of this characterisation is much larger than at subsequent pixels, exemplified in Figure 8.23b, which suggests that there are significant electrostatic effects when high potentials are first applied. To mitigate this, preliminary sweeps should

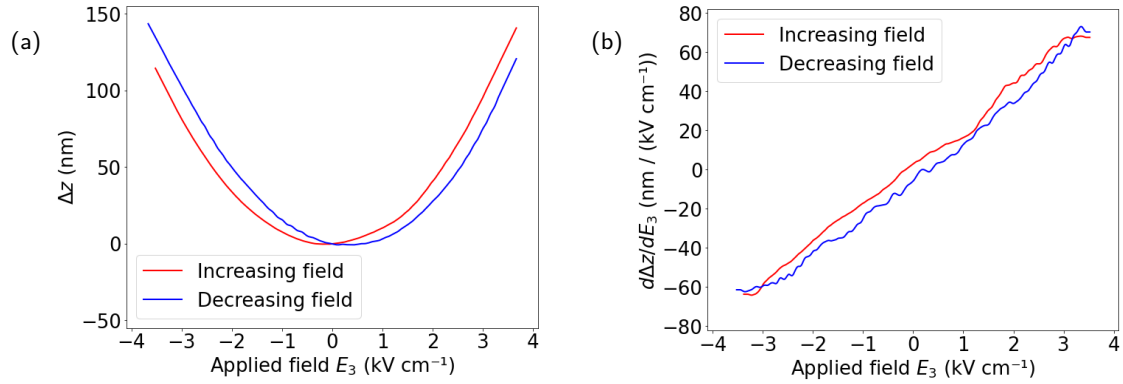


Figure 8.22: An example field sweep from the PSS field-spectroscopy measurement at site A. (a) The height-change curve Δz . (b) The differential height-change curve $d\Delta z/dE_3$.

be carried out prior to full characterisation to allow these initial effects to resolve, and this was done prior to the characterisation at site A. Despite the capacitive contributions introducing distinct features in the Δz curves of these sweeps, the differential still provides a superior fit due to reducing the significance of the parabolic contribution.

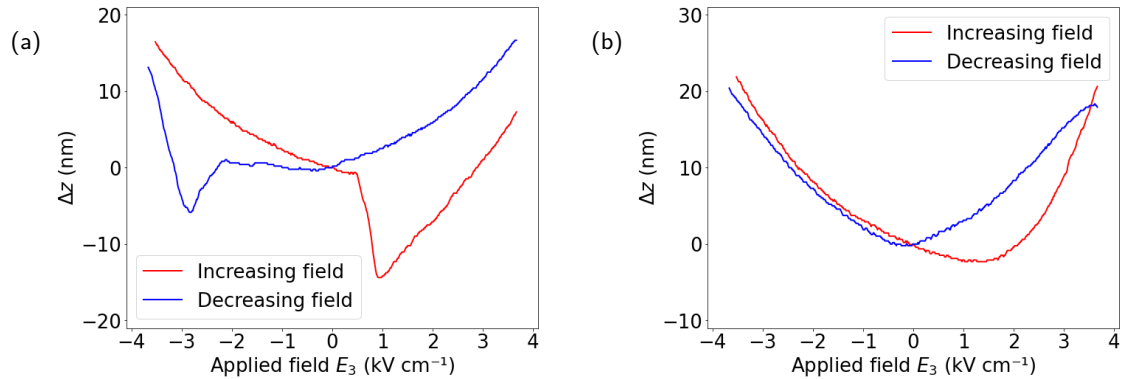


Figure 8.23: Two example field sweeps from the PSS field-spectroscopy measurement at site B. (a) The sweep at the first pixel. (b) The sweep at the diagonally opposite pixel.

Despite showing a seemingly weaker response, the data from the characterisation of site A in Figure 8.22 is more useful due to the absence of the capacitive contribution, which simplifies the fitting process and removes the possible second value of $E_{c,3}$. The weakening of this contribution over successive sweeps is likely due to a residual charge being left at the prior imaging site, as a consequence of the charged nanofluid discussed in Section 4.8.4 or the alternate residual charge mechanism discussed in Section 8.4. This pocket causes additional electrostatic effects and is the expected cause of the weakening capacitive effects and the poor quality decreasing-field curves. In all cases the decreasing-field curves were poorer than the increasing-field counterparts, producing either symmetric curves (Figure 8.23b) or a shunt to the applied field thus moving the apparent coercive field (Figure 8.23a).

8.6.3 Analysis of the PSS measurement at site A

The functions for differential height-change, as defined in Section 8.5, were fitted to all field-spectroscopy sweeps at both sites. However, the capacitive term was only included for the characterisation of site B. The resulting values of coercive field are summarised for the increasing-field sweeps from the characterisation of site A in Figure 8.24. The decreasing-field data for this measurement was poor, suggesting that the surface was disrupted in some way by the increasing sweep. The contour shows no contrast of significance, with the dark central region appearing as a feature in all fit parameters and so is assumed to be a measurement artefact, possibly relating to debris on the AFM tip. The coercive field values extend far beyond the expected range, and these extreme values are indicative of differential curves with no coercive feature but instead a slight curve which the algorithm was able to fit to using a very high $E_{c,3}$ and low a_3 .

The histogram proves to be far more useful, with the peaks being quantified by fitting scaled Lorentzian peaks using SciPy, similarly to the resonance data in Section 8.6.1. The central peak is located at $(2.326 \pm 0.019) \text{ kV cm}^{-1}$ with a HWHM of $(0.65 \pm 0.03) \text{ kV cm}^{-1}$, yielding a summary metric of $(2.3 \pm 0.7) \text{ kV cm}^{-1}$. This is likely to have been formed by the coercive field, however this peak is significantly wider than the expected metric of $(2.00 \pm 0.03) \text{ kV cm}^{-1}$ predicted in Section 8.2.2 and so any contrast would be obscured by the large measurement uncertainty. The difference between measured and expected value for the peak position is likely to be a consequence of the subtle curves and the complicated functions being fitted, rather than a physical phenomenon.

There are two additional peaks observed in the histogram which are consequences of sweeps featuring no clear transition. One is located at $(0.02 \pm 0.02) \text{ kV cm}^{-1}$ with a HWHM of $(0.02 \pm 0.03) \text{ kV cm}^{-1}$, yielding a summary metric of $(0.02 \pm 0.02) \text{ kV cm}^{-1}$, and occurs if the fitting algorithm does not adjust the value from the initial estimate. The second is located at $(3.74 \pm 0.05) \text{ kV cm}^{-1}$ with a HWHM of $(0.36 \pm 0.08) \text{ kV cm}^{-1}$, yielding a summary metric of $(3.7 \pm 0.4) \text{ kV cm}^{-1}$, which is slightly larger than the maximum field of the differentiated data, 3.52 kV cm^{-1} . This is the larger of the two additional peaks, and this value occurs when the fitting algorithm was not able to locate any transition and so placed the coercive field slightly beyond the measurement range.

Despite the lack of nanoscale characterisation this is still a positive result. The coercive field was able to be observed through seemingly featureless parabolae and the results clearly show that this $5 \mu\text{m}$ square of PMN-PT is a ferroelectric with a coercive field of $\sim 2 \text{ kV cm}^{-1}$, which has not previously been demonstrated using AFM on thick samples such as these $250 \mu\text{m}$ PMN-PT substrates.

The empirical parabolic coefficient β was also considered. This is expected to be constant across the sample surface due to the theorised origins being independent of the precise local material properties, and

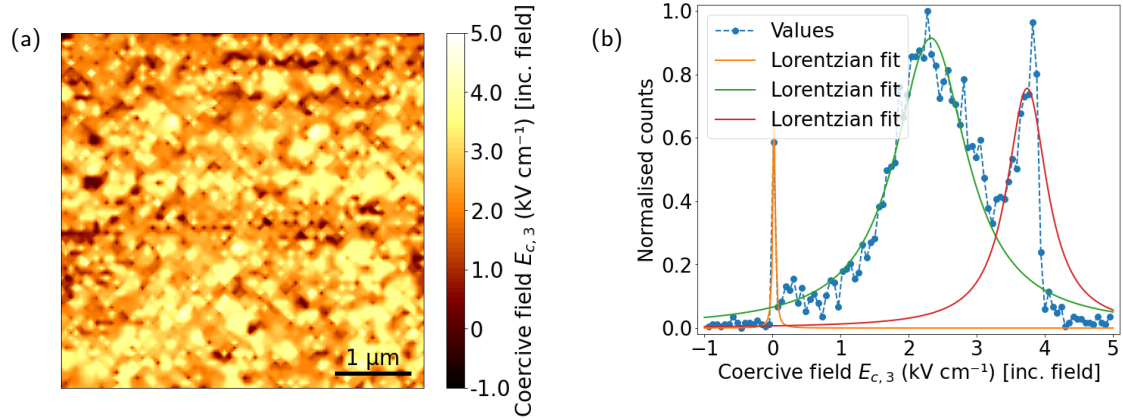


Figure 8.24: PSS characterisation of the coercive field over a $5\mu\text{m}$ square of the PMN-PT sample at site A. (a) Contour map of the coercive field across the surface. (b) Histogram of the results with Lorentzian fits.

as a parameter is well defined and thus easy to fit as a consequence of being the overall gradient of each differential height-change curve. The results are shown in Figure 8.25. The contour plot shows the values to be largely constant, as predicted, but does also show similar contrast to Figure 8.24a and other fit parameters. The histogram shows a single well-defined peak located at $(17.173 \pm 0.009) \text{ pm V}^{-2}$ with a HWHM of $(0.656 \pm 0.012) \text{ pm V}^{-2}$, yielding a summary metric of $(17.2 \pm 0.7) \text{ pm V}^{-2}$, thus confirming the consistency of the fit values.

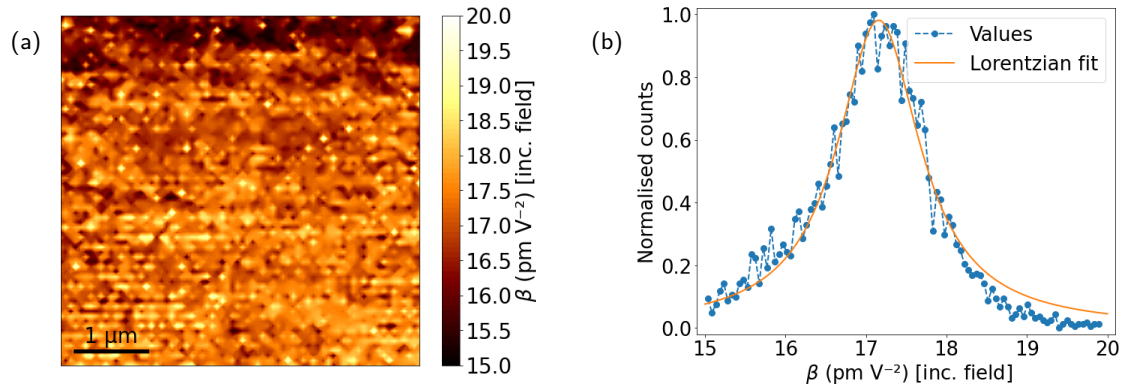


Figure 8.25: PSS characterisation of the empirical coefficient β over a $5\mu\text{m}$ square of the PMN-PT sample at site A. (a) Contour map of the empirical coefficient across the surface. (b) Histogram of the results with Lorentzian fit.

All fit parameters demonstrated similar features in their contour plot, even the theoretically constant β . One advantage of PSS, and also DCUBE-PFM, is that it should be independent of topography and not exhibit any shadowing, however the topography shows a similar contrast. Figure 8.26 shows the topography before and after the PSS measurement; the initial scan in Figure 8.26a shows the

characteristic terraces of PMN-PT but the scan in Figure 8.26b shows that severe disruption of the surface has occurred in the same pattern as the fit coefficients. This correlation coupled with the fact that the disruption is independent of the initial topography suggests that this is a consequence of the charged nanofluid formation discussed in Section 4.8.4. The surface disruption explains why the decreasing-field sweeps failed to yield accurate results and poses a significant problem for all high-voltage sweep-based methodologies such as PSS and DCUBE-PFM.

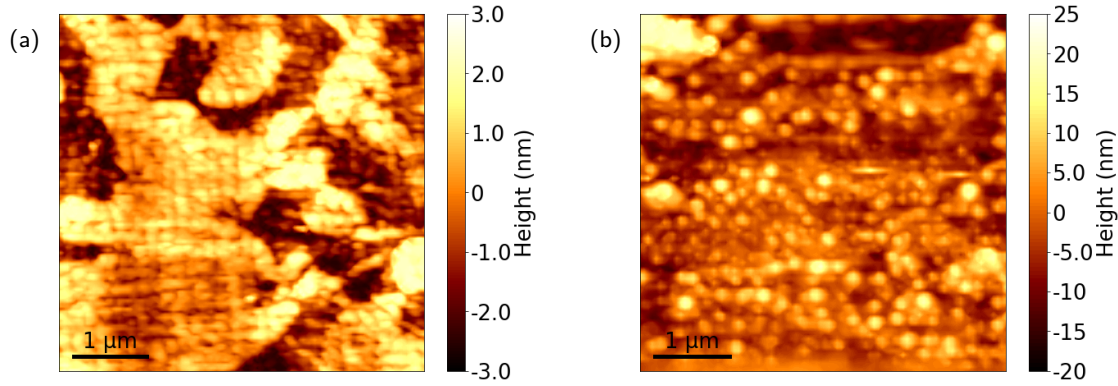


Figure 8.26: The PMN-PT sample surface at site A before and after carrying out PSS field-spectroscopy measurements, captured at a scan size of $5\ \mu\text{m}$. (a) The surface before PSS. (b) The surface after PSS.

8.6.4 Analysis of the PSS measurement at site B

The differential height-change expression was fitted to the PSS characterisation data for site B and the resulting values of coercive field are summarised for the increasing-field sweeps in Figure 8.27. The contour plot in Figure 8.27a is featureless except for the clear artefact in the centre and a subtle underlying contrast, which again appears in all parameter contour plots and suggests that similar surface degradation has occurred.

The histogram in Figure 8.27b demonstrates a clear improvement over Figure 8.24b, with the $0\ \text{kV cm}^{-1}$ peak absent and the $\sim 4\ \text{kV cm}^{-1}$ peak significantly reduced in size. The central peak was determined to be located at $(2.494 \pm 0.007)\ \text{kV cm}^{-1}$ with a HWHM of $(0.360 \pm 0.011)\ \text{kV cm}^{-1}$, yielding a summary metric of $(2.5 \pm 0.4)\ \text{kV cm}^{-1}$. This peak is narrower and smoother than its predecessor but similarly offset from the expected value of $2\ \text{kV cm}^{-1}$, and this offset may be attributed to local electrostatic effects which alter the true field from the set value. Electrostatic effects will be exacerbated due to the reduced separation between sweep sites, meaning that any residual charges will have an increased effect on the following site. The smoother peak is likely to be a consequence of the capacitive term providing a much more distinct feature to fit to, however this means the result is the averaged coercive field across the sample thickness rather than a local surface property; the difference between these values is insignificant at this precision though. The small peak at the high-field end is located at $(3.862 \pm 0.019)\ \text{kV cm}^{-1}$

with a HWHM of $(0.32 \pm 0.03) \text{ kV cm}^{-1}$, yielding a summary metric of $(3.9 \pm 0.3) \text{ kV cm}^{-1}$, and will be the consequence of any curves which did not display clear polarisation reversal effects because this once again lies slightly beyond the 3.52 kV cm^{-1} maximum field.

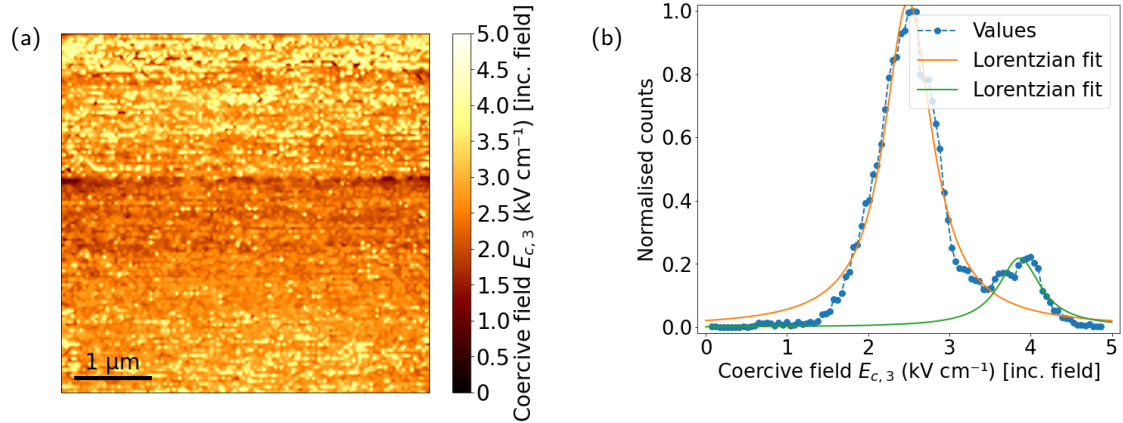


Figure 8.27: PSS characterisation of the coercive field over a $5 \mu\text{m}$ square of the PMN-PT sample at site B. (a) Contour map of the coercive field across the surface. (b) Histogram of the results with Lorentzian fits.

8.6.5 PSS conclusions

Frequency-spectroscopy has been achieved using the PSS methodology and the resonance frequency of the characterised area was found to have a summary metric of $(218.4 \pm 0.3) \text{ kHz}$. This small range of $\pm 0.14\%$ suggests that the resonance frequency remains constant across the sample surface, which is a very useful property for substrates used to manufacture composite multiferroics.

It has been shown that field-spectroscopy via PSS or DCUBE-PFM may be used to obtain the approximate coercive field of a $250 \mu\text{m}$ thick sample by characterising a $5 \mu\text{m}$ square of the surface. This is the first known demonstration of such a measurement.

The coercive field characterisation could not yield truly localised values nor show any contrast, however the measurement is localised to the $5 \mu\text{m}$ square which is a notable result. The presence of the single coercive peaks with summary metrics $(2.3 \pm 0.7) \text{ kV cm}^{-1}$ and $(2.5 \pm 0.4) \text{ kV cm}^{-1}$ is very promising for multiferroic applications of PMN-PT because it is consistent with the Gaussian distribution model developed at the start of this chapter in Section 8.2. The concern was that the two distinct crystal phases in Figure 8.1 and apparent distinct piezoelectric coefficients in Figure 8.2 would result in a second peak in the coercive field histogram, which would present difficulties when using PMN-PT substrates in composite multiferroics.

This measurement can not be optimised further, due to the surface degradation, significant electrostatics,

and probe 'chasing' effects, and thus sweep-based methodologies are not suitable for field-spectroscopy of thick samples due to the high potentials required. OFF-field measurements are required for further optimisation, and these may be performed on a standard AFM using the methodology developed in the following section.

8.7 MultiScan Spectroscopy (MSS)

Spectroscopy measurements may also be made by capturing scans at a series of set values and importing the results into Python, where they are combined to form a 3D array containing a spectral curve at each image pixel. This will be referred to as MultiScan Spectroscopy (MSS), and may be used for a variety of measurement parameters such as drive frequency and DC field. OFF-field field-spectroscopy may be achieved through the use of interleave, first introduced in Section 4.3, where the 'main' measurement is carried out with a field applied and the 'interleave' measurement is made with the field removed. This is similar to SS-PFM in that a poling field is temporarily applied and then removed prior to the measurement being made, the difference being that instead of doing a single point at a time this method involves scanning a row. One scan must be made at each field value and this means the process is very time consuming and the spectral point density is low, however the use of scans rather than sweeps does allow for higher spatial point densities to be used than in PSS. Additionally, the surface topography is recorded during every scan so any surface disruption such as the kind seen following PSS may be tracked as it occurs.

8.7.1 Resonance characterisation

The first characterisation that will be performed with this methodology is the resonance frequency. PSS has already shown that this is approximately constant across the PMN-PT surface, however resonance curves provide a simple known curve with which to validate the MSS methodology. A frequency sweep was performed at a single point to identify the approximate resonance frequency for this probe-sample system, and the result was used to determine the drive frequency values for the MSS characterisation. These ranged from 316 to 330 kHz, with increments of 0.5 kHz to be used close to the expected resonance and 1.0 kHz further away. This varying increment is used to optimise the resolution in the pertinent region whilst also exploring the wider behaviour to aid when fitting the Lorentzian curve.

The PFM measurements were performed over a square with side length $5.0\text{ }\mu\text{m}$, at a resolution of 128 pixels per side giving a pixel size of 39 nm. The scan rate was 1.0 Hz and the rounding value was 0.0 giving a scan speed of $10\text{ }\mu\text{m s}^{-1}$. The piezoelectric drive amplitude was 1.0 V. The sample was imaged using a Bruker MESP-V2 probe at a setpoint of $0.09\text{ V} \sim 28\text{ nN}$ yielding a Hertzian contact radius of 1.8 nm. The AC potential therefore completes over 60 cycles before the probe travels a distance equal to

the the contact diameter and thus clears a particular site, meaning that it is scanning sufficiently slowly to accurately measure amplitude and phase. An example curve is provided in Figure 8.28, demonstrating the success of the MSS methodology. The expected Lorentzian resonance peak is seen and the fit provides a resonance frequency of (322.91 ± 0.06) kHz, however the point spacing of 0.5 kHz suggests that a more realistic summary is (322.9 ± 0.3) kHz.

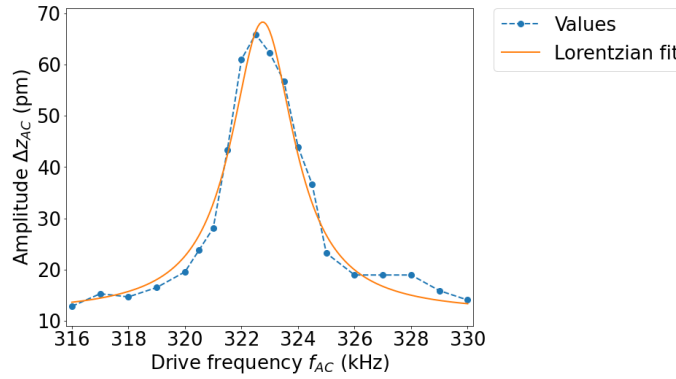


Figure 8.28: Example amplitude curve from MSS frequency-spectroscopy which shows the expected Lorentzian peak.

The contour plot of the resonance frequency across the measured area is provided in Figure 8.29 along with the topography for reference. The resonance values are consistent and show no intrinsic contrast, however there is some correlation with the terrace edges visible. This is likely a measurement artefact owing to the scan being performed in contact mode and cannot be avoided. The alternative would be to use PSS or DCUBE-PFM with short hold periods and constant parameters rather than sweeps, however the resulting duration of the measurement would be prohibitive unless it could be wholly automated through some kind of scripting.

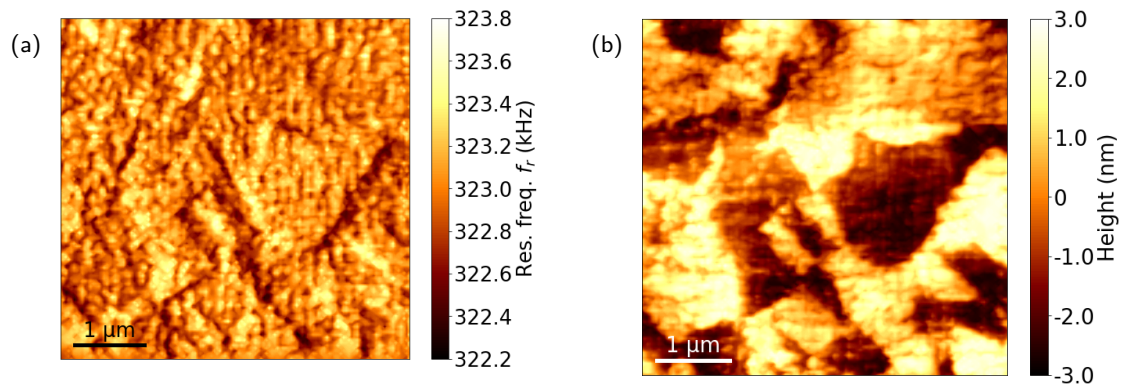


Figure 8.29: MSS characterisation of resonance frequency over a $5 \mu\text{m}$ square of the PMN-PT sample with topography for reference. (a) Contour map of the resonance frequency across the surface. (b) Surface topography featuring characteristic terraces.

The resonance frequency histogram is shown in Figure 8.30, and a Lorentzian fit determined the peak to be located at (322.960 ± 0.004) kHz with a HWHM of (0.281 ± 0.006) kHz, yielding a summary metric of (323.0 ± 0.3) kHz. This is the same width distribution as demonstrated by PSS in Figure 8.21b so the PMN-PT surface continues to exhibit a constant resonance frequency. This enables MSS field-spectroscopy to be performed and suggests that variation in resonance frequency is not a concern when using PMN-PT substrates in composite multiferroics. The tail to the right of the peak implies that a skewed distribution may be present, however the resolution of the data is too poor to conclude anything regarding this.

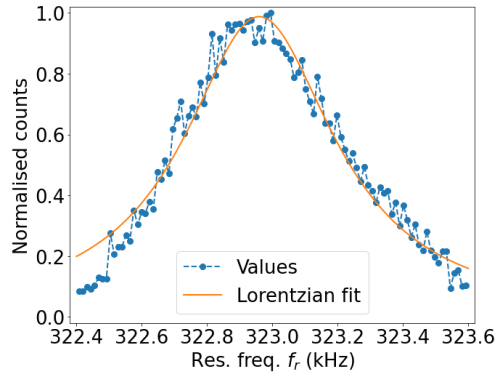


Figure 8.30: Histogram of the MSS characterisation of resonance frequency over a $5 \mu\text{m}$ square of the PMN-PT sample.

A consequence of the repeated scans comprising MSS is that drift may occur between captured images and especially over the course of the full MSS measurement cycle. This means that spectral characterisation of a precise single site is not possible. However, it does not prohibit accurate sample characterisation from being performed. The determined resonance frequency and coercive field variation over the surface should not be unduly affected by drift because they are expected to be sufficiently consistent properties that the effects from the change in the swept parameter dominate the effects of drifting to a neighbouring measurement location. Additionally, when performing field-spectroscopy the change in the phase curve is expected to be sharp and thus span very few scans. This means the effect of drift on the accuracy of the coercive field measurement is minimal.

The drift over the resonance frequency characterisation was quantified manually by tracking a topographic feature between scans, and the result is shown in Figure 8.31. The drift in the x -direction, y -direction, and the total drift each increase steadily during the scans which were captured in approximately 2.5 minute intervals, and linear fits were applied to each set of data. These yielded gradients of $(8.0 \pm 0.3) \text{ nm scan}^{-1} = (3.21 \pm 0.11) \text{ nm min}^{-1}$ in the x -direction, $(6.0 \pm 0.2) \text{ nm scan}^{-1} = (2.40 \pm 0.09) \text{ nm min}^{-1}$ in the y -direction, and $(10.0 \pm 0.2) \text{ nm scan}^{-1} = (3.99 \pm 0.11) \text{ nm min}^{-1}$ for total drift. These are significant values given that the contact radius during PFM measurements is of

the order of nanometres, which means that the probe will be in contact with different points of the surface during each scan. This appears to be a concern for field-spectroscopy because the initial poling of the sample is achieved by the first scans of the MSS cycle, however the field is applied over a wider region of the sample than just the contact area so spans a sufficiently large area that the entire scan area may be assumed to be poled.

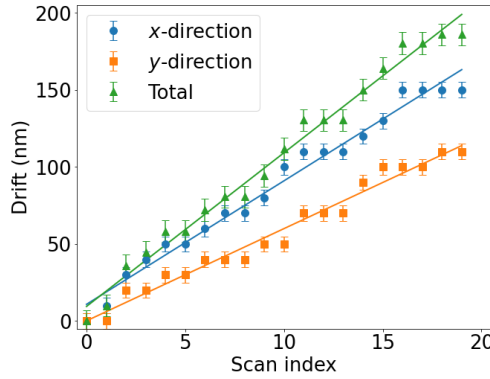


Figure 8.31: The drift of the PMN-PT sample during the resonance frequency characterisation over a 45 minute period. The scan region was a $5\ \mu\text{m}$ square so even a total drift of 200 nm is just 4% of the scan size. The drift over time is much larger than is typical for an AFM to exhibit, however this is attributed to each scan being recorded with the tip in constant contact with the sample, thus the lateral forces from the scanning are likely to be exacerbating any drift.

8.7.2 In situ sample polarisation

The previous section states that the sample poling is applied using the field between the tip and stage, but it is worth considering the possibility of poling the sample as a whole by charging the plate below the sample with no probe present. The upper bound for the field from a uniform plate with charge density σ is^[58]

$$E_3 = \frac{\sigma}{2\varepsilon}, \quad (8.27)$$

which is valid when close to a plane with radius much larger than the height above the plane surface. The self-capacitance of a rectangular plate is not analytical but for a circular plate with radius r the self-capacitance is well-known to be

$$C = 8r\varepsilon \quad (8.28)$$

thus

$$\sigma = \frac{CV}{\pi r^2} = \frac{8\varepsilon V}{\pi r} \quad (8.29)$$

and

$$E_3 = \frac{4V}{\pi r}. \quad (8.30)$$

The coercive field of PMN-PT is 2 kV cm^{-1} and the limit of the high-voltage line is 220 V, thus the maximum possible radius of this circular plate would be 1.4 mm. This value is not only impractical to implement but also violates the requirement for $r \gg z_0$, thus the field will be reduced below $E_{c,3}$ due to the infinite plane approximation being invalidated. Consequently, the in situ polarisation of the sample must be performed by the field between tip and sample stage.

8.7.3 Phase characterisation

The phase of the piezoelectric oscillation may be characterised by performing MSS with interleave and incrementing the applied potential used for each poling field. The amplitude of the response is not a suitable metric because it depends on multiple parameters including measurement settings, as well as the curve forming a dip which is more difficult to locate and accurately fit to than the sigmoid of a phase curve. The range of applied field values was chosen such that they start and end beyond the coercive field, but the limits are closer to the coercive field than for PSS because the MSS process is manual and time consuming thus it is important to minimise the number of scans. The applied field was cycled from -2.57 kV cm^{-1} to 2.57 kV cm^{-1} and back and was incremented in steps of 0.18 kV cm^{-1} , which are larger than the 0.03 kV cm^{-1} half-width at half maximum of the coercive field model in Figure 8.4 but could not be smaller due to available time. This does mean that fine precision may be lost if the phase reversal occurs wholly between two applied field values, but this is still theoretically more precise than the PSS results were able to show and thus should provide an improvement.

The PFM measurements used for the coercive field characterisation were performed over a square with side length $5.0 \text{ }\mu\text{m}$, at a resolution of 128 pixels per side giving a pixel size of 39 nm. The scan rate was 1.0 Hz and the rounding value was 0.1 giving a scan speed of $11 \text{ }\mu\text{m s}^{-1}$ and 25 ms of charging time. The piezoelectric drive amplitude was 0.5 V at a calibrated drive frequency of 224 kHz. The sample was imaged using a Bruker PFTUNA probe at a setpoint of $0.5 \text{ V} \sim 20 \text{ nN}$ yielding a Hertzian contact radius of 1.6 nm. The AC potential therefore completes over 60 cycles before the probe travels a distance equal to the the contact diameter and thus clears a particular site, meaning that it is scanning sufficiently slowly to accurately measure amplitude and phase. The ferroelectric switching time is expected to be the same order of magnitude as the period of the AC drive, thus the switching should readily occur below the probe and ferroelectric reversal should be observed at this scan speed.

The MSS phase measurements were carried out using the 'rounding' setting on the AFM which instructs the raster to overscan the region being captured. This allows the system to charge the tip-stage capacitor to the set field value outside the capture area because this charging was shown in trial PSS field sweeps to take up to $\sim 10 \text{ ms}$. Additionally, the rapid charging is responsible for the surface degradation observed following the PSS measurements, which is evidenced in Figure 8.32. This figure shows a $7 \text{ }\mu\text{m}$ topography scan and its cross-section following a trial run of an MSS field-spectroscopy characterisation

over a square of side length $5\text{ }\mu\text{m}$ with the rounding value set to 0.1. The ridges at each side are up to 80 nm in height, which completely obscures any piezoelectric surface properties and hence demonstrates the difficulties encountered during PSS. The overscan allows these ridges to be placed outside the characterisation region. The origin of these ridges is believed to be the rapid charging and discharging of the tip of the AFM probe at the end of each row, causing intense Joule heating in the insulating surface of the PMN-PT and thus localised melting. This mechanism is discussed in Section 4.8.4.

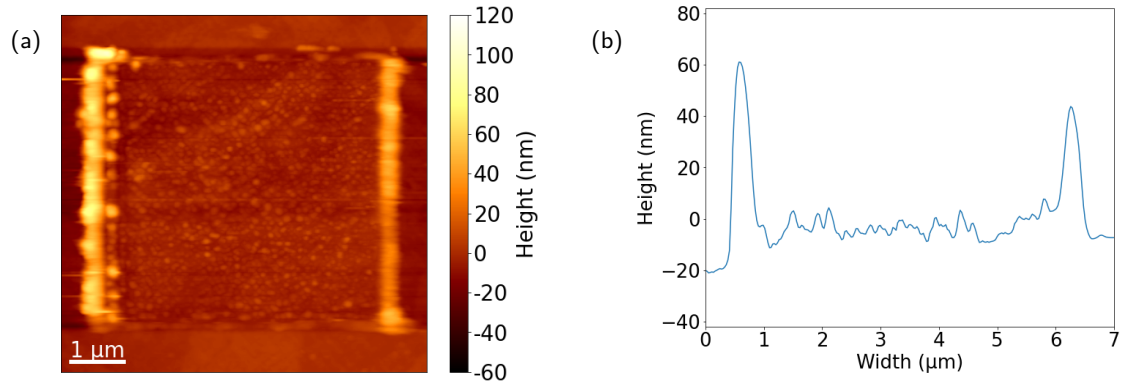


Figure 8.32: Topography of a $7\text{ }\mu\text{m}$ square of the PMN-PT sample following a trial of MSS field-spectroscopy over a square of side length $5\text{ }\mu\text{m}$. (a) Contour map of the topography. (b) Horizontal cross-section through the centre of the contour.

The surface topography of the PMN-PT sample at two significant instances of the MSS cycle is provided in Figure 8.33. Figure 8.33a shows the topography at the maximum field of $E_3 = 2.57\text{ kV cm}^{-1}$, after the increasing-field part of the cycle, and Figure 8.33b shows the end of the MSS measurement after the final -2.57 kV cm^{-1} scan. The first contour clearly exhibits the characteristic terraces of PMN-PT, demonstrating how the MSS methodology does not immediately result in the surface disruption observed following PSS. However, the second contour does show the beginnings of surface disruption and the decreasing-field values did not exhibit a phase transition, which means that the surface is still disrupted but not to the same extent as by PSS. This suggests that the high potential of the AFM tip is still able to induce nanodots of surface disruption and thus there is an upper bound on the possible spectral point density of the field-spectroscopy. Increasing the scan speed would decrease the exposure time, which is correlated to the size of the nanodots^[148], but would result in poorer surface characterisation, especially because slower speeds are preferred to improve surface contact and minimise topographic artefacts in the coercive field data.

Section 4.8.1 explained the concept of phase-wrapping, and this needs to be accounted for automatically during the data analysis process. This is achieved through a two-step process, shown for two exemplar increasing-field curves in Figure 8.34. The first step is explained in Section 4.8.1 and involves moving the phase limits from the range $-\pi < \phi_s \leq +\pi$, as used by the AFM, to the alternative limits of

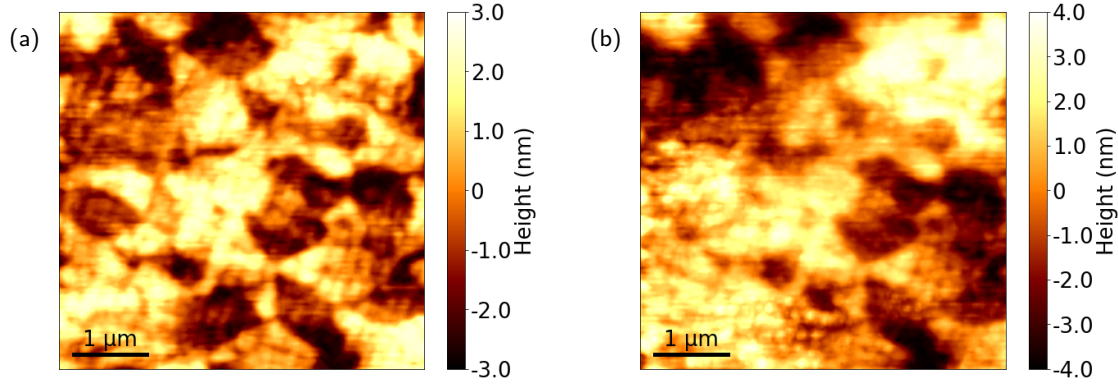


Figure 8.33: Topography of a $5\mu\text{m}$ square of the PMN-PT sample during and after the MSS field-spectroscopy measurement. (a) Topography after the increasing-field sweep. (b) Topography after the decreasing-field sweep, showing the formation of surface disruption.

$0 < \phi_s \leq 2\pi$, which results in the yellow ‘Alt. limits’ curves in Figure 8.34. The second step is to iterate over the values of each curve in turn and check for any consecutive data points separated by more than π , because this is highly unlikely to be caused by anything other than phase-wrapping, and adjust the value of one of the points by 2π to reduce the difference below π . The resulting curves are then translated to each be centred on $\phi_s = \pi/2$, and this results in the green ‘Corrected’ curves in Figure 8.34.

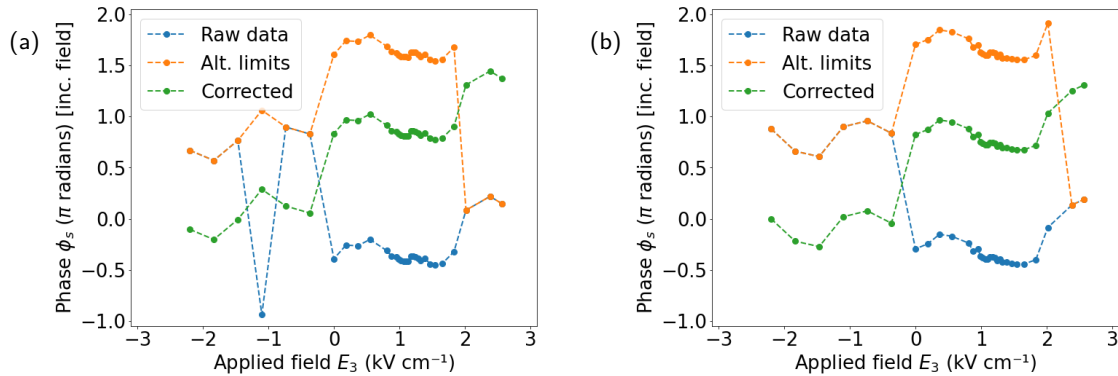


Figure 8.34: Two exemplar phase curves from MSS field-spectroscopy data demonstrating the phase correction algorithm. The sigmoid at $\sim 2\text{ kV cm}^{-1}$ is caused by the polarisation reversal of the sample.

Unusually, the phase curves contain two transitions, one at 0 kV cm^{-1} and the other at $\sim 2\text{ kV cm}^{-1}$. The first of these is likely to be the consequence of residual charges from the poling pass prior to the OFF-field interleave measurement pass. This would result in a non-zero contribution of electrostatic amplitude A_ω , which is described in equations (4.55) and (4.57) and exhibits a phase reversal between positive and negative applied fields. The coercive field was determined from the corrected phase curves by fitting a sigmoid to just the positive field values and the result is shown in Figure 8.35. The contour plot

shows constant coercive field values with the only contrast being the topographic shadow. This shadow demonstrates that the coercive field data is the result of a real signal and varies with location, which means that, as hypothesised, the transition is sharp enough that drift did not hinder the localisation of the characterisation. The lower portion of the contour shows reduced variation relative to the upper portion, but this boundary appears as an artefact in all piezoelectric channels of the nearest captured scan, meaning that this difference is an AFM artefact and not a feature of the PMN-PT sample.

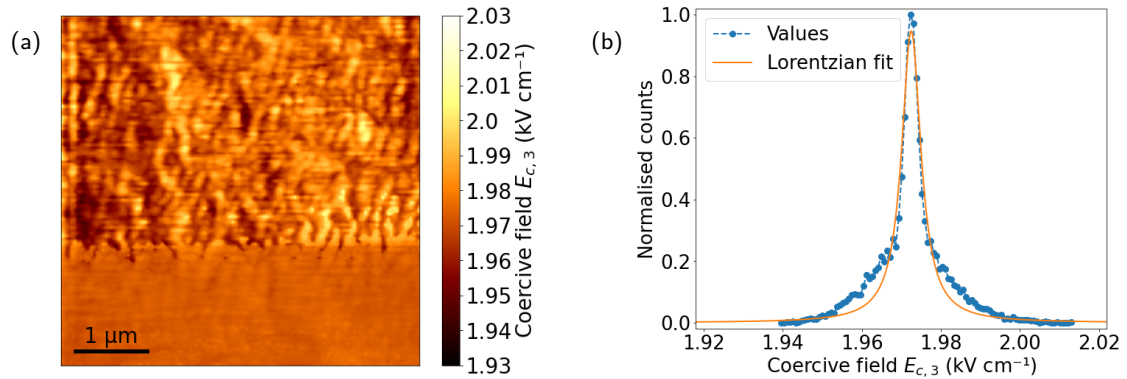


Figure 8.35: MSS characterisation of the coercive field over a $5 \mu\text{m}$ square of the PMN-PT sample. (a) Contour map of the coercive field across the surface. (b) Histogram of the results with Lorentzian fit.

The histogram in Figure 8.35b is located at the expected coercive field for the sample but is narrower than predicted, with a peak position of $(1.973 \pm 0.005) \text{ kV cm}^{-1}$ and HWHM of $(0.003 \pm 0.006) \text{ kV cm}^{-1}$. In this case the HWHM is so low that the summary metric used for the previous histograms in this chapter is not useful for this data. The spectral point density is also very low and thus the jump occurs almost entirely between consecutive scans, which means the exact value of the coercive field is unable to be precisely located and the narrow spread is a consequence of the fitting algorithm terminating at one of the first values it trials between the scan values. Inspection of the captured field values provides that the transition occurs between 1.8 kV cm^{-1} and 2.2 kV cm^{-1} , thus a more accurate interpretation of the results is a transition with summary metric $(2.0 \pm 0.2) \text{ kV cm}^{-1}$. However, assuming a lower gradient for the transition sigmoid than vertical reduces this possible range, so the upper bound for the coercive field range is $(2.0 \pm 0.2) \text{ kV cm}^{-1}$ but a more realistic range would be $\pm 0.1 \text{ kV cm}^{-1}$.

This data therefore suggests that the coercive field and thus the piezoelectric properties are expected to be constant on the nanoscale. This is especially true over short distances due to the predicted smooth variation in PT concentration x , and the strain dissipation resulting from low d_{33} regions constraining the motion of neighbouring high d_{33} regions and vice versa.

8.7.4 MSS conclusions

Frequency-spectroscopy has been achieved using the MSS methodology and the resonance frequency of the measured area was found to be (323.0 ± 0.3) kHz. This small range of $\pm 0.09\%$ suggests that the resonance frequency remains constant across the sample surface, which aids when performing field-spectroscopy MSS and is a very useful property for substrates used to manufacture composite multiferroics.

It has been shown that the MSS methodology is able to perform OFF-field field-spectroscopy to characterise a $5\text{ }\mu\text{m}$ square of a $250\text{ }\mu\text{m}$ thick sample, and does so much more successfully than the PSS methodology and thus other more sophisticated site-by-site modes such as DCUBE-PFM and SS-PFM.

The coercive field summary metric of $(2.0 \pm 0.1)\text{ kV cm}^{-1}$ matches the expected value of $\sim 2\text{ kV cm}^{-1}$ obtained from the XRD characterisation of these samples by Griggs and Thomson^[7]. This characterisation involved measuring the rhombohedral lattice spacing at a series of applied fields, and plotting the resulting strain against the applied field to obtain a butterfly curve^[7]. Topographic shadow is clearly visible in the results in Figure 8.35a which is an artefact of the contact-mode basis of the PFM measurement used to perform this MSS characterisation, just as was observed for the resonance frequency contour in Figure 8.29a. This may be reduced through decreased scan speeds and increased gain, but its presence demonstrates that the coercive field data is indeed the result of a physical localised phenomenon.

The variation of the data in Figure 8.35 is very low and no anomalous fits occurred, meaning that every single pixel demonstrated a phase shift at the expected coercive field, and demonstrating MSS to be a reliable technique that consistently observes the ferroelectric reversal of the top $1.7\text{ }\mu\text{m}$ of a sample. The lack of observed contrast suggests that a PMN-PT ferroelectric substrate may be considered to be homogeneous, in agreement with the models at the start of this chapter, which makes them ideal for use as substrates for composite multiferroics.

8.8 Summary

This chapter presents the first known demonstration of characterising the coercive field and thus the local stoichiometry of a thick ferroelectric sample using AFM, via two methodologies which were developed and evaluated in this work. A model was developed for the distribution of $E_{c,3}$ and d_{33} for the sample under investigation and used to reconcile the disagreement between the d_{33} values measured by Li et al.^[8] in Figure 3.13 and the apparent d_{33} values observed by Griggs and Thomson^[7] in Figure 8.2. Further models were developed considering the effects of applied field and polarisation reversal on piezoelectric properties, including typically constant parameters such as relative electrical permittivity, and using these the piezoelectric coefficient d_{33} was modelled considering the contributions from electrostrictive

and shear piezoelectric mechanisms. ON-field field-spectroscopy using PSS caused significant surface disruption due to the rapidly charging AFM tip and so high-voltage spectroscopic modes such as this, including DCUBE-PFM and SS-PFM, are not suitable for characterising the ferroelectric properties of a thick sample. OFF-field field-spectroscopy using MSS was developed to resolve the difficulties associated with high-voltage measurements of thick samples, and demonstrated much reduced surface disruption with the majority confined to the overscan regions.

Chapter 9

Conclusions and future work

This final chapter will present detailed summaries and conclusions from the three advanced AFM characterisation investigations in this work. The metrological methodologies are the principle focus of this thesis, and the novel techniques developed to perform new types of measurements are evaluated in particular detail. These developed methodologies include the ability to characterise the local electrical resistivity of metallic thin films and the ability to perform field-spectroscopy across thick ferroelectric samples such as substrates. Propositions are also made regarding future work which may be done to further develop these developed AFM techniques, and to continue the investigation of magnetically patterned FeRh and of composite multiferroics using PMN-PT substrates.

9.1 Metallic resistivity characterisation on the AFM

In Chapter 5 the different sources of resistance were outlined and the spreading resistance was identified as the localisation mechanism for nanoscale resistivity measurements. The resistance change in FeRh from magnetoresistance results in a decrease of $25\ \Omega$ which is theoretically observable with idealised solid platinum or PtIr coated silicon probes. The resistance of the platinum probe was shown to be much less dependent on temperature with a theoretical temperature change of 43 K required to increase the measured resistance by $1\ \Omega$ while the coated probe required just 8.7 K.

The limitations of the existing hardware were explained, with the low resistance and discretised bias requiring currents beyond the abilities of coated probes or existing Bruker application modules. Resistive heating was acknowledged through power considerations and the Preece equation. The probe is expected to heat up but the cantilever is not expected to fail as a consequence, although the tip-apex is likely to be weakened. The resulting limit on parameters such as scan duration was stated.

The choice of probe was discussed with the RMN-25PT300B probe selected due to resistivity, spring constant, and length. The setpoint compromise was considered and a setpoint of 3 to $4\ \mu\text{N}$ determined to be optimal. The contact and spreading radius was considered and it was confirmed that resolving electrical patterns of size less than 100 nm should be possible. The motivation and process for surface

cleaning and oxide removal were also explained. The development process for the voltage divider measurement system was presented and the final design explained. An alternative approach to enable existing hardware to be used on specially designed samples was considered but rejected.

Chapter 6 introduced the experimental procedure for putting the system developed in Chapter 5 into practice and evaluated the success of the methodology. The results from the electrical measurement trials have shown that the underlying electrical resistivity pattern may be determined for two resistivities with the same order of magnitude. Additionally, the local resistivity of FeRh thin films has been empirically confirmed to change as a result of the magnetic patterning process.

The measurement methodology has been proven to be functional and robust and Joule heating did not seem to manifest. Unfortunately, only one contrasting map was produced, with the other measurements exhibiting severe noise that could only be compensated for through the use of mean cross-sections perpendicular to the stripes. The prototype used here serves as an excellent proof-of-concept which was the primary aim of this work. In future developments the system could be refined into a dedicated bespoke device rather than the prototype constructed here.

Lower contact resistances were observed than anticipated and this enhanced the relative change in resistance between magnetically ordered sites. However, the percentage changes were still an order of magnitude smaller than expected due to a myriad of effects, discussed in each case individually. A large area, high-resolution scan was attempted but the conduction signal was lost early on, likely due to debris becoming attached to the tip.

It was shown that preliminary scans using the silicon RTESPA-300 probe are able to remove the oxide layer and allow electrical conduction, suggesting the stoichiometry to be Fe_3O_4 . The recommended settings for these scans were also stated. It was concluded that this mode is especially suited to non-oxidising structures with order of magnitude resistance differences because mechanical oxide erosion is a destructive technique that cannot be used reliably across metal boundaries or over structures. This suggests that a chemical oxide-removal technique would be more suitable where possible.

Nanomechanical characterisation of FeRh was attempted but no contrast was observed. This was a likely outcome due to the magnetoelastic effect being known to be very low in force curve measurements and also to be very low during hard-axis stressing; both of which are true for QNM measurements of FeRh films. The DCUBE-MFM-TUNA mode to unify two or three measurement techniques into one was introduced, but the inability of existing magnetic probes to carry high currents was acknowledged and the need for a solid metal ferromagnetic probe to resolve this was outlined.

9.1.1 Future work

The characterisation procedure has been demonstrated to be viable using the prototype, and so the methodology can now be developed further. The voltage divider may be refined and simplified by integrating the components into the dummy application module to form a custom application module for this methodology, just requiring a single BNC cable to link to the Input1 connector on the NanoScope Controller. However, a configurable dividing resistor would be required in order to characterise a wider range of metals, and this would require further considerations to be implemented; it was demonstrated in equation (5.20) that the voltage divider sensitivity to sample resistance is optimal when the divider resistance is approximately equal to the probe and sample resistance. This would also permit larger applied potentials to be used for the same current, which would in turn further increase the relative precision of the voltage divider measurement. Ultimately, this could be implemented as a true AFM mode which calculates resistance in real time featuring a dedicated application module with dynamic variable resistor and built-in voltage measurement circuitry.

It was concluded that this methodology was only suitable for structures comprised from non-oxidising metals with resistivities differing by at least an order of magnitude. Consequently, further work on optimising this methodology should be performed on samples satisfying these criteria. These samples would produce higher contrast images and thus aid with refining the methodology itself.

The final avenue of future work stemming from this metrological development is to combine the metallic resistivity measurements with magnetic measurements using DCUBE-MFM-TUNA. This should be possible through the development of a new electrically conductive uncoated probe with ferromagnetic properties, which would allow the tip to be magnetised for the MFM measurements whilst being able to support the high currents of the methodology developed in this work. Nickel was stated to potentially be a very good candidate but a full investigation of the ideal probe is beyond the scope of this thesis.

9.2 Magnetic characterisation of noble ion irradiated FeRh

Chapter 7 discussed MFM characterisation of ion irradiated FeRh and compared the results with those from XMCD-PEEM. The deposition and patterning process for the ion irradiated FeRh films has been described, and the expected domain structure present in the film was explained along with how it was expected to manifest in MFM scans. The ambient MFM characterisation was presented and the intended magnetic patterning was observed for 1 μm and 10 μm images and the data was contrasted with the XMCD-PEEM results. A wider scan of 25 μm was compared between the two modes and it was shown how MFM provides superior resolution at such large scan sizes.

The strip widths were considered, commencing with a simulation which predicted the stripes would

bulge outwards due to ion scattering to a width of up to ~ 135 nm, or ~ 115 nm if the threshold is considered to be 90% of maximum stripe magnetisation. However, the simulation did show the stripe to be the expected width for the first few nanometres which is also the depth probed by each of the measurement techniques. The apparent imbalance between AF and FM regions was addressed and it was shown that this is an artefact of both measurement techniques, but MFM shows evidence of this whilst XMCD-PEEM does not, making MFM the more comprehensive technique. In a similar vein it was shown that while the MFM scans may appear to show oscillating AF lines rather than straight stripes, this is another measurement artefact with the same cause.

The stripe periodicity was investigated and was confirmed via Fourier transform to have the expected pitch of $5 \mu\text{m}^{-1}$, although this was measured as $(4.95 \pm 0.02) \mu\text{m}^{-1}$ due to an approximately 8° tilt of the stripes from the vertical. A second FFT peak was observed at $10 \mu\text{m}^{-1}$ and this was explained to be the result of multiple magnetic features observed in the FM stripes. The Height Sensor data from higher scan speeds also showed a small FFT peak at $5 \mu\text{m}^{-1}$, and this was attributed to the cantilever oscillations being modified by magnetic forces faster than the feedback control could rectify. The topography is not actually affected by the patterning process.

The observed magnetic structure was observed to be stable over a period exceeding 5 hours and also when moved between the heater stage and the main sample stage. The heater stage was shown to result in less noise and higher contrast so is the favoured stage even for ambient measurements where possible. The effect of strong external fields $|\vec{B}| \approx 2$ T applied parallel and perpendicular to the stripes was shown, and it was observed that the parallel field slightly reoriented domains whilst the perpendicular field significantly disrupted the neat ordering. It was then demonstrated how AC demagnetisation decaying from 0.1 T was able to recover MFM contrast which was lost when the domains began to align. The corner of the patterned region was located and it was discovered that the patterning formed a neat edge parallel to the stripes with no rogue domains. However, it was also observed that the patterning continued inconsistently beyond the intended end of the stripes.

The patterned FeRh film was heated to 160°C and then cooled back down to room temperature with scans taken at each intermediary temperature. The stripes disappeared into FM domains then reappeared with cooling, showing the patterned regions to be robust to both the applied temperature and the field from neighbouring domains, even so far as to exhibit an FFT peak in the fully magnetised state. The domain structure of the irradiated stripes appears to remain consistent throughout the thermal cycle, and not change as a result of heating or due to magnetically coupling to the transitioning stripes. The transition temperatures were qualitatively found to be approximately 100°C and 110°C with a hysteresis width of approximately 10°C , in accordance with the expected values, showing the unirradiated regions to be mostly unaffected by the patterning process.

9.2.1 Future work

The response of the ferromagnetic domain structure during heating and cooling may be investigated further by capturing a series of scans with higher spatial and spectral resolution than presented here. Additionally, the characterisation should be repeated at multiple sites across the sample to verify whether the persistence is a feature of the whole sample or a specific region.

The metamagnetic phase transition may also be driven by an external magnetic field, and characterisation of this for the sample as a whole will be performed on the vibrating sample magnetometer (VSM) by Dr William Griggs in due course. It is expected that if the stripes feature exchange coupling then the centre of the hysteresis loop will be shifted away from zero field. Additionally, Bruker announced the development of an External Magnetic Field Module for the Dimension AFM platform at their *European AFM User Meeting* on 23rd March 2022. Once this device is available then additional MFM measurements can be performed to locally characterise the metamagnetic transition as a function of external magnetic field.

The MFM and XMCD-PEEM measurements presented in this thesis successfully demonstrate the ability to magnetically pattern an FeRh thin film with stripes of width 100 nm. This may be further investigated by patterning a variety of widths and more complex designs with an ultimate aim of using this technique in the manufacture of a spintronic device.

9.3 Ferroelectric characterisation of thick samples of PMN-PT

Chapter 8 presents the first known demonstration of characterising the coercive field and thus the local stoichiometry of a thick ferroelectric sample using AFM, via two methodologies which were developed and evaluated in this work.

The chapter commenced by developing a model for the distribution of $E_{c,3}$ and d_{33} for the sample under investigation, and using it to reconcile the disagreement between the d_{33} values measured by Li et al.^[8] and the apparent d_{33} values observed by Griggs and Thomson^[7]. The histograms generated by this model suggest that the surface distribution of ferroelectric properties is very minor to the point of being negligible. This means that while resolving any contrast will be difficult, it may not be essential to precisely characterise PMN-PT substrates for use in composite multiferroics.

Further models were developed considering the effects of applied field and polarisation reversal on piezoelectric properties, including typically constant parameters such as relative electrical permittivity. The piezoelectric coefficient d_{33} was modelled considering the contributions from electrostrictive and shear piezoelectric mechanisms. These models were used to develop an expression for the capacitance

of a tip-stage system over thick ferroelectrics, which was used to determine the constant and oscillating deflections of the AFM cantilever due to electrostatics arising from the applied field.

Histograms of ON-field field-spectroscopy using PSS yielded coercive fields with summary metrics of $(2.3 \pm 0.7) \text{ kV cm}^{-1}$ from one measurement and $(2.5 \pm 0.4) \text{ kV cm}^{-1}$ from a second, which are wider than expected but are close to the expected value of $\sim 2 \text{ kV cm}^{-1}$. The wide peak and multiple failed fits are attributed to the surface disruption from the rapidly charging AFM tip and to the complexity of the model, which means that the existing sophisticated modes such as DCUBE-PFM and SS-PFM would not be suitable either.

OFF-field field-spectroscopy using MSS is a new methodology which was developed to resolve the difficulties associated with high-voltage measurements of thick samples. This technique yielded a coercive field with summary metric $(2.0 \pm 0.1) \text{ kV cm}^{-1}$. This is a narrow histogram peak but matches the expected value and features no failed fits or unobserved transitions. The contrast is strongly affected by topography but slower scan speeds with higher gain would reduce this effect, and higher spectral point density would improve the measurement precision. MSS demonstrated much reduced surface disruption with the majority confined to the overscan regions. It is a very time-consuming process involving constant manual interaction, however this may be automated using scripting tools such as the 'recipe' functionality of the NanoScope software.

The two methodologies successfully reported resonance frequencies with metrics of $(218.4 \pm 0.3) \text{ kHz}$ using PSS and $(323.0 \pm 0.3) \text{ kHz}$ using MSS, which are constant across the PMN-PT sample surface with narrow distributions. These differ significantly, however the value is dependent on the exact properties of the AFM probe used as well as the sample itself, so this is not an unexpected result. This is the reason the resonance frequency should always be determined using a frequency sweep after first engaging on the sample surface.

The resonance frequency and coercive field measurements exhibited no significant contrast in the contour plots, and also did not produce any unexpected features in the histograms such as a second peak. This does not mean that PT concentration does not vary over short length scales compared with the characterisation depth, however the lattice strain on such length scales is likely to be sufficient that any variation in local piezoelectric response would be significantly suppressed. This means that if no contrast is observed via PFM then variation in local PT concentration is not likely to be a concern for composite multiferroics grown upon PMN-PT substrates, provided that the surface distribution is the same as the depth distribution. It is therefore reasonable to conclude from the results in Chapter 8 that the resonance frequency and coercive field, and thus PT concentration x and piezoelectric response, are very smoothly and negligibly varying across the surface. This suggests that the proposed models at the start of Chapter 8 are accurate, and that the two crystal geometries and two apparent d_{33} values are not

the concern that one would assume upon first inspection. Hence, it has been shown both theoretically and experimentally that PMN-PT with $x = (0.29 \pm 0.01)$ is an ideal candidate for use as a substrate in composite multiferroics, without requiring comprehensive nanoscale characterisation prior to deposition.

9.3.1 Future work

The MSS methodology has been demonstrated to be successful at characterising the ferroelectric properties of the top $\sim 1.7 \mu\text{m}$ of a thick sample without severely disrupting the surface. This should now be refined further and automation should be pursued to enable this measurement technique to be performed without a user being required to remain at the AFM throughout. This automation would also enable higher spectral densities to be used due to the resulting ability to run the AFM for an extended period of time including overnight. Carrying out these high spectral density MSS measurements at a series of sites across a sample with high spatial resolution will allow a thorough characterisation of the surface of thick samples to be obtained, which has hitherto remained unachievable.

The data shown in this work suggests that the piezoelectric response of the surface of the PMN-PT sample is effectively homogeneous, and this is significant for future work on composite multiferroic devices. The consequence is that the strain may be accurately and precisely used to couple the ferromagnetic and ferroelectric properties of the device, without the requirement to characterise and account for variation in the piezoelectric coefficient across the surface of the ferroelectric substrate. This opens the door to the many potential applications of a composite magnetoelectric multiferroic, which may now be investigated in future work.

References

- [1] G. Binnig, C. F. Quate, and C. Gerber, "Atomic Force Microscope," *Physical Review Letters*, vol. 56, no. 9, pp. 930–934, 1986.
- [2] J. J. Sáenz, N. García, P. Grütter, E. Meyer, H. Heinzelmann, R. Wiesendanger, L. Rosenthaler, H. R. Hidber, and H. J. Güntherodt, "Observation of magnetic forces by the atomic force microscope," *Journal of Applied Physics*, vol. 62, no. 10, pp. 4293–4295, 1987.
- [3] P. De Wolf, J. Snauwaert, T. Clarysse, W. Vandervorst, and L. Hellemans, "Characterization of a point-contact on silicon using force microscopy-supported resistance measurements," *Applied Physics Letters*, p. 1530, 1995.
- [4] M. Fallot and R. Hocart, "Sur l'apparition du ferromagnétisme par élévation de température dans des alliages de fer et de rhodium," *La Revue Scientifique*, vol. 77, pp. 498–500, 1939.
- [5] J. S. Kouvel and C. C. Hartelius, "Anomalous magnetic moments and transformations in the ordered alloy FeRh," *Journal of Applied Physics*, vol. 33, no. 3, pp. 1343–1344, 1962.
- [6] B. Eggert, A. Schmeink, J. Lill, M. O. Liedke, U. Kentsch, M. Butterling, A. Wagner, S. Pascarelli, K. Potzger, J. Lindner, *et al.*, "Magnetic response of FeRh to static and dynamic disorder," *RSC Advances*, vol. 10, no. 24, pp. 14386–14395, 2020.
- [7] W. Griggs and T. Thomson, "Repeatable and deterministic all electrical switching in a mixed phase artificial multiferroic," *Scientific Reports*, vol. 12, no. 1, p. 5332, 2022.
- [8] F. Li, S. Zhang, Z. Xu, X. Wei, J. Luo, and T. R. Shrout, "Composition and phase dependence of the intrinsic and extrinsic piezoelectric activity of domain engineered $(1 - x)\text{Pb}(\text{Mg}_{1/3}\text{Nb}_{2/3})\text{O}_3$ - $x\text{PbTiO}_3$ crystals," *Journal of Applied Physics*, vol. 108, no. 3, 2010.
- [9] R. Skulski, P. Wawrzęta, K. Ćwikiel, and D. Bochenek, "Dielectric and electromechanical behaviors of PMN-PT ceramic samples," *Journal of Intelligent Material Systems and Structures*, vol. 18, no. 10, pp. 1049–1056, 2007.
- [10] G. Binnig, H. Rohrer, C. Gerber, and E. Weibel, "Surface studies by scanning tunneling microscopy," *Physical Review Letters*, vol. 49, no. 1, p. 57, 1982.

- [11] A. Robinson, “Electron Microscope Inventors Share Nobel Physics Prize,” *Science*, vol. 234, no. 4778, pp. 821–822, 1986.
- [12] N. A. Burnham and R. J. Colton, “Measuring the nanomechanical properties and surface forces of materials using an atomic force microscope,” *Journal of Vacuum Science and Technology A: Vacuum, Surfaces and Films*, vol. 7, no. 4, pp. 2906–2913, 1989.
- [13] I. Tanaka, I. Kamiya, H. Sakaki, N. Qureshi, S. Allen Jr, and P. Petroff, “Imaging and probing electronic properties of self-assembled InAs quantum dots by atomic force microscopy with conductive tip,” *Applied Physics Letters*, vol. 74, no. 6, pp. 844–846, 1999.
- [14] L. Muldower and F. de Bergevin, “Antiferromagnetic-ferromagnetic transformation in FeRh,” *The Journal of Chemical Physics*, vol. 35, no. 5, pp. 1904–1905, 1961.
- [15] S. B. Palmer, P. Dentschuk, and D. Melville, “Elastic properties of an iron-rhodium alloy,” *physica status solidi (a)*, vol. 32, no. 2, pp. 503–508, 1975.
- [16] X. Marti, I. Fina, C. Frontera, J. Liu, P. Wadley, Q. He, R. J. Paull, J. D. Clarkson, J. Kudrnovský, I. Turek, J. Kuneš, D. Yi, J. H. Chu, C. T. Nelson, L. You, E. Arenholz, S. Salahuddin, J. Fontcuberta, T. Jungwirth, and R. Ramesh, “Room-temperature antiferromagnetic memory resistor,” *Nature Materials*, vol. 13, no. 4, pp. 367–374, 2014.
- [17] I. Fina, N. Dix, E. Menéndez, A. Crespi, M. Foerster, L. Aballe, F. Sánchez, and J. Fontcuberta, “Flexible antiferromagnetic FeRh tapes as memory elements,” *ACS Applied Materials and Interfaces*, vol. 12, no. 13, pp. 15389–15395, 2020.
- [18] W. Griggs, B. Eggert, M. O. Liedke, M. Butterling, A. Wagner, U. Kentsch, E. Hirschmann, M. Grimes, A. Caruana, C. Kinane, *et al.*, “Depth selective magnetic phase coexistence in FeRh thin films,” *APL Materials*, vol. 8, no. 12, p. 121103, 2020.
- [19] N. A. Spaldin, *Magnetic Materials: Fundamentals and Applications*. Cambridge University Press, 2010.
- [20] N. A. Spaldin and R. Ramesh, “Advances in magnetoelectric multiferroics,” *Nature Materials*, vol. 18, no. 3, pp. 203–212, 2019.
- [21] N. Ortega, A. Kumar, J. Scott, and R. S. Katiyar, “Multifunctional magnetoelectric materials for device applications,” *Journal of Physics: Condensed Matter*, vol. 27, no. 50, p. 504002, 2015.
- [22] L. Bellaiche and D. Vanderbilt, “Intrinsic piezoelectric response in perovskite alloys: PMN-PT

- versus PZT," *Physical Review Letters*, vol. 83, no. 7, pp. 1347–1350, 1999.
- [23] M. Dresselhaus, G. Dresselhaus, S. B. Cronin, and A. G. S. Filho, *Solid State Properties*. Berlin: Springer, 1st ed., 2018.
- [24] M. J. Mehl, D. Hicks, C. Toher, O. Levy, R. M. Hanson, G. Hart, and S. Curtarolo, "The AFLOW library of crystallographic prototypes: part 1," *Computational Materials Science*, vol. 136, pp. S1–S828, 2017.
- [25] N. W. Ashcroft and N. D. Mermin, *Solid State Physics*. Saunders College Publishing, 1976.
- [26] M. I. Aroyo, ed., *International Tables For Crystallography*, vol. A. published for the International Union of Crystallography by Wiley, 6th ed., 2016.
- [27] Standards Committee of the IEEE Ultrasonics, Ferroelectrics, and Frequency Control Society, "Ieee standard on piezoelectricity," 1987.
- [28] D. Zekria, V. A. Shuvaeva, and A. M. Glazer, "Birefringence imaging measurements on the phase diagram of $\text{Pb}(\text{Mg}_{1/3}\text{Nb}_{2/3})\text{O}_3\text{--PbTiO}_3$," *Journal of Physics Condensed Matter*, vol. 17, no. 10, pp. 1593–1600, 2005.
- [29] S. O. Mariager, F. Pressacco, G. Ingold, A. Caviezel, E. Möhr-Vorobeva, P. Beaud, S. Johnson, C. Milne, E. Mancini, S. Moyerman, *et al.*, "Structural and magnetic dynamics of a laser induced phase transition in FeRh," *Physical Review Letters*, vol. 108, no. 8, p. 087201, 2012.
- [30] L. J. Swartzendruber, "The Fe-Rh (Iron-Rhodium) System," *Bulletin of Alloy Phase Diagrams*, vol. 5, no. 5, pp. 456–462, 1984.
- [31] M. De Graef and M. E. McHenry, *Structure of Materials: An Introduction to Crystallography, Diffraction and Symmetry*. Cambridge University Press, 2012.
- [32] R. Cowley, S. Gvasaliya, S. Lushnikov, B. Roessli, and G. Rotaru, "Relaxing with relaxors: a review of relaxor ferroelectrics," *Advances in Physics*, vol. 60, no. 2, pp. 229–327, 2011.
- [33] K. Doig, F. Aguesse, A. Axelsson, N. Alford, S. Nawaz, V. Palkar, S. Jones, R. Johnson, R. Synowicki, and J. Lloyd-Hughes, "Coherent magnon and acoustic phonon dynamics in tetragonal and rare-earth-doped BiFeO_3 multiferroic thin films," *Physical Review B*, vol. 88, no. 9, p. 094425, 2013.
- [34] F. Heusler, "Über magnetische manganlegierungen," *Verhandlungen der Deutschen Physikalischen*

Gesellschaft, vol. 5, p. 219, 1903.

- [35] T. Graf, C. Felser, and S. S. Parkin, "Simple rules for the understanding of Heusler compounds," *Progress in Solid State Chemistry*, vol. 39, no. 1, pp. 1–50, 2011.
- [36] E. Tiesinga, P. J. Mohr, D. B. Newell, and B. N. Taylor, "CODATA recommended values of the fundamental physical constants: 2018," *Journal of Physical and Chemical Reference Data*, vol. 50, no. 3, p. 033105, 2021.
- [37] M. Stock, R. Davis, E. de Mirandés, and M. J. Milton, "The revision of the SI-the result of three decades of progress in metrology," *Metrologia*, vol. 56, no. 2, p. 022001, 2019.
- [38] S. Blundell, *Magnetism in Condensed Matter*. Oxford University Press, 2001.
- [39] B. D. Cullity and C. D. Graham, *Introduction to Magnetic Materials*. Hoboken, New Jersey: John Wiley & Sons, Inc., 2nd ed., 2009.
- [40] E. R. Cohen, T. Cvitas, J. G. Frey, B. Holström, K. Kuchitsu, R. Marquardt, I. Mills, F. Pavese, M. Quack, J. Stohner, H. L. Strauss, M. Takami, and A. J. Thor, eds., *Quantities, Units and Symbols in Physical Chemistry*. The Royal Society of Chemistry, 2007.
- [41] S. Brodsky, V. Franke, J. Hiller, G. McCartor, S. Paston, and E. Prokhvatilov, "A nonperturbative calculation of the electron's magnetic moment," *Nuclear Physics B*, vol. 703, no. 1-2, pp. 333–362, 2004.
- [42] D. J. Griffiths and D. F. Schroeter, *Introduction to Quantum Mechanics*. Cambridge University Press, 2018.
- [43] L. Pauling and E. B. Wilson, *Introduction to quantum mechanics with applications to chemistry*. Courier Corporation, 2012.
- [44] R. M. White and B. Bayne, *Quantum Theory of Magnetism: Magnetic Properties of Materials*. Springer, 2007.
- [45] T. Kasuya, "A theory of metallic ferro-and antiferromagnetism on Zener's model," *Progress of Theoretical Physics*, vol. 16, no. 1, pp. 45–57, 1956.
- [46] M. A. Ruderman and C. Kittel, "Indirect exchange coupling of nuclear magnetic moments by conduction electrons," *Physical Review*, vol. 96, no. 1, pp. 99–102, 1954.
- [47] K. Yosida, "Magnetic properties of Cu-Mn alloys," *Physical Review*, vol. 106, no. 5, pp. 893–898,

1957.

- [48] J. C. Slater, "Atomic shielding constants," *Physical Review*, vol. 36, no. 1, p. 57, 1930.
- [49] N. A. Hill, "Why are there so few magnetic ferroelectrics?," *The Journal of Physical Chemistry B*, vol. 104, no. 29, pp. 6694–6709, 2000.
- [50] P. S. University, *Introduction to Inorganic Chemistry*. LibreTexts, 2021.
- [51] J. C. Slater, "Cohesion in monovalent metals," *Physical Review*, vol. 35, no. 5, p. 509, 1930.
- [52] J. H. Hetherington and F. D. C. Willard, "Two-, Three-, and Four-Atom Exchange Effects in bcc ^3He ," *Physical Review Letters*, vol. 35, no. 21, pp. 1442–1444, 1975.
- [53] B. Tsukerblat and A. Tarantul, "The nanoscopic V15 cluster: a unique magnetic polyoxometalate," in *Molecular Cluster Magnets* (R. Winpenny, ed.), p. 119, World Scientific Publishing, 2011.
- [54] A. Bocdanov and A. Hubert, "The properties of isolated magnetic vortices," *physica status solidi (b)*, vol. 186, no. 2, pp. 527–543, 1994.
- [55] G. S. Abo, Y. K. Hong, J. Park, J. Lee, W. Lee, and B. C. Choi, "Definition of magnetic exchange length," *IEEE Transactions on Magnetics*, vol. 49, no. 8, pp. 4937–4939, 2013.
- [56] J. M. Coey, *Magnetism and Magnetic Materials*. Cambridge University Press, 2010.
- [57] J. Warren, C. Barton, C. Bull, and T. Thomson, "Topography dependence of the metamagnetic phase transition in FeRh thin films," *Scientific Reports*, vol. 10, no. 1, pp. 1–12, 2020.
- [58] H. D. Young, R. A. Freedman, and A. L. Ford, *University Physics with Modern Physics*. Pearson Education, 2013.
- [59] N. F. Mott and H. H. Wills, "The electrical conductivity of transition metals," *Proceedings of the Royal Society of London. Series A, Mathematical and Physical Sciences*, vol. 153, no. 880, pp. 699–717, 1936.
- [60] S. Mankovsky, S. Polesya, K. Chadova, H. Ebert, J. Staunton, T. Gruenbaum, M. Schoen, C. Back, X. Chen, and C. Song, "Temperature-dependent transport properties of FeRh," *Physical Review B*, vol. 95, no. 15, p. 155139, 2017.
- [61] C. Hepburn, "Britney Spears' Guide to Semiconductor Physics: Density of States." <http://britneyspears.ac/physics/dos/dos.htm>, 1999.

- [62] E. E. Fullerton, M. Conover, J. Mattson, C. Sowers, and S. Bader, "Oscillatory interlayer coupling and giant magnetoresistance in epitaxial Fe/Cr (211) and (100) superlattices," *Physical Review B*, vol. 48, no. 21, p. 15755, 1993.
- [63] W. F. Gale and T. C. Totemeier, *Smithells metals reference book*. Elsevier, 8th ed., 2004.
- [64] R. Serway and J. Jewett, *Physics for Scientists and Engineers*, vol. 2. Cengage Learning, 2010.
- [65] D. Damjanovic, "Ferroelectric, dielectric and piezoelectric properties of ferroelectric thin films and ceramics," *Reports on Progress in Physics*, vol. 61, p. 1267, 1998.
- [66] Y. Chiang, D. Birnie, and W. Kingery, *Physical Ceramics: Principles for Ceramic Science and Engineering*. Wiley, 1996.
- [67] S. Santucci and V. Esposito, "Electrostrictive Ceramics and Their Applications," in *Reference Module in Materials Science and Materials Engineering*, Elsevier, 2021.
- [68] A. V. Turik, A. A. Yesis, and L. A. Reznitchenko, "Piezoelectric effect and electrostriction in ceramic ferroelectrics," *Ferroelectrics*, vol. 359, no. 1, pp. 111–116, 2007.
- [69] P. Chandra and P. B. Littlewood, "A Landau primer for ferroelectrics," in *Physics of ferroelectrics*, pp. 69–116, Springer, 2007.
- [70] H. Kay and J. Dunn, "Thickness dependence of the nucleation field of triglycine sulphate," *Philosophical Magazine*, vol. 7, no. 84, pp. 2027–2034, 1962.
- [71] S. L. Miller, R. D. Nasby, J. R. Schwank, M. S. Rodgers, and P. V. Dressendorfer, "Device modeling of ferroelectric capacitors," *Journal of Applied Physics*, vol. 68, no. 12, pp. 6463–6471, 1990.
- [72] J. F. Scott, *Switching Kinetics*, pp. 121–132. Berlin, Heidelberg: Springer Berlin Heidelberg, 2000.
- [73] J. D. Anderson, J. Merkel, D. Macmahon, and S. K. Kurinec, "Evaluation of Si:HfO₂ ferroelectric properties in MFM and MFIS structures," *IEEE Journal of the Electron Devices Society*, vol. 6, pp. 525–534, 2018.
- [74] A. K. Bain and P. Chand, *Ferroelectrics: Principles and applications*. John Wiley & Sons, 2017.
- [75] C. Carreras-Casas, O. García-Zaldívar, A. Peláiz-Barranco, Y. González-Abreu, F. Calderón-Piñar, J. Guerra, *et al.*, "Relaxor ferroelectric behavior: An approach considering both the dipolar and

- electrical conductivity contributions," *Journal of Advanced Dielectrics*, vol. 11, no. 03, p. 2140008, 2021.
- [76] V. Polinger and I. B. Bersuker, "Origin of polar nanoregions and relaxor properties of ferroelectrics," *Physical Review B*, vol. 98, no. 21, p. 214102, 2018.
- [77] J. Liu, H. Wen, W. Chen, and Y. Zheng, "Atomistic studies of temporal characteristics of polarization relaxation in ferroelectrics," *Physical Review B*, vol. 103, no. 1, p. 014308, 2021.
- [78] N. A. Spaldin, M. Fiebig, and M. Mostovoy, "The toroidal moment in condensed-matter physics and its relation to the magnetoelectric effect," *Journal of Physics: Condensed Matter*, vol. 20, no. 43, p. 434203, 2008.
- [79] J. Balun, L. Eleno, and G. Inden, "Phase equilibria in the Fe–Rh–Ti systemI. Experimental results," *Intermetallics*, vol. 15, no. 9, pp. 1237–1247, 2007.
- [80] F. Bertaut, F. de Bergevin, and G. Roullet, "Magnétisme-étude par diffraction neutronique de $\text{Fe}_{0.47}\text{Rh}_{0.53}$," *Comptes Rendus Hebdomadaires des Seances de l'Académie des Sciences*, vol. 256, no. 8, p. 1688, 1963.
- [81] Y. Wang, M. M. Decker, T. N. Meier, X. Chen, C. Song, T. Grünbaum, W. Zhao, J. Zhang, L. Chen, and C. H. Back, "Spin pumping during the antiferromagnetic-ferromagnetic phase transition of iron-rhodium," *Nature Communications*, vol. 11, no. 1, 2020.
- [82] Y. J. Hao, L. Zhang, and J. Zhu, "The electronic structure, phase transition, elastic, thermodynamic, and thermoelectric properties of FeRh: high-temperature and high-pressure study," *Zeitschrift für Naturforschung - Section A Journal of Physical Sciences*, vol. 75, no. 9, pp. 789–801, 2020.
- [83] W. Griggs, C. Bull, C. Barton, R. Griffiths, A. Caruana, C. Kinane, P. Nutter, and T. Thomson, "Polarized neutron reflectometry characterization of interfacial magnetism in an FePt/FeRh exchange spring," *Physical Review Materials*, vol. 6, no. 2, p. 024403, 2022.
- [84] M. Grimes, N. Gurung, H. Ueda, D. G. Porter, B. Pedrini, L. J. Heyderman, T. Thomson, and V. Scagnoli, "X-ray investigation of long-range antiferromagnetic ordering in FeRh," *AIP Advances*, vol. 12, no. 3, p. 035048, 2022.
- [85] M. Grimes, H. Ueda, D. Ozerov, F. Pressacco, S. Parchenko, A. Apseros, M. Scholz, Y. Kubota, T. Togashi, Y. Tanaka, *et al.*, "Determination of sub-ps lattice dynamics in FeRh thin films," *Scientific Reports*, vol. 12, no. 1, pp. 1–11, 2022.

- [86] M. G. Loving, R. Barua, C. Le Graët, C. J. Kinane, D. Heiman, S. Langridge, C. H. Marrows, and L. H. Lewis, "Strain-tuning of the magnetocaloric transition temperature in model FeRh films," *Journal of Physics D: Applied Physics*, vol. 51, no. 2, 2018.
- [87] C. Baldasseroni, C. Bordel, A. X. Gray, A. M. Kaiser, F. Kronast, J. Herrero-Albillos, C. M. Schneider, C. S. Fadley, and F. Hellman, "Temperature-driven nucleation of ferromagnetic domains in FeRh thin films," *Applied Physics Letters*, vol. 100, no. 26, p. 262401, 2012.
- [88] G. Shirane, C. Chen, P. Flinn, and R. Nathans, "Mössbauer study of hyperfine fields and isomer shifts in the Fe-Rh alloys," *Physical Review*, vol. 131, no. 1, p. 183, 1963.
- [89] G. Shirane, R. Nathans, and C. W. Chen, "Magnetic moments and unpaired spin densities in the Fe-Rh alloys," *Physical Review*, vol. 134, no. 6A, pp. A1547–A1553, 1964.
- [90] C. Bordel, J. Juraszek, D. W. Cooke, C. Baldasseroni, S. Mankovsky, J. Minár, H. Ebert, S. Moyerman, E. Fullerton, and F. Hellman, "Fe spin reorientation across the metamagnetic transition in strained FeRh thin films," *Physical Review Letters*, vol. 109, no. 11, p. 117201, 2012.
- [91] M. Gruner, E. Hoffmann, and P. Entel, "Instability of the rhodium magnetic moment as the origin of the metamagnetic phase transition in α -FeRh," *Physical Review B*, vol. 67, no. 6, p. 064415, 2003.
- [92] L. . Chua, "Memristor-The Missing Circuit Element," *IEEE Transactions on Circuit Theory*, vol. 18, no. 5, p. 507, 1971.
- [93] D. B. Strukov, G. S. Snider, D. R. Stewart, and R. S. Williams, "The missing memristor found," *Nature*, vol. 453, no. 7191, pp. 80–83, 2008.
- [94] M. Jiang, X. Chen, X. Zhou, Y. Wang, F. Pan, and C. Song, "Influence of film composition on the transition temperature of FeRh films," *Journal of Crystal Growth*, vol. 438, pp. 19–24, 2016.
- [95] C. W. Barton, T. A. Ostler, D. Huskisson, C. J. Kinane, S. J. Haigh, G. Hrkac, and T. Thomson, "Substrate induced strain field in FeRh epilayers grown on single crystal MgO(001) substrates," *Scientific Reports*, vol. 7, p. 44397, 2017.
- [96] G. Kästle, T. Müller, H.-G. Boyen, A. Klimmer, and P. Ziemann, "Resistivity and phonon softening in ion-irradiated epitaxial gold films," *Journal of Applied Physics*, vol. 96, no. 12, pp. 7272–7277, 2004.
- [97] C. Bull, C. W. Barton, W. Griggs, A. Caruana, C. J. Kinane, P. W. Nutter, and T. Thomson,

- “PNR study of the phase transition in FeRh thin films,” *APL Materials*, vol. 7, no. 10, 2019.
- [98] D. G. Merkel, A. Lengyel, D. L. Nagy, A. Németh, Z. E. Horváth, C. Bogdán, M. A. Gracheva, G. Hegedűs, S. Sajti, G. Z. Radnóczy, *et al.*, “Reversible control of magnetism in FeRh thin films,” *Scientific Reports*, vol. 10, no. 1, pp. 1–11, 2020.
- [99] C. Baldasseroni, G. K. Pálsson, C. Bordel, S. Valencia, A. A. Unal, F. Kronast, S. Nemsak, C. S. Fadley, J. A. Borchers, B. B. Maranville, and F. Hellman, “Effect of capping material on interfacial ferromagnetism in FeRh thin films,” *Journal of Applied Physics*, vol. 115, no. 4, 2014.
- [100] W. J. Griggs, *Disorder- and strainmediated magnetic phase modifications in FeRh thin films*. PhD thesis, The University of Manchester, Manchester UK, 2021.
- [101] B. Moskowitz, M. Jackson, and V. Chandler, “11.05 - Geophysical Properties of the Near-Surface Earth: Magnetic Properties,” in *Treatise on Geophysics* (G. Schubert, ed.), pp. 139–174, Oxford: Elsevier, 2nd ed., 2015.
- [102] J. Launay and G. Horowitz, “Crystal growth and photoelectrochemical study of Zr-doped α -Fe₂O₃ single crystal,” *Journal of Crystal Growth*, vol. 57, no. 1, pp. 118–124, 1982.
- [103] E. Verwey, “Electronic conduction of magnetite (Fe₃O₄) and its transition point at low temperatures,” *Nature*, vol. 144, no. 3642, pp. 327–328, 1939.
- [104] S. Todo, N. Takeshita, T. Kanehara, T. Mori, and N. Mori, “Metallization of magnetite (Fe₃O₄) under high pressure,” *Journal of Applied Physics*, vol. 89, no. 11, pp. 7347–7349, 2001.
- [105] A. Jain, S. P. Ong, G. Hautier, W. Chen, W. D. Richards, S. Dacek, S. Cholia, D. Gunter, D. Skinner, G. Ceder, *et al.*, “Commentary: The Materials Project: A materials genome approach to accelerating materials innovation,” *APL Materials*, vol. 1, no. 1, p. 011002, 2013.
- [106] J. A. Arregi, M. Horký, K. Fabianová, R. Tolley, E. E. Fullerton, and V. Uhliř, “Magnetization reversal and confinement effects across the metamagnetic phase transition in mesoscale FeRh structures,” *Journal of Physics D: Applied Physics*, vol. 51, no. 10, pp. 105001–, 2018.
- [107] L. Jiang, J. Weber, F. M. Puglisi, P. Pavan, L. Larcher, W. Frammelsberger, G. Benstetter, and M. Lanza, “Understanding current instabilities in conductive atomic force microscopy,” *Materials*, vol. 12, no. 3, 2019.
- [108] B. Noheda, D. E. Cox, G. Shirane, J. Gao, and Z. G. Ye, “Phase diagram of the ferroelectric relaxor $(1-x)\text{PbMg}_{1/3}\text{Nb}_{2/3}\text{O}_3-x\text{PbTiO}_3$,” *Physical Review B - Condensed Matter and Materials*

- Physics*, vol. 66, no. 5, pp. 541041–5410410, 2002.
- [109] Z. Kutnjak, J. Petzelt, and R. Blinc, “The giant electromechanical response in ferroelectric relaxors as a critical phenomenon,” *Nature*, vol. 441, no. 7096, pp. 956–959, 2006.
- [110] P. Virtanen et al., “SciPy 1.0: Fundamental Algorithms for Scientific Computing in Python,” *Nature Methods*, vol. 17, pp. 261–272, 2020.
- [111] M. Eremenko, V. Krayzman, A. Bosak, H. Playford, K. Chapman, J. Woicik, B. Ravel, and I. Levin, “Local atomic order and hierarchical polar nanoregions in a classical relaxor ferroelectric,” *Nature Communications*, vol. 10, no. 1, pp. 1–9, 2019.
- [112] H. Fu and R. E. Cohen, “Polarization rotation mechanism for ultrahigh electromechanical response in single-crystal piezoelectrics,” *Nature*, vol. 403, no. 6767, pp. 281–283, 2000.
- [113] H. Takahashi, H. Suzuki, and Y. Namba, “Surface topography and dielectric properties of polished PMN-PT single crystals,” *CIRP Annals - Manufacturing Technology*, vol. 65, no. 1, pp. 541–544, 2016.
- [114] R. Wongmaneeerung, R. Guo, A. Bhalla, R. Yimnirun, and S. Ananta, “Thermal expansion properties of PMN–PT ceramics,” *Journal of Alloys and Compounds*, vol. 461, no. 1-2, pp. 565–569, 2008.
- [115] C. Li, S. Minne, B. Pittenger, and A. Mednick, “Simultaneous Electrical and Mechanical Property Mapping at the Nanoscale with PeakForce TUNA,” Tech. Rep. 132, Bruker Corporation, Santa Barbara, CA, 2011.
- [116] Bruker Nano Surfaces Division, *The Latest Advances in AFM Nanoelectrical Modes*. Santa Barbara: Bruker Corporation, 2020.
- [117] S. B. Kaemmer, “Introduction to Bruker’s ScanAsyst and PeakForce Tapping AFM Technology,” Tech. Rep. 133, Bruker Corporation, Santa Barbara, CA, 2011.
- [118] Bruker Corporation, “Dimension Icon with ScanAsyst,” Tech. Rep. 004-1023-000, Bruker Corporation, Santa Barbara, CA, 2010.
- [119] Bruker Corporation, “Bruker AFM Probes | Scanning Probe and Atomic Force Instrumentation.” <https://www.brukerafmprobes.com>, 2022.
- [120] B. Ohler, “Practical advice on the determination of cantilever spring constants,” Tech. Rep. AN94,

Veeco Instruments, Santa Barbara, CA, 2007.

- [121] J. E. Sader, I. Larson, P. Mulvaney, and L. R. White, "Method for the calibration of atomic force microscope cantilevers," *Review of Scientific Instruments*, vol. 66, no. 7, pp. 3789–3798, 1995.
- [122] R. Burdett, "Amplitude Modulated Signals: The Lock-in Amplifier," in *Handbook of Measuring System Design* (P. H. Sydenham and R. Thorn, eds.), New Jersey: John Wiley & Sons, 2005.
- [123] Bruker Corporation, "NanoScope V Controller Manual NanoScope Software Version 8," Tech. Rep. 004-1030-000, Bruker Corporation, Santa Barbara, CA, 2011.
- [124] Rocky Mountain Nanotechnology, "Atomic Force Microscopy Applications - Rocky Mountain Nano." <https://rmnano.com/tech-data>, 2021.
- [125] O. Kazakova, R. Puttock, C. Barton, H. Corte-León, M. Jaafar, V. Neu, and A. Asenjo, "Frontiers of magnetic force microscopy," *Journal of Applied Physics*, vol. 125, no. 6, p. 060901, 2019.
- [126] J. Lohau, S. Kirsch, A. Carl, G. Dumpich, and E. F. Wassermann, "Quantitative determination of effective dipole and monopole moments of magnetic force microscopy tips," *Journal of Applied Physics*, vol. 86, no. 6, pp. 3410–3417, 1999.
- [127] V. M. Muller, V. S. Yushchenko, and B. V. Derjaguin, "On the influence of molecular forces on the deformation of an elastic sphere and its sticking to a rigid plane," *Journal of Colloid and Interface Science*, vol. 77, no. 1, pp. 91–101, 1980.
- [128] M. D. Pashley, "Further consideration of the DMT model for elastic contact," *Colloids and Surfaces*, vol. 12, pp. 69–77, 1984.
- [129] I. N. Sneddon, "The relation between load and penetration in the axisymmetric boussinesq problem for a punch of arbitrary profile," *International Journal of Engineering Science*, vol. 3, no. 1, pp. 47–57, 1965.
- [130] B. V. Derjaguin, V. M. Muller, and Y. P. Toporov, "Effect of contact deformations on the adhesion of particles," *Journal of Colloid and Interface Science*, vol. 53, no. 2, pp. 314–326, 1975.
- [131] K. L. Johnson, K. Kendall, and A. D. Roberts, "Surface energy and the contact of elastic solids," *Proceedings of the Royal Society of London. Series A, Mathematical and Physical Sciences*, vol. 324, no. 1558, pp. 301–313, 1971.
- [132] Bruker Corporation, ed., *The Latest Advances in AFM Nanoelectrical Modes*. Bruker Corporation,

2019.

- [133] G. Benstetter, A. Hofer, D. Liu, W. Frammelsberger, and M. Lanza, "Fundamentals of CAFM Operation Modes," in *Conductive Atomic Force Microscopy: Applications in Nanomaterials* (M. Lanza, ed.), ch. 3, pp. 59–83, John Wiley and Sons, 1st ed., 2017.
- [134] V. B. Engelkes, J. M. Beebe, and C. D. Frisbie, "Analysis of the causes of variance in resistance measurements on metal-molecule-metal junctions formed by conducting-probe atomic force microscopy," *Journal of Physical Chemistry B*, vol. 109, no. 35, pp. 16801–16810, 2005.
- [135] R. Holm, "Calculation of constriction resistances with constant resistivity ρ in an isotropic material," in *Electric Contacts Theory and Application*, ch. 4, pp. 9–16, Berlin: Springer-Verlag, 4th ed., 1967.
- [136] P. De Wolf, J. Snauwaert, L. Hellemans, T. Clarysse, W. Vandervorst, M. D'Olieslaeger, and D. Quaeys, "Lateral and vertical dopant profiling in semiconductors by atomic force microscopy using conducting tips," *Journal of Vacuum Science and Technology A: Vacuum, Surfaces, and Films*, vol. 13, no. 3, pp. 1699–1704, 1995.
- [137] P. De Wolf, T. Clarysse, W. Vandervorst, L. Hellemans, P. Niedermann, and W. Hänni, "Cross-sectional nano-spreading resistance profiling," *Journal of Vacuum Science and Technology B: Microelectronics and Nanometer Structures Processing, Measurement, and Phenomena*, vol. 16, no. 1, pp. 355–361, 1998.
- [138] M. Febvre, "Nano-Electrical Characterisation using AFM - Part 2: Advanced Modes." Online Webinar, April 2020.
- [139] P. D. Foote, "The total emissivity of platinum and the relation between total emissivity and resistivity," *Journal of the Washington Academy of Sciences*, vol. 5, no. 1, pp. 1–7, 1915.
- [140] W. H. Preece, "II. On the heating effects of electric currents," *Proceedings of the Royal Society of London*, vol. 36, no. 228-231, pp. 464–471, 1883.
- [141] K. C.-Y. Chen, L. K. Warne, Y. T. Lin, R. L. Kinzel, J. D. Huff, M. B. McLean, M. W. Jenkins, and B. M. Rutherford, "Conductor fusing and gapping for bond wires," *Progress In Electromagnetics Research M*, vol. 31, pp. 199–214, 2013.
- [142] D. Brooks, "Fusing Current-When Traces Melt Without a Trace," *Printed Circuit Design, a Miller Freeman publication*, 1998.

- [143] T. Glatzel, M. C. Lux-Steiner, E. Strassburg, A. Boag, and Y. Rosenwaks, "Principles of Kelvin Probe Force Microscopy," in *Scanning Probe Microscopy*, vol. I, ch. 4, pp. 113–131, New York: Springer Science+Business Media LLC, 1st ed., 2007.
- [144] S. Hudlet, M. Saint Jean, C. Guthmann, and J. Berger, "Evaluation of the capacitive force between an atomic force microscopy tip and a metallic surface," *The European Physical Journal B - Condensed Matter and Complex Systems*, vol. 2, pp. 5–10, 1998.
- [145] S. Hong, J. Woo, H. Shin, J. U. Jeon, Y. E. Pak, E. L. Colla, N. Setter, E. Kim, and K. No, "Principle of ferroelectric domain imaging using atomic force microscope," *Journal of Applied Physics*, vol. 89, no. 2, pp. 1377–1386, 2001.
- [146] S. M. Neumayer, S. Saremi, L. W. Martin, L. Collins, A. Tselev, S. Jesse, S. V. Kalinin, and N. Balke, "Piezoresponse amplitude and phase quantified for electromechanical characterization," *Journal of Applied Physics*, vol. 128, no. 17, p. 171105, 2020.
- [147] F. Johann, Y. J. Ying, T. Jungk, A. Hoffmann, C. L. Sones, R. W. Eason, S. Mailis, and E. Soergel, "Depth resolution of piezoresponse force microscopy," *Applied Physics Letters*, vol. 94, no. 17, 2009.
- [148] H. J. Chung, X. N. Xie, C. H. Sow, A. A. Bettiol, and A. T. S. Wee, "Polymeric conical structure formation by probe-induced electrohydrodynamical nanofluidic motion," *Applied Physics Letters*, vol. 88, no. 2, pp. 1–3, 2006.
- [149] O. Custance, R. Perez, and S. Morita, "Atomic force microscopy as a tool for atom manipulation," *Nature Nanotechnology*, vol. 4, no. 12, pp. 803–810, 2009.
- [150] Bruker Corporation, "nanoscope · PyPI." <https://pypi.org/project/nanoscope/1.0.300/>, 2021.
- [151] A. S. Paul B. Kelter, Michael D. Mosher, *Chemistry: The Practical Science*. Cengage Learning, 2008.
- [152] Fisher Scientific UK, "Propan-2-ol Safety Data Sheet," Tech. Rep. FSUP7507, Fisher Scientific UK, Loughborough, UK, 2021.
- [153] Fisher Scientific UK, "Acetone Safety Data Sheet," Tech. Rep. FSUA0606, Fisher Scientific UK, Loughborough, UK, 2020.
- [154] RS Components Ltd., "RS Pro Bottle of Silver Conductive Adhesive Paint Datasheet," Tech. Rep. 186-3593, RS Components Ltd., Corby, UK, 2022.

- [155] J. L. Warren, *Fabrication and characterisation of novel materials and devices for spintronics*. PhD thesis, The University of Manchester, Manchester UK, 2018.
- [156] Asylum Research, “25PT300B - Asylum Research AFM Probe Store.” <https://estore.oxinst.com/asia/zid808.RMN.25PT300B>, 2022.
- [157] Y. Zhou, X. Chong, M. Hu, Y. Wei, C. Hu, A. Zhang, and J. Feng, “Probing the mechanical properties of ordered and disordered Pt-Ir alloys by first-principles calculations,” *Physics Letters A*, vol. 405, p. 127424, 2021.
- [158] F. Smits, “Measurement of sheet resistivities with the four-point probe,” *Bell System Technical Journal*, vol. 37, no. 3, pp. 711–718, 1958.
- [159] Adama Innovations, “Apex Sharp Diamond AFM Probes – Adama Innovations.” <https://www.adama.tips/products-apex-sharp>, 2022.
- [160] P. De Wolf, M. Geva, T. Hantschel, W. Vandervorst, and R. B. Bylsma, “Two-dimensional carrier profiling of InP structures using scanning spreading resistance microscopy,” *Applied Physics Letters*, vol. 73, no. 15, pp. 2155–2157, 1998.
- [161] K. Natori, “Ballistic/quasi-ballistic transport in nanoscale transistor,” *Applied Surface Science*, vol. 254, no. 19, pp. 6194–6198, 2008.
- [162] S. Dutta, K. Sankaran, K. Moors, G. Pourtois, S. Van Elshocht, J. Bömmels, W. Vandervorst, Z. Tőkei, and C. Adelmann, “Thickness dependence of the resistivity of platinum-group metal thin films,” *Journal of Applied Physics*, vol. 122, no. 2, p. 025107, 2017.
- [163] J. Agustsson, U. Arnalds, A. Ingason, K. B. Gylfason, K. Johnsen, S. Olafsson, and J. T. Gudmundsson, “Electrical resistivity and morphology of ultra thin Pt films grown by dc magnetron sputtering on SiO₂,” in *Journal of Physics: Conference Series*, vol. 100, p. 082006, IOP Publishing, 2008.
- [164] J. G. Tobin, S. A. Morton, S. W. Yu, G. D. Waddill, I. K. Schuller, and S. A. Chambers, “Spin resolved photoelectron spectroscopy of Fe₃O₄: the case against half-metallicity,” *Journal of Physics: Condensed Matter*, vol. 19, no. 31, p. 315218, 2007.
- [165] D. Chicot, J. Mendoza, A. Zaoui, G. Louis, V. Lepingue, F. Roudet, and J. Lesage, “Mechanical properties of magnetite (Fe₃O₄), hematite (α -Fe₂O₃) and goethite (α -FeO · OH) by instrumented indentation and molecular dynamics analysis,” *Materials Chemistry and Physics*, vol. 129, no. 3, pp. 862–870, 2011.

- [166] A. C. Fischer-Cripps, *Introduction to contact mechanics*, vol. 101. Springer, 2007.
- [167] Hudson Institute of Mineralogy, “Hematite: Mineral information, data and localities..” <https://www.mindat.org/min-1856.html>, 2022.
- [168] Hudson Institute of Mineralogy, “Magnetite: Mineral information, data and localities..” <https://www.mindat.org/min-2538.html>, 2022.
- [169] Element Collection Inc, “Vickers Hardness for all the elements in the Periodic Table.” <https://periodictable.com/Properties/A/VickersHardness.al.html>, 2017.
- [170] Goodfellow, “Properties: Supplier Data - Silicon (Si) (Goodfellow).” <https://www.azom.com/article.aspx?ArticleID=1851>, 2003.
- [171] S. Dub, P. Lytvyn, V. Strelchuk, A. Nikolenko, Y. Stubrov, I. Petrusha, T. Taniguchi, and S. Ivakhnenko, “Vickers hardness of diamond and cBN single crystals: AFM approach,” *Crystals*, vol. 7, no. 12, p. 369, 2017.
- [172] G. M. Pharr, E. G. Herbert, and Y. Gao, “The indentation size effect: a critical examination of experimental observations and mechanistic interpretations,” *Annual Review of Materials Research*, vol. 40, pp. 271–292, 2010.
- [173] Keithley Instruments, Inc., “Series 2400 SourceMeter User’s Manual,” Tech. Rep. 2400S-800-01, Keithley Instruments, Inc., Cleveland, Ohio, 2011.
- [174] PyVISA Authors, “PyVISA: Control your instruments with Python – PyVISA 1.11.3 documentation.” <https://pyvisa.readthedocs.io/en/1.11.3/>, 2020.
- [175] Engineering ToolBox, “Cantilever Beams - Moments and Deflections.” https://www.engineeringtoolbox.com/cantilever-beams-d_1848.html, 2013.
- [176] Engineering ToolBox, “Area Moment of Inertia - Typical Cross Sections I.” https://www.engineeringtoolbox.com/area-moment-inertia-d_1328.html, 2008.
- [177] A. Savitzky and M. J. Golay, “Smoothing and differentiation of data by simplified least squares procedures,” *Analytical Chemistry*, vol. 36, no. 8, pp. 1627–1639, 1964.
- [178] E. O. Brigham and R. Morrow, “The fast Fourier transform,” *IEEE Spectrum*, vol. 4, no. 12, pp. 63–70, 1967.
- [179] Element Collection Inc, “Thermal Conductivity for all the elements in the Periodic Table.” <https://periodictable.com/Properties/T/ThermalConductivity.al.html>, 2017.

[//periodictable.com/Properties/A/ThermalConductivity.al.html](http://periodictable.com/Properties/A/ThermalConductivity.al.html), 2017.

- [180] K. Wasa, I. Kanno, and H. Kotera, *Handbook of sputter deposition technology: fundamentals and applications for functional thin films, nano-materials and MEMS*. William Andrew, 2012.
- [181] P. Schattschneider, S. Rubino, and C. Hébert, “Circular Dichroism in the Transmission Electron Microscope,” in *Encyclopedia of Materials: Science and Technology* (K. J. Buschow, R. W. Cahn, M. C. Flemings, B. Ilshner, E. J. Kramer, S. Mahajan, and P. Veyssi re, eds.), pp. 1–11, Oxford: Elsevier, 2007.
- [182] M. L. Baker, M. W. Mara, J. J. Yan, K. O. Hodgson, B. Hedman, and E. I. Solomon, “K- and L-edge X-ray absorption spectroscopy (XAS) and resonant inelastic X-ray scattering (RIXS) determination of differential orbital covalency (DOC) of transition metal sites,” *Coordination Chemistry Reviews*, vol. 345, pp. 182–208, 2017.
- [183] C. Baldasseroni, C. Bordel, C. Antonakos, A. Scholl, K. H. Stone, J. B. Kortright, and F. Hellman, “Temperature-driven growth of antiferromagnetic domains in thin-film FeRh,” *Journal of Physics Condensed Matter*, vol. 27, no. 25, p. 256001, 2015.
- [184] J. St hr, H. Padmore, S. Anders, T. St mmler, and M. Scheinfein, “Principles of X-ray magnetic dichroism spectromicroscopy,” *Surface Review and Letters*, vol. 5, no. 06, pp. 1297–1308, 1998.
- [185] NT-MDT, “Mfm01 – nt-mdt tips.” <https://www.ntmdt-tips.com/products/view/mfm01>, 2022.
- [186] M. Lente, A. Zanin, S. Assis, I. Santos, D. Garcia, and J. Eiras, “Ferroelectric domain dynamics in PMN-PT ceramics,” *Ferroelectrics*, vol. 296, no. 1, pp. 149–155, 2003.
- [187] F. Li, L. Jin, Z. Xu, and S. Zhang, “Electrostrictive effect in ferroelectrics: An alternative approach to improve piezoelectricity,” *Applied Physics Reviews*, vol. 1, no. 1, 2014.
- [188] F. Cordero, “Elastic properties and enhanced piezoelectric response at morphotropic phase boundaries,” *Materials*, vol. 8, no. 12, pp. 8195–8245, 2015.
- [189] V. Aleshin and I. Raevski, “Negative Poisson’s ratio and piezoelectric anisotropy of tetragonal ferroelectric single crystals,” *Journal of Applied Physics*, vol. 112, no. 11, p. 114101, 2012.
- [190] Bruker Corporation, “Switching Spectroscopy Piezoresponse Force Microscopy (SS-PFM) | Bruker.” <https://www.bruker.com/en/products-and-solutions/microscopes/materials-afm/afm-modes/ss-pfm.html>, 2022.

- [191] K. Qian, B. Fang, Q. Du, J. Ding, X. Zhao, and H. Luo, "Phase development and electrical properties of $\text{Pb}(\text{Mg}_{1/3}\text{Nb}_{2/3})\text{O}_3\text{--PbTiO}_3$ ceramics prepared by partial oxalate route," *physica status solidi (a)*, vol. 210, no. 6, pp. 1149–1156, 2013.

Appendix A

Derivations

A.1 Crystal plane separation - equation (2.7)

By definition, one crystal plane must pass through each lattice point, so the origin $(0, 0, 0)$ is on a plane.

By definition of the Miller indices, three points on the nearest plane in the triclinic system are

$$\begin{aligned}\vec{p}_1 &= \frac{1}{h} \vec{a} = \frac{a}{h} \hat{x} \\ \vec{p}_2 &= \frac{1}{k} \vec{b} = \frac{b \cos(\gamma)}{k} \hat{x} + \frac{b \sin(\gamma)}{k} \hat{y} \\ \vec{p}_3 &= \frac{1}{l} \vec{c} = \frac{c_x}{l} \hat{x} + \frac{c_y}{l} \hat{y} + \frac{c_z}{l} \hat{z}\end{aligned}$$

using the lattice vectors defined in equation (2.3).

A vector orthogonal to the crystal planes is thus

$$\begin{aligned}\vec{V} &= (\vec{p}_2 - \vec{p}_1) \times (\vec{p}_3 - \vec{p}_1) \\ &= \frac{bc_z \sin(\gamma)}{kl} \hat{x} + \left(\frac{ac_z}{hl} - \frac{bc_z \cos(\gamma)}{kl} \right) \hat{y} + \left(\frac{bc_y \cos(\gamma) - bc_x \sin(\gamma)}{kl} + \frac{ab \sin(\gamma)}{hk} - \frac{ac_y}{hl} \right) \hat{z} \quad (\text{A.1}) \\ &\equiv V_x \hat{x} + V_y \hat{y} + V_z \hat{z} .\end{aligned}$$

Now, the interplanar spacing is given by

$$d = |t\vec{V}|$$

where t is a coefficient such that some point \vec{p}_i in a plane plus the vector $t\vec{V}$ gives some point \vec{r}_i in the neighbouring plane.

It is clear that for all i, j ,

$$\vec{V} \cdot (\vec{r}_i - \vec{r}_j) = 0 ,$$

so t satisfies

$$\vec{V} \cdot (\vec{p}_i + t\vec{V} - \vec{r}_j) = \vec{V} \cdot [(\vec{p}_i - \vec{r}_j) + t\vec{V}] = 0 , \quad (\text{A.2})$$

where $\vec{p}_i - \vec{r}_j$ is any vector between the two planes.

A possible vector uses the Miller indices. The vectors \vec{p}_1 , \vec{p}_2 , and \vec{p}_3 each run between adjacent planes, so the sum will run between three planes, thus

$$\vec{p}_i - \vec{r}_j = \frac{1}{3} (\vec{p}_1 + \vec{p}_2 + \vec{p}_3) = \frac{1}{3} \left(\frac{a}{h} + \frac{b \cos(\gamma)}{k} + \frac{c_x}{l} \right) \hat{x} + \frac{1}{3} \left(\frac{b \sin(\gamma)}{k} + \frac{c_y}{l} \right) \hat{y} + \frac{1}{3} \left(\frac{c_z}{l} \right) \hat{z}. \quad (\text{A.3})$$

Note that the sum of the three vectors was used because the plane may intercept as few as one lattice vector, thus all must be included to ensure the resulting vector does run between the two planes.

Substituting equation (A.3) into (A.2) produces

$$\begin{aligned} 0 &= \vec{V} \cdot \left[\frac{1}{3} \left(\frac{a}{h} + \frac{b \cos(\gamma)}{k} + \frac{c_x}{l} \right) \hat{x} + \frac{1}{3} \left(\frac{b \sin(\gamma)}{k} + \frac{c_y}{l} \right) \hat{y} + \frac{1}{3} \left(\frac{c_z}{l} \right) \hat{z} + t \vec{V} \right] \\ &= \begin{pmatrix} V_x \\ V_y \\ V_z \end{pmatrix} \cdot \begin{pmatrix} tV_x + \frac{a}{3h} + \frac{b \cos(\gamma)}{3k} + \frac{c_x}{3l} \\ tV_y + \frac{b \sin(\gamma)}{3k} + \frac{c_y}{3l} \\ tV_z + \frac{c_z}{3l} \end{pmatrix} \\ &\Rightarrow tV_x^2 + tV_y^2 + tV_z^2 = -\frac{a}{3h}V_x - \frac{b \cos(\gamma)}{3k}V_x - \frac{c_x}{3l}V_x - \frac{b \sin(\gamma)}{3k}V_y - \frac{c_y}{3l}V_y - \frac{c_z}{3l}V_z \\ &\Rightarrow t = -\frac{1}{V_x^2 + V_y^2 + V_z^2} \left[\frac{a}{3h}V_x + \frac{b \cos(\gamma)}{3k}V_x + \frac{c_x}{3l}V_x + \frac{b \sin(\gamma)}{3k}V_y + \frac{c_y}{3l}V_y + \frac{c_z}{3l}V_z \right]. \quad (\text{A.4}) \end{aligned}$$

Equation (A.4) may be simplified to

$$\begin{aligned} t &= -\frac{1}{|\vec{V}|^2} \frac{abc_z \sin(\gamma)}{hkl} \\ &= -\frac{1}{|\vec{V}|^2} \frac{abc}{hkl} [1 - \cos^2(\alpha) - \cos^2(\beta) - \cos^2(\gamma) + 2 \cos(\alpha) \cos(\beta) \cos(\gamma)]^{1/2}, \end{aligned}$$

where equation (2.6) for the unit cell volume was used. Thus the plane separation may be written as

$$\frac{1}{d^2} = \frac{1}{t^2 |\vec{V}|^2} = \frac{\left(\frac{hkl}{abc} \right)^2 |\vec{V}|^2}{1 - \cos^2(\alpha) - \cos^2(\beta) - \cos^2(\gamma) + 2 \cos(\alpha) \cos(\beta) \cos(\gamma)}. \quad (\text{A.5})$$

Finally, by substituting equation (A.1) into (A.5), expanding the brackets, and simplifying, the final result of

$$\frac{1}{d^2} = \frac{\begin{pmatrix} \frac{2hk}{ab} [\cos(\alpha) \cos(\beta) - \cos(\gamma)] + \frac{2hl}{ac} [\cos(\alpha) \cos(\gamma) - \cos(\beta)] \\ + \frac{2kl}{bc} [\cos(\beta) \cos(\gamma) - \cos(\alpha)] + \frac{h^2}{a^2} \sin^2(\alpha) + \frac{k^2}{b^2} \sin^2(\beta) + \frac{l^2}{c^2} \sin^2(\gamma) \end{pmatrix}}{1 - \cos^2(\alpha) - \cos^2(\beta) - \cos^2(\gamma) + 2 \cos(\alpha) \cos(\beta) \cos(\gamma)} \quad (\text{A.6})$$

may be obtained.

A.2 Deformation in the Hertzian model - equation (4.26)

The dashed lines drawn on Figure (4.12b) form a clear right-angled triangle, from which Pythagoras' theorem provides

$$(r_t)^2 = \left(r_t - \delta_t - \frac{\delta_s}{2}\right)^2 + (r_{c,0})^2 \equiv (r_t - \Delta)^2 + (r_{c,0})^2 . \quad (\text{A.7})$$

The substitution $\Delta \equiv \delta_t + \frac{\delta_s}{2}$ has been introduced for clarity.

This may be expanded and rearranged to form the quadratic

$$\Delta^2 - 2r_t\Delta + r_{c,0}^2 = 0 , \quad (\text{A.8})$$

thus giving

$$\Delta = r_t \pm \sqrt{r_t^2 - r_{c,0}^2} . \quad (\text{A.9})$$

The Hertzian model requires $\Delta < r_t$ so

$$\Delta = r_t \left[1 - \sqrt{1 - \left(\frac{r_{c,0}}{r_t}\right)^2} \right] . \quad (\text{A.10})$$

Additionally, for this model it may be assumed that $r_{c,0} \ll r_t$, so the binomial approximation may be used giving

$$\Delta = r_t \left\{ 1 - \left[1 - \frac{1}{2} \left(\frac{r_{c,0}}{r_t}\right)^2 \right] \right\} = \frac{1}{2} \frac{r_{c,0}^2}{r_t} . \quad (\text{A.11})$$

A.3 Resistance of a truncated cone - equation (5.2)

The truncated cone of height h_t and side angle α has a lower radius of r_b and an upper radius of $r_b + h_t \tan(\alpha)$. Let the normal distance from the centre of the smaller face be z .

Consider the cone to be formed by a series of circular discs with resistivity ρ , cross-sectional area $A(z) = \pi r(z)$, and thickness dz . The resistance of each disc is therefore

$$dR = \frac{\rho}{A(z)} dz = \frac{\rho}{\pi r(z)^2} dz . \quad (\text{A.12})$$

The radius at some height z is simply

$$r(z) = r_b + z \tan(\alpha) \quad (\text{A.13})$$

so the resistance is

$$\begin{aligned}
 R &= \int_{z=0}^{h_t} dR(z) \\
 &= \int_0^{h_t} \frac{\rho}{\pi} \frac{1}{[r_b + z \tan(\alpha)]^2} dz \\
 &= \frac{\rho}{\pi} \left\{ \frac{1}{r_b \tan(\alpha)} - \frac{1}{\tan(\alpha) [h_t \tan(\alpha) + r_b]} \right\}.
 \end{aligned} \tag{A.14}$$

The cone base radius r_b is inevitably much smaller than the height of the tip, so $1/h_t \ll 1/r_b$ yielding

$$R \approx \frac{\rho}{\pi r_b \tan(\alpha)}. \tag{A.15}$$

Finally, $r_b = r_t \cos(\alpha)$ so

$$R \approx \frac{\rho}{\pi r_t \sin(\alpha)}. \tag{A.16}$$

A.3.1 Resistance of a hollow truncated cone - equation (5.3)

The cone is now a shell with wall width normal to the surface of r_t , so horizontal width is equal to the base radius $r_b = r_t \cos(\alpha)$ and each disc is replaced by an annulus with area

$$A(z) = \pi r(z)^2 - \pi [r(z) - r_b]^2 = \pi r_b [2r(z) - r_b] = \pi r_b [2z \tan(\alpha) + r_b], \tag{A.17}$$

hence the resistance is

$$\begin{aligned}
 R &= \int_{z=0}^{h_t} dR(z) \\
 &= \int_0^{h_t} \frac{\rho}{\pi r_b} \frac{1}{2z \tan(\alpha) + r_b} dz \\
 &= \frac{\rho}{2\pi r_b \tan(\alpha)} \ln \left[\frac{2h_t \tan(\alpha) + r_b}{r_b} \right].
 \end{aligned} \tag{A.18}$$

The cone base radius r_b is inevitably much smaller than the height of the tip h_t , so substituting $r_b = r_t \cos(\alpha)$ back in yields

$$R \approx \frac{\rho}{2\pi r_t \sin(\alpha)} \ln \left[\frac{2h_t \sin(\alpha)}{r_t \cos^2(\alpha)} \right]. \tag{A.19}$$

A.4 Resistance of a truncated spherical cap - equation (5.4)

The truncated spherical cap is characterised by its radius r_t , as well as the radii of the lower and upper circular faces, which for an engaged AFM probe are known to be r_c and $r_t \cos(\alpha)$ respectively. Let the height above the base of the sphere be z .

Consider the cap to be formed by a series of circular discs with resistivity ρ , cross-sectional area $A(z) = \pi r(z)$, and thickness dz . The resistance of each disc is therefore

$$dR = \frac{\rho}{A(z)} dz = \frac{\rho}{\pi r(z)^2} dz . \quad (\text{A.20})$$

The parameter to integrate over for a sphere is the polar angle from the vertical θ , so write

$$z(\theta) = r_t [1 - \cos(\theta)] \quad (\text{A.21})$$

$$r(\theta) = r_t \sin(\theta) . \quad (\text{A.22})$$

The integral is simpler in terms of the parameter $u = \sin(\theta)$, so

$$z(u) = r_t (1 - \sqrt{1 - u^2}) \quad (\text{A.23})$$

$$\frac{dz}{du} = \frac{r_t u}{\sqrt{1 - u^2}} \quad (\text{A.24})$$

$$r(u) = r_t u \quad (\text{A.25})$$

yielding

$$\begin{aligned} R &= \int_{u=r_c/r_t}^{\sin(\alpha)} dR(u) \\ &= \int_{r_c/r_t}^{\sin(\alpha)} \frac{\rho}{\pi} \frac{1}{r_t^2 u^2} \frac{r_t u}{\sqrt{1 - u^2}} du = \frac{\rho}{\pi r_t} \int_{r_c/r_t}^{\sin(\alpha)} \frac{1}{u \sqrt{1 - u^2}} du \\ &= \frac{\rho}{\pi r_t} \left\{ \tanh^{-1} \left[1 - \left(\frac{r_c}{r_t} \right)^2 \right] - \tanh^{-1} [\cos(\alpha)] \right\} . \end{aligned} \quad (\text{A.26})$$